THE STABILITY PROPERTIES OF SOME RHEOLOGICAL FLOWS

by

HUSEYIN DEMIR B. Sc., M. Sc.

A thesis submitted in partial fulfilment of the requirements of the

University of Glamorgan/Prifysgol Morgannwg

for the degree of Doctor of Philosophy.

School of Accounting and Mathematics

Division of Maths and Computing

The University of Glamorgan

Mid Glamorgan

CF37 1DL

1996

Everything flows if you wait long enough,

Even the mountains!

In dedication to my Grandmother ZELIHA DEMIR who brought me up as well as my brothers and sisters, and my parents ISMAIL and SAHIDE DEMIR. Also in dedication to my wife AYNUR, my daughter HILAL and son OGUZHAN with my best wishes forever.

DECLARATION

This is to certify that neither this thesis or any part of it has been presented or is currently being submitted in candidature for any other degree other than the degree of Doctor of Philosophy of the University of Glamorgan/Prifysgol Morgannwg.

Canditate .....

Acknowledgements

Firstly, I wish to acknowledge my sincere gratitude to my director of studies, Dr. R. W. Williams, and to my supervisor Dr. D. G. Knight for their help, encouragement, guidance and constructive criticism during this research project.

Secondly, I am grateful to the Ondokuzmayis University for their financal support during the my research period, and also to the Turkish Goverment and peoples for their support.

Lastly, I would like to express my appreciation to my wife Aynur for her support and constant encouragement during the period of accomplishing this thesis. Also my thanks to my colleague Dr. A. Ware, J. Undery and the technicians of the Maths and Computing Division.

THE STABILITY PROPERTIES OF SOME RHEOLOGICAL FLOWS

by HUSEYIN DEMIR B. Sc., M. Sc.

A thesis submitted in partial fulfilment of the requirements of the University of Glamorgan/Prifysgol Morgannwg for the degree of Doctor of Philosophy.

ABSTRACT

The stability of wall driven and thermally driven cavity flow is investigated for a wide range of viscous and viscoelastic fluids. The effect of inertia, elasticity, temperature gradients, viscous heating and Biot boundary conditions are of particular interest. Both destabilisation and bifurcation phenomenon are found.

For Newtonian constant viscosity flow the instabilities are characterised by a critical Reynolds number which represents the ratio of inertial forces to viscous forces, and instability occurs when the inertial forces become large.

For non-Newtonian viscoelastic fluids the instability is characterised by a critical Weissenberg number, which represents the ratio of elastic forces to viscous forces, and instability also occurs when elastic forces dominate the viscous forces.

For thermally driven flow the instability is characterised by a critical Rayleigh number, which represents the ratio of temperature gradient to viscosity, and instability occurs when the Rayleigh number become large. In this case the instability is also characterised by both Eckert and Biot number.

The work has relevance to thermal convection and mixing processes which occur in the viscous and viscoelastic fluid within the Earth's mantle.

Three-dimensional steady and transient flow in a cylindrical cavity and three-dimensional steady flow in a spherical cavity, are also considered for both viscous and

viscoelastic fluids. Instabilities in these three-dimensional flow depend on the same parameters as the flow in square cavity.

CONTENTS

CONTENTS

CONTENTS

NOMENCLATURE

In order of first appearance

d_{ik} ..... Rate of strain tensor p14

$N_1(\dot{\gamma})$ .....Primary normal stress p15

$N_2(\dot{\gamma})$ .....Secondary normal stress p15

$\eta(\infty)$ ..... Infinite shear viscosity p15

$\eta(0)$ .....Zero shear viscosity p15

K ..... Thermal conductivity p17

∇T ..... Temperature gradient p17

C_V .....Heat capacity constant volume p17

Φ ..... Viscous dissipation source p18

C ..... Concentration p19

K_c ..... Diffusion coefficient p19

Ψ ..... Stream function p19

ω_{ij} ..... Vorticity p19

g .....Gravity p22

x,y,z .....Cartesian co-ordinates p22

u,v,w .....Velocity components p22

M,L ..... Differential operators p28

Sc ..... Schmidt number p31

Δt ..... Time increment p36

h,k ..... Grid size p36

X_M ..... Width of the geometry p36

Y_N .....Height of the geometry p36

α ..... Aspect ratio of the geometry p36

Φ_{ij} ..... Dependent function on FDM p37

B_i, A_i ..... Computational coefficient by FDM p41

P, E, W, N, S ..... Computational points p39

e, w, n, s ..... Computational inner points p39

rr,r,s .....Time arrays p42

ε ..... Convergence tolerance p43

U_T .....Top and bottom walls speed p32

r,θ,z .....Cylindrical polar co-ordinates p145

T_0,T_1 ..... Constant temperature on the walls p101

ρ_0 .....Reference fluid density p101

β ..... Coefficient of the thermal expansion p101

$\eta(T)$ .....Temperature dependent viscosity p103

k ..... Constant value of exp. term p103

Ω ..... Rotational speed p145

r,ϕ,θ ..... Spherical co-ordinates p229

R_1,R_2 ..... Radii p237

Ω_T,Ω_B .....Rotational speed on the walls p150

CHAPTER I : INTRODUCTION

The primary purpose of this research project is a numerical study of the stability properties of some non-Newtonian fluid motion. We concentrate on a fluid which is bounded by various 2D and 3D flow geometries where the flow is generated by either wall motion or thermal gradients. For the wall driven cases we consider (a) cavity driven flow in 2D Cartesian co-ordinates (b) cavity driven flow in 3D cylindrical co-ordinates and (c) cavity driven flow in 3D spherical co-ordinates. The fluid models used are generalised first and second order fluids whose rheological equations of state are encompassed by the Criminale-Erikson-Filbey model. We seek results for both Newtonian and non-Newtonian fluid cases with constant and variable shear-rate parameters, and assume the flow geometries are axially symmetric in 3D.

Mankind is always in contact with fluids in both a domestic and an engineering context. Many scientists have tried to describe fluid motion since early times. For example, the first known study was carried out by Egyptians in 3000 B. C., and later Archimedes discovered the fundamental law of buoyancy. As understanding improved the basics of fluid motion were analysed by many mathematicians such as Galileo, Newton, Laplace etc. More recently much advancement has been achieved by Navier, Stokes, Prandtl and Von-Karman.

Rheology is concerned with the deformation and flow properties of materials. The constitutive equation which is also called the rheological equation of the state, defines the engineering behaviour of materials. In a real process it is very complicated (usually impossible) to solve the flow equations analytically since the flow motion is so complex. However towards the end of this century the widespread use of

computational methods and increased computing power has enabled the solution of the basic equations in simple, real geometries. Moreover many problems useful to industry can be validated experimentally.

There are many situations in which the fluid flow has industrial applications, such as flow in pipes and channels, in machinery such as pumps, compressors, jets, rockets engines etc.. Two main areas of interest are the mixing and thermal convection process which occur in the industrial processing of the fluid. Mixing of visco-elastic fluids is industrially important in areas such as processing of polymer solutions and melts as well as the mixing of paints, pharmaceuticals and the fermentation of broths. Although a very important process, mixing is not very well understood due to difficulties that occur with computing the velocity field **[27]** and these difficulties make the analysis of mixing flow very complicated. In this research project mixing has been examined by the tracking of a number of selected particles, and by simulation of the dispersive mixing of a coloured fluid element which is carried along by the flow.

The other main subject which is important in this research project is thermal convection problem such as the Rayleigh-Benard problem in a 2D flow domain. In this case the flow is generated by a buoyancy force through differentially heated walls. We use a Biot boundary condition on the walls to simulate conduction and also consider viscous heating in the flow equations. Physical examples are the circulation of the atmosphere and the oceans which may determine weather conditions. The convection process is also considered in the loss of heat from buildings.

We shall produce results from this steady flow in the form of stream function plots, temperature profiles, concentration maps, particle paths and circulation. In order to selective we illustrate in graphic form only that data which are most pertinent to this thesis.

To solve a coupled non-linear partial differential flow equation numerically, a powerful workstation is required. We solve our equations by using our own programs on the University Alpha network system. The main reason for not using off the shelf package program is that we have non-Newtonian models which would make adjustments to package code (if available) rather awkward. In the following figure we outline the methods and problems considered in both the steady and the unsteady cases used.

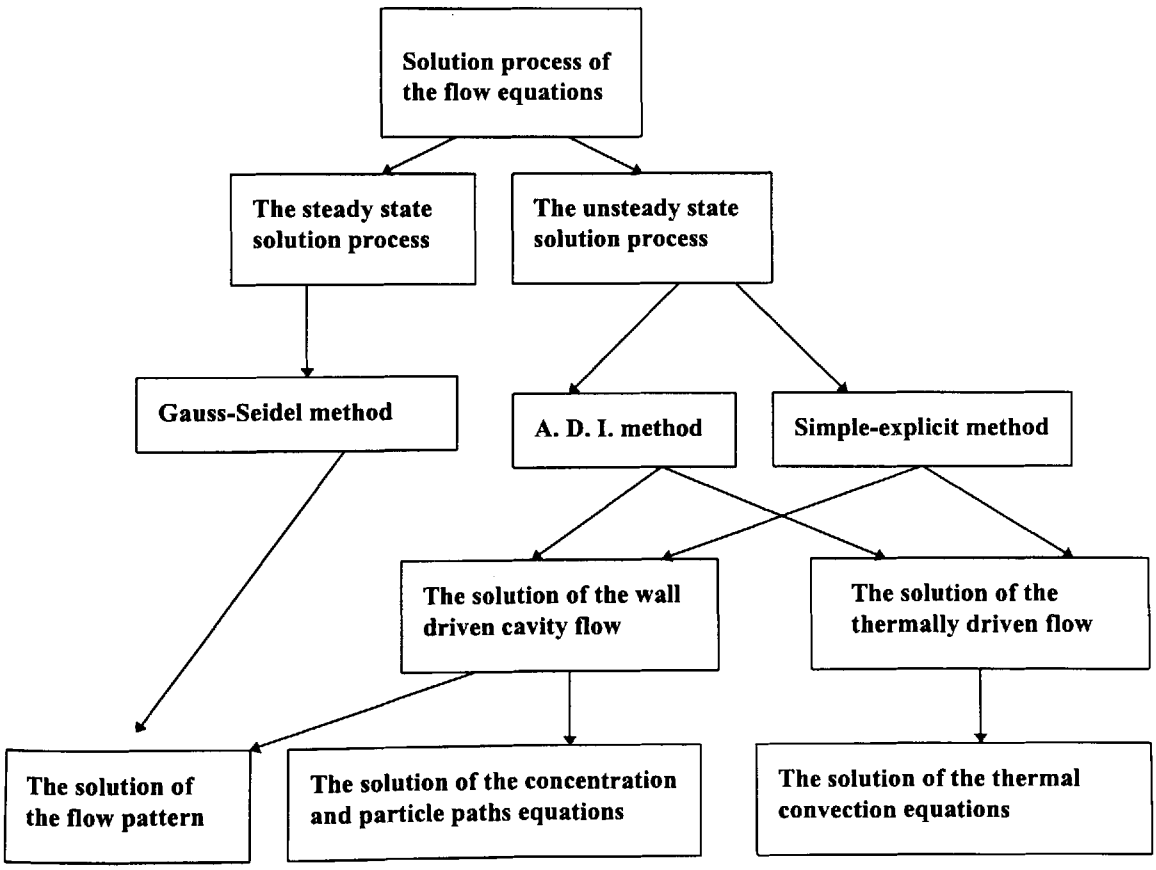

Figure 1. 1; The solution process of the flow equations

CHAPTER II : BASIC EQUATIONS OF NON-NEWTONIAN COMPUTATIONAL FLUID DYNAMICS.

2.1 COMPUTATIONAL FLUID DYNAMICS

Computational Fluid Dynamics (CFD) is now a well established and well developed field finding applications in many different areas of science as well as engineering. Much attention is given to high Reynolds number flows in aerodynamic industrial and environmental modelling applications, where topics such as turbulence modelling are of major importance. Although given lower attention, research in problems of low inertia, incompressible flows might be thought of as dealing with a computationally straightforward exercise of apparently little industrial interest, but such an opinion would be mistaken for the materials which are used can be awkward non-Newtonian viscoelastic fluids. There is scope in these areas for extremely wide application to industry. Some of the many examples that describe viscoelastic fluids can be found in Crochet et al**[21]**.

Materials are generally called non-Newtonian if they exhibit a viscosity which varies under shear or extension. In other words the viscosities of non-Newtonian fluids are affected by either time or any applied forces. These fluids are commonly divided into the following categories:

a) Pseudoplastic (shear-thinning) fluids are the most common type of non-Newtonian fluids, where the fluid viscosity decreases with shear forces. Examples include polymer melts and solutions, foodstuffs, cleaning materials, printing inks, paints, pharmaceutical materials, and many others.

b) Dilatant (shear-thickening) fluids have a viscosity which increases with shear forces. Very few materials exhibit shear-thickening but examples are clay slurries, corn flour, custard and starch suspensions. In typical industrial processes such fluids would be pumped through conduits, extruded or injected into materials, or perhaps just mixed in a batch or continuous mixer.

c) Thixotropic fluids have a viscosity which decreases with time while the shear rate is kept constant (no change with any applied forces). The stirring of these fluids, such as tomato ketchup, salad cream, and non-drip paints, at a fixed rate can result in a significant lowering of the viscosity with time. When the stirring has finished, the fluid will return to its initial viscosity.

d) Rheopectic fluids have a viscosity which slowly increases with time for a constant shear rate. An example of this uncommon phenomenon is latex solution, Walters**[96]**.

e) Viscoelastic fluids which are capable of exhibiting both viscous properties and elastic properties. Examples are shower gels, blue-tack and silly putty.

f) Plastic fluids, which have the property of being able to suspend abrasive particles. These materials behave as solids under small stresses and as fluids after a critical value of the stress has been exceeded and possess a property known as the "apparent" yield stress. Examples are domestic liquid cleaners and thick pastes. We do not consider plastic fluids within the thesis because of difficulties in the numerical simulation of yield stress or thixotropic and rheopectic fluids.

Another very important CFD area is mixing processes, which has only a limited amount of theoretical study devoted to it because the mixing problems

encountered in industry are rheologically complex. Mixing is probably one of the most important process in large scale production. In the production of breads and many other baked products the quality of the mixing of the initial ingredients can have a very significant effect on the overall quality of the final product. Mixing is usually achieved in both batch and continuous mode using blades rotating in a fixed container having various baffles. The rheology of the fluid dough is very complex, and changes with time. Although the process is not well understood, it is still a fundamental operation in industry involving the mixing of resins, adhesives, paints and also in the polymer processing, water, petroleum, chemical and bio-chemical industries. Also much use is made of the mixing process in the home such as manual stirring of sauces, food mixing; blenders and processors are used to aid in the making of sponges and souffles, and the liquidisation of soups.

As we consider the flow pattern, thermal and mixing process with a number of different fluids the flow process must be stable and predictable for general application.

2.2 DIMENSIONLESS NUMBERS

Since dimensionless number which play a vital role in the field of the fluid dynamics, the relevant ones are described below:

2.2.1 Reynolds Number

The nature of the speed of fluid flows can be characterised by a dimensionless parameter, the Reynolds number(Re) which is defined as the ratio of the inertial forces to the viscous forces within the flow. Using the Reynolds number three distinct general types of flow usually occur e.g. for Newtonian flow in tubes ,

i)**Re<10**; This is known as the primary flow and occurs when material forces are negligible and the viscous forces dominate the flow[3]. When the Reynolds number tends to zero the flow is known as creeping or Stokes flow. In this case, we have very slow mixing for processing viscous liquids as well as free convection for thermally driven cavity flow.

ii)**10<Re<2100**; This is known as the laminar or streamline region which occurs at higher values of Reynolds number and involves secondary inertial flow. In this region as the Reynolds number increases the flow tends to become more unstable.

iii)**Re>2100**; this region is known as the turbulent region which occurs at high Reynolds number. When turbulence occurs the flow breaks down and become 'chaotic'. This type of flow is ideal for mixing of certain fluids to occur quickly and efficiently. However , in this thesis , we shall not consider flows with Re>1000 due to limitations in numerical simulations.

2.2.2 Rayleigh Number

The Rayleigh number (Ra) can be defined as the product of the applied temperature gradient of the viscous terms and is the product of two other dimensionless variables namely the Grashof and Prandtl numbers, which are defined later. It is the main governing parameter when free convection thermally driven flows are considered in both 2D and 3D flows. We shall encounter two different flow regimes. Firstly, at low Rayleigh numbers at small temperature gradients, viscous forces dominate the flow and the flow remains stable in uniform equilibrium until a certain critical temperature gradient value is reached. It is, therefore said that for $Ra \leq 10^6$ the flow is generally found to be ordered and streamlined. Secondly for

higher Ra values, usually in the range $10^6 \leq Ra \leq 10^{10}$, the flow tends to become more disordered and turbulent at the higher values of Ra near the top of this range. In this thesis, only the range, $Ra \leq 10^6$ will be considered.

2.2.3 Biot Number

The Biot number (Bi) appears in thermally driven flow and it measures the conduction of heat from the fluid to the surroundings. A very low value of the Biot number is that internal conduction resistance is negligible in comparison with wall-convection resistance. We therefore have an insulated wall condition for Bi=0, whereas when Bi tends to infinity we have an isothermal wall condition; for example Davies and Li **[22]**.

2.2.4 Eckert Number

The Eckert number is pertinent to fluid viscous heating due to internal friction. In many texts the Eckert number(Ec) is given as the quotient of the other two dimensionless numbers namely Brinkman number and Prandtl number respectively; see for example Bird et al**[8]**.

2.2.5 Weissenberg Number

This can be defined as the product of the relaxation time, or some other characteristic time of a fluid which is elastic, to the rate of shear of the fluid flow. In this work , it will be denoted by (Wi).

We will study the interaction of these number on flow stability. For example when Wi and Re are generally in competition, they create a conflict within the flow

until one of them dominates the other . Similarly the Rayleigh number plays a vital role for flow stability in the thermal driven flow case.

2.3 THE MATHEMATICAL EQUATIONS GOVERNING FLOW

The governing equations of fluid can be divided into two categories which are respectively conservation equations and constitutive equations.

2.3.1 Conservation Equations

The derivation of the differential equations which represent the conservation of mass and momentum is standard and can be found in [7], for example. In component form they are written as follows

Conservation of Mass

$$\frac{D\rho}{Dt} + \rho(\nabla . V_i) = 0 \qquad 2.1$$

Conservation of Momentum

$$\rho\frac{DV_i}{Dt} - \nabla \cdot P_{ik} - \rho F_i = 0 \qquad 2.2$$

where

$$\frac{D(\bullet)}{Dt} = \frac{\partial(\bullet)}{\partial t} + (V_i \cdot \nabla)(\bullet)$$

is the convected derivative, ρ is the density of the fluid, P_{ik} is the stress tensor; V_i is the velocity vector, F_i is the body force per unit mass, and t is time. Here the operators $\nabla(\bullet) = \left(\frac{\partial}{\partial x} + \frac{\partial}{\partial y} + \frac{\partial}{\partial z}\right)(\bullet)$.

Conservation of Energy

Since the conservation of energy (the energy equation) is not widely seen in rheological studies, we give its derivation. Consider the arbitrary

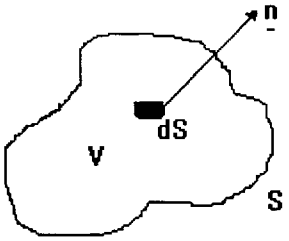

Figure 2. 1; Arbitrary control volume

control volume shown in figure (2.1): a volume V bounded by a surface S with surface element dS. The outward normal in the positive direction is denoted by the unit vector n with components n_i .The volume rate of flow across dS is $(n_i \cdot V_i)dS$. If the kinetic energy is $\frac{1}{2}\rho\overline{v^2}$ per unit volume, where $\overline{v^2}$ represents the square of the magnitude of the velocity, then the rate of convective flow of kinetic energy across dS is, in summation notation

$$(n_i \cdot \frac{1}{2}\rho\overline{v^2}V_i)dS .$$

Assuming that U represents the internal energy per unit mass of the fluid, then the rate of convective flow of internal energy across dS is written as

$$(n_i \cdot \rho U V_i)dS .$$

The rate of heat transfer by conduction across dS is

$$(n_i \cdot q_i)dS ,$$

where q_i are the components of the heat flux vector q.When the fluid moves across the surface of V it is expected that some work will be done in the fluid and this is $(n_i \cdot P_{ik})dS$. Therefore the rate of doing work by the stresses is

$$(n_i \cdot [P_{ik} \cdot V_k])dS .$$

The body forces do work on the fluid at a rate $(V_i \cdot \rho F_i)dV$. We may now write the law of conservation of energy as the expression of the first law of thermodynamics as

$$\frac{d}{dt}\iiint_V (\frac{1}{2}\rho\overline{v^2} + \rho U)dV = -\iint_S (n_i \cdot [\frac{1}{2}\rho\overline{v^2} + \rho U]V_i)dS - \iint_S (n_i \cdot q_i)dS$$

$$+\iint_S (n_i \cdot [P_{ik} \cdot V_k]dS + \iiint_V (V_i \cdot \rho F_i)dV \qquad 2.3$$

where

$\frac{d}{dt}\iiint_V (\frac{1}{2}\rho\overline{v^2} + \rho U)dV$ = Rate of increase of kinetic and internal energy,

$\iint_S (n_i \cdot [\frac{1}{2}\rho\overline{v^2} + \rho U]V_i)dS$ =Rate of addition of kinetic and internal energy by convective flow,

$\iint_S (n_i \cdot q_i)dS$ =Rate of addition of energy by conduction,

$\iint_S (n_i \cdot [P_{ik} \cdot V_k]dS$ =Rate of doing work by the stresses,

$\iiint_V (V_i \cdot \rho F_i)dV$ =Rate of doing work by the body forces.

After applying Gauss' divergence theorem to the surface integrals of (2.3) then since the volume V is arbitrary, the combined integral must be zero at any point in V. Therefore, since V is arbitrary we have

$$\frac{\partial}{\partial t}(\frac{1}{2}\rho\overline{v^2} + \rho U) + \nabla \cdot (\frac{1}{2}\rho\overline{v^2} + \rho U)V_i + \nabla \cdot q_i - \nabla \cdot (P_{ik} \cdot V_i) - V_i \cdot \rho F_i = 0 \qquad 2.4$$

This can be re-written, after application of (2.1), as

$$\rho\frac{D}{Dt}(\frac{1}{2}\overline{v^2}+U)+\nabla\cdot q_i-\nabla\cdot(P_{ik}\cdot V_i)-V_i.\rho F_i=0. \qquad 2.5$$

The scalar product of the momentum equation (2.2) with velocity vector V_i gives the equation of change of kinetic energy:

$$\rho\frac{D}{Dt}(\frac{1}{2}\overline{v^2})-V_i\cdot(\nabla\cdot P_{ik})-V_i\cdot\rho F_i=0 \qquad 2.6$$

which can be subtracted from (2.5) to give

$$\rho\frac{DU}{Dt}+\nabla\cdot q_i-\nabla\cdot(P_{ik}\cdot V_i)+V_i\cdot\nabla\cdot P_{ik}=0 \qquad 2.7$$

If we use the identity

$$\nabla\cdot(P_{ik}\cdot V_i)=V_i\cdot\nabla\cdot P_{ik}+P_{ik}:\nabla V_i$$

assuming P_{ik} is a symmetric tensor, a more familiar form of the internal energy equation is obtained as

$$\rho\frac{DU}{Dt}+\nabla\cdot q_i-P_{ik}:\nabla V_i=0 \qquad 2.8$$

where ":" represents the tensor product. The term $P_{ik}:\nabla V_i$ represents the work done by stresses.

Next we define some rheological equations, involving temperature, before giving the final form of the energy equation.

2.3.2 Incompressibility

The density ρ of a fluid is generally dependent on pressure, p, and temperature, T;

$$\text{i.e. } \rho = \rho(p,T) \tag{2.9}$$

which defines the thermodynamic equation of state of the fluid. In this thesis, we consider that the fluids are incompressible and therefore have constant density. When the fluid is incompressible the stress tensor can be written as

$$P_{ik} = -p\delta_{ik} + \sigma_{ik} \tag{2.10}$$

where P_{ik} is the stress tensor , p is a isotropic hydrostatic pressure, δ_{ik} is the Kronecker delta tensor, and σ_{ik} is known as the extra-stress tensor.

The equations of conservation of mass, (2.1), and momentum, (2.2), for an incompressible fluid are respectively,

$$\nabla \cdot V_i = 0 \tag{2.11}$$

and

$$\rho\frac{DV_i}{Dt} + \nabla p - \nabla \cdot \sigma_{ik} + \rho F_i = 0, \tag{2.12}$$

and the term representing the work done by the stress in (2.8) is now

$$P_{ik}:\nabla V_i = -p(\nabla \cdot V_i) + \sigma_{ik}:\nabla V_i. \tag{2.13}$$

By using (2.11), we can see that the pressure term can be removed from (2.13) and the internal energy equation (2.8) can be re-written as

$$\rho\frac{DV_i}{Dt} + \nabla \cdot q_i - \sigma_{ik}:\nabla V_i = 0 \tag{2.14}$$

2.3.3 Extra-Stress Tensor

In our work, the extra-stress is related to the deformation suffered by the fluid in flow for a general shear-rate (or deformation rate) $(\dot{\gamma})$ through a decomposition into a viscous solvent part and an elastic polymeric part. The viscous solvent part $\bar{\sigma}_{ik}$ is defined as is usual with the 'stress directly proportional to rate of strain', i.e.

$$\bar{\sigma}_{ik} = 2\eta_s(\dot{\gamma})d_{ik} \qquad 2.15$$

where $\eta_s(\dot{\gamma})$ is the solvent viscosity and d_{ik} is the rate of strain tensor and defined as

$$d_{ik} = \frac{1}{2}\left\{\frac{\partial V_k}{\partial x_i} + \frac{\partial V_i}{\partial x_k}\right\}. \qquad 2.16$$

The polymeric part S_{ik} is modelled here by the Criminale-Erickson-Filbey (CEF)[7] constitutive equation of which may be written as

$$S_{ik} = 4\chi(\dot{\gamma})d_{ij}d_{jk} - 2\xi(\dot{\gamma})d_{ik} \qquad 2.17$$

where $\dot{\gamma} = 2(d_{ik}:d_{ik})$, and

$$d_{ik} = (1-\frac{a}{2})\overset{\nabla}{d}_{ik} + \frac{a}{2}\overset{\Delta}{d}_{ik} \quad ,$$

where a is constant. For a=0 we have the "∇" upper convected derivative, for a=1 we have the a co-rotational derivative, and for a=2 we have the a "Δ" lower convected derivative. In this thesis, the upper convected CEF model will be considered for reasons given in section 3.2.1. Therefore we can write

$$\sigma_{ik} = \bar{\sigma}_{ik} + S_{ik}$$

$$= 2\eta_s(\dot{\gamma})d_{ik} + 4\chi(\dot{\gamma})d_{ij}d_{jk} - 2\xi(\dot{\gamma})\overset{\nabla}{d}_{ik}. \qquad 2.18$$

Now $4\chi(\dot{\gamma}) = \frac{1}{2}N_1(\dot{\gamma}) + N_2(\dot{\gamma})$, $2\xi(\dot{\gamma}) = N_1(\dot{\gamma})$,where $N_1(\dot{\gamma})$ and $N_2(\dot{\gamma})$ are material functions known as the primary and secondary normal stress coefficients, respectively. Since we work with the CEF model $\dot{\gamma}, N_1, N_2$ completely determine the state of stress in a rheological shear flow. It remains only to define the upper convected derivative in equation (2.18) as;

$$\overset{\nabla}{d}_{ik} = \frac{D}{Dt}d_{ik} - Ld_{ik} - d_{ik}L^T \qquad 2.19$$

where

$$L = \nabla V_i \quad \text{and} \quad L^T = (\nabla V_i)^T .$$

In this thesis η is the viscosity function used to model the viscosity for non-Newtonian fluids which have a shear dominating influence. Later in this report, when thermally driven flows are investigated the viscosity is set to be a function of temperature as well as of shear-rate. The primary and secondary normal stresses will be defined in section 3.2.1.

2.3.4 The Viscosity Model

There are two main choices for modelling of the viscosity function $\eta(\dot{\gamma})$ are:

i) The Cross model which is given by:

$$\eta(\dot{\gamma}) = \eta(\infty) + \frac{(\eta(0) - \eta(\infty))}{1 + (\lambda\dot{\gamma})^{1-n}} \qquad 2.20$$

ii) The Carreau model which is given by:

$$\eta(\dot{\gamma}) = \eta(\infty) + (\eta(0) - \eta(\infty))(1 + (\lambda\dot{\gamma})^2)^{(n-1)/2} \qquad 2.21$$

In both models $\eta(\infty)$ represents the infinite shear viscosity for very large deformation rates, and $\eta(0)$ represents the zero shear rate viscosity for very small rates of shear. For comparative purposes we have chosen the Cross model, since in practice there is little qualitative difference between the models.

The Cross model will be used for both shear thinning and shear thickening. Assuming n=0.5, $\lambda = 1$, $\eta(0) = 1$ and $0 \le \eta(\infty) \le 1$, we obtain shear thinning or so-called pseudoplastic behaviour. Alternatively with n and λ as above and $\eta(\infty) = 1$, $0 \le \eta(0) \le 1$, we obtained the model of shear thickening or so-called dilatant

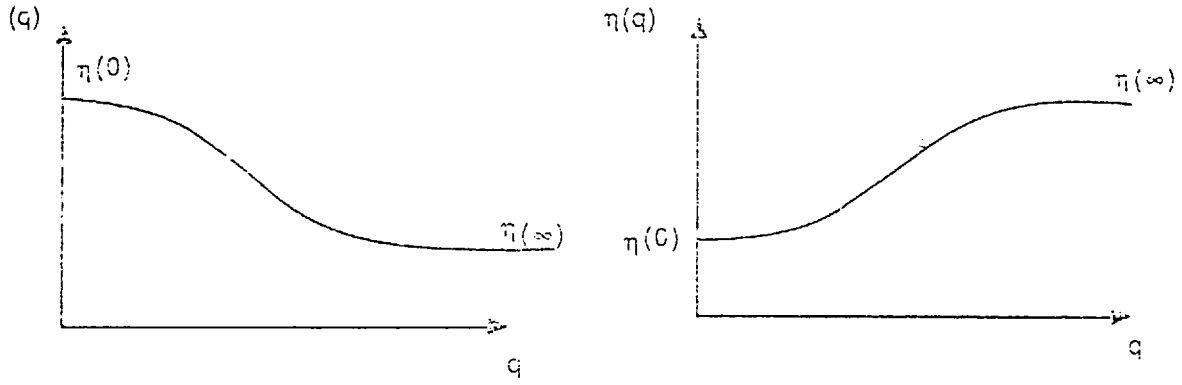

Figure 2. 2; Shear-thinning and shear-thickening behaviour

THERMODYNAMIC CONSIDERATIONS

The internal energy equation (2.14) will be applied to heat transfer problems by incorporating the relation between the heat flux, q_i, and the internal energy, U, to temperature.

2.3.5 Heat Flux

The term $\nabla \cdot V_i$ in (2.14) represents heat conduction in the flowing fluid. Heat is transferred by conduction due to the existence of a temperature gradient. According to Fourier's Law of heat conduction [7], the relation between heat flux and temperature is

$$q_i = -K\nabla T \qquad 2.22$$

where k is the thermal conductivity. Equation(2.22) states that the heat flux vector q_i is directly proportional to the temperature gradient ∇T and is oppositely directed. The minus sign is employed since heat is conducted from the higher temperature regions to the lower temperature regions.

2.3.6 Internal Energy

The internal energy of the fluid is defined in terms of temperature and kinematic variables by an energetic equation of state. The internal energy of the fluids depends on specific volume and temperature. We therefore re-write the equation in these terms by recognising that internal energy U may be considered as a function of V and T, so that

$$dU = \left(\frac{\partial U}{\partial V}\right)_T dV + \left(\frac{\partial U}{\partial T}\right)_V dT. \qquad 2.23$$

Since incompressible fluids are considered,

$$dU = C_V dT \qquad 2.24$$

where

$$C_V = (\frac{\partial U}{\partial T})_V$$

is the heat capacity of the fluid at constant volume, per unit mass.

The internal energy equation (2.15) can then be written with the inclusion of (2.22), as

$$\rho C_V \frac{DT}{Dt} - \nabla \cdot (K \nabla T) - \sigma_{ik} : \nabla V_i = 0 . \qquad 2.25$$

This is the energy equation in terms of the fluid temperature T. Since viscoelastic fluids are considered, the fluid possesses some degree of elasticity, so a simplification of equation (2.25) is obtained by expressing σ_{ik} in terms of velocity gradients. Thus equation (2.25) becomes

$$\rho C_V \frac{DT}{Dt} = K \nabla^2 T + \eta \Phi . \qquad 2.26$$

The term Φ now represents the sum of the dissipation and the accumulation of elastic energy. Equation (2.26) is useful in describing heat transfer in viscoelastic fluids in terms of heat conduction, expansion effects, and viscous heating.

To complete our investigation of the energy equation we note that the viscous dissipation source Φ is found to be $-\sigma_{ik} : \nabla V_i$. In this thesis there is no chemical heat source as we consider only pure fluids.

2.3.7 Concentration equation

The other partial differential equation to be solved numerically is that of the time dependent concentration equation. Using this equation, we shall investigate of colour band dispersive mixing produced within the cavity in 2D and 3D due to fluid motion. This equation can be derived from the application of the law of conservation of a material to a moving continuum and the derivation can be found in many text such as Bird et al**[8]**.

We assume that there is no generation or loss of concentration due to chemical sources within fluid, and we neglect any buoyancy effects.

The concentration equation is

$$\rho\frac{DC}{Dt} = K_c\nabla^2 C, \qquad 2.27$$

where K_c is the diffusion coefficient and C is the concentration.

2.3.8 Stream Function

The stream function (Ψ) measures the flux across any streamline in the flow as a function of position, where the equation of the streamline is given by $V_i x \underline{dr} = 0$. Here the velocity tensor V_i is tangential to the streamline at every point in the flow. Therefore, the velocity components can be expressed in term of derivatives of the stream function and must satisfy equation (2.12).

2.3.9 Vorticity Equation

The vorticity ω_i is a measure of the swirl or rotation of the flow and is defined to be the curl of the velocity vector as:

$$\omega_i = curl\, V_i.$$

The vorticity equation can be expressed in term of the stream function.

2.3.10 Motion of a Fluid Particle

The Hamiltonian system of equations (2.28) shown below describe the trajectory of a fluid particle in any type of cavity driven flow. The solution of the equation is dependent on the initial condition $x_i(0) = x_0$ for each fluid particle under consideration. The particle path is given by the solution of

$$\frac{dx_i}{dt} = V_i. \qquad 2.28$$

In this work, we restrict ourselves to a maximum of 10 particles initially placed within the cavity. We will discuss the numerical solution of the equations for particles trajectories within Chapter 3.

2.4 SUMMARY OF EQUATIONS OF BEING SOLVED

The equations of motion of unsteady incompressible flow of a CEF fluid with constant C_V and K_c and shear-rate or temperature dependent viscosity may be written as:

Mass

$$div\, V_i = 0, \tag{2.29}$$

Momentum

$$\rho\frac{DV_i}{Dt} + \nabla p - \nabla\cdot\sigma_{ik} - \rho F_i = 0, \tag{2.30}$$

Energy

$$\rho C_V \frac{DT}{Dt} - K\nabla^2 T + \Phi = 0, \tag{2.31}$$

Extra-Stress

$$\sigma_{ik} = 2\eta(\dot{\gamma})d_{ik} + 4\chi(\dot{\gamma})d_{ij}d_{jk} - 2\xi(\dot{\gamma})\overset{\nabla}{d}_{ik}, \tag{2.32}$$

Concentration

$$\rho\frac{DC}{Dt} - K_c\nabla^2 C = 0 \tag{2.33}$$

The first term in the energy equation is the transfer of heat by convection, the second is the transfer of heat by conduction and third is the viscous dissipation. The last term which represents the respectable conversion of the work done by the stress into heat. Equations (2.29)-(2.33) will be solved by the stream function and vorticity equation approach. If we set $\frac{\partial}{\partial t} = 0$, then we obtain the corresponding steady state equations.

CHAPTER III: DRIVEN CAVITY FLOW IN 2D

3.1 GEOMETRY AND PREVIOUS WORK

The governing equations of motion are now applied to driven cavity flow. With references to the natural choice of a Cartesian (x,y) co-ordinate system with velocity vector $V_i = (u,v)$, the driven cavity geometry is shown in fig. 3.1 with gravity acting vertically as usual.

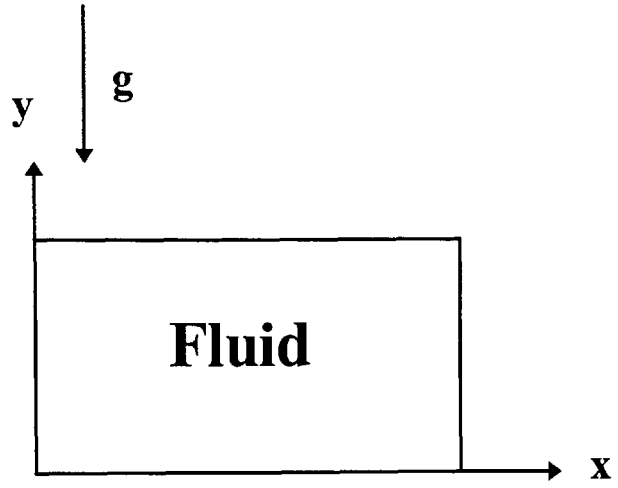

Figure 3. 1; Flow geometry of 2D

The object of this work is to extend the range of solutions from the viscous case to the viscoelastic case by solving the partial differential equations governing the conservation of mass, momentum and concentration in problems of forced convection. Numerous studies have been made on the flow of a viscous fluid in a square cavity with its upper plate sliding at a constant speed (e.g. Bozeman and Dalton**[10]**, Havard**[40]**, Davies**[23]**, Ling and Zhang**[53]**, and Sasmal**[81]**).

In this chapter, we consider the flow of viscoelastic Criminale-Erickson-Filbey liquids, contained in an enclosed cavity. We also study the flow patterns and

mixing processes associated with different types of flow with various moving walls and different geometry aspect ratios.

The cavity driven flow problem is of theoretical importance because it is a part of the larger class of test problem for both steady and unsteady flows which are reviewed and discussed in detail by Burggraf**[14]**. The first numerical study of driven cavity flow within an enclosed rectangular geometry was by Kawaguti**[42]**. He generated numerical solutions for Reynolds number up to 64. The features of the cavity flow are now well known and reproduced by others (Pan and Acrivos**[72]**). The latter authors have sought accurate numerical solutions to this problem over a range of Reynolds' numbers. In 1967 Pan and Acrivos carried out the driven cavity flow with steady state Newtonian fluid flow equations and generated numerical solutions up to Reynolds' number 400 for various aspect ratios. Later work was conducted by Bozemann and Dalton**[10]**, who used various implicit finite difference methods to give a solution for Newtonian fluids in cavities with Reynolds' number up to 1000. They obtained a weaker secondary flow where a rotating vortex occupies the entire lower half of the cavity with aspect ratio 2. According to Batchelor's report**[3]**, the general results obtained by all of the above mentioned researchers indicate that at high Re the steady Newtonian fluid flow pattern appears as a single vortex with an inviscid core possessing uniform vorticity, with any viscous effects being confined to the outer shear layers near the boundary walls. Buggraf**[14]** also conducted an extensive numerical study on the cavity flow problem, and examined secondary vorticies behaviour in the lower corners of the cavity. He reported that secondary vortex pattern was viscosity dominated in contrast with the relatively non-viscous primary eddy.

The cavity flow problem, for a range of Reynolds' number and aspect ratio, still interests a number of researchers, both numerically and experimentally since it is the simplest model of flow with closed streamlines, and is a relative simple model for examining and validating numerical solution techniques. There are some problems in undertaking a numerical study of the fluid flows, particularly the instability which depends on grid size, (e.g. upwinding) so that when Reynolds' number is increased the grid size has to be decreased. By considering such a problem some researchers have improved both the accuracy and acceleration to convergence of the Newtonian flow equations within the cavity's geometry by using various finite difference techniques such as implicit modelling, and also improving the vorticity boundary conditions, for example Nalasamy and Prasad**[63]** and Gupta and Manhoar**[39]**. Recently, two dimensional enclosed cavity flow studies have been illuminated by using both finite difference and finite element techniques, and a good review of numerical solutions within enclosed cavity flow is the book Computer Methods in Fluids**[18]**. Another useful book is that of Chow**[16]** which is an introduction to computational fluid mechanics. He considered both Stokes flow and temperature equation modelling for the cavity, so that the flow equations of the cavity are examined by using the biharmonic stream function equation for Stokes flow. He also produced a simulation of the Rayleigh-Benard fluid system for Rayleigh numbers up to 7000.

As mentioned above, some workers solved the flow equations by using the finite element method for comparative purposes, an example of which is Cliffe et al.**[17]**, who generated the solutions up to Reynolds' number 1000. We want in this

chapter to pay attention to the numerical solutions obtained by a number of the workers that may be compared with useful analytic solutions by considering the nature of the flow near a singular corner. As a good example, useful work has been carried out in detail by Demir[25].

Another useful investigation has been conducted by Havard[40], in 1989, for both Newtonian and shear-thinning fluid flow by using the finite element method following Cliffe et al.[17]. Havard produced steady state solutions for Newtonian fluids at various Reynolds' numbers up to 1000, as well as for shear-thinning fluids at various Reynolds' number up to 200. The dispersive mixing of a 'coloured' fluid band as a solution of the time dependent advection-diffusion equation, was also examined.

In this case Havard obtained Newtonian fluid results for Reynolds' number up to 100 and the fluid is only slightly artificial as the dyed line element is allowed to be 'injected' into cavity when the flow equations have reached steady solution. Both Havard[40] and Bodalia[9] considered the flow and mixing process in more realistic three dimensional flows such as Taylor-Coutte flow with both Newtonian and non-Newtonian fluids, and gave a comprehensive review of published work on mixing. Apart from the numerical studies for the cavity flow problems, much experimental work has been generated within the last decade by Ottino and Chella[68], Chien et al[15], Aref[1] and Moon[61].

Ottino and Chella[68] used the cavity geometry to develop an understanding of the types of flow refined within industrial screw extruders and helical annular mixers. Later experimental work was conducted by Chien et al[15] by considering various two dimensional driven cavity flows in laminar mixing processes for the

Newtonian case. Motion is generated by moving belts which are connected to motors, whose speeds are regulated by computer, for Reynolds' number up to 100 and for aspect ratios up to 10. A subsequent study of driven cavity flow, by making some modifications such as multiple wall motions and periodic discontinuous co-rotational type of flow, has been undertaken by Aref[1], who reported that the flow gives rise to chaotic mixing. Aref considered the mixing process by analysing the deformation of a large collection of fluid particles placed near two point vorticies which were periodically switched on and off, and at the end of the process the blinking vortex flow attained a fixed period due to its inherent periodic motion. From a numerical simulation viewpoint his system is time dependent which he found not to be a sufficient condition for highly desirous chaotic mixing. Recently Moon[61] has also considered same system with chaotic mixing being of a plastic model, and provided a good understanding into the stretching and folding of material which may take place in the Earth's mantle over geological time.

Chaotic mixing has also been considered from a theoretical point of view in two types of periodic flow models, respectively the 'tendril-whorl' flow and a blinking vortex flow. These flows were also examined by analysing the complex motions of line elements within a system, by Khakhar et al[43]. Recent work has been undertaken by Niederkorn and Ottino[65] and Leong et al[50] on the analysis of chaotic mixing within enclosed cavity, while the present state of chaotic mixing knowledge is reviewed in Ottino[69]. In [69] the deformation of coloured material line elements in a variety of cavity flows with sinusoidal wall motion is considered. Ottino[69] also produces a comparison between simulation and experiment for the

journal bearing flow, the applications of which extend to flows occurring within the earth's mantle.

Consideration was given to cavity flow for both Newtonian and non-Newtonian fluids for steady and unsteady cases by Davies[23]. In this study Davies investigated flow from two view points, firstly by analysing the dispersive mixing of a 'coloured' portion of the fluid 'injected' into cavity at rest as it is carried with the flow, and secondly by the tracing of a selected number of fluid particles which are placed within the fluid flow. The flow process is very stable for slow flow but when Re number increases the advection term starts dominating the flow. He therefore showed that the poorest mixing was obtained in the flow where either one wall or simultaneous opposing wall motion exists; and most rapid mixing was found occur at low Reynolds' number. He also reported that the aspect ratio was a significant factor with respect to the unsteady flow and mixing ability of a dilatant fluid.

Finally we report two studies in this area have been carried out for viscous and viscoelastic fluid flows. The first by Sasmal [81] used the finite volume method to solve the axisymmetric viscoelastic fluid, with an upper convected Maxwell model. He reported on the axisymmetric contraction problem as well as on the singularity on the corner of the contraction. The second study is the mixing progress for generalised Newtonian fluid in a 2D cavity generated by Ling et al[53]. It was seen that the mixing quality was changed by shear thinning effects. However they stated that the mixing process for a Newtonian fluid is faster than its viscoelastic counterparts. In other words, mixing of the viscoelastic fluids is slower due to the elastic effect, so we can say that mixing improves with stronger inertial forces.

3.2 DRIVEN CAVITY FLOW EQUATION IN 2D

In this work, the governing equations are applied to cavity driven flow in a rectangular geometry with reference to the usual Cartesian (x,y) co-ordinate system. We have velocity components u and v in the directions x and y respectively. The governing equations of the motion can then be expressed for a viscoelastic flow as:

Conservation of Mass

$$\frac{\partial u}{\partial x}+\frac{\partial v}{\partial y}=0, \tag{3.1}$$

where u and v can be defined in term of a stream function Ψ as

$$u=-\frac{\partial \Psi}{\partial y}\ ,\ v=\frac{\partial \Psi}{\partial x}.$$

Conservation of Momentum

Using equations (2.1) and (2.2) with respect to the Cartesian co-ordinates (x,y) we have

$$\left.\begin{aligned}\rho\frac{Du}{Dt}&=-\frac{\partial p}{\partial x}+\frac{\partial}{\partial x}\sigma_{xx}+\frac{\partial}{\partial y}\sigma_{xy}\\ \rho\frac{Dv}{Dt}&=-\frac{\partial p}{\partial y}+\frac{\partial}{\partial x}\sigma_{xy}+\frac{\partial}{\partial y}\sigma_{yy}-\rho g\end{aligned}\right\} \tag{3.2}$$

By taking the curl of equation (3.1) we have:

$$\frac{M}{2}\left(\sigma_{xx}-\sigma_{yy}\right)+L\left(\sigma_{xy}\right)=\rho\frac{D\omega}{Dt}, \tag{3.3}$$

where the operators $M(\bullet)=2\dfrac{\partial^2(\bullet)}{\partial x\partial y}$ and $L(\bullet)=\left\{\dfrac{\partial^2(\bullet)}{\partial y^2}-\dfrac{\partial^2(\bullet)}{\partial x^2}\right\}$. Now ω denotes the vorticity and σ the extra-stress defined by equation (2.18).

The notation in further clarified in the following

Vorticity equation

$$\omega_i = curl V_i \tag{3.4}$$

$$= (0,0,\omega) \tag{3.5}$$

$$\omega = \nabla^2 \Psi \tag{3.6}$$

$$\nabla^2(\bullet) = \left\{ \frac{\partial^2(\bullet)}{\partial x^2} + \frac{\partial^2(\bullet)}{\partial y^2} \right\}$$

We shall also later make use of following

Concentration Equation

$$\rho \frac{DC}{Dt} = K_c \nabla^2 C \tag{3.7}$$

Motion of a Fluid Particle

$$\frac{dx}{dt} = u = -\frac{\partial \Psi}{\partial y}$$
$$\frac{dy}{dt} = v = \frac{\partial \Psi}{\partial x} \tag{3.8}$$

3.2.1 Normal Stress Behaviour

In this study we have chosen the CEF model for the flow equation and it must exhibit consistency with known viscometric material behaviour. Since the relaxation time is dependent on shear-rate, we incorporate the known normal stress behaviour from viscometric flows. The Criminale-Erickson-Filbey equation is a comprehensive model to describe viscometric flow but the first and second normal stresses are not known in our case. We, therefore, consider the more realistic upper convected Oldroyd 8 constant model and introduce the normal stresses and matched them in the following form (Bird[7]).

$$\left.\begin{aligned} N_1 &= 2\lambda_1(\eta - \eta(\infty)) \\ N_2 &= 0 \end{aligned}\right\} \qquad 3.9$$

3.3 NON-DIMENSIONALISATION

The benefit of writing the equations in non-dimensional form is that it gives a physical expression for a number of related problems, and gives a facility to compare different fluids in different geometries.

The flow equation can be non-dimensionalised by using

$$x' = {}^{x}/_{l}, \quad y' = {}^{y}/_{l}, \quad u' = {}^{u}/_{U}, \quad v' = {}^{v}/_{U}, \quad \omega' = {}^{l\omega}/_{U}, \quad t' = {}^{tU}/_{l}$$

$$\Psi' = {}^{\Psi}/_{Ul}, \quad \dot{\gamma}' = {}^{\dot{\gamma}}/_{U} \quad \eta' = {}^{\eta}/_{\eta(0)},$$

where the dashed notation "$(\bullet)'$" is the non-dimensionalised variable, U is a characteristic velocity, l is a characteristic length, u and v are the velocity components in x and y direction respectively, η is the viscosity, ω the vorticity, Ψ the stream function, t is the time and $\dot{\gamma}$ the shear-rate. For convenience from now on we shall omit the dashes after the non-dimensionalisation process.

Subsequently, equation (3.3) becomes

$$\frac{\partial \omega}{\partial t} = \frac{1}{\eta \mathrm{Re}} H(\eta^2;\omega) - \eta\left\{u\frac{\partial \omega}{\partial x} + v\frac{\partial \omega}{\partial y}\right\} + \frac{1}{\mathrm{Re}}F \qquad 3.10$$

$$\omega = \nabla^2 \Psi, \qquad 3.11$$

where

$$H(\eta^2;\omega) = \left\{\frac{\partial}{\partial x}\left(\eta^2\frac{\partial \omega}{\partial x}\right) + \frac{\partial}{\partial y}\left(\eta^2\frac{\partial \omega}{\partial y}\right)\right\} \qquad 3.12$$

$$F = M(\Psi)M(\eta) + L(\Psi)L(\eta) - \frac{1}{2}M\{S_{xx} - S_{yy}\} - L\{S_{xy}\} \quad . \qquad 3.13$$

Here Re represent the dimensionless Reynolds' number which is defined as

$\mathrm{Re} = {\rho U l}/{\eta(0)}$.

The concentration equation becomes

$$\frac{DC}{Dt} = \frac{1}{Sc\mathrm{Re}}\nabla^2 C \qquad 3.14$$

where Sc represent the Schmidt number and describes the relationship between the viscosity and the molecular diffusity (K_c), with Sc defined as:

$$Sc = {\eta(0)}/{\rho K_c}. \qquad 3.15$$

In using equation (3.14) the Schmidt number is taken up to 50 since in practice when Re number is increased the concentration equation becomes advection dominated.

3.4 BOUNDARY CONDITIONS

To solve equations (3.10). (3.11) and (3.14) numerically, appropriate boundary and initial conditions are required. The dependent variable of a PDE must therefore satisfy, at each point along the boundary, various wall conditions.

To impose a no-slip boundary condition on the walls of the cavity, the velocity components to be same as the speed of the boundary. Although the actual values of vorticity on the walls are not known analytically there exists a 'boundary' layer where vorticity is generated. The vorticity on the boundaries can be formulated in two ways. The first way is the Woods formula **[21]**, based on interior values of stream-function and two levels of vorticity. An alternative to the Woods method is to use known interior stream function values only. We choose the known interior stream function values to solve the stream and vorticity equation for driven cavity flow.

The boundary conditions for equations (3.10) and (3.11) are of the Dirichlet type as shown for example in figure (3.2) and (3.3)

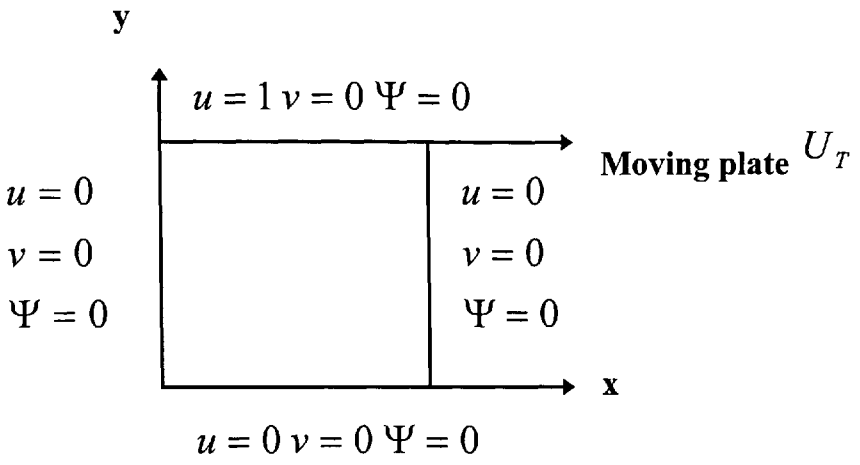

Figure 3.2 ; Boundary conditions

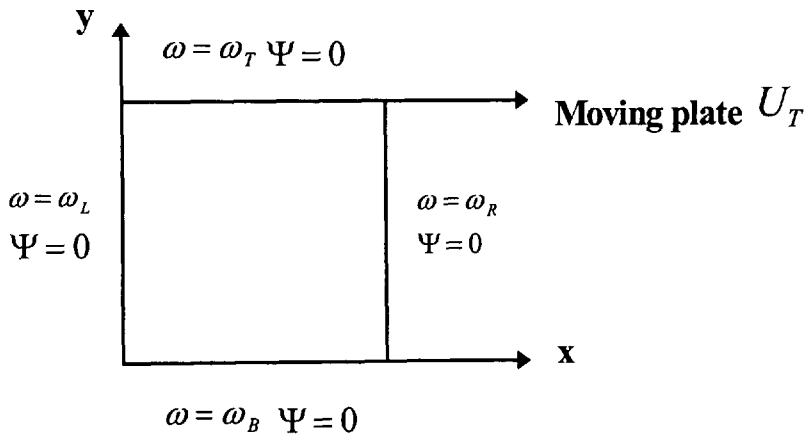

Figure 3.3; Boundary conditions used in analysis of cavity driven flow

We note that on using

$$\dot{\gamma}^2 = U\left\{2M(\Psi)^2 - L(\Psi)^2\right\} \qquad 3.16$$

on the boundaries it can be shown that $\dot{\gamma} = |\omega|$. We note here for future reference that if the viscosity is temperature dependent, we shall use a similar process to find the

shear-rate on the walls. However the boundary viscosity will be given in terms of temperature as well.

For the concentration equation we employ the homogenous Neumann type boundary for impermeable walls, so we don't need to specify the dependent variable of PDE on the cavity walls directly. We use the gradient or flux condition at every point of boundary which is $\frac{\partial C}{\partial n} = 0$, where $\underline{n}$ is outward normal. The boundary condition for equation (3.14) is in the figure below

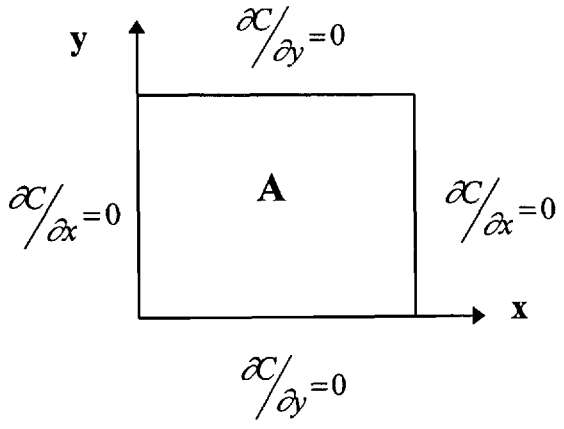

Figure 3.4; Boundary conditions for concentration equation

The other consideration for the concentration equation is the initial condition. As mentioned earlier, the colour material is "injected" into the top half of the cavity within which the fluid is initially at rest. Subsequently we 'observe' how the concentration intensity varies with respect to time, due to fluid motion. We choose the overall concentration in the area (**A**) to be unity and the amount of dye within the geometry remaining a constant because of conservation. Therefore, we have

$$\iint_A C(x,y,t)dA = 1 \qquad 3.17$$

The integral is calculated numerically to second order by using the trapezium rule. The initial condition of the concentration equation is shown in figure (3.5).

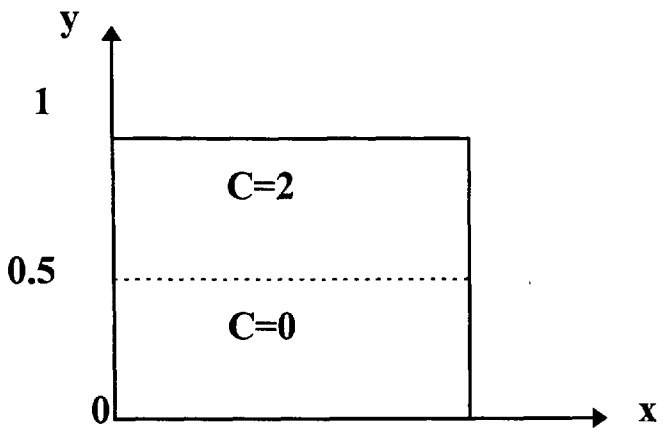

Figure 3.5; The initial condition for concentration dispersion

3.5 THE NUMERICAL MODELLING OF DRIVEN CAVITY FLOW

In this section we discuss the numerical solution of the partial differential equations which were formulated in the previous section for various cavity driven flows. Numerical techniques achieve approximations to the solutions of PDEs by reducing the problem under study to an ordered series of arithmetic operations (additions, subtractions, multiplications and divisions). This reduction is achieved by approximating some aspect of a problem so that simplification is obtained with little loss of accuracy. There are four main popular numerical methods used to solve fluid flow problems:

i)The Finite Difference Method (FDM);

ii)The Finite Element Methods (FEM);

iii)The Boundary Element Methods (BEM);

iv)Spectral Methods (SM).

All our problems will fall within the categories of topological rectangular domains and we use the simple FDM, rather than the others methods mentioned above, to solve the fluid flow problems. The FDM provides a traditional, much tried and tested approach in which differential operators are replaced by difference operators and the resulting difference equations may be solved as accurately as desired (in theory). The FDM is derived from Taylor's series as explained in section 3.6.2, and derivatives are defined at specific points over a small interval. Many texts are available on FDM, for example, Smith**[89]**, Roache**[78]**, Tucker**[95]**, CDW**[21]** and Morton and Mayers**[62]**. Smith gives a comprehensive approach to the method as applied to all types of problems. The book outlines the methods of solution as well as the question of consistency, compatibility and stability. Roache and Tucker consider the FDM as applied to incompressible Newtonian fluid flow problems where the flow equations are non-linear. They also provide information on how to discretise PDEs in terms of the stream function-vorticity (Ψ,ω) or u,v,P. By considering steady state or time dependent incompressible fluids in two dimensions, the governing equations of the problem can be re-formulated from the natural u,v,P variables into the stream function-vorticity (Ψ,ω) formulation and this formulation is easily adopted in FDM. The advantage of this process is that the number of unknowns is reduced from three (u,v,P) to two (Ψ,ω). The same ideas are used for thermally driven flow and will be discussed later. An excellent book by Crochet et al.**[21]** is considered as our basic text where in various types of non-Newtonian incompressible flow problems are approximated using both the FDM and FEM. We here note other books which have

been of use to us namely Mitchell and Griffiths[59], Young[99], Lapidus and Pinder[47], and Scraton[84].

3.6 THE FINITE DIFFERENCE METHOD

3.6.1 The Finite Difference Grid

In this section, we describe the FDM to solve the equation of motion of cavity driven flow in 2D. In solving differential equations by the finite difference method, differential operators are replaced by difference expressions.

The whole geometry, with reference to the Cartesian co-ordinates (x,y), is divided into a finite number of mesh cells and bounded with a uniform square grid. The division is into M grid spaces of size Δx and N grid spaces of size Δy, in the x and y directions respectively. We therefore have M+1 grid points in the x-direction and N+1 grid points in the y-direction, so that

$$x_i = i\Delta x \qquad i = 0,1,\ldots,M \tag{3.18}$$

$$y_j = j\Delta y \qquad j = 0,1,\ldots,N \tag{3.19}$$

define grid lines.

Also $t = n\Delta t$, n=0,1,... with Δt as the time increment where n is the number increments needed to reach some desired time $n\Delta t$. For simplicity, we call the grid spacing $\Delta x = h$ and $\Delta y = k$ and so $h = \frac{X_M}{M}$, $k = \frac{Y_N}{N}$, where X_M and Y_N represent the height and width of the geometry , respectively. The quantity $\alpha = \frac{k}{h}$ is termed as the grid aspect ratio of the cavity.

The point which lies at the intersection of the lines given by (3.18) and (3.19) is termed as the (i,j) grid point. The point vertically above (i,j) is the point $(i,j+1)$ and that below (i,j) is the point $(i,j-1)$. Similarly the points $(i+1,j)$ and $(i-1,j)$ lie to the right and left of (i,j), (see fig.3.6). If Φ is the dependent variable, the approximated value of the function Φ at the (i,j)th grid point is denoted by $\Phi_{i,j}$.

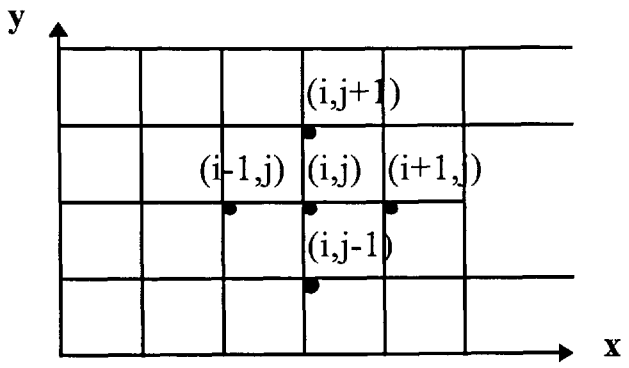

Figure 3.6; Finite difference mesh structure.

3.6.2 Finite Difference Approximation to Derivatives

We assume Φ has an analytic solution $\Phi(x,y,t)$ whose derivatives are finite and continuous functions of x and y. The partial differential derivatives are approximated as finite differences by means of Taylor series, which is the most usual and best known method.

The first order partial derivative of the function Φ, in the x-direction, can be approximated by one of the standard forms as follows:

i)Central difference approximation

$$\frac{\partial \Phi}{\partial x}_{(x_i,y_j)} = \frac{\Phi_{(i+1,j)} - \Phi_{(i-1,j)}}{2h} + O(h^2) \qquad 3.20$$

ii)Forward difference approximation

$$\frac{\partial \Phi}{\partial x}_{(x_i,y_j)} = \frac{-3\Phi_{i,j} + 4\Phi_{i+1,j} - \Phi_{i+2,j}}{2h} + O(h^2) \qquad 3.21$$

iii)Backward difference approximation

$$\frac{\partial \Phi}{\partial x}_{(x_i,y_j)} = \frac{3\Phi_{i,j} - 4\Phi_{i-1,j} + \Phi_{i-2,j}}{2h} + O(h^2) \qquad 3.21$$

The main source of error with this approach is the truncation error $O(h^2)$ associated with the approximation of the differential operator. The truncation error depends on grid size and can be neglected as $h \to 0$.

The time derivative is approximated in a simple explicit method by using the forward difference approximation in the increasing time direction as:

$$\frac{\partial \Phi}{\partial t}_{(x_i,y_j,t_n)} = \frac{\Phi^{n+1}{}_{i,j} - \Phi^{n}{}_{i,j}}{\Delta t} \qquad 3.22$$

The second order and the 'cross' partial derivatives can be approximated using central differences;

$$\frac{\partial^2 \Phi}{\partial x^2}_{(x_i,y_j)} = \frac{\Phi_{i+1,j} + \Phi_{i-1,j} - 2\Phi_{i,j}}{h^2} + O(h^2) \qquad 3.23$$

$$\frac{\partial^2 \Phi}{\partial x \partial y}_{(x_i,y_j)} = \frac{\Phi_{i+1,j+1} - \Phi_{i+1,j-1} - \Phi_{i-1,j+1} + \Phi_{i+1,j+1}}{4hk} + O(h^2). \qquad 3.24$$

Here we note that the 'cross' derivative can be approximated near the geometry corners by using special formula are defined in CDW[21]. Second order partial derivatives in the y-direction are approximated in a similar way.

3.7 DISCRETISION OF THE FLOW EQUATIONS

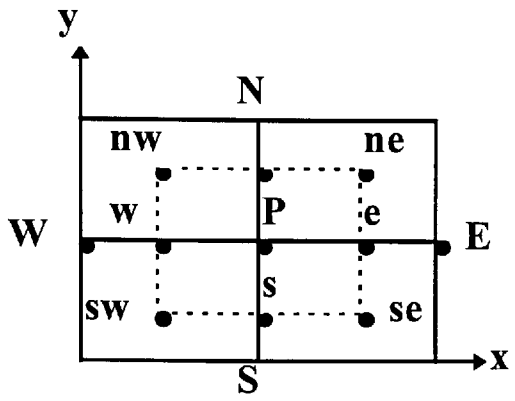

Figure 3.7; Computational mesh structure for FDM

The partial differential equations of the motion are discretised by using a mesh system as shown in fig.(3.7). In this figure **P** indicates the **(i,j)th** point at which known variable is computed. The computational points are indicated as **E, W, N,and S**. An inner mesh is shown by the dotted lines and the intersection of the mesh sides and lower case points are **e, w, n, s, ne, nw, se, sw**. In the above expression **E=(i+1,j), W=(i-1,j), N=(i,j+1), and S=(i,j-1)**. We have the equations which will be discretised by using finite difference approximation as follows

$$\omega = \nabla^2 \Psi, \tag{3.25}$$

$$\frac{\partial \omega}{\partial t} = \frac{1}{\mathrm{Re}\,\eta}\left\{H\left(\eta^2;\omega\right)\right\} + \frac{1}{\mathrm{Re}} F_\omega, \tag{3.26}$$

$$\frac{\partial C}{\partial t} = \frac{1}{\mathrm{Re}Sc}\nabla^2 C + \frac{1}{\mathrm{Re}} F_C, \tag{3.27}$$

where

$$\nabla^2(\bullet) = \left\{\frac{\partial^2(\bullet)}{\partial x^2} + \frac{\partial^2(\bullet)}{\partial y^2}\right\}, \tag{3.28}$$

$$H(\eta^2;\omega) = \left\{\frac{\partial}{\partial x}\left[\eta^2\frac{\partial\omega}{\partial x}\right] + \frac{\partial}{\partial y}\left[\eta^2\frac{\partial\omega}{\partial y}\right]\right\}, \tag{3.29}$$

$$F_\omega = F_{\omega I} + F_{\omega\eta} + F_{\omega\sigma},$$

$$F_C = -F_{CI}.$$

Here

$$F_{\omega I} = -\mathrm{Re}\left\{\frac{\partial}{\partial x}[u\omega] + \frac{\partial}{\partial y}[v\omega]\right\}, \tag{3.30}$$

$$F_{\omega\eta} = M(\Psi)M(\eta) + L(\Psi)L(\eta), \tag{3.31}$$

$$F_{\omega\sigma} = -\frac{1}{2}M[S_{xx} - S_{yy}] - L[S_{xy}], \tag{3.32}$$

$$F_{CI} = \mathrm{Re}\left\{\frac{\partial}{\partial x}[uC] + \frac{\partial}{\partial y}[vC]\right\}, \tag{3.33}$$

where M and L are differential operators are defined as before.

The stream function-vorticity equation (3.25), the vorticity equation (3.26) and the concentration equation (3.27) can be discretised by using (3.20)-(3.24). We have two different cases to be solved namely steady state and unsteady cases. On taking $\frac{\partial}{\partial t} = 0$ we have the steady state case.

i)Steady State

We can express our finite difference equations in a standard notation for this thesis as

$$B_1\Phi_{i,j} = B_2\Phi_{i+1,j} + B_3\Phi_{i-1,j} + B_4\Phi_{i,j+1} + B_5\Phi_{i,j-1} + B_6, \tag{3.34}$$

If we consider the stream function equation as the dependent function, the coefficients in equation (3.34) become

$$B_1 = 2\left(\alpha^2 + 1\right),\ B_2 = B_3 = \alpha^2,\ B_4 = B_5 = 1, \text{ and } B_6 = k^2\omega_{i,j}\ .$$

Considering the vorticity as the dependent function then we have

$$B_1 = \alpha^2\left\{\left(\eta^2\right)^e + \left(\eta^2\right)^w\right\} + \left\{\left(\eta^2\right)^n + \left(\eta^2\right)^s\right\},$$

where **e**, **w**, **s** and **n** indicate inner mesh points.

$$B_2 = \alpha^2\left\{\frac{\left(\eta^2\right)^e}{\mathrm{Re}} - h\eta^P u^E\right\},\ B_3 = \alpha^2\left\{\frac{\left(\eta^2\right)^w}{\mathrm{Re}} + h\eta^P u^W\right\},\ B_4 = \left\{\frac{\left(\eta^2\right)^n}{\mathrm{Re}} - k\eta^P v^N\right\},$$

$$B_5 = \left\{\frac{\left(\eta^2\right)^s}{\mathrm{Re}} + k\eta^P v^S\right\},\quad B_6 = k^2\eta_{i,j}F_{i,j},$$

For computational solution stability, we require

$B_1 \geq B_2 + B_3 + B_4 + B_5$ and also $B_2, B_3, B_4, B_5 \geq 0$ **[21]**.

ii)Unsteady state

In this case the time-independent Poisson stream function is calculated as in the steady case. On using the simple explicit method to solve the time-dependent equations we have the equation for Φ as

$$\Phi_{i,j}^{n+1} = B_1\Phi_{i,j}^n + B_2\Phi_{i+1,j}^n + B_3\Phi_{i-1,j}^n + B_4\Phi_{i,j+1}^n + B_5\Phi_{i,j-1}^n + B_6\,. \qquad 3.35$$

For the vorticity equation, we have

$$B_1 = \left\{1 - \left[r\frac{\left(\eta^2\right)^e}{\mathrm{Re}\,\eta^P} + r\frac{\left(\eta^2\right)^w}{\mathrm{Re}\,\eta^P} + s\frac{t\left(\eta^2\right)^n}{\mathrm{Re}\,\eta^P} + s\frac{t\left(\eta^2\right)^s}{\mathrm{Re}\,\eta^P}\right]\right\},\ B_2 = r\left\{\frac{\left(\eta^2\right)^e}{\mathrm{Re}\,\eta^P} - \frac{hu^E}{2}\right\},$$

$$B_3 = r\left\{\frac{\left(\eta^2\right)^w}{\mathrm{Re}\,\eta^P} + \frac{hu^W}{2}\right\},\ B_4 = s\left\{\frac{\left(\eta^2\right)^n}{\mathrm{Re}\,\eta^P} - \frac{kv^N}{2}\right\},\ B_5 = s\left\{\frac{\left(\eta^2\right)^s}{\mathrm{Re}\,\eta^P} + \frac{kv^S}{2}\right\},\ B_6 = \frac{\Delta t}{2\,\mathrm{Re}}F_{i,j}^n$$

Here $r = \frac{\Delta t}{h^2}$, and $s = \frac{\Delta t}{k^2}$ and lower case letters.

For the concentration equation we have

$$B_1 = \left\{1 - \left[r\frac{2}{\mathrm{Re}\,Sc} + s\frac{2}{\mathrm{Re}\,Sc}\right]\right\},\ B_2 = r\left\{\frac{1}{\mathrm{Re}\,Sc} - \frac{hu^E}{2}\right\},\ B_3 = r\left\{\frac{1}{\mathrm{Re}\,Sc} + \frac{hu^W}{2}\right\},$$

$$B_4 = s\left\{\frac{1}{\mathrm{Re}\,Sc} - \frac{kv^N}{2}\right\},\ B_5 = s\left\{\frac{1}{\mathrm{Re}\,Sc} + \frac{kv^S}{2}\right\},\ B_6 = 0.$$

For stability we require $r \le \frac{1}{4}\mathrm{Re}$ and $s \le \frac{1}{4}\mathrm{Re}$ for the vorticity equation and $r \le \frac{1}{4\,\mathrm{Re}\,Sc}$ and $s \le \frac{1}{4\,\mathrm{Re}\,Sc}$ for the concentration equation **[21]**. The stability, consistency and convergence of the parabolic vorticity, concentration and Poisson stream function will be discussed in the our section 3.8 section for both steady and unsteady cases.

3.8 CONSISTENCY, STABILITY AND CONVERGENCES

The mathematical foundations of the questions of consistency and stability of the discretised finite difference approximations to partial differential equations are well developed only for linear systems. Therefore the results of the linear system are used as guidelines to non-linear problems. There are many techniques which are needed to investigate the stability and consistency of the difference equations, depending on whether steady or unsteady problems are involved. We examine both cases separately.

i)Steady case

For the steady case, the iterative method we use to solve the partial differential equation numerically is always consistent and stable. It is consistent because the truncation error tends to zero and it is stable because of diagonal dominance. We

define the iterative method later in section (3.9). The values of $\Phi_{i,j}$ obtained in two successive iterations are denoted by $\Phi^n_{i,j}$ and $\Phi^{n+1}_{i,j}$. If $\left|\Phi^n_{i,j}\right|$ is large the absolute difference $\left|\Phi^{n+1}_{i,j} - \Phi^n_{i,j}\right|$ may not be sufficient for absolute convergence, but close enough for relative convergence which may be desirable. If $\left|\Phi^n_{i,j}\right|$ is small the relative difference $\dfrac{\left|\Phi^{n+1}_{i,j} - \Phi^n_{i,j}\right|}{\left|\Phi^n_{i,j}\right|}$ may not be sufficient for relative convergence but appropriate for absolute convergence. This latter criterion is more meaningful but is obviously dangerous, when $\left|\Phi^n_{i,j}\right|$ approach zero values. It may therefore cause divide overflows in relative difference equation.

To overcome these difficulties the convergence criterion is taken to be

$$\Phi^{n+1} = \underset{i,j}{Max}\left\{\frac{\left|\Phi^{n+1}_{i,j} - \Phi^n_{i,j}\right|}{1+\left|\Phi^n_{i,j}\right|}\right\} \angle \varepsilon, \qquad 3.36$$

for some tolerance ε. Here values of ε stated in the open literature, have varied from $\varepsilon = 10^{-3}$ to 10^{-8}.

We have absolute convergence when $\left|\Phi^n_{i,j}\right|$ is 'small' and relative convergence when $\left|\Phi^n_{i,j}\right|$ is 'large'.

ii)Unsteady case

For the unsteady case, when the difference approximations are stable then any computational errors can be made arbitrarily small. For a linear partial differential equation the Lax**[49]** theorem states that the difference between two iterations satisfies some convergence criterion. However, for non-linear partial differential equations

even if the difference approximation is stable there is no theorem in existence which guarantees convergence of the system (see for example CDW[21]).

In our case, the algebraic equations arising from finite difference equations are solved by both simple explicit and Peacemann-Rachford methods. For the simple explicit case, the two main stability methods are the unsteady matrix and Von-Neumann methods.

The local truncation error for unsteady PDEs , such as the vorticity and concentration equations, is found to be $O(\Delta t, h^2, k^2)$, so if the mesh becomes more refined,$(h, k \to 0)$, and if the time increment is sufficiently small , then the error due to discretisation tends to zero. Therefore the difference equations and PDEs are compatible in the limit. From applying Von-Neumann analysis to these equations the vorticity equation is stable as long as $\Delta t \le \frac{\mathrm{Re} h^2}{4}$ and the concentration equation is stable provided that $\Delta t \le \frac{h^2}{4\,\mathrm{Re}\,Sc}$. (See for example CDW[21])

The unsteady system is also solved by the Peacemann-Rachford method, which shall be discussed shortly, whose discretisation error is second order in both time and space $O(\Delta t^2, h^2, k^2)$. This method although being considerably more difficult to use in program, has advantages. For example, the overall accuracy of the solution obtained decreased due to the time derivative being approximated by a forward difference operator. This situation is eased by using the A. D. I. method i.e. this method increase the overall accuracy of the solution is obtained because it allows the use of a larger time step Δt. Also at low Reynolds number enabled the time step to be significantly

raised, thus enabling longer simulation times to be considered. As is easily seen the method is always consistent, and stable (in theory).

These methods are well examined in texts such as CDW[21], Smith[89], Lapidus and Pinder[47], Mortan and Mayers[62], and Roache[78].

The stability may however breakdown in the case of upwinding at 'high' Reynolds numbers. However, by taking small h and k we overcome this problem.

3.9 NUMERICAL METHODS FOR LINEAR EQUATIONS

The finite difference method gives to rise to systems of non-linear algebraic equations, which may be very large, and that require a powerful computational environment. The two main classes of method for solving the systems of equations are direct and iterative methods.

We let **Ax=b** denote the non-linear algebraic equations, with **A** an **NxN** matrix, **b** a given **Nx1** column vector and **x** the **Nx1** vector of **N** unknown interior mesh values. Direct methods solve the algebraic system of equations in a pre-determined number of steps using algorithms such as Gaussian elimination or triangular decomposition. For the steady state case, we solve the algebraic system by using iterative methods because it is much easier to code and uses less computer memory, as well as being faster than direct methods. Well-known iterative methods are the Jacobi, Gauss-Seidel and S.O.R methods. The difference between them is that the Gauss-Seidel method is similar to the Jacobi method but has faster convergence. The S.O.R. method is a modified form of the Gauss-Seidel iteration incorporating a relaxation parameter best determined by experience. The matrix **A** is a real, symmetric and positive definite in

each case. The best texts which found most useful are Morton and Mayers[62], CDW[21], Smith[89], Froberg[32].

3.10 THE A.D.I. METHOD

The alternating direction implicit method developed by Peacemann-Rachford[62, 84] is an excellent mixture of explicit and implicit methods and is used to solve parabolic PDEs for concentration, vorticity as well as temperature equation in thermal driven cavity flow. The solution domain is bounded by a uniform grid points consisting of **MxN** grid points and the PDE is approximated at each point by an algebraic discretised equation. This method allows the solution process by splitting into two steps. The first step solves the problem for variables along grid-lines parallel to the x-axis while the second step solves the problem along grid-lines parallel to the y-axis. This splitting process is achieved by introducing an intermediate set of values. Let the partial differential equation have the form

$$\frac{\partial \Phi}{\partial t} = L\Phi + f\,, \tag{3.37}$$

where L contains space derivatives and $L = L_x + L_y$, with L_x having only x derivatives and L_y only y derivatives, with L having no mixed derivatives. Let Φ^n be the value of Φ at $t = n\Delta t$ and Φ^{n+1} that at $t = (n+1)\Delta t$.

We then have the following expression from Taylor series

$$\Phi^{n+1} = e^{\Delta t \frac{\partial}{\partial}} \Phi^n \tag{3.38}$$

and as $\frac{\partial \Phi^n}{\partial t} = L\Phi^n$ and (3.38) becomes (on neglecting f)

$$\Phi^{n+1} = e^{\Delta t L}\Phi^n$$

$$= e^{\Delta t L_x} e^{\Delta t L_y} \Phi^n$$

Therefore we have

$$e^{-\frac{\Delta t}{2} L_x} e^{-\frac{\Delta t}{2} L_y} \Phi^{n+1} = e^{\frac{\Delta t}{2} L_x} e^{\frac{\Delta t}{2} L_y} \Phi^n \qquad 3.39$$

These can be re-written in terms of intermediate values Φ^* as for with non-zero f term as

$$e^{-\frac{\Delta t}{2} L_x} \Phi^* = e^{\frac{\Delta t}{2} L_y} \Phi^n + P^n \qquad 3.40$$

$$e^{-\frac{\Delta t}{2} L_y} \Phi^{n+1} = e^{\frac{\Delta t}{2} L_x} \Phi^* + Q^* \qquad 3.41$$

where "*" denotes intermediate approximation between the old time t and the new time $t + \Delta t$.

To discretise the equations (3.40) and (3.41) by using standard central differences we have

$$L_x \Phi = \frac{1}{2} h^2 L_x^h + O(h^2),$$
$$L_y \Phi = \frac{1}{2} k^2 L_y^k + O(k^2),$$

and with $r = \frac{\Delta t}{h^2}$ and $s = \frac{\Delta t}{k^2}$ we write

$$\left(1 - \frac{r}{2} L_x^h\right) \Phi^* = \left(1 + \frac{s}{2} L_y^k\right) \Phi^n + \frac{\Delta t}{2} f^n, \qquad 3.42$$

$$\left(1 - \frac{s}{2} L_y^k\right) \Phi^{n+1} = \left(1 + \frac{r}{2} L_x^h\right) \Phi^* + \frac{\Delta t}{2} f^n. \qquad 3.43$$

For a PDE, such as the vorticity and concentration equations, the error due to discretsion is found to be second order in both time and space.

However, the method gives to a pair of implicit equations. The solution of each equation is obtained through the Gaussian Elimination direct type method which is well explained in Smith[89].

The A.D.I. method can be used easily when the boundary conditions are of the Dirichlet type , but requires modification for use with Neumann type boundary conditions, or a mixture of both Dirichlet and Neumann type. As used by us the Dirichlet boundary conditions is defined as

$$\Phi^* = \frac{1}{2}\left\{\left(1+\frac{s}{2}L_y^k\right)\Phi^n + \left(1-\frac{s}{2}L_y^k\right)\Phi^{n+1}\right\}, \qquad 3.44$$

The Neumann boundary condition are given by

$$\frac{\partial\Phi^*}{\partial n} = \frac{1}{2}\left\{\left(1+\frac{s}{2}L_y^k\right)h^n + \left(1-\frac{s}{2}L_y^k\right)h^{n+1}\right\}, \qquad 3.45$$

where we assume $\left(\frac{\partial\Phi}{\partial n}\right)^n = h^n$ and $\left(\frac{\partial\Phi}{\partial n}\right)^{n+1} = h^{n+1}$ on the boundary and $\frac{\partial\Phi^*}{\partial n}$ does not involve the f term.

3.11 THE NUMERICAL CHECKS IN 2D FLOW MODELS

In this section, we give the vorticity and concentration equation which are checked by the trapezium integration rule over the solution domain. This numerical check gives us information that the solution of these equations is well behaved as we get the solution to converge during the running process. We check total vorticity and concentration constraints as generated by the flow.

For cavity driven flow, we have the vorticity constraint to second order as

$$\iint_A \omega dA = \iint_A curlV_i dA. \qquad 3.46$$

Applying Stokes' theorem to the above equation gives

$$\iint_A \left(\frac{\partial v}{\partial x} - \frac{\partial u}{\partial y} \right) dxdy = \left[U_B - U_T \right], \tag{3.47}$$

where U_T and U_B represent the top and bottom wall speeds respectively.

By using The Green's Theorem, the concentration constraint to second order is given by

$$\frac{\partial}{\partial t} \iint_A C dA = D \oint_{\delta A} \frac{\partial C}{\partial n}. \tag{3.48}$$

The first integration of the right hand side is zero over δA due to the fluid not being allowed to pass through walls, so $\frac{\partial C}{\partial n} = 0$ at each wall. As a result, we have

$$\iint_A C dxdy = c \tag{3.49}$$

where c is a constant value.

3.12 THE SINGULARITIES NEAR THE CORNER

The nature of corner singularities is examined in the case of cavity driven flow in which the fluid is contained and the flow generated by the motion of one or more walls. As a result for viscoelastic flow behaviour remains largely unknown despite the Newtonian nature being well known. We want to examine the corner singularities for cavity driven flow, although we do not always directly encounter the corner singularities in the work. The reason for examining singularity behaviour is that it is a important current issue in fluid dynamics.

In standard cavity flow, singularities exist near the top two corners because the shear-rate becomes increasingly large and therefore both shear-rate and vorticity become singular.

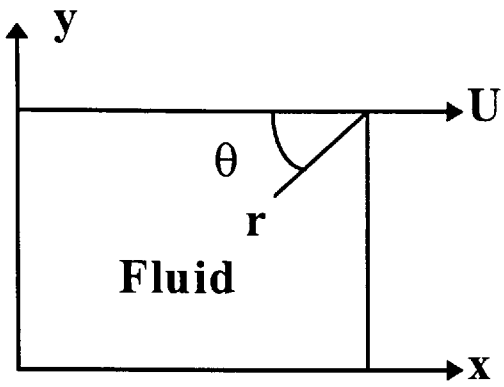

Figure 3.8 ;Diagram of the corner singularity

To consider the standard cavity flow whose top plate moves with constant speed U we assume that no-slip boundary conditions are applied. We next examine the nature of the corner singularities separately for both Newtonian and non-Newtonian flow.

3.12.1 The Corner Singularities of Viscous Flow

i)Newtonian Flow

In steady two-dimensional viscous incompressible flow the stream function and vorticity equations are

$$\nabla^2\omega = \mathrm{Re}\frac{D\omega}{Dt} \qquad 3.50$$

$$\nabla^2\Psi = \omega . \qquad 3.51$$

Moffat[84] has shown that the viscous forces dominate the inertial forces near the corner itself. Then equation (3.50) becomes

$$\nabla^2\omega = 0 \qquad 3.52$$

and equation (3.51) and (3.52) give to rise to

$$\nabla^4 \Psi = 0. \tag{3.53}$$

Equation(3.53) is called the Stokesian flow equation.

Considering the polar co-ordinates (r,θ) with origin at one singular corner the stream function takes the form as

$$\Psi(r,\theta) = r^m f_m(\theta) \tag{3.54}$$

where only the solution for $m = 1$ is allowed due to the boundary conditions.

In this case the vorticity and shear-rate near the corner are given by

$$\omega = \frac{1}{r} g(\theta) \tag{3.55}$$

and

$$\dot{\gamma} = \frac{1}{r} h(\theta). \tag{3.56}$$

where $g(\theta)$ and $h(\theta)$ incorporate $f_1(\theta)$ and its derivatives. As seen from into (3.55) and (3.56) , when $r \to 0$ the vorticity and shear-rate become infinite and singularities exist at the corner points.

Similarly by using equation (3.53) in terms of polar-co-ordinates and on using (3.54), we have the general form of $f_m(\theta)$ as

$$f_m(\theta) = A\cos m\theta + B\sin m\theta + C\cos(m-2)\theta + D\sin(m-2)\theta, \tag{3.57}$$

where A, B, C and D are constants. In the special case m=1 the solution takes the form (which is for the Stokesian flow equation)

$$f_1(\theta) = A\cos\theta + B\sin\theta + C\theta\cos\theta + D\theta\sin\theta. \tag{3.58}$$

The boundaries may be rigid walls on which the velocity is defined, or surfaces on which the stress is defined. Therefore, for standard cavity flow with one wall moving and the other stationary we have

$$\left.\begin{aligned} &f_1(0)=0,\\ &f_1\left(\frac{\pi}{2}\right)=0,\\ &\frac{d}{d\theta}f_1(0)=U,\\ &\frac{d}{d\theta}f_1\left(\frac{\pi}{2}\right)=0 \end{aligned}\right\} \qquad 3.59$$

where $\theta=0$ and $\theta=\frac{\pi}{2}$ represent moving wall and stationary wall respectively. The solution of the Stokesian flow equation near the corner is

$$\Psi(r,\theta)=\frac{rU}{\left(\pi^2-4\right)}\left(-\pi^2\sin\theta+4\theta\cos\theta+2\pi\sin\theta\right) \qquad 3.60$$

$$\omega(r,\theta)=\frac{-4U}{r\left(\pi^2-4\right)}\left(\pi\cos\theta-2\sin\theta\right). \qquad 3.61$$

Our solution agrees with Davies**[30]**.

ii)Non-Newtonian Flow

To use Moffat's assumption, we need to see how inelastic non-Newtonian flow behaves near the corner. In this case the flow equation is

$$\eta\nabla^2\omega+2\left(\frac{\partial}{\partial x}\eta\frac{\partial}{\partial x}\omega+\frac{\partial}{\partial y}\eta\frac{\partial}{\partial y}\omega\right)+M(\eta)M(\Psi)+L(\eta)L(\Psi)=0, \qquad 3.62$$

where M and L are defined as before. Equation (3.62) is usually solved with equation (3.51).

We consider the viscosity near the corner through the Cross-model for non-Newtonian viscous flow. Since we work with polar co-ordinates the velocity components are defined in term of polar co-ordinates by

$$\begin{aligned} u(\theta) &= -\left(sf + c\frac{\partial f}{\partial \theta} \right) \\ v(\theta) &= cf - s\frac{\partial f}{\partial \theta} \end{aligned} \qquad 3.63$$

where $f = f_1(\theta)$, $s = \sin\theta$ and $c = \cos\theta$. The Cross-model viscosity, therefore, takes the form

$\eta = a + b(\theta)r^{1-n}$, as $r \to 0$ 0<n<1, where $a = \eta(\infty)$.

When we substitute the stream, vorticity and viscosity function, are defined in terms of polar co-ordinates, into (3.62) the equation of the non-Newtonian flow near the corner is

$$\left(a + b(\theta)r^{1-n}\right)\nabla^2\omega + C(\theta)r^{-n-2} = 0. \qquad 3.64$$

Here $C(\theta)$ incorporates terms including $f(\theta)$ since ω has the form $\omega = \frac{1}{r}g(\theta)$, $\nabla^2\omega$ assumes the form

$$\nabla^2\omega = \frac{1}{r^3}D(\theta). \qquad 3.65$$

Therefore, we can write for equation (3.64)

$$\nabla^2\omega\left\{1 + \frac{C(\theta)r^{-n-2}}{\left(a + b(\theta)r^{1-n}\right)r^{-3}D(\theta)}\right\} = 0. \qquad 3.66$$

Finally we obtain

$$\nabla^2\omega\left\{1+\frac{C(\theta)r^{1-n}}{\left(a+E(\theta)r^{1-n}\right)D(\theta)}\right\}=0. \qquad 3.67$$

When $r\to 0$, $\nabla^2\omega\to 0$ and $\nabla^4\Psi\to 0$. We can therefore say that the flow near the corner is Stokesian for shear-dependent non-Newtonian viscous flow with these approximations.

3.12.2 The Corner Singularities of Viscoelastic Fluids

The flow of viscoelastic fluids in regions involving high stresses, it shows the different behaviour from the viscous flow near the singularity. It is a matter of fact that in non-Newtonian flows little is known about local behaviour near the corner apart from a few cases. (See for example Demir[25], Tanner[91])

We use a similar analysis as before and examine the steady viscoelastic fluid behaviour near the corner, for simplicity, whose model is denoted by CEF. It appears likely that the corner singularity of the viscoelastic fluids may create significant numerical problems. We assume as previously the Moffat assumption that the viscous force still dominate the inertial force as $\mathrm{Re}\to 0$. Under these circumstances, for the viscoelastic fluid

$$\eta^2 H(\eta;\omega)+M(\Psi)M(\eta)+L(\Psi)L(\eta)-\frac{1}{2}M\left(S_{xx}-S_{yy}\right)-L\left(S_{xy}\right)=0 \qquad 3.68$$

where H, M and L are defined as before.

Near the corner, we use a similar analysis to that used earlier to examine the singularity behaviour.

When the polar forms for Ψ,ω,η are substituting into (3.68) we have

$$\left(a+b(\theta)r^{1-n}\right)\nabla^2\omega+A(\theta)r^{-n-2}+B(\theta)r^{-n-3}=0. \qquad 3.69$$

Here $A(\theta)$ and $B(\theta)$ depend on $f(\theta)$ since

$$\nabla^2\omega = \frac{1}{r^3}D(\theta),$$

we have

$$\nabla^2\omega\left\{1+\left[\frac{A(\theta)+B(\theta)r^{-1}}{\left(a+E(\theta)r^{1-n}\right)D(\theta)}\right]r^{1-n}\right\}=0, \qquad 3.70$$

where $\mathrm{B}(\theta)$ represents the elastic part of the viscoealstic flow equation and

$$B(\theta)=(n+1)(n+2)F_1(\theta)+(n+2)F_2(\theta)+(n+1)F_3(\theta)+F_4(\theta). \qquad 3.71$$

Here $F_1(\theta)$, $F_2(\theta)$, $F_3(\theta)$ and $F_4(\theta)$ involves too many functions of θ to incorporate have and we omit their full expression. For n=1 equation (3.71) takes the form

$$B(\theta)=6F_1(\theta)+3F_2(\theta)+2F_3(\theta)+F_4(\theta). \qquad 3.72$$

If $B(\theta)=0$ and $0\le n\le 1$, then we may say from equation (3.70) that the viscoelastic fluid behaviour near the corner is Stokesian as is its counterpart Newtonian fluid

Then we can say that the well known Giesekus-Tanner theorem for second order fluids $(n=1)$ is consistent with the Moffat's assumption which has been used to examine the flow behaviour near the corner earlier i.e. $B(\theta)=0$ for n=1 in equation (3.70).

If the Moffat assumption is true for all n close to 1 (where $n<1$), we require $B(\theta)=0$.

We obtain the equation

$$(n-1)\left[(n+4)F_1(\theta)+F_2(\theta)+F_3(\theta)\right]=0 \qquad 3.73$$

by subtracting the right hand side of equation (3.72) (which must now be zero) from the right hand side of equation (3.71) and assuming $B(\theta) = 0$ for $n < 1$.

In our analysis we find $F_1(\theta) \neq 0$, therefore $B(\theta) \neq 0$ for all $n < 1$, whereas $B(\theta) = 0$ for $n = 1$.

In this case when viscosity is not a constant there may be elastic domination near the corner invalidating the Moffat assumption. This is a problem for future study. In conclusion we can say that the flow is Stokesian near the corner for shear dependent Newtonian and non-Newtonian viscous flow. Under same circumstance the fluid is Stokesian near the corner for the viscoelastic fluid with constant viscosity but the problem remains many questions unanswered for the flow with variable viscosity.

3.13 THE NUMERICAL SOLUTION OF THE FLUID PARTICLE PATHS

The ordinary differential equations are given in the following system with respect to Cartesian co-ordinates(x,y)

$$\frac{d}{dt}\underline{x}_i(t) = V_i\left(\underline{x}_i(t)\right) \qquad 3.74$$

where $i = 1,2$, $x_1 = x$ and $x_2 = y$. The variable V_i represents the velocity components in the x and y direction respectively.

The above system is considered with initial conditions $x(0) = x_0$ and $y(0) = y_0$. The velocity field is obtained numerically by the setting initially of starting points $\left(x_i, y_j\right)$ and then proceeding with the solution through using $u = -\frac{\partial \Psi}{\partial y}$ and $v = \frac{\partial \Psi}{\partial x}$. The system is solved only for the unsteady case.

The solution is obtained to $O(\Delta t, h^2, k^2)$ in the simple explicit approach but $O(\Delta t^2, h^2, k^2)$ with the A.D.I. method.

For both approaches we employ the second order modified-Euler method[17] to track particles. We also initially sought the solution by using the Alternative Predictor-Corrector method but this solution process was undesirable. We formulate the Euler method by re-arrange (3.74) with initial conditions to obtain

$$\underline{x}_{i+1} = \underline{x}_i + \frac{\Delta t}{2}\left[V^O(\underline{x}_i) + V^N(\underline{y}_i)\right] \qquad 3.75$$

where $\underline{y}_i = \underline{x}_i + \Delta t V^O(\underline{x}_i)$. The system uses known value V^0 and V^N which are old and new values of the velocity components respectively.

CHAPTER IV: RESULTS FROM THE 2D CAVITY

In this section we present results for the flow patterns and concentration equation arising from the various types of cavity flow configuration of the 2D model. As discussed earlier, we solved the cavity driven flow in both steady and unsteady cases by considering the configuration as the standard cavity flow domain. Walls were allowed to move with the top wall or both walls moving in same direction, or with walls moving in opposite directions. We have produced results for various grids ranging from 10x10 to 50x50.

We first consider the convergence of the solution by comparing calculations for various grid widths denoted by h. Fig(4.1), (4.2) show vorticity results for the Newtonian and non-Newtonian fluids evaluated near the top wall $(x = 0.4, y = 0.8)$. Also fig(4.3) and (4.4) show results for stream function at the same point. Thus, comparing values of vorticity and stream function it is evident that convergence to 4 decimal places has been achieved at Re=1 and Re=100 as h decreases. In this comparison we also checked the effect of the convergence tolerance, ε, on the accuracy of the solution for both vorticity and stream function. We found that different sufficiently small values of ε did not make significant difference to the overall solution, but when ε had small values (ranging from 10^{-1} to 10^{-5}) for both vorticity and stream function the solution was seen to be more quickly convergent with respect to the mesh size. Therefore we used the convergence criterion for stream function as $\varepsilon_2 = 10^{-5}$ and for vorticity as $\varepsilon_1 = 10^{-4}$ in our subsequent work. We want to note that fig(4.1) - (4.4) represent several fluids evaluated at Re=1 and Re=100. It

was observed the Newtonian and Boger fluids usually take the same value in fig(4.1) - (4.4).

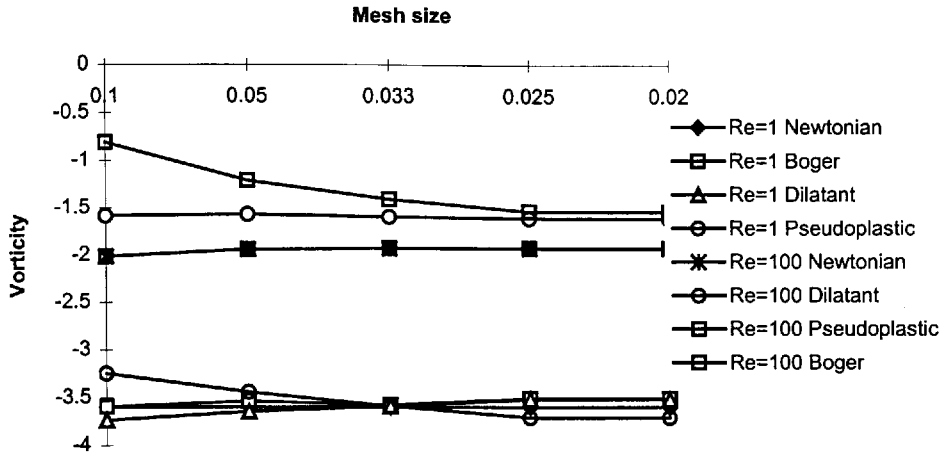

Figure 4.1 ; Convergence criterion for vorticity at Re=1 and Re=100 for time-independent fluid flow.

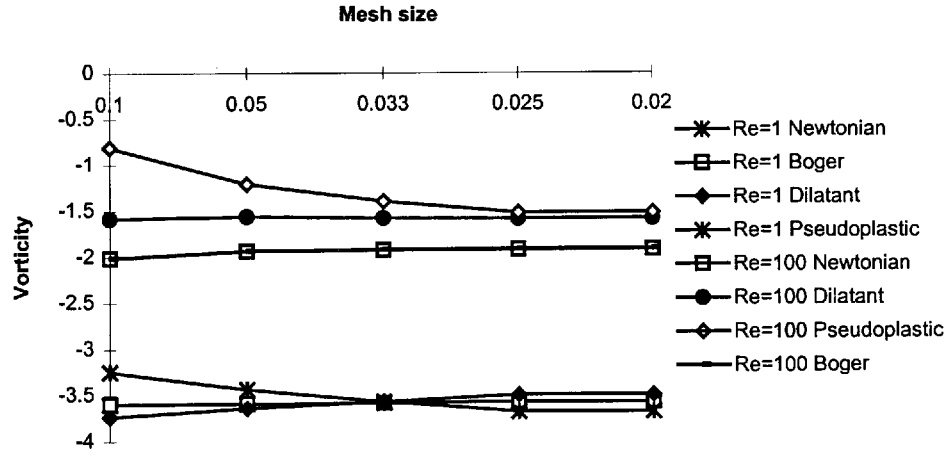

Figure 4.2 ; Convergence criterion for vorticity at Re=1 and Re=100 for time-dependent fluid flow.

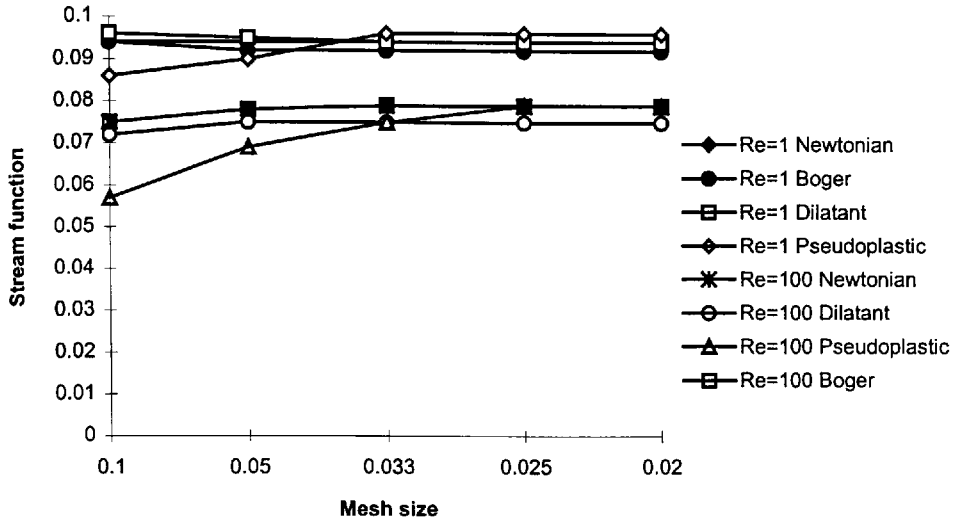

Figure 4.3 ; Convergence criterion for stream function at Re=1 and Re=100 for time-dependent fluid flow.

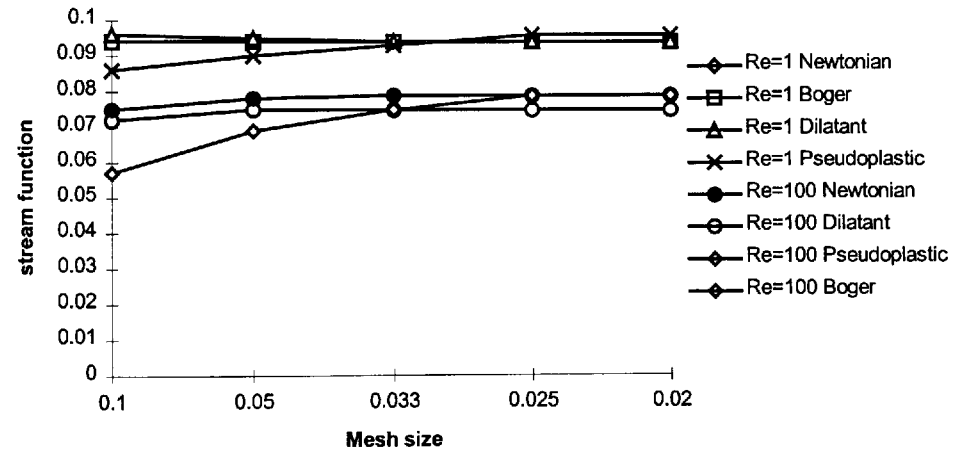

Figure 4.4 ; Convergence criterion for stream function at Re=1 and Re=100 for time-independent fluid flow.

A second comparison was made to check the convergence of the vorticity test criterion. This is seen to be more strict than pointwise convergence with respect to the

mesh size as seen in fig(4.5) with slower convergence. This figure indicates that as mesh size decreases the convergence values decreases for both time-dependent and time-independent flow problem for Newtonian fluids at Re=100.

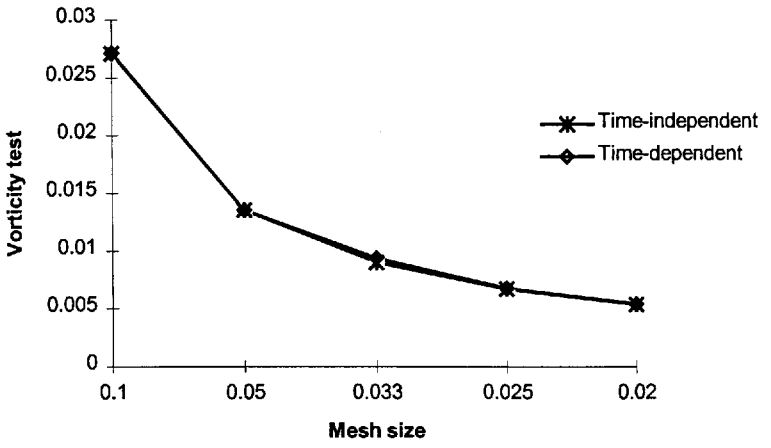

Figure 4.5 ; Convergence criterion for vorticity test problem

A third comparison was made for a graphical comparison of centre line u-velocity for a Reynolds number of 100 and 1000 obtained in this research with the ones available in the literature. In this case we examined the centre line u-velocity for Newtonian and non-Newtonian cases. In the literature only Newtonian fluid data was readily found to compare with our results. These are shown in fig(4.8) and produced by Tosoka et al.**[94]**. Our results are agree very well with those both qualitatively and quantitatively as seen in fig(4.6). In addition we present in fig(4.7) non-Newtonian pseudoplastic behaviour at Re=100 and Re=1000 that display for interest significant change from the Newtonian case. Here there is lesser viscosity near the top wall and flow is faster there. However Boger and dilatant fluids flow show similar behaviour to the Newtonian fluid and results are not presented.

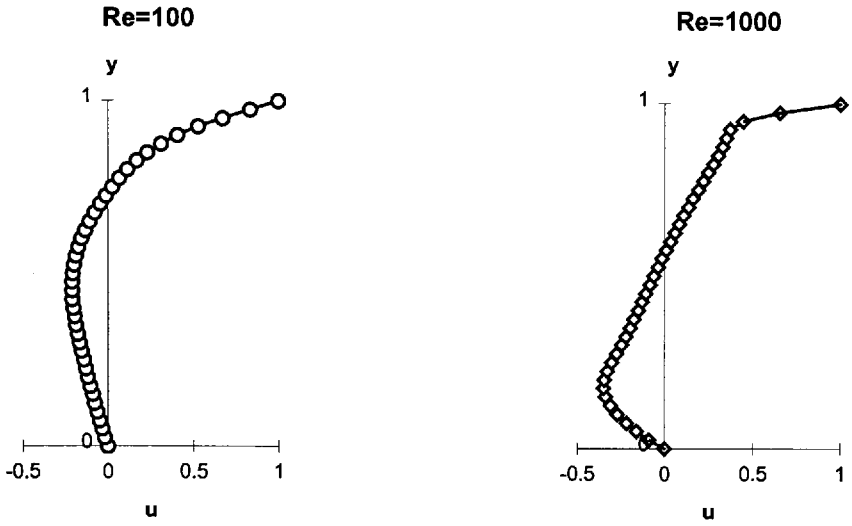

Figure (4.6); u-velocity profile along vertical centre line at Re=100 and Re=1000 for Newtonian fluid by author

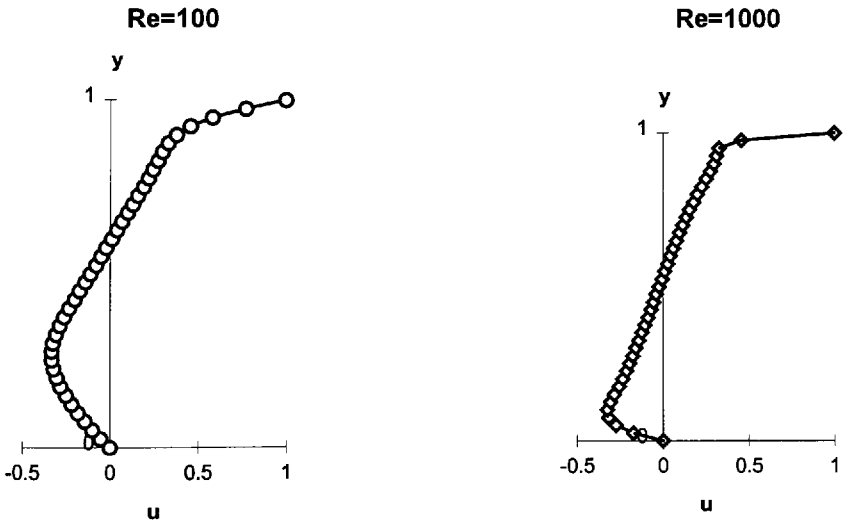

Figure (4.7); u-velocity profile along vertical centre line at Re=100 and Re=1000 for pseudoplastic fluid by author

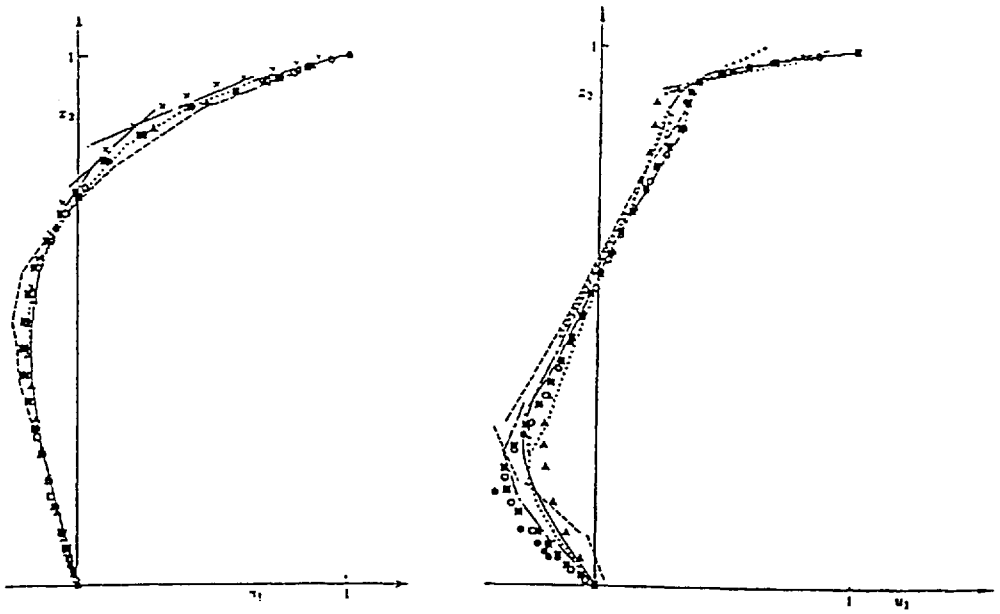

Comparison of u-velocity profiles along vertical centre line at Re=100. Tosaka et al (o 23 by 25, Δ 21 by 21, ■ 25 by 25 BEM) ; □ Ghia et al. (129 by 129 FDM) ; xxx Burggraf (40 by 40 FDM) ; — Thomasset FEM; ...Bercovier et al. FEM : – – Borrel FEM.

Comparison of u-velocity profiles along vertical centre line at Re=1000. Tosaka et al (o 23 by 25, Δ 21 by 21, ■ 25 by 25 BEM) ; ■ Ghia et al. (129 by 129 FDM) ;; — Nallasamy et al. FDM; ...Bercovier et al. FEM : – – Benazeth FEM ; – . – Thomasset ; + + + Figueroa FEM.

Figure (4.8); u-velocity profile along vertical centre line at Re=100 and Re=1000 by Tosaka et al.

Finally we compare our results qualitatively and quantitatively to establish the accuracy of the results obtained in this research with those obtained by Cliffe et al[17], Ottino[67-68], Chien et al[15], Davies[23] and Harvard[40]. From convergence monitoring we therefore present all results on a 40x40 grid for the steady case, and a 30x30 grid for the time-dependent case. We also present some results regarding the aspect ratio of the flow domain. The numbers shown in the figures represent the actual value of the streamlines or concentration contours or temperature

profile as approximate in the flow domain. We organise all results in terms of the following cases.

i) Standard cavity driven flow with the top wall moving

ii) Two walls moving in the opposite direction

iii) Two walls moving in the same direction

iv) The Aspect Ratio of the cavity

v) Concentration Field Results

Before summarising the results for each case, we shall explain how we simulated the flow of shear-thinning and shear-thickening, viscous and viscoelastic fluids. For the shear-thinning fluid the zero shear viscosity is taken as 1 and the infinite zero viscosity is taken 0.1, and vice-versa in the case of shear-thickening fluids. Various small values of Weissenberg numbers can be incorporated with these fluids and a second order Boger fluid equivalent can then be modelled. We, therefore, also simulate the Boger fluid.

4.1: STANDARD CAVITY DRIVEN FLOW

In this case both steady and unsteady flows are solved numerically to compare our results with the work of others for constant shear-rate and variable shear-rate of the viscous and viscoelastic flow as modelled by the CEF model. Our results will be seen to be totally in agreement qualitatively and quantitatively with Davies**[23]**, Chien et al**[15]** and Ottino**[67-69]** and qualitatively with Cliffe et al**[17]**. We also note that the stream function formulation and Woods formulation for vorticity equation on the boundary gave same results. The main parameters that are expected to effect the stability of the flow solution are the Reynolds number and Weissenberg number. We

are restricted, due to program convergence, to a Weissenberg number from 0 to 10^{-3} in most cases. We have mostly seen both viscous and visco-elastic fluid solutions to be similar qualitatively in both steady and unsteady flows. For the Newtonian and Boger fluid cases and Re=1 the solution produces one main vortex and its centre is located at (0.5,0.75) in the flow domain as shown in figure (4.9) and the streamlines are symmetric about cavity's mid vertical line.

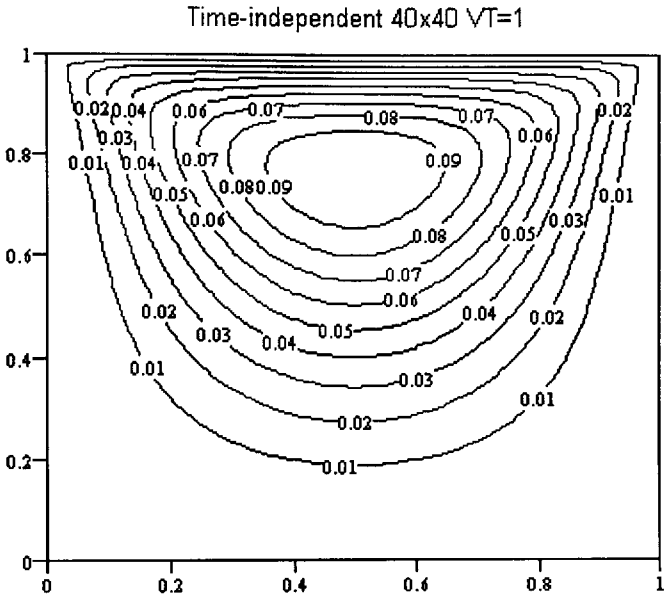

Figure 4.9; Streamlines for Newtonian fluid at Re=1

When the Reynolds number increases, the vortex centre is found to move in the direction of the moving plate, symmetry is lost and the vortex centre is located lower in the cavity. For Reynolds number 400, for example in fig(4.10) it can be seen that the vortex centre moves downstream and is found to be at (0.55, 0.60). We note that when the Reynolds number increases a far weaker barely discernable secondary vortex appears in the bottom right corner. Similar results have been found by Cliffe[17], who used the FEM to solve Newtonian fluid problem, by using 57x57 nodded mesh and published his results for Re=1 and Re=400 shown in fig(4.11) and

(4.12). These figures show close agreement qualitatively with our results, which are shown in fig(4.9) and (4.10). Also, recent experimental results at low Reynolds numbers concerning the standard test case for Newtonian fluids have been produced by Chien et al**[15]**, Leong et al**[50]** and Ottino**[69]**. The cavity was taken as a rectangular with width 10.3 cm and height 6.2 cm, the top wall velocity is 2.69 cm/s and Re=1.7. The streamlines picture is shown in fig(4.13) and is qualitatively close to our results for Re=1 for a square cavity.

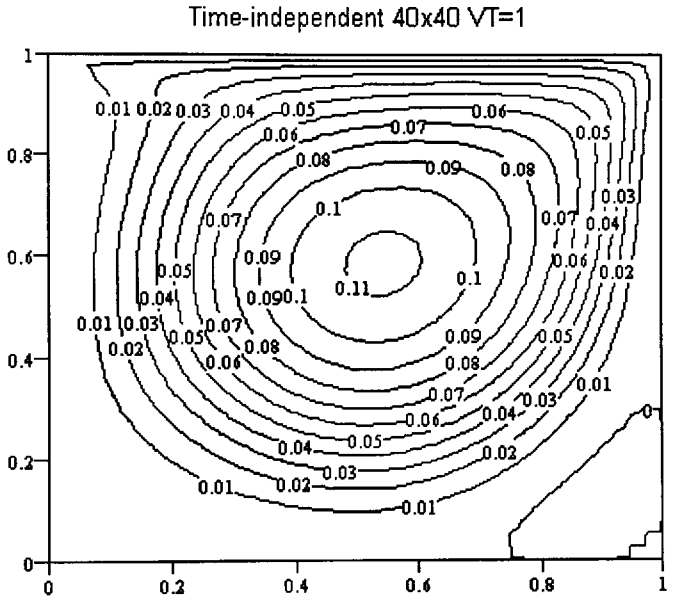

Figure (4.10); Streamlines for Newtonian fluid at Re=400

So as not to overburden the reader with a plethora of figures only the salient pictures of others simulation are mentioned. For non-Newtonian shear-thinning fluid in the cavity, results have been found for Re=1 and Re=100. The vortex centre of the pseudoplastic fluid was found higher than in the corresponding Newtonian case since shear-thinning properties allow the fluid to move faster near the top wall where the viscosity is then least. This fact was also seen for Re=100.

For non-Newtonian dilatant fluid, we have results for Re=1 and Re=100 and very little difference was seen between Newtonian and dilatant fluids. The only difference was that the contour lines were more compact around the vortex centre for the dilatant fluid. As Re increased the vortex centre for the dilatant fluid was located lower than the Newtonian case since the dilatant nature of the fluid near the top wall. We note that this non-Newtonian behaviour is valid for both viscous and viscoelastic fluids.

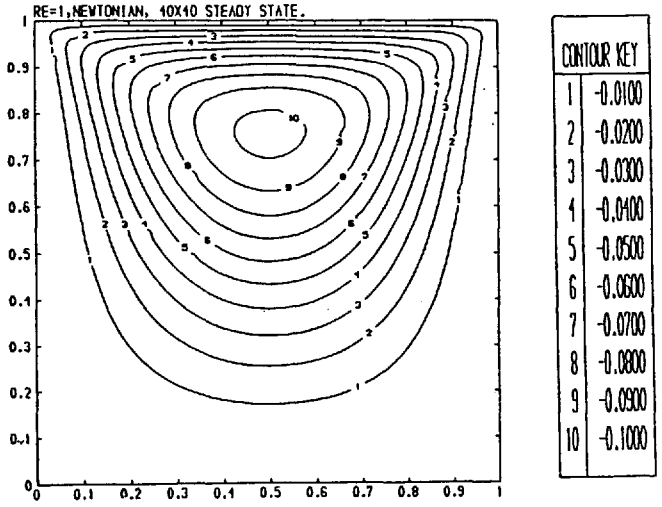

Figure (4.11); Streamlines of Davies[23] for Newtonian fluid at Re=1

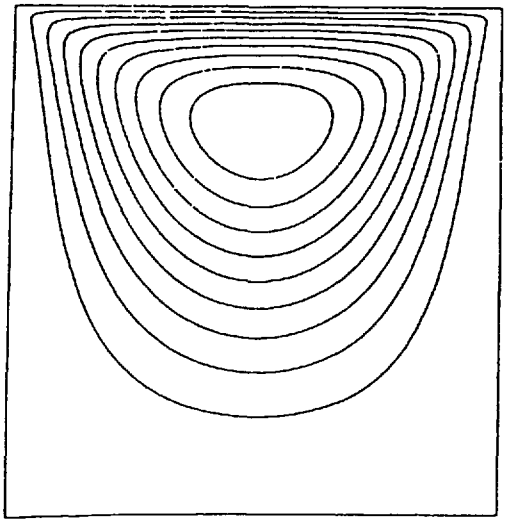

Figure (4.12); Streamlines of Cliffe[17] for Newtonian fluid at Re=1

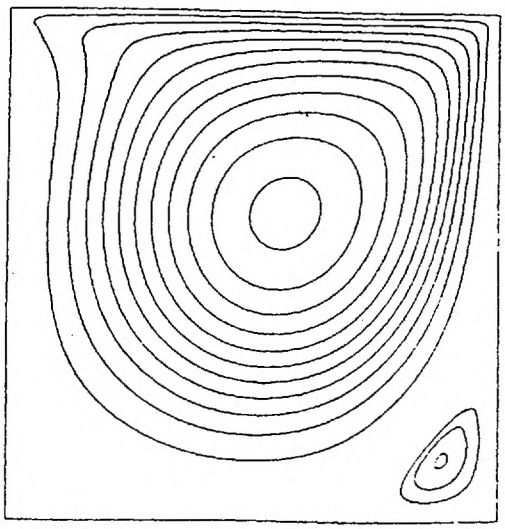

Figure (4.13); Streamlines of Cliffe[17] for Newtonian fluid at Re=400

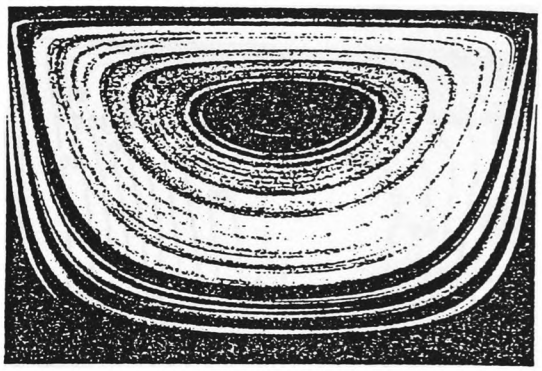

Figure (4.14); Streamlines of Ottino[69] for Newtonian fluid at R=1.7

4.2: TWO PLATES ARE MOVING IN THE OPPOSITE DIRECTION

This type of the flow domain is also called the continuous co-rotational flow domain, and it has been studied mostly experimentally with the top wall moving in the positive x-direction, and the bottom wall moving in the negative x-direction. This case has been examined by Chien et al**[17]**, fig(4.17) Leong et al**[50]** and Ottino**[69]** fig(4.16) for Reynolds number 0.1 to 100. Our results are found to be in agreement qualitatively with the above authors. An example for Re=1 in the case of steady state viscous flow

is shown in fig(4.15) the two walls are moving in the opposite direction the streamlines almost take a "square" shape near the walls of the cavities. In the central part of the cavity the streamlines become more "rectangular". Experimental results for streamlines produced by Ottino**[69]** fig(4.16) also show similar behaviour, becoming more circular around the cavity centre. Also fig(4.17) shows the resulting streamlines by Chien et al**[17]** that are similar to the author's. When the Reynolds number increases the inner streamlines become more oval in shape for all cases of the viscous and viscoelastic fluids studied. As an example we take the Reynolds number 500 steady state Newtonian solution, and it is easily seen that the streamlines are diagonally symmetric with respect to the y=x line shown in fig(4.18).

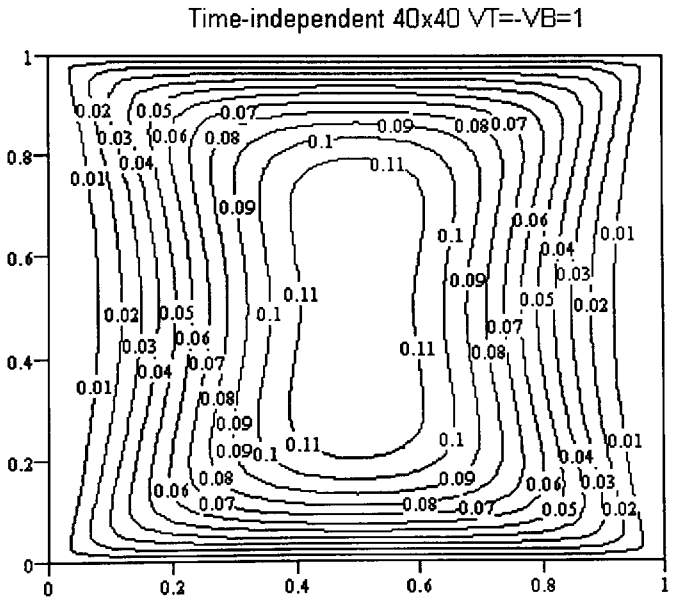

Figure (4.15); Streamlines for Newtonian viscous flow at Re=1

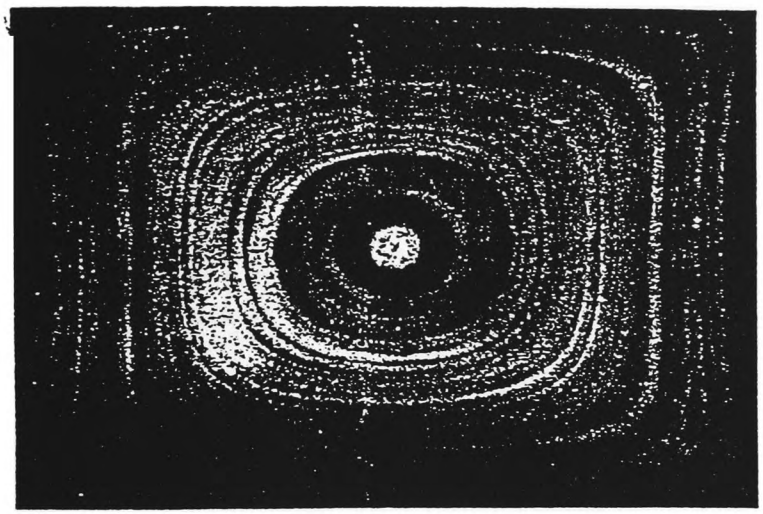

Figure (4.16); Experimental streamlines at Re=1.7 by Ottino[69], VT=-VB=1

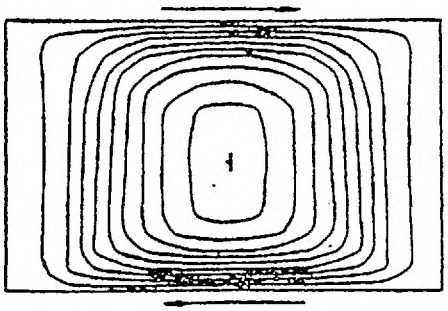

Figure (4.17); Experimental streamlines at Re=1 by Chien et al[17], VT=-VB=1

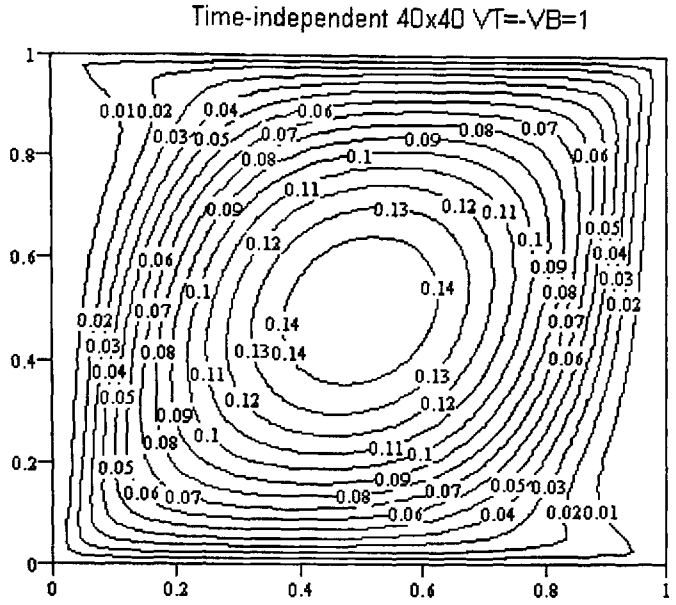

Figures (4.18) ; Streamlines for Newtonian fluid at Re=500

4.3: TWO PLATES ARE MOVING IN THE SAME DIRECTION

This type of flow is also called counter co-rotational flow. It is the most studied case of the cavity driven flow in mixing, with the two walls moving in the positive x-direction. In this case two main vortices are produced in the configuration and they appear symmetric both vertically and horizontally at Re=1 for the case of Newtonian and Boger fluid in the steady case. This is also so for the unsteady viscous case as shown by fig(4.19). The vortex centres were found to be (0.5,0.8) and (0.5,0.2) from the top and bottom walls respectively. We also have similar results from the both unsteady and steady state viscous pseudoplastic and dilatant cases, and they are similar to the Newtonian case at Re=1. These results are in agreement qualitatively with Chien et al[17], shown in fig(4.20).

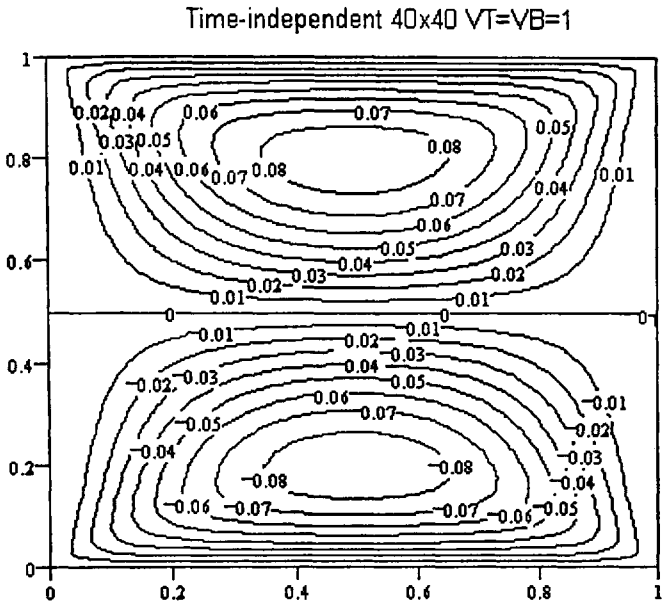

Figure (4.19); Streamlines for Newtonian fluid at Re=1

When the Reynolds number increases the vortex centres were seen to move in the direction of the moving walls and symmetry is maintained horizontally up to Reynolds number 600 for Newtonian and Boger fluid flow, for the steady and unsteady cases. Moreover for non-Newtonian fluids with time dependent viscous flow, the symmetry was seen to be maintained at Re=1000.

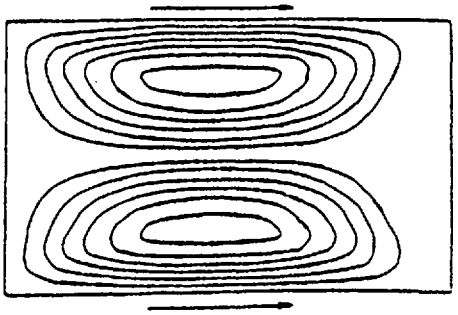

Figure (4.20); Experimental streamlines at Re=1.7 by Chien et al[17], VT=VB=1

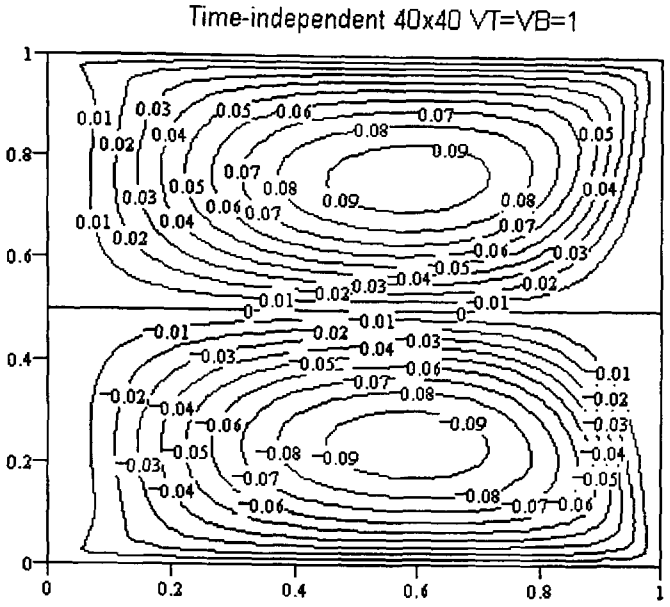

Figure (4.21); Streamlines for Newtonian fluid at Re=600

For time-dependent viscoelastic fluid at Re=1 the horizontal symmetry line was seen to be marginally broken in all cases whether the viscosity is constant or variable fig(4.22). To confirm this, all possible grid meshes with a certain Weissenberg number were checked as to whether this effect was due to the grid size or not. However the same effect was seen in all possible grid meshes used. When the Reynolds number increases the symmetry line appears again, so that at low Reynolds number elasticity 'breaks' the symmetry until inertia effect begins to dominate the flow. We present this behaviour for shear-thinning flow at Re=1 and at Re=100 in fig(4.22) and (4.23). Another difference between the unsteady and the steady state was that the vortex centres moved in the direction of the moving plates and were located at approximately (6.25,7.75) and (6.25,2.25). It is the first occurrence of destabilisation that we have encountered.

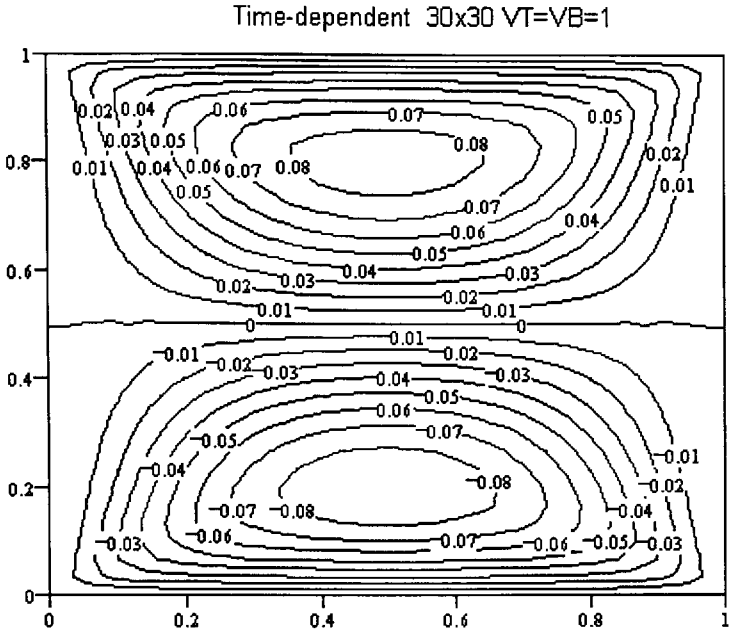

Figure (4.22); Streamlines for visco-elastic pseudoplastic flow at Re=1

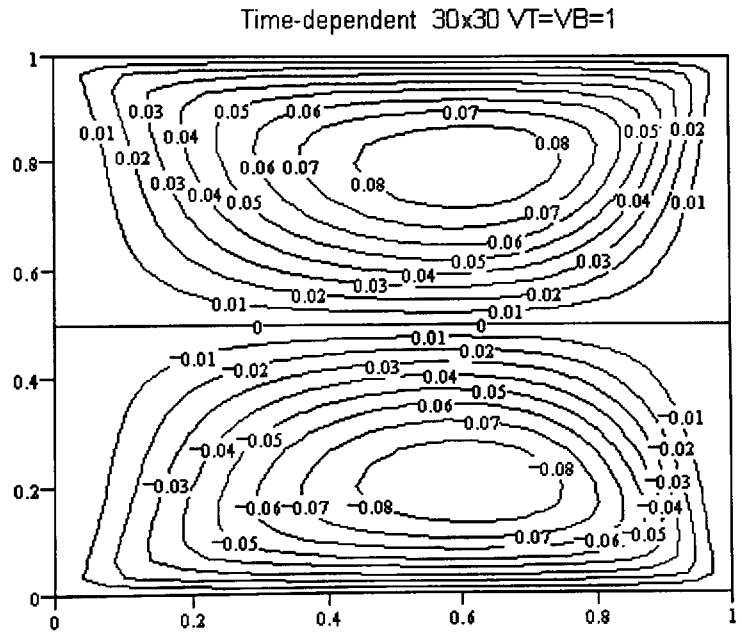

Figure (4.23); Streamlines for visco-elastic pseudoplastic flow at Re=100

4.4: THE ASPECT RATIO OF THE CAVITY

In this section the effect of the aspect ratio for cavity driven flow is considered and flow patterns produced for two cases: two walls moving in the same, and in opposite directions. We determined numerical solutions in both steady and unsteady cases with constant and variable viscosity for viscous and visco-elastic fluids. The grid meshes usually used are 80x40 or 40x80 in the steady case and 40x20 or 20x40 in the unsteady case.

We define the aspect ratio as cavity height to cavity width and wish to consider the aspect ratio problem in each case separately; firstly the aspect ratio 0.5 is studied, then we consider aspect ratio as 2, 0.33 and 1.3 successively.

4.4.1. Aspect Ratio 0.5

The fluid flow is generated in the wide cavity configuration with two walls moving in the same or in opposite directions respectively. In the case of walls moving in opposite direction with Reynolds number up to 200. One main vortex produced for all fluids considered. The flow pattern is seem to be in agreement for both viscous and visco-elastic case where we have one main vortex. When inertial forces dominate flow the streamline pattern becomes more oval than near the cavity's wall as seen in fig(4.24)

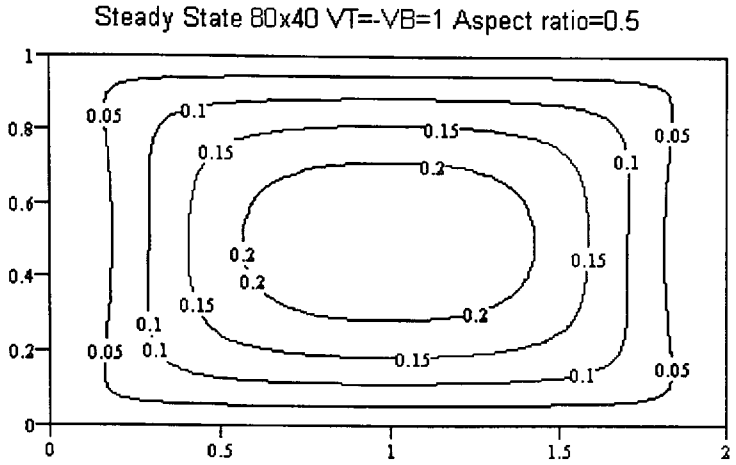

Figure (4.24); Streamlines for Newtonian fluid at Re=1

As the Re increases, for example Re=100, streamline plots become more 'oval' and smoother than at Re=1. Also, as expected, the vortex "moves with the walls" as seen in the fig(4.25) as follows.

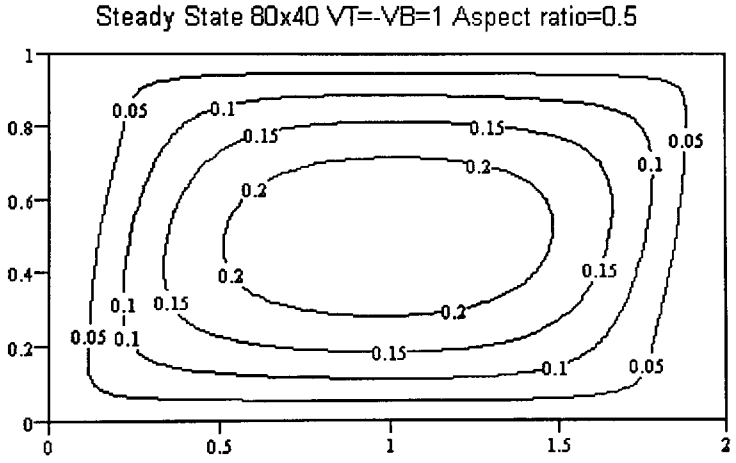

Figure (4.25); Streamlines for viscous dilatant flow at Re=100

We produced some results for the time-dependent case for both viscous and viscoelastic fluids with various Reynolds and Weissenberg number with aspect ratio 0.5. When two walls move in opposite direction (at Re=1) we have one main vortex with constant and variable viscosity for Newtonian and non-Newtonian fluids.

When two walls move in same direction, two counter-rotating vortices are obtained each occupying half of the cavity about horizontal centre line at Re=1. This is so for both steady and unsteady viscous case with constant viscosity as shown in fig(4.26). We also have similar results from the both steady and unsteady state simulations for non-Newtonian viscous fluids, and they are in agreement with constant viscosity fluids at Re=1.

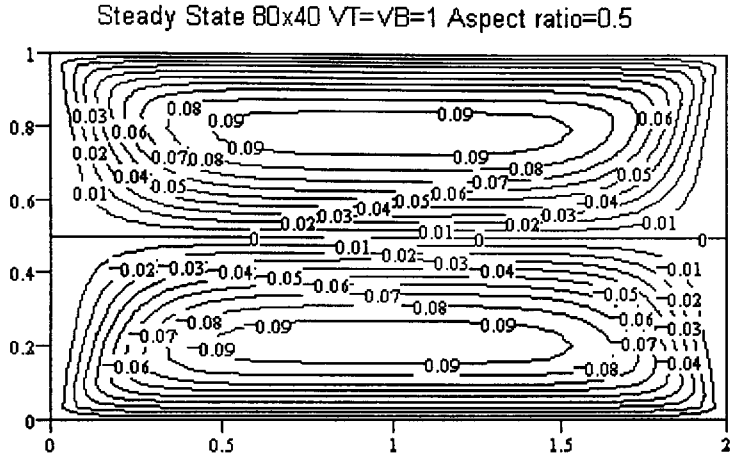

Figure (4.26); Streamlines for Newtonian fluid at Re=1

When the Reynolds increases (e.g. to Re=100) the vortex centres move "with moving walls", and symmetry is seen to be maintained for both steady and unsteady viscous flow cases..

For the time dependent case the viscoelastic fluid gives different results at Re=1. We obtained a destabilisation in this case where the horizontal symmetry line is lost for all fluids whether viscosity is constant or variable. When Re increases the symmetry line reappears. Therefore we can say that the elasticity 'breaks' the symmetry line until inertial effects begins to dominate the flow. We illustrate this behaviour for a viscoelastic dilatant fluid at Re=1 in fig(4.27) and (4.28), at Re=1 and Re=100 respectively.

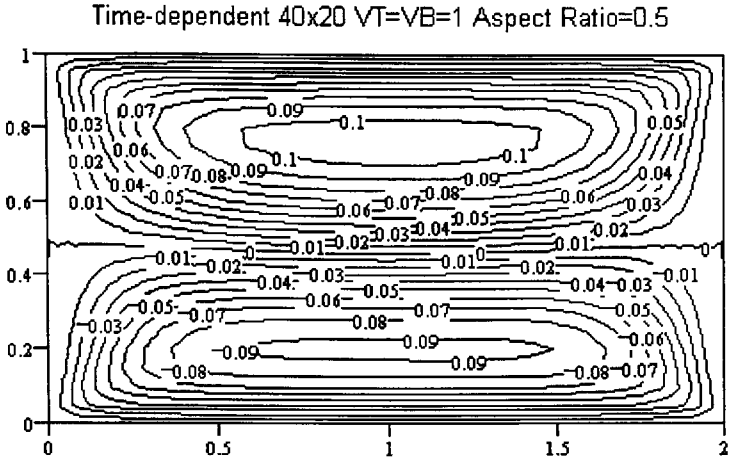

Figure (4.27); Streamlines for viscoelastic dilatant fluid at Re=1

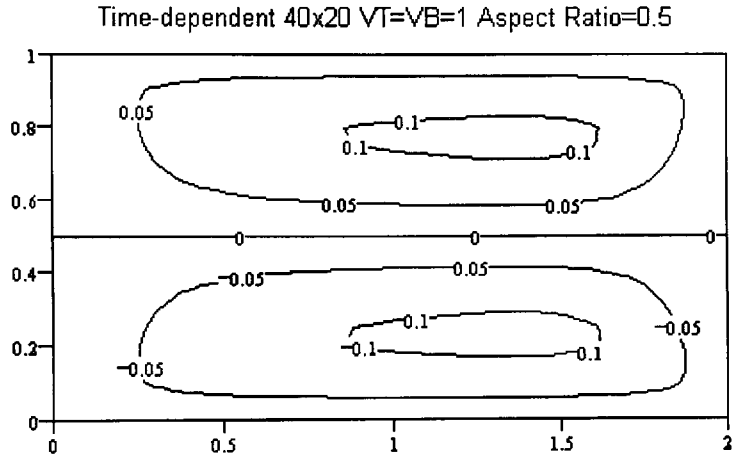

Figure (4.28); Streamlines for viscoelastic dilatant fluid at Re=100

4.4.2. The Aspect Ratio is 2

In this case flow is generated in the tall cavity configuration with two walls moving in the same or opposite directions. We produced results for Reynolds number up to 100 in both steady and unsteady cases. When two walls move in opposite directions for steady state (with constant or variable viscosity) we obtained the same behaviour at Re=1 for both viscous and viscoelastic fluids. Two vortices are surrounded by one outer streamline for Newtonian and non-Newtonian fluids as well. The resulting streamlines are shown in fig(4.29) which adopt an "hour glass" formation.

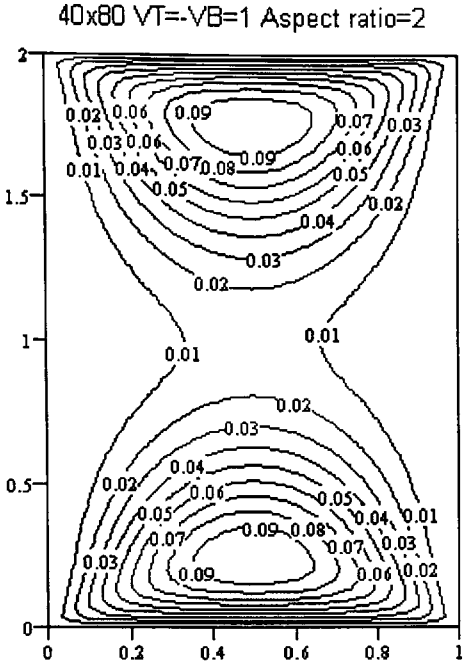

Figure (4.29); Streamlines for Newtonian fluid at Re=1

As Re increases, for example to Re=100 one main vortex is found and the vortex is found to move "with moving walls" for all cases of viscous and viscoelastic fluids. The vortex centre is located at (0.5,1) and streamlines around the centre of the cavity become more circular. This behaviour is shown in fig(4.30). Moreover, time-dependent fluid results are in agreement both qualitatively and quantitatively with time-independent case, for example one decimal places.

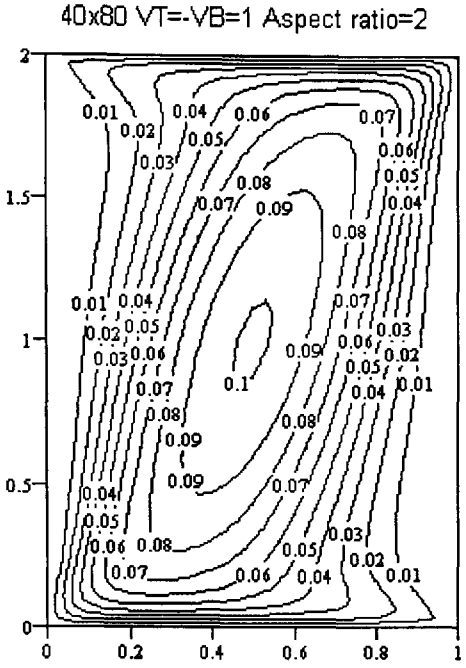

Figure (4.30); Streamlines for viscous pseudoplastic fluid at Re=100

When two walls move in the same direction for the steady case for both viscous and viscoelastic fluids, we see that two counter-rotating vortices occur at Re=1. These vortex centres are located from top and bottom walls respectively at (0.5,0.2) and (0.5,1.8), shown in fig(4.31). Our results are in agreement qualitatively and quantitatively with other published experimental and theoretical work with Ottino**[67]**, shown in fig(4.34) for a Newtonian fluid. When Re increases the vortex centres move in the direction of the moving walls and are located at (0.6,0.2) and (0.6, 1.8) at Re=100, shown in fig(4.32).

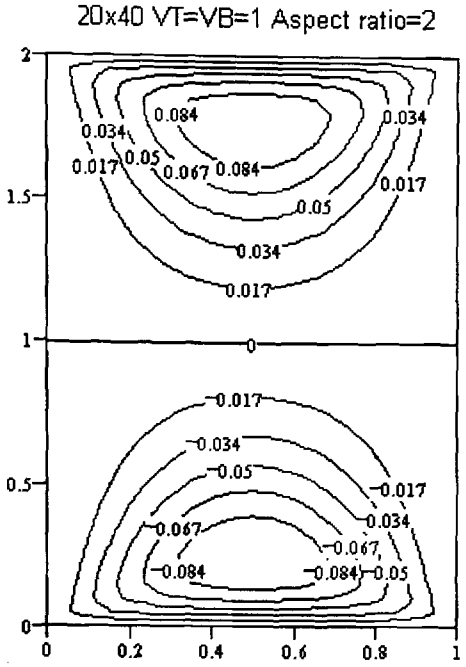

Figure (4.31); Streamlines for Newtonian fluid at Re=1

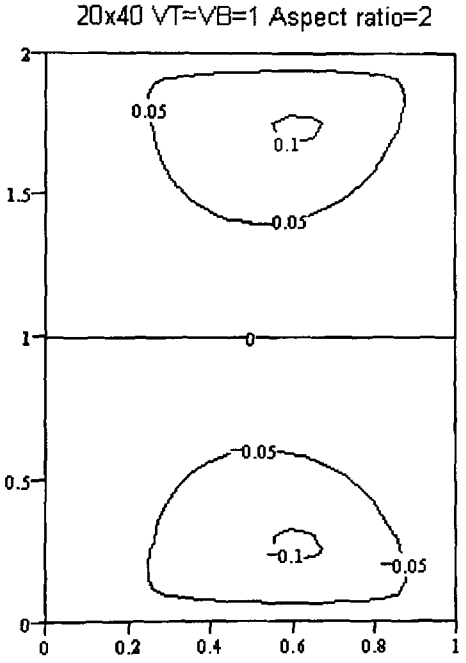

Figure (4.32); Streamlines for viscous pseudoplastic fluid at Re=100

For the time-dependent case it is observed that both viscous and viscoelastic fluid have the same behaviour with various Reynolds and Weissenberg numbers, except that for Re=1 in the case of a visco-elastic fluid. Here it is seen that the symmetry on

the centre line is lost (as happened in the square box flow domain). We therefore illustrate this behaviour at Re=1 for viscoelastic case in fig(4.33).

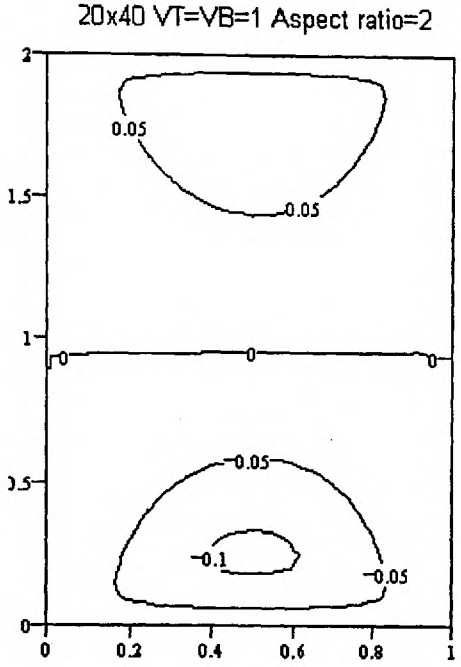

Figure (4.33); Streamlines for Boger fluid at Re=1

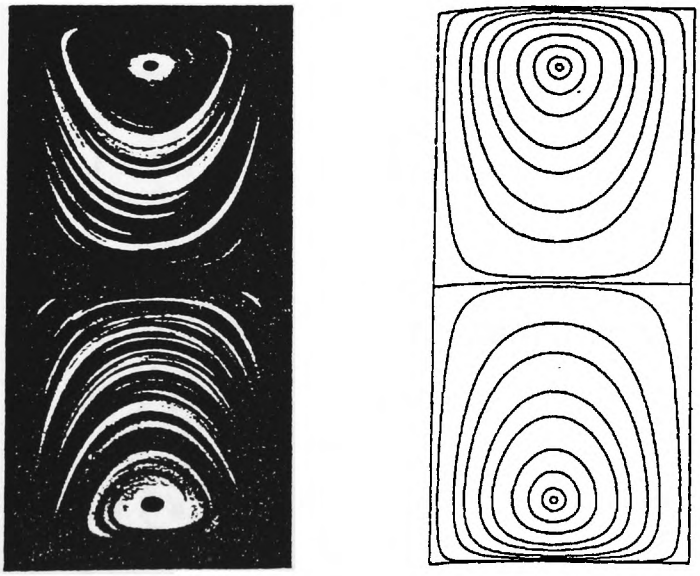

Figure (4.34); Experimental and theoretical streamlines produced by Ottino et al[67] at Re=1

4.4.3. Aspect Ratio is 1.33

We produced results with the aspect ratio of the cavity flow taken as 1.33 and considered two walls moving in the same direction and later in opposite directions. In this particular case we have many results for time dependent and time independent formulation in both viscous and visco-elastic flow cases. We see that the fluid pattern exhibits similar behaviour whether the flow is viscous or visco-elastic with variable or constant viscosity. We therefore give results for the time dependent flow only. If two walls move in opposite directions at Re=1, we see in fig(4.35) that there are two vortices which are symmetric and located near the top and bottom half of the cavity, and are surrounded by an outer vortex. This result is in agreement qualitatively with Ottino**[67]**, as shown in fig(4.36). As the Reynolds number increases it is seen that the centre of the each vortex moves to the corner with the moving wall and the main vortex becomes more oval than at Re=1.

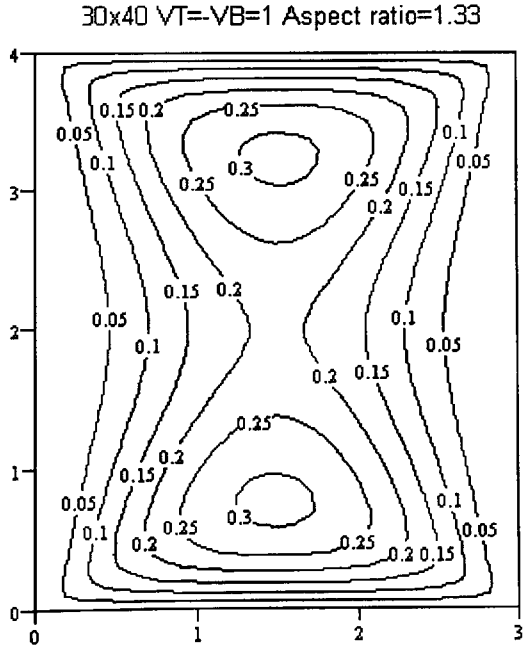

Figure (4.35); Streamlines for Newtonian fluid at Re=1

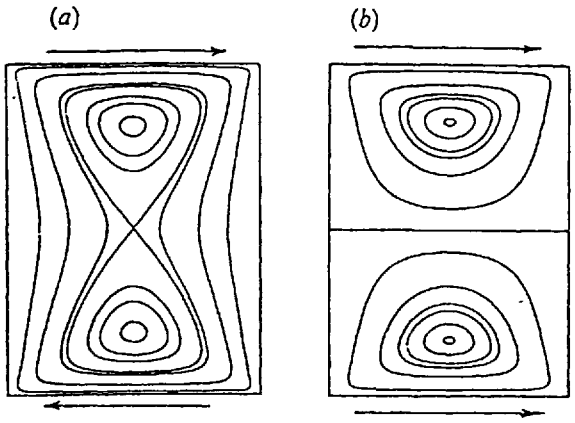

Figure (4.36); Experimental streamlines produced by Ottino et al[] at Re=1 a)VT=-VB=1, b) VT=VB=1

If two walls move in the same direction we see similar behaviour consistently for Newtonian and non-Newtonian cases, with various Reynolds and Weissenberg numbers. Initially at Re=1 two counter-rotating vortices were found and then as the Reynolds number increases these vortices move in the same direction as the moving walls. We present this behaviour in fig(4.37) for Re=100

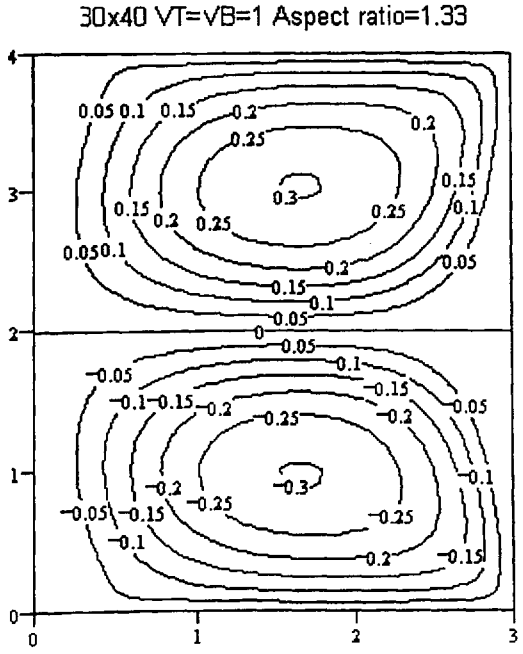

Figure (4.37); Streamlines for viscoelastic pseudoplastic fluid at Re=100

We note that when elasticity is involved in the case of two walls moving in the same direction we still have a destabilisation effect due to elasticity for Re=1. So again elasticity breaks the symmetry line which later straighters as the Re number increases.

4.4.4. Aspect Ratio is 0.33

In this section we examine the cavity driven flow in two cases as previously. For an aspect ratio 0.33 of the flow domain we observe that the flow patterns are in agreement in all cases whether two walls move in same or opposite directions for viscous and viscoelastic fluids. If two walls move in opposite directions at Re=1 one main vortex was obtained with vortex centre located at (1.5, 0.5), as shown in fig(4.38). As the Reynolds number increases the vortex moves in same direction with the moving wall.

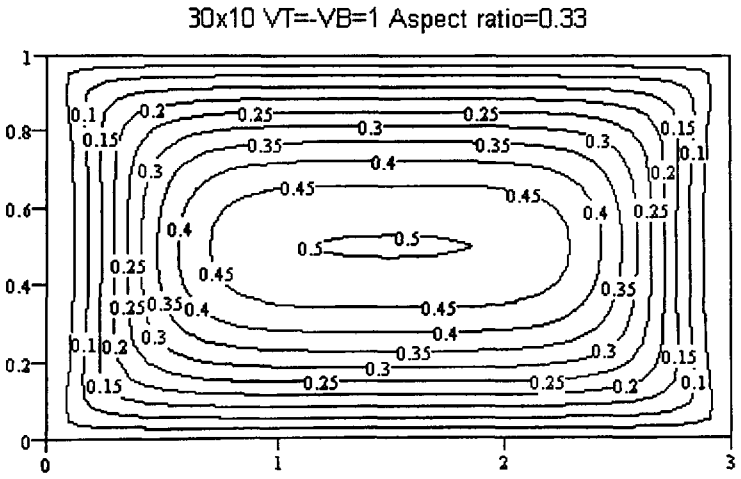

Figure (4.38); Streamlines for Newtonian fluid at Re=1

If two walls move in the same direction, as expected two counter rotating vortices were again found to occur, for both viscous and visco-elastic cases with constant and variable viscosity models. This behaviour is shown in fig(4.39) and as the Reynolds

number increases the vortex centre move to near the corners in the same direction as the moving walls.

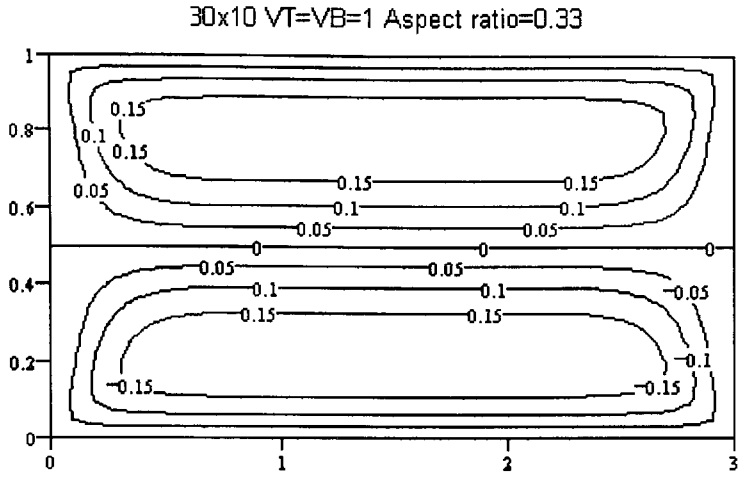

Figure (4.39); Streamlines for Newtonian fluid at Re=1

4.5 CONCENTRATION RESULTS OF 2D FLOW EQUATIONS

In this section results are produced for the time-dependent viscous and visco-elastic fluid flow, for the colour band and the dispersive mixing generated by the flow patterns of the cavity flows. This problem has been undertaken by Havard[**40**] for Newtonian fluids only and by Davies[**23**] for viscous flow only, in both Newtonian and inelastic non-Newtonian cases. We now extend their studies to viscous and certain types of viscoelastic fluid flow. We assume that the dye initially occupies the top half of the cavity. We also assume there is no chemical reaction in the concentration flow equation. We usually obtain results for Re=1 and Re=100 and where Schmidt number is taken as 50 for comparative in Chapter 4.1. Fig(4.40) shows results for the convergence of the concentration test criterion with respect to the mesh size and Sc number. As seen, while the mesh size decreases the convergence values decrease as well for the time-dependent flow case. In the unsteady cases the results are acceptable as long as the time increment is sufficiently small.

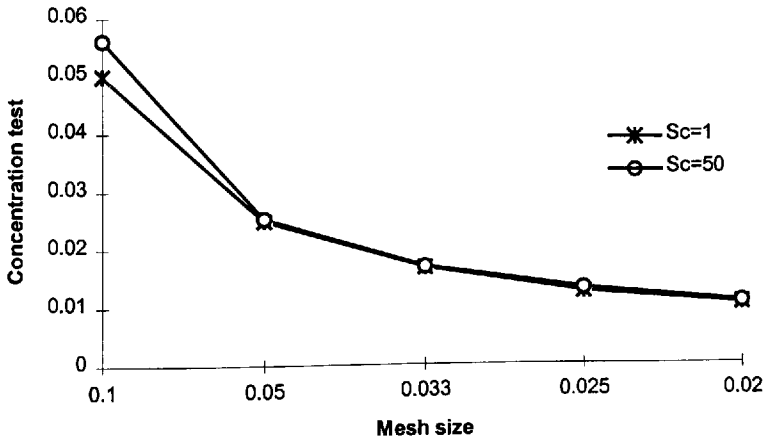

Figure 4.40 ; Convergence criterion for concentration test problem

We compared our results qualitatively and quantitatively with those quoted by Havard[30] and Davies[23] and found then to be in agreement, as demonstrated in the following figures (4.41) - (4.47).

4.5.1 Standard Cavity Driven Flow

We produced results in the cases of Re=1 and Re=100 to test our numerical solution with Havard[40] and Davies[23]. We derived the solution for viscous and visco-elastic fluid flow with various Reynolds and Weisenberg numbers for the time-dependent case. When Re=1 both viscous and viscoelastic fluids exhibit similar behaviour. On comparison of our results with Davies[23], shown fig(4.41) it can be seen that they are in close agreement qualitatively and quantitatively.

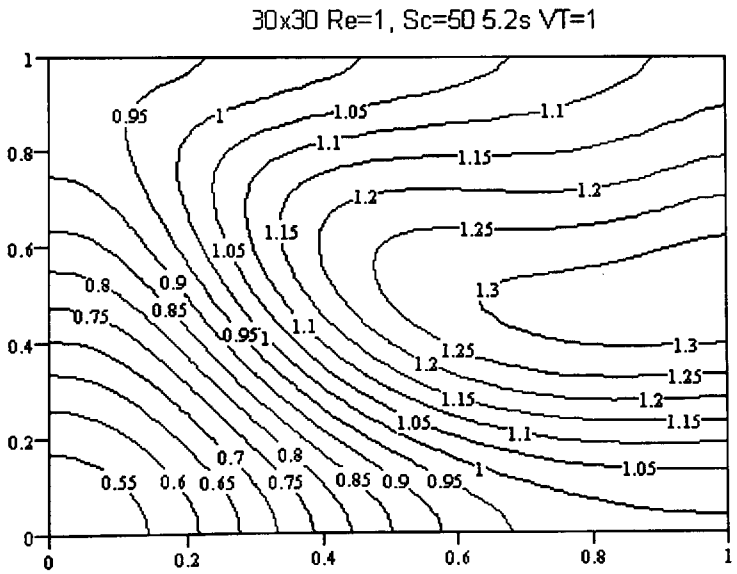

Figure (4.41); Concentration contours for Newtonian flow at Re=1, Sc=50

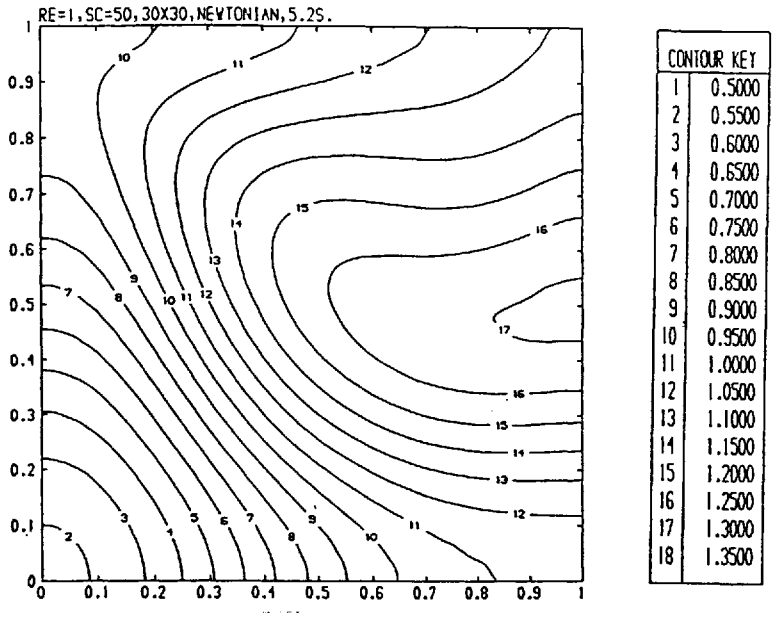

Figure (4.42); Concentration contours By Davies[23] for Newtonian flow

The non-Newtonian cases are similar to the Newtonian case but the pseudoplastic fluid streamlines are located in a relatively higher position in the flow domain as compared with Newtonian flow due to the fluid properties. This is because the shear-thinning fluid moves more rapidly near the top plate where the fluid is thinner. For a dilatant fluid, due to shear-thickening properties, streamlines are lower than for the Newtonian case and the fluid is slower moving near the top plate.

For Re=100 the advection force is more dominant in the concentration equation. Similar results were seen in this case for Newtonian and Boger fluids. It is easy to see that separation of the coloured band takes in the streamline flow pattern shape, and concentration is therefore high near the top plate. The dilatant and pseudoplastic fluid's colour distribution were in agreement for any viscous fluid. The results for a dilatant fluid are similar to the Newtonian fluid, except the coloured band is a little higher in the cavity and less spread out near the top plate. We present a figure for Newtonian at Re=100 below.

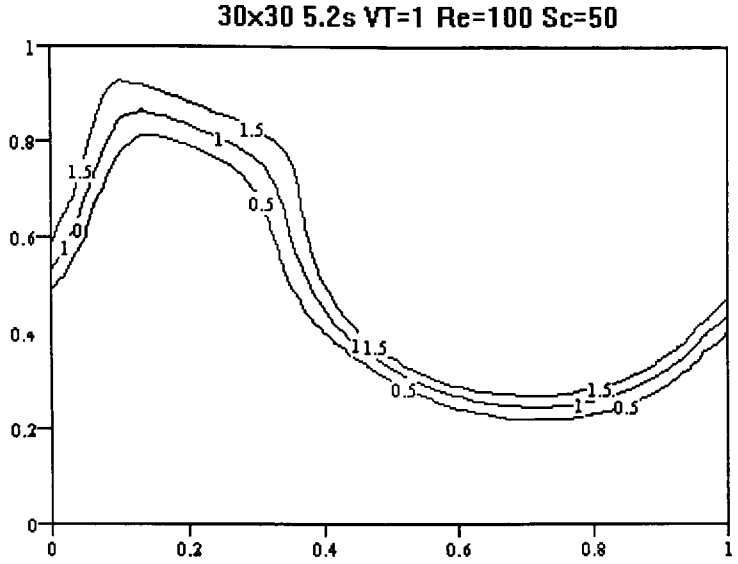

Figure (4.43); Concentration contours for Newtonian fluid

For the viscoelastic case it was seen that both the Boger and dilatant fluid showed similar behaviour was the Newtonian fluid. The elastic pseudoplastic concentration distribution fluid still resembled its viscous counterpart.

4.5.2 Two Walls Moving In Opposite Direction

In this case the flow is generated by two walls moving in opposite direction and we examine the unsteady viscous and viscoelastic fluids with constant and variable shear-rate. For Re=1 all three fluids showed little difference as compared with Newtonian fluid shown in fig(4.44). The contours indicate that the concentration intensity are more wave like in appearance, and they are seen to be more wavy and almost symmetric about the positive diagonal (y=x) of the cavity.

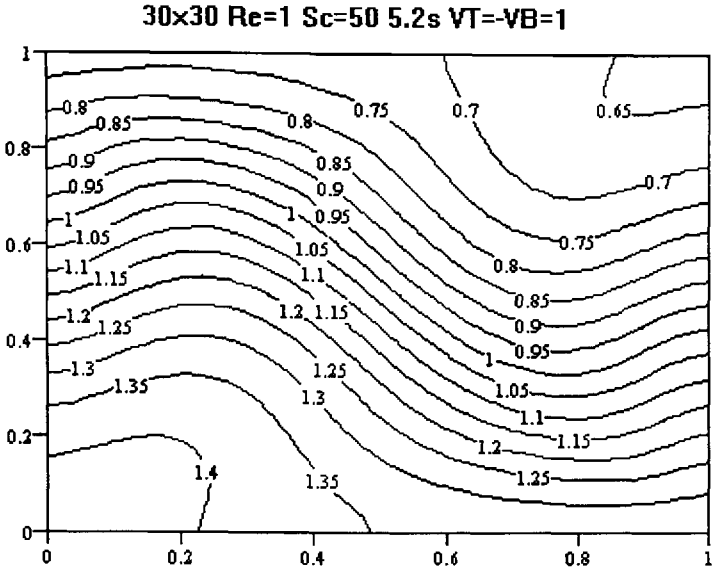

Figure (4.44); Concentration contours for Newtonian fluid

For Re=100 we again observed that the advection terms dominate to whether the fluid viscosity is defined by constant or variable viscosity. Therefore the coloured band plots was seen to be a reverse 'S' shape, asymmetrical about the cavity's vertical centre line. Results for all fluids considered show similarity and differences due to nature of the fluids themselves. Moreover in the pseudoplastic fluid case the location of the coloured band is higher in the cavity and less spread out near the top wall. We illustrate this behaviour in fig(4.45).

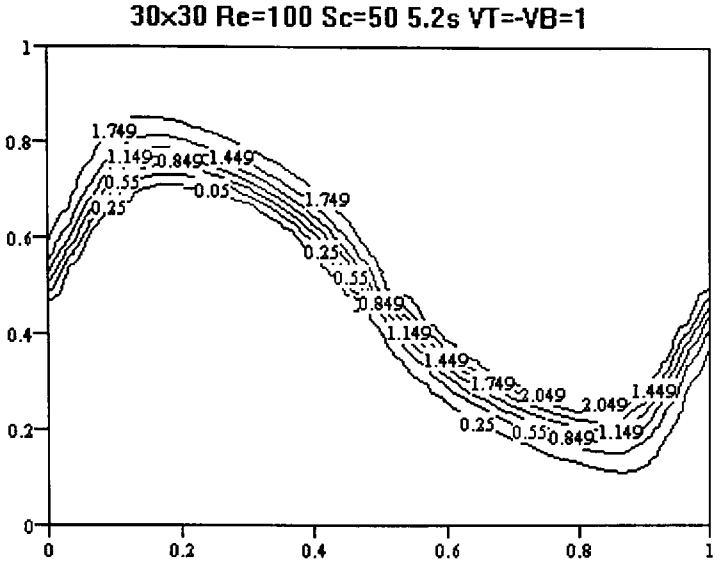

Figure (4.45); Concentration contours for viscous pseudoplastic fluid

4.5.3 Two Walls Moving in Same Direction

In this section we firstly considered the concentration field contours at Re=1 and all three types of fluid were studied in both viscous and viscoelastic cases. Our results agree in both cases i.e. the fluid shows the same behaviour regarding their own properties whether the fluid is viscous or viscoelastic and our results are in agreement with Davies[23]. In the case of Newtonian fluid which is shown in fig(4.46), the concentration field plot is almost symmetric about the horizontal mid-line of the flow domain, and the concentration contours intensity being mirror images of one an other. However the concentration values are roughly twice as high in the top half of the cavity than in the lower half.

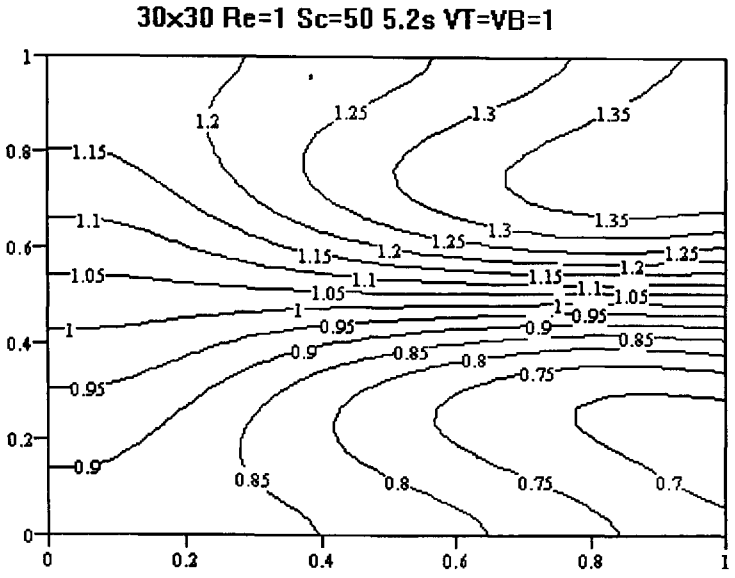

Figure (4.46); Concentration contours for Newtonian fluid

For Re=1 we found a concentration within the cavity and this behaviour, shown above, due to the nature of the flow is true for all simulation times up to 11 seconds. As shown before, the streamlines for the case of two walls moving in same direction have two vortices occurring on the each half of the cavity and they are symmetric (fig(4.19)). Therefore this flow model produces quick mixing within the cavity where diffusion plays a vital role in the overall mixing process. For Re=100 the advection forces dominate flow and the coloured band spreads out between the streamlines in the 'slow' flow region and this is easy to see from fig(4.47). Here the concentration is slightly more spread out near the left wall because the circulation is weaker and diffusion effects are greatest. All three fluids considered for both viscous and viscoelastic cases produced very similar results, comparable with a viscoelastic dilatant fluid shown in fig(4.47).

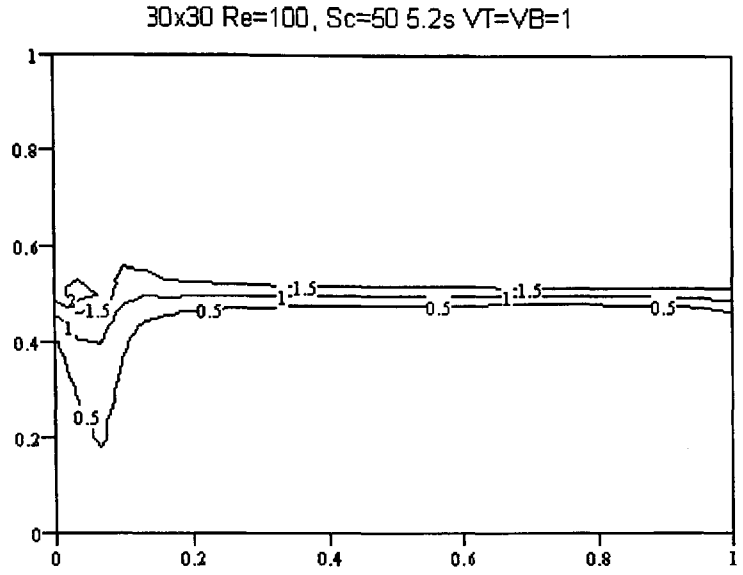

Figure (4.47); Concentration contours for viscoelastic dilatant fluid

4.6. PARTICLE PATHS AND DISCONTINUOUS PERIODIC CAVITY FLOW

In this section we investigate particle paths by using a discontinuous periodic motion with two wall motion as the top and bottom plates move with a periodic motion as shown in, fig(4.48). This motion is also similar to a mixing process, so that the method may suggest a means to improve the mixing process. Davies**[23]** gives a good account as to how better mixing can be obtained with time-dependent and periodic stream functions. Therefore to follow the particle paths we consider discontinuous periodic cavity flow as was originally investigated by Aref**[1]** within a cylindrical configuration for incompressible fluid. This solution depends on the period of motion(**T**), the Reynolds number Re. Initially we assumed that top wall moves periodically with period **T**. Then, after one period, the top wall stops and the bottom wall starts moving in an opposite direction to the top wall but, with the same time period. This is repeated until the desired simulated time, consisting of a fixed number of time periods, is reached.

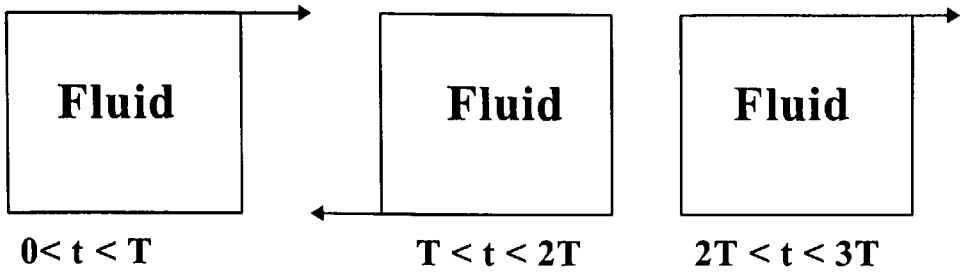

Figure (4.48); Discontinuous periodic motion for cavity flow

Aref[1] described the numerical solutions to the Hamiltonian equations for the particle motion and observed them to be chaotic. Later, this flow was studied by Chien et al[17], Leong et all[50], and Ottino[67-69] of the Newtonian fluid at low Reynolds number. These researchers obtained for this flow horseshoe mappings that indicated that the system was chaotic. We have therefore extended the work of this flow study of the particle paths for viscous and certain types of the viscoelastic fluid with constant and various shear-rate for Re=1 and Re=100. We also consider the period of the motion as **T**=1 and **T**=2 and for a duration of 60 seconds simulation time. Results are presented as fluid particle periodic motion which are located in the (x,y) co-ordinate system of the cavity.

We have always considered three particles which may have taken to be located initially in the cavity's vertical middle line $(x = 0.5)$. The results are produced by considering all types of fluid in both viscous and viscoelastic case. For a Newtonian fluid at Re=1, **T**=1s and end time of 60s, results are to be seen in fig(4.49). It shows the trace paths of three particles. The outer particle (top figure) paths travel a wider orbit in the cavity. By contrast the inner particle paths of the Newtonian fluid travel an shorter circuits in the cavity. However, all three particle paths become flatter near the cavity's top wall. The middle and lower figures show the traces obtained for the

periodic motion of the particles by considering the x and y positions with time. Also for pseudoplastic and dilatant fluids the particle dispersal almost looks similar to the Newtonian fluid. Later we produced results for higher Reynolds number of 100 and we saw that the fluid particle paths tend to become flatter near the top wall of the cavity due to the increase in the fluid inertia. Fig(4.50) shows that all three particles move more quickly and travel wider distances in the cavity. Moreover, the outer particle path become more "tightly bound"

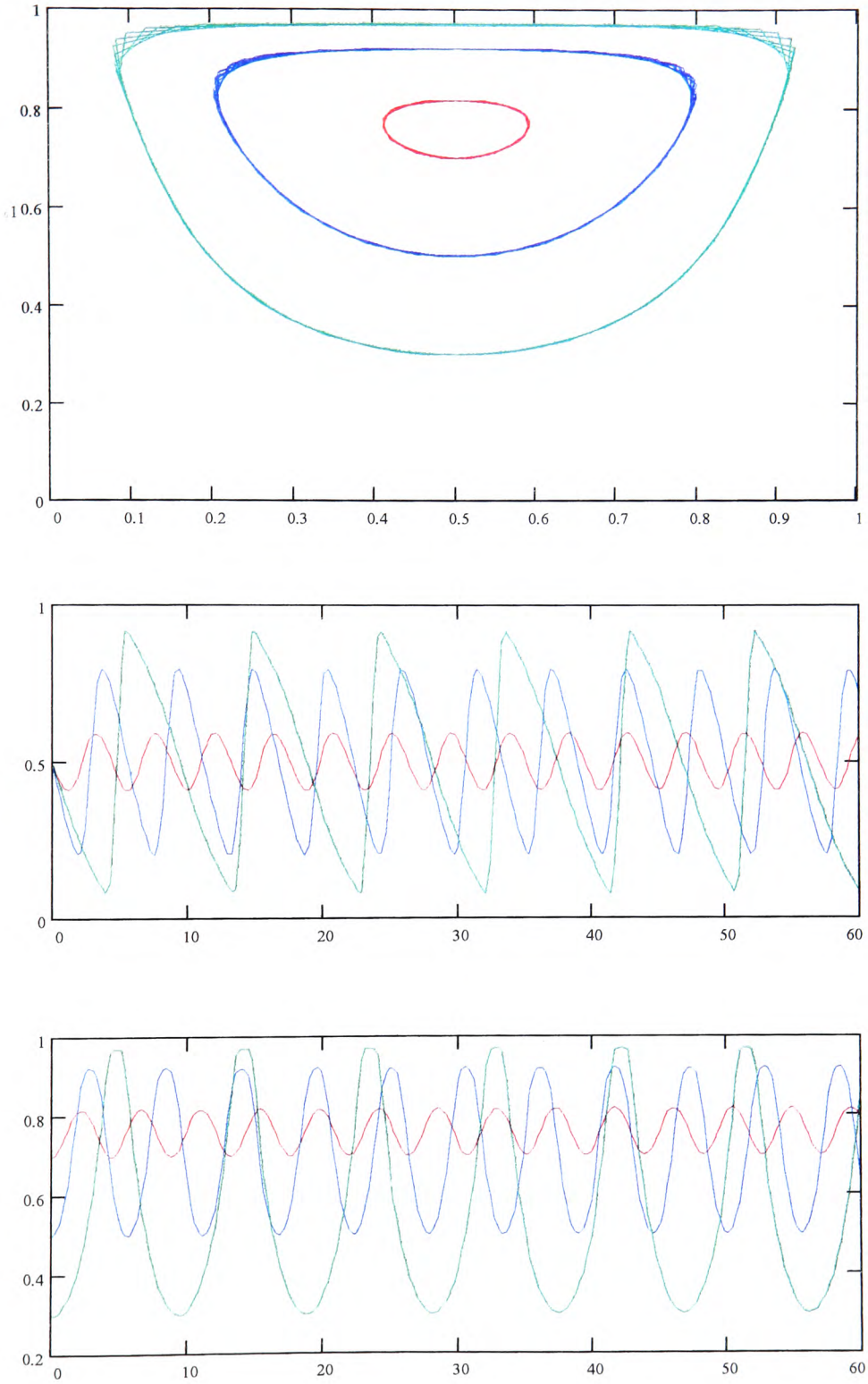

Figure (4.49); Re=1, Newtonian fluid after 60s, T=1s Initially placed in vertical line

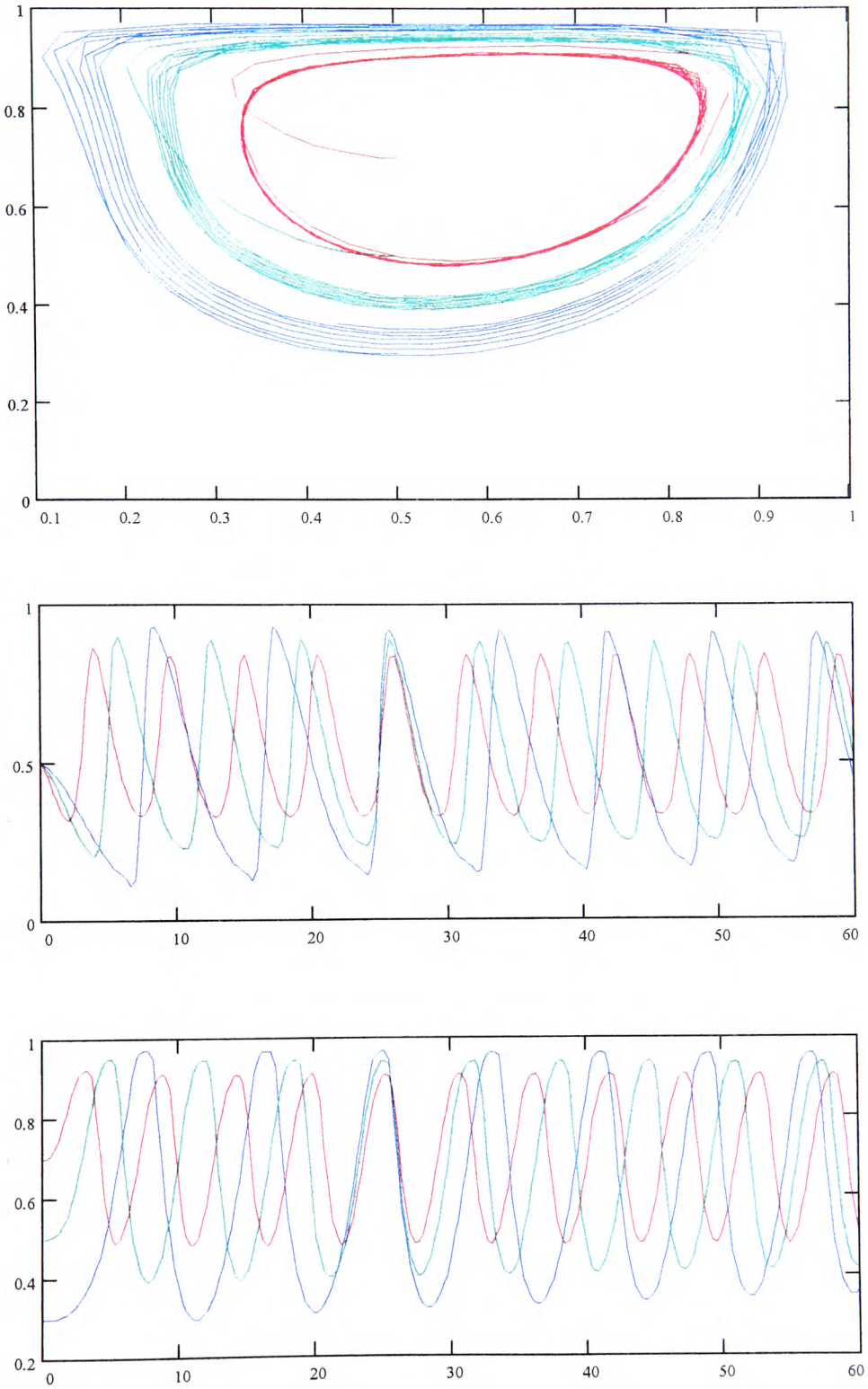

Figure (4.50); Re=100, viscoelastic dilatant fluid after 60s, T=2s Initially placed in vertical line

CHAPTER V: THERMALLY DRIVEN CAVITY FLOW

5.1 FLOW GEOMETRY AND PREVIOUS WORK

Here we present results and monitor the stability properties of mainly various flows by solving the relevant non-linear partial differential equations in situations of natural or free convection in an enclosed geometry. The motion of a fluid in a horizontal enclosure of square cross section heated from below is studied with respect to various aspect ratios. The two vertical sides are taken to have a Biot boundary conduction condition. We also study the double glazing problem where the motion of a fluid in a vertical enclosure of square cross section is heated from the one vertical side. This problem has been used in industry in many areas such as nuclear reactor insulation etc., and there are excellent numerical and analytical results which can be used for comparison (De Vahl Davies[24], Batchelor]5], Poots[75] and Schnipke and Rice[82]).

The stability and thermal convection in an enclosure has been subject of theoretical research since the time of Rayleigh[77]. Although the study of internal convection flows is more complicated than external flows, there has recently been a considerable interest in convection flows within closed geometries such as squares or rectangles. Thermal convection in enclosures occurs in many industrial applications such as building insulation, solar energy, and the electrical and nuclear industries. There are, for example, applications in heat transfer across double glazing windows and in sterilisation of foods. Such flows are also of interest in geophysics so that several important examples can be applied in the circulation of the atmosphere and of magma in the Earth's upper mantle. Reviews of the literature for two dimensional free

convection in rectangular enclosures have been reported by Gebhart et al.[33] and Siginer et al.[88].

The vertical cavity, with two vertical walls at different temperatures, is probably the most studied configuration due to its simplicity and importance. In a horizontal cavity with heating from below we have thermal instability. The other important phenomena in both cases is the buoyancy term involving in the flow equation. In thermal convection the fluid density is no longer constant and depends on temperature in buoyancy term. Therefore in such a region the temperature of the cold wall T_0 is used as a reference to give the buoyancy term as $\rho\beta(T - T_0)$.

Although many fluids encountered in various industries exhibit non-Newtonian behaviour, there are very few studies reported in the literature for thermal convection problems. Two recent surveys by Shenoy[86] and Gebhart et al.[33] mention only two studies on natural convection in enclosures.

Newtonian free convection has been extensively studied by Batchelor[5], Elder[29], Eckert and Carlson[28], Gill[34], Carmack et al.[19-20], Imberger[41], Wilkes and Churchill[98], De Vahl Davis[24], Roux et al.[80], and Ozoe et al.[70, 71]. Emery et al.[30] experimentally determined a correlation for the case of one wall at a constant temperature and a condition of constant heat flux at the other vertical wall for several pseudoplastic power law fluids. Ropke and Schummer[79] studied the unsteady natural convection of a four parameter Oldroyd viscoelastic fluid in a rectangular enclosure with differentially heated end walls. In 1993 Davies[23] carried out for inelastic non-Newtonian fluid flow in a square cavity.

5.2 THERMALLY DRIVEN CAVITY FLOW EQUATION OF 2D

The flow equations are derived from the basic laws of conservation of mass, momentum and energy. The only difference is in this chapter is that the buoyancy force term is manifest through the fluid density being dependent on temperature. We wish to note that the temperature gradients which exist between walls are not significantly large, therefore the density may be accepted as a constant apart from a small buoyancy term. This is incorporated by using Boussineq approximation Bird[8].

We take here non dimensionalised of variables. (Here U is defined as $U = \frac{\eta_0}{\rho l}$ [8])

$$x' = {}^{x}/_{l}, \quad y' = {}^{y}/_{l}, \quad u' = {}^{u}/_{U}, \quad v' = {}^{v}/_{U}, \quad \omega' = {}^{l\omega}/_{U}, \quad t' = {}^{tU}/_{l}$$

$$\Psi' = {}^{\Psi}/_{Ul}, \quad \dot{\gamma}' = {}^{\dot{\gamma}}/_{U} \quad \eta' = {}^{\eta}/_{\eta(0)}, \quad T' = {}^{T-T_0}/_{T_1-T_0}$$

where T_0 and T_1 are the constant temperature respectively of cold and hot walls. The governing equations (on dropping the prime notation) become

$$\rho(T) = \rho_0\left(1-\beta\left(T-T_0\right)\right) \tag{5.1}$$

$$\frac{\partial\omega}{\partial t} = \frac{1}{\eta \mathrm{Re}} H\left(\eta^2;\phi\right) - \eta\left\{u\frac{\partial\omega}{\partial t} + v\frac{\partial\omega}{\partial t}\right\} + Gr\left(c\theta\frac{\partial T}{\partial x} + s\theta\frac{\partial T}{\partial y}\right) + F \tag{5.2}$$

$$\frac{\partial T}{\partial t} = \frac{1}{\mathrm{PrRe}}\nabla^2 T - \left\{\frac{\partial}{\partial x}(uT) + \frac{\partial}{\partial y}(vT)\right\} + \frac{Ec}{\mathrm{Re}}\Phi \tag{5.3}$$

$$\omega = \nabla^2\Psi \tag{5.4}$$

$$\frac{\partial u}{\partial x} + \frac{\partial v}{\partial y} = 0 \tag{5.5}$$

where F denote the elastic part defined by the equation (3.13) earlier, ρ_o is the reference fluid density, β is the coefficient of thermal expansion for the fluid,

$H(\eta^2;\phi)$ is defined as in Chapter 3, $c\theta = \cos\theta$, $s\theta = \sin\theta$, and θ is the angle of inclination between cavity and gravity. On taking the non-dimensionalised form of the governing equations we have several non-dimensional parameters namely the Grashof number(Gr), the Prandtl number(Pr) and the Eckert number (Ec). The Grashof number is a measure of the ratio of buoyancy force to viscous effects within the flow and defined as $Gr = {g\rho^2\beta L^3(T_1 - T_0)}/{\eta^2(0)}$ while the Prandtl number is a measure the ratio of the fluid's kinematic viscosity to the thermal conductivity constant K and defined as $\Pr = {C_v\eta}/{K}$. The Eckert number is a measure of the viscous heating or the viscous dissipation part of the energy equation and defined as $Ec = {U^2}/{C_v(T_1 - T_0)}$. The product of Pr and Gr gives the Rayleigh number Ra.

5.3 VISCOSITY MODELS

For thermally driven cavity flow, we assumed that the viscosity η depends on both shear-rate and temperature. For a Newtonian fluid 'η' is a constant in equation (5.2), and given the non-dimensional value of one. For shear-thinning and shear-thickening fluids for viscous and viscoelastic fluids whose viscosity is dependent upon shear-rate alone, the viscosity may be approximated by using the Cross-model.

We also consider a thermal convection problem in a cavity where the fluid's viscosity depends on temperature as well as shear-rate. Such flows are of interest in geophysics as well as in many technical processes. Temperature dependence on viscosity can be modelled as follows:-

i. Reynolds formula $\eta(T) = \eta(0)e^{-kT}$

ii. Arrhenius reaction formula $\eta(T) = \eta(0)e^{-k/T}$

where k is a constant depending on the fluid considered in the simulation. Also Torrance and Turcotte[93] studied the convective flow of a fluid whose viscosity strongly depended on temperature which could be used in many geophysical flows, especially to Earth's mantle. Their model is

iii. Torrance and Turcotte formula $\eta(T) = \eta(0)e^{k(0.5-T)}$.

We choose to use the Torrance and Turcotte model in this study because of the temperature gradient which exists between top and bottom walls and then material whose properties affected by temperature changes. Therefore temperature values vary between 1 and 0 and the Torrance-Turcotte formulations make the viscosity vary about the mean.

5.4 BOUNDARY CONDITIONS

We need well prescribed boundary and initial conditions to solve equations (5.2)-(5.5). The cavity square cross-section is heated from below and we have either isothermal or insulated wall conditions. In the isothermal wall case the wall temperature is considered to remain constant $(T = T_0)$. Heat is therefore transferred through the boundary without affecting the temperature. For the insulated wall case, the temperature gradient at the wall is $\frac{\partial T}{\partial x} = 0$, and therefore heat is not leaving the system. As for cavity driven flow the stream function is taken as zero at each point of the boundary, and the vorticity on the boundary can be specified in two ways. Firstly,

it is calculated by using the well known Wood formulation CDW[21], as explained previously in Chapter 3. Secondly we use the shear free boundary condition where vorticity is zero at all points of the boundary. The shear-free boundary condition is used to examine the cell motion with liquid boundaries in the Rayleigh-Benard system.

We are now ready to give the boundary conditions for each system considered. These are thermally driven, Rayleigh-Benard convection and double glazing convection flows.

i.Boundary conditions for thermally driven cavity flow

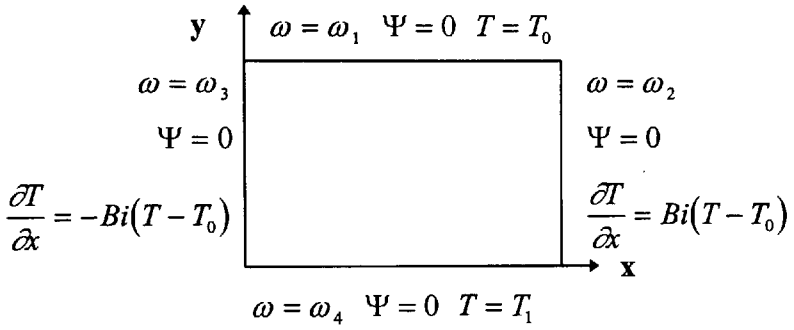

Figure 5.1; Boundary conditions for thermal driven flow

Here the vorticity equation is defined on the boundaries by using the interior points of the stream function. The boundary conditions for temperature are seen in figure (5.1). In this case the cavity flow regime is heated from below and $T_1 > T_0$. On the left and right wall we have the Biot number condition so that at very low value of the Biot number the internal conduction resistance is negligible in comparison with surface convection resistance.

ii. Boundary conditions for Rayleigh-Benard convection flow

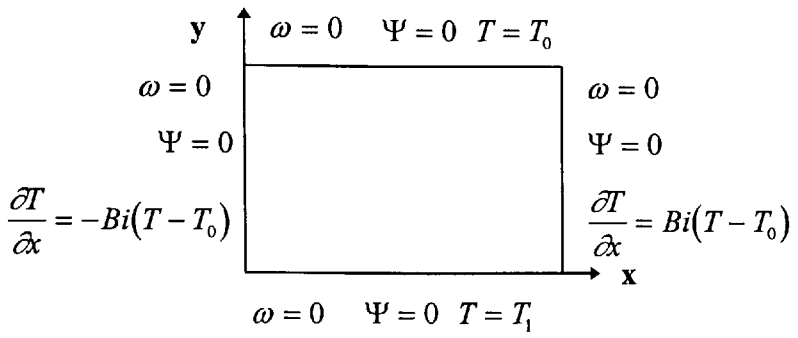

Figure 5.2; Boundary conditions for Rayleigh-Benard flow problem

In this special case, the only difference from the first case is that wall vorticity is defined by a using shear-free boundary condition. It is, therefore, taken as zero at all points on the boundary.

iii. Boundary conditions of the Double-Glazing convective problem

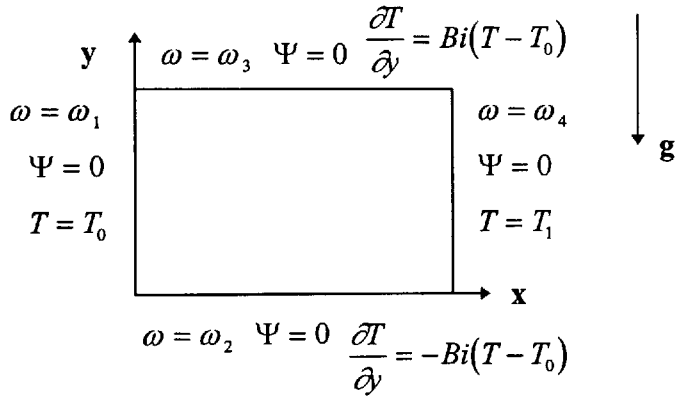

Figure 5.3; Boundary conditions for the double-glazing problem

In this case, the cavity square region is chosen to be vertical and is heated from the right vertical side and the remaining horizontal walls have the approximating Biot condition. Vorticity along the boundaries is defined by using the interior points of the stream function. The main point here is that the temperature gradient is between the vertical walls and the buoyancy force is perpendicular to the temperature gradient.

5.5 THE NUMERICAL SOLUTION, CONSISTENCY AND STABILITY OF THE THERMALLY DRIVEN CAVITY FLOW EQUATIONS

We solve equations (5.2)-(5.5) numerically as previously. Unsteady flow is solved by either the simple explicit or A.D.I. methods. We now explain the A. D. I. method as it applies here.

We have

$$\left(1-\frac{r}{2}L_x^h\right)T^* = \left(1+\frac{s}{2}L_y^k\right)T^n + \frac{\Delta t}{2}f^n, \qquad 5.6$$

$$\left(1-\frac{s}{2}L_y^k\right)T^{n+1} = \left(1+\frac{r}{2}L_x^h\right)T^* + \frac{\Delta t}{2}f^n. \qquad 5.7$$

The temperature equation(5.3) is discretised as follows

$$T^*_{i,j} - \frac{r}{A_1}\left(T^*_{i+1,j} + T^*_{i-1,j} - 2T^*_{i,j}\right) + \frac{rh}{2}u\left(T^*_{i+1,j} - T^*_{i-1,j}\right)$$

$$= T^n_{i,j} + \frac{s}{A_1}\left(T^n_{i,j+1} + T^n_{i,j-1} - 2T^n_{i,j}\right) - \frac{sk}{2}v\left(T^n_{i,j+1} - T^n_{i,j-1}\right) + A_2\frac{\Delta t}{2}f^n \qquad 5.8$$

and

$$T^{n+1}_{i,j} - \frac{s}{A_1}\left(T^{n+1}_{i,j+1} + T^{n+1}_{i,j-1} - 2T^{n+1}_{i,j}\right) + \frac{sk}{2}v\left(T^{n+1}_{i,j+1} - T^{n+1}_{i,j-1}\right)$$

$$= T^*_{i,j} + \frac{r}{A_1}\left(T^*_{i+1,j} + T^*_{i-1,j} - 2T^*_{i,j}\right) - \frac{rh}{2}u\left(T^*_{i+1,j} - T^*_{i-1,j}\right) + A_2\frac{\Delta t}{2}f^n \qquad 5.9$$

where $A_1 = \mathrm{Pr}\,\mathrm{Re}$ and $A_2 = \dfrac{Ec}{\mathrm{Re}}$.

We note that in equation(5.8) all the unknown intermediate values "$*$" contain the same suffix "j" while "i" varies. Therefore for a given value of "j" the equation can be written for each value of "i" from 1 to M-1. This set of (M-1) equations in (M-1)

unknowns can then be solved by using direct Gaussian elimination. This process is repeated similarly for each value of "j" from 1 to N-1. Therefore this solution process has to solve at each time step an (M-1)(N-1) set of equations in (M-1)(N-1) unknowns.

The boundary conditions are the same as given in Chapter 3 for both Dirichlet and Neumann types. After discretion of the temperature equation, stability can be assumed if $\frac{r}{2A_1} \geq \frac{rh}{4}u$ in equation (5.8) and $huA_1 \leq 2$.

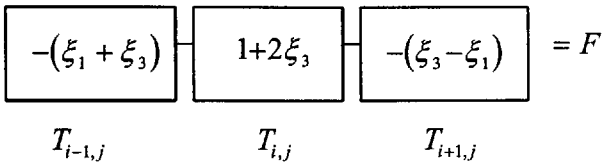

Figure 5.4; Diagram for the stability condition

where $\xi_1 = \frac{rh}{4}u$, $\xi_2 = \frac{sk}{4}v$, $\xi_3 = \frac{r}{2A_1}$, $\xi_3 = \frac{s}{2A_1}$ and F is a composition of discretised values.

For equation (5.9) we have the same stability requirements as for equation (5.8) except that $vkA_1 \leq 2$.

For the non-Newtonian vorticity equation (5.2) we have the stability requirement

$$-\frac{(\eta^2)_{i-1,j}}{h\eta_{i,j}} \leq \frac{u}{2} \leq \frac{(\eta^2)_{i+1,j}}{h\eta_{i,j}} \text{ and } \frac{(\eta^2)_{i,j-1}}{k\eta_{i,j}} \leq \frac{v}{2} \leq \frac{(\eta^2)_{i,j+1}}{k\eta_{i,j}}.$$

5.6 RESULTS FROM THE 2D THERMAL DRIVEN CAVITY FLOW EQUATION

The five main parameters which play a vital role in the stabilisation of the fluid are the Prandtl (Pr), Rayleigh (Ra), Weissenberg (Wi), Eckert (Ec) and Biot (Bi) numbers. Pr is usually taken as 7 and Ra is defined in the range 10^4 and 10^6. We employ Wi in the same range as in the previous chapter, Ec in the range 0 to 10^{-3} and Bi from 0 to 10. We also examine the double-glazing problem in order to compare our program results with De Vahl Davis[24], Schnipke and Rice[82], Batchelor[5] and Poots[75]. In this case the Prandtl number is taken as 1. We usually require ten seconds of simulation time to obtain a steady solution and although the solutions are found to be consistent with grid meshes from 10x10 to 50x50, we usually display results for 30x30. We consider the initial distributions $T(x,y)=0$ or $T(x,y)=1-y$ at $t=0$ and then heat is supplied to the bottom wall. For low Ra even though no visible motion is observed, subtle changes have been seen within the flow and the lighter fluid is found at the bottom with denser material near the top of the cavity. As Ra increases the system become unstable and loses its equilibrium. We also use the Eckert number and Biot number for this problem and it is observed that when the Eckert number increases the system moves further away from equilibrium and instability occurs within the fluid.

We firstly consider the convergence of the solutions by comparing calculations for various mesh size, which is denoted by grid widths h, in both A.D.I. and simple explicit method cases. Fig(5.5) and (5.6) show results for the several fluids evaluated near the top wall (x=0.4, y=0.8) for vorticity. Similarly fig(5.7) and (5.8) show results

at the same point for temperature. In this case we have chosen the Bench-Mark problem where the control parameters are taken as Re=1, Pr=1 and Ra=10^5. Therefore comparing values of vorticity and temperature it is evident that convergence to 4 decimal places has been achieved as h decreases, and the A. D. I. method was found to be more desirable than simple explicit method. Therefore A. D. I. method was chosen to illustrate the results.

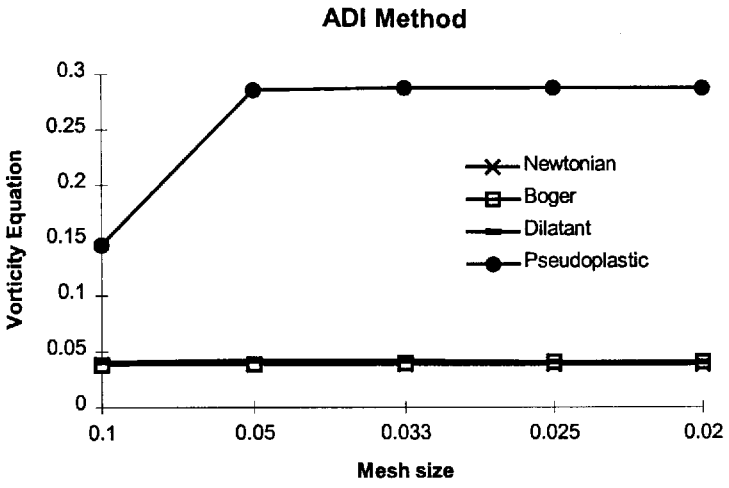

Figure 5.5; Convergence criterion for vorticity at Ra= 10^5 by A. D. I. method

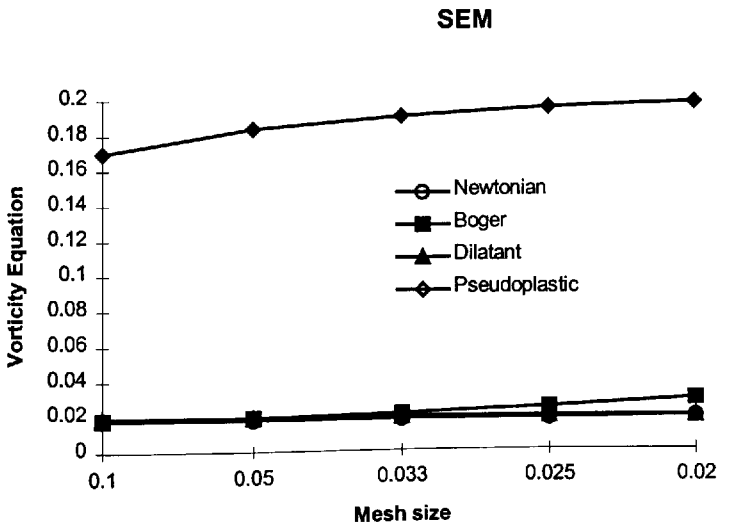

Figure 5.6; Convergence criterion for vorticity at Ra=10^5 by simple explicit. method

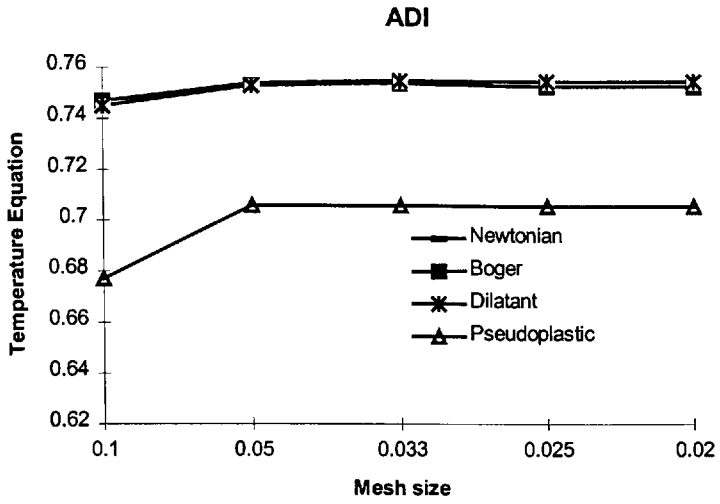

Figure 5.7; Convergence criterion for Temperature at Ra=10^5 by A. D. I. method

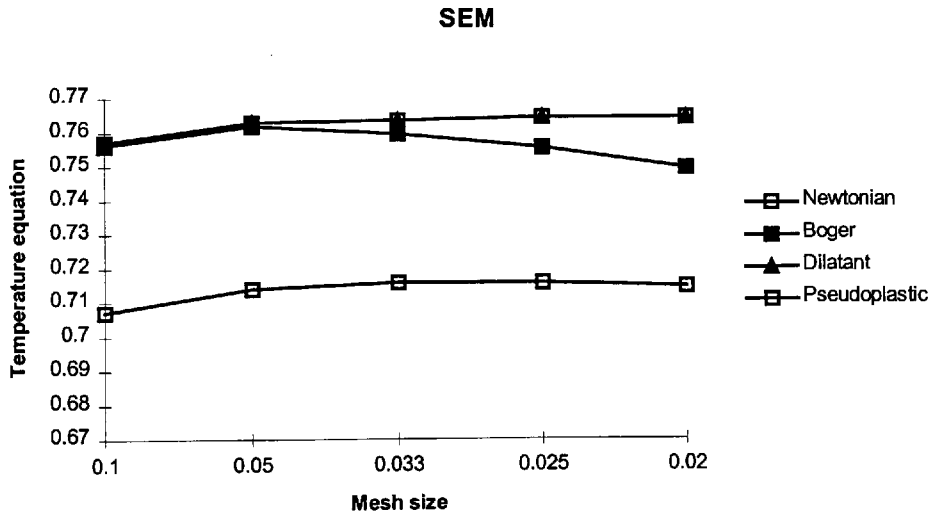

Figure 5.8; Convergence criterion for Temperature at Ra=10^5 by simple explicit. method

The second comparison was to compare our results qualitatively and quantitatively with those obtained by Torrance and Turcotte**[93]**, shown in fig (5.13).Mckenzie**[57, 58]**, shown in fig(5.14) and De Vahl Davis**[24]**, shown in fig(5.21).

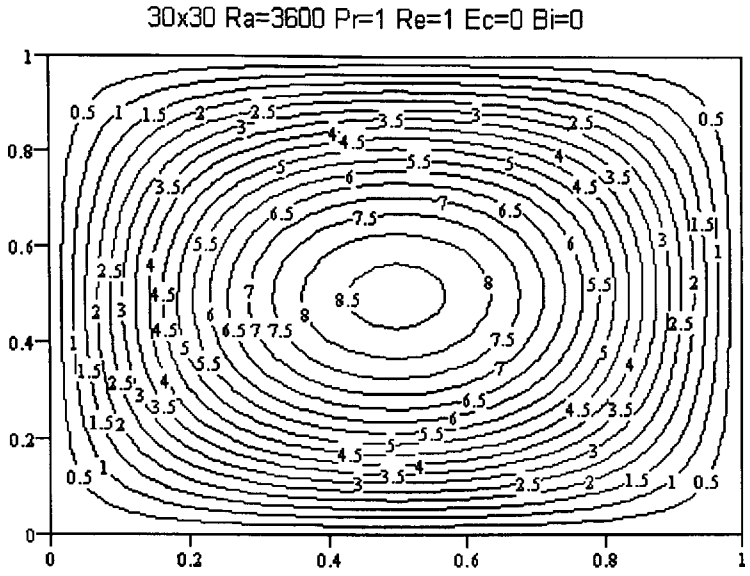

Figure (5.9); Streamline contours of Newtonian fluid for shear-free flow

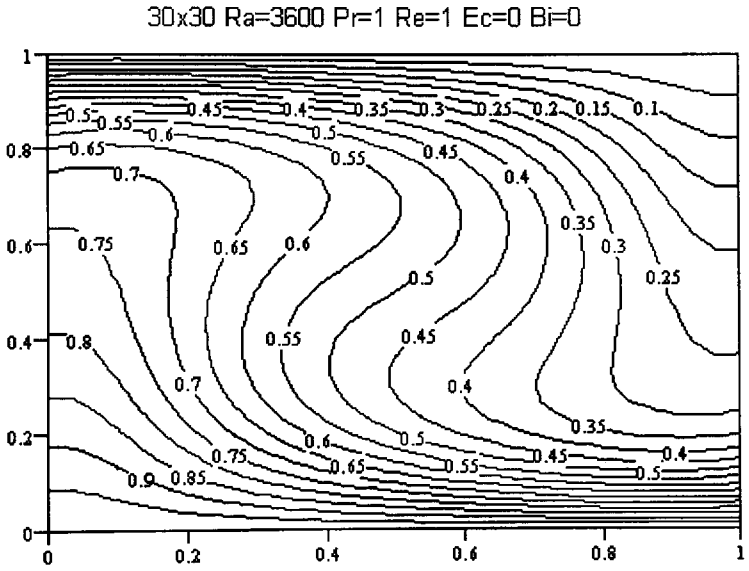

Figure (5.10); Temperature contours of Newtonian fluid for shear-free flow

Fig(5.9) and (5.10) indicate streamlines and temperature profiles respectively at Ra=3600. In this case vorticity is calculated by using a shear-free flow condition on the boundary and one large symmetric clockwise rotating vortex fills the whole cavity. The streamlines are elliptical around the vortex centre located in the middle of the cavity, shown in fig(5.9). The temperature profile shows that temperature rises

near the bottom wall and cold fluid is located near the top wall, shown in fig(5.10). Our results are in good agreement with Torronce and Turcotte[93] qualitatively, and quantitatively shown in fig(5.13)

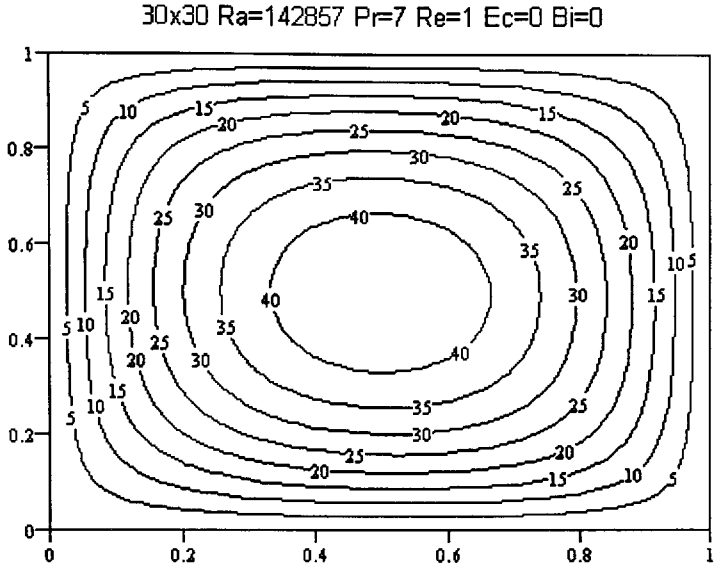

Figure (5.11); Streamline contours of Newtonian fluid for shear-free flow

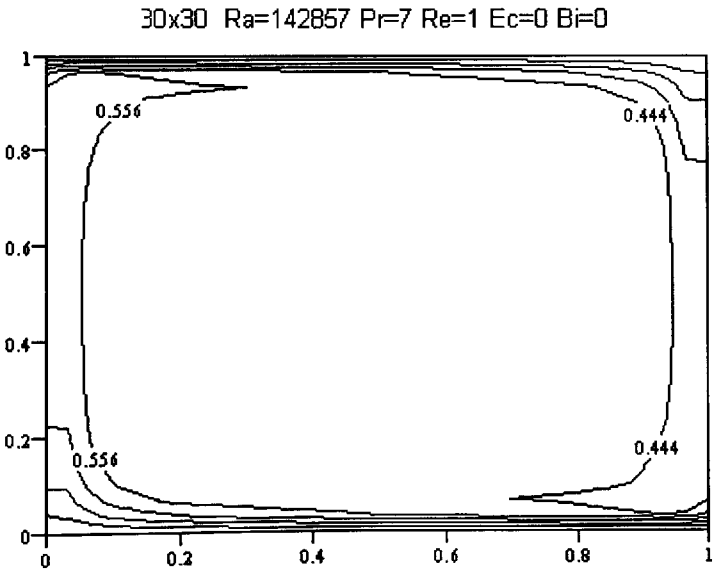

Figure (5.12); Temperature contours of Newtonian fluid for shear-free flow

Fig(5.11) and (5.12) represent streamline plots and temperature profile at $Ra=10^6$ respectively. Fig(5.11) shows that the steady solution gives one large symmetric rotating vortex which fills the whole flow domain. The streamlines looks 'square' in shape near the walls of cavity and become more circular around the vortex centre located in the middle of the cavity. The temperature profile shows in fig(5.12) the temperature throughout most of the cavity is uniform obtaining a value which average of the top and bottom walls. These results agree with the published work of Mckenzie, who considered the same geometry and boundary conditions, as shown in fig(5.14).

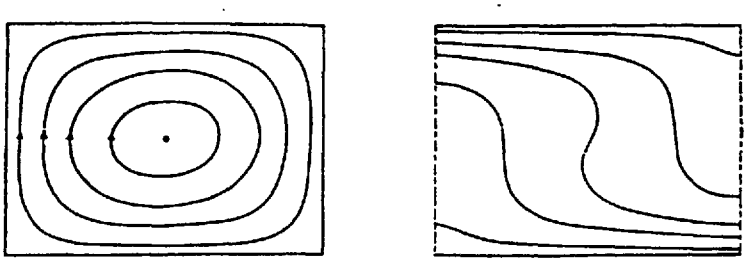

Figure (5.13) ; Streamlines and temperature plots of Torrance and Turcotte[93] at Ra=3600

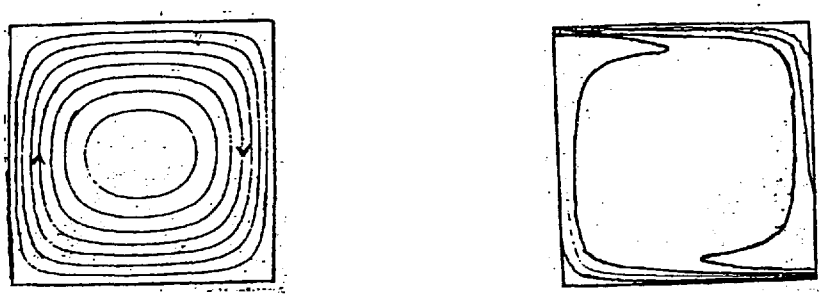

Figure (5.14) ; Streamlines and temperature plots of Mckenzie[58] at Ra=10^6

5.6.1 Double-Glazing Problem

In this particular case we simulate buoyancy induced thermally driven cavity flow, with differentially heated side walls, to compare with the "bench-mark" solution

known as 'the double glazing problem'. Many authors have considered this problem in both analytically (Batchelor[5] and Poots[75]) and numerically by Schnipke and Rice[82]. We have chosen the bench-mark solution studied by De Vahl Davis[24]. He solved this problem for Ra in a range of 10^3 to 10^5 and used the (Ψ,ω) formulation with a modified A. D. I. method, which is similar to our approach.

Our results fig(5.15)-(5.20) show good agreement both qualitatively and quantitatively with the bench-mark streamlines and temperature profile fig(5.21) which was produced by De Vahl Davis[24]. It can be seen that in fig(5.15), (5.17) and (5.19) as Ra increases from 10^3 to 10^5 one large clockwise rotating vortex is produced. The corresponding temperature profiles are almost vertical near the side walls and horizontal around the cavity's centre at Ra=10^5, shown in fig(5.20).

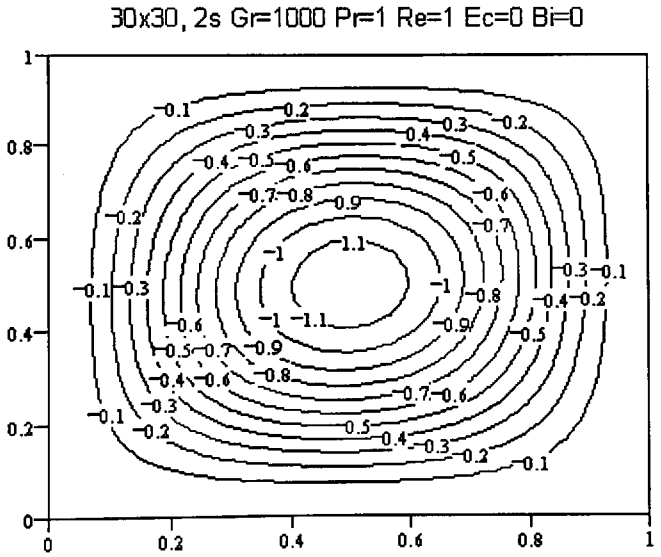

Figure (5.15); Streamline contours of Newtonian fluid for solid wall case

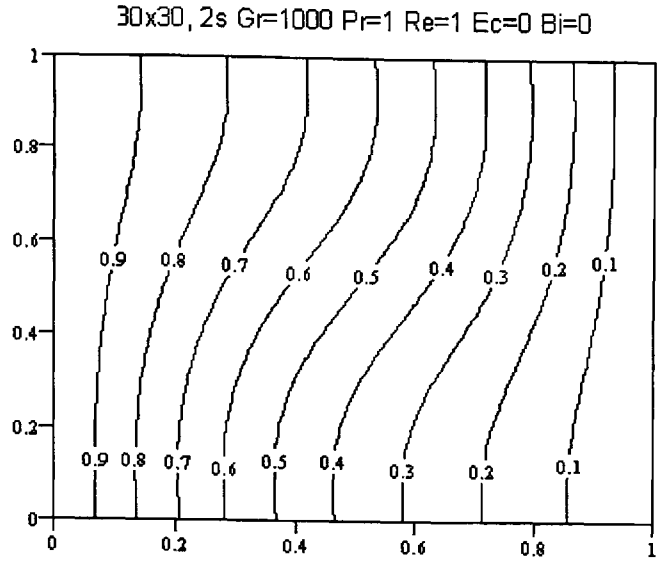

Figure (5.16); Temperature contours of Newtonian fluid for solid wall case

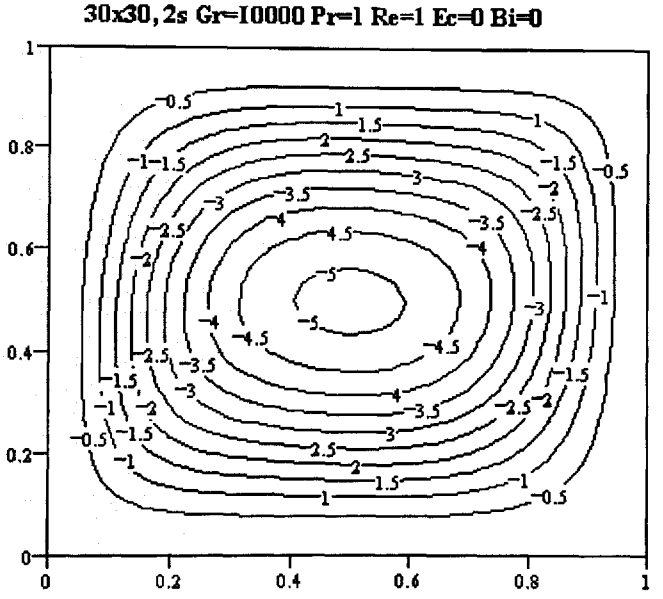

Figure (5.17); Streamline contours of Newtonian fluid for solid wall case

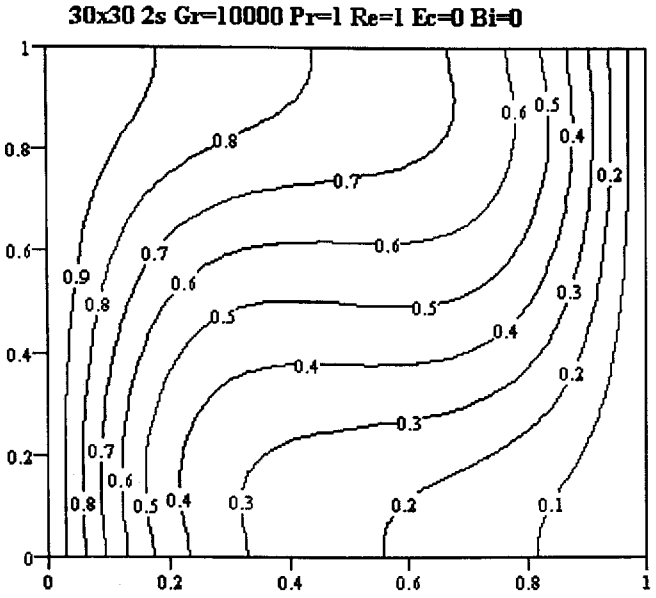

Figure (5.18); Temperature contours of Newtonian fluid for solid wall case

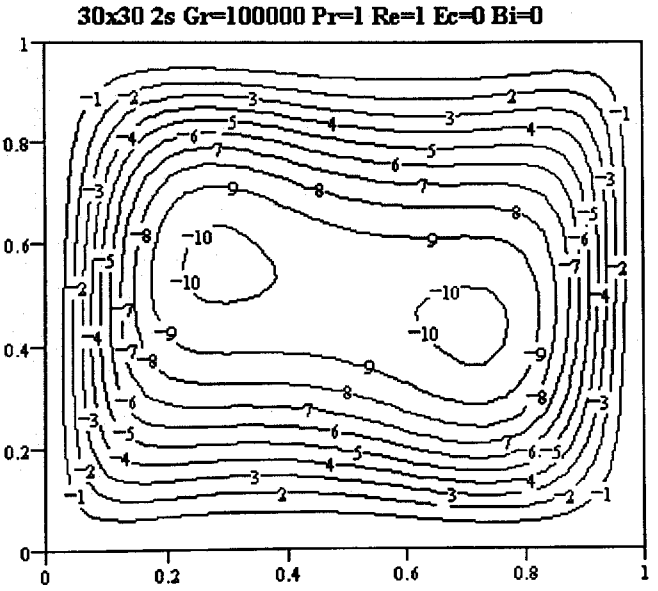

Figure (5.19); Streamline contours of Newtonian fluid for solid wall case

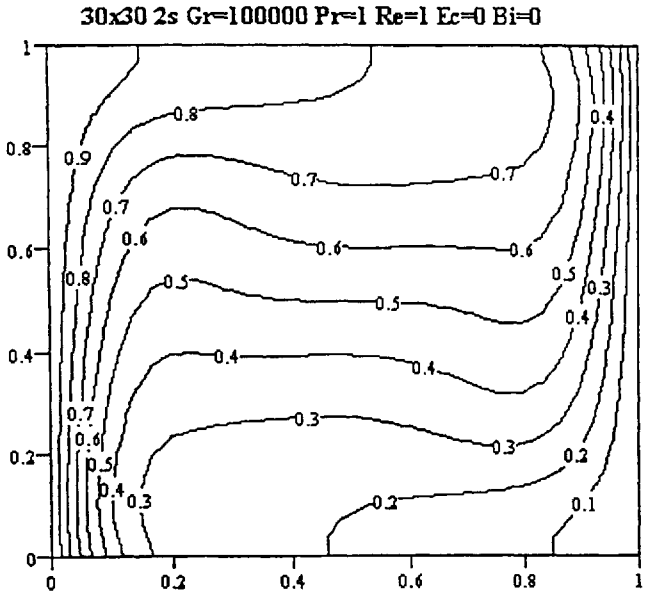

Figure (5.20); Temperature contours of Newtonian fluid for solid wall case

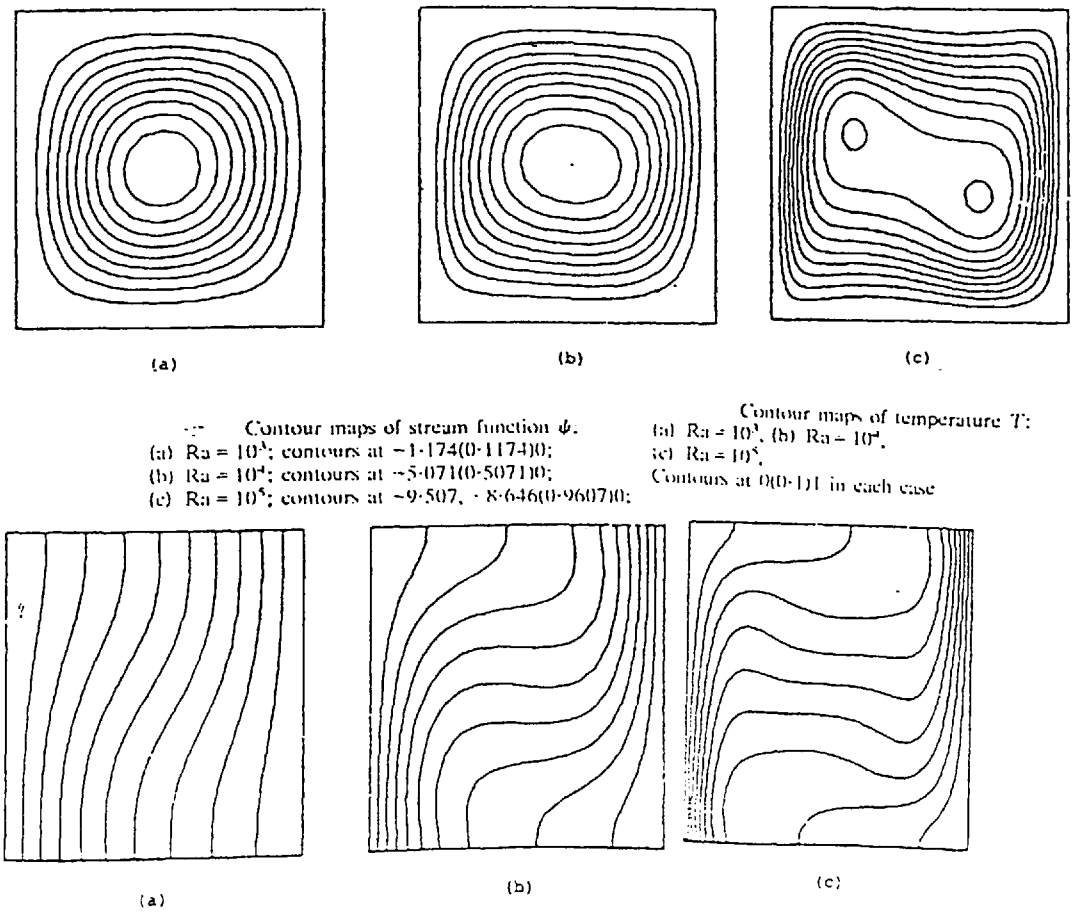

Figure (5.21); Streamline and temperature contours by De Vahl Davis[]

5.6.2 Thermally Driven 2D Cavity Flow

After testing our work with that of others both free-shear wall and solid wall boundary condition for vorticity, we considered the results obtained for viscous and viscoelastic fluids in thermal convection.

For a Newtonian fluid in both viscous and visco-elastic cases it was found one cell filled whole cavity at $Ra=10^4$ for all fluids considered, as shown in fig(5.22). Similarly a one cell solution was found in the pseudoplastic fluid case at $Ra=10^5$, but for the dilatant fluid solution consisted of two counter rotating cells and they were not symmetric and one vortex dominated to other vortex as shown in fig(5.24).

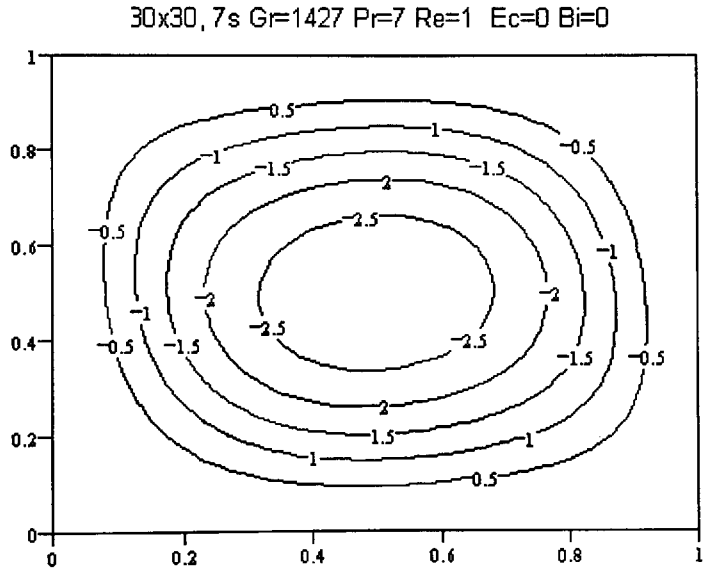

Figure (5.22); Streamline contours for viscous pseudoplastic fluid in thermal case

The corresponding temperature profiles are shown in the fig(5.23) and (5.25) below. The first indicates that warm fluid rises near the right wall with the colder fluid falling near the opposite wall. The second fig(5.25) indicates that it is almost symmetric vertically and warm fluid rises near the bottom while colder fluid located near the top wall

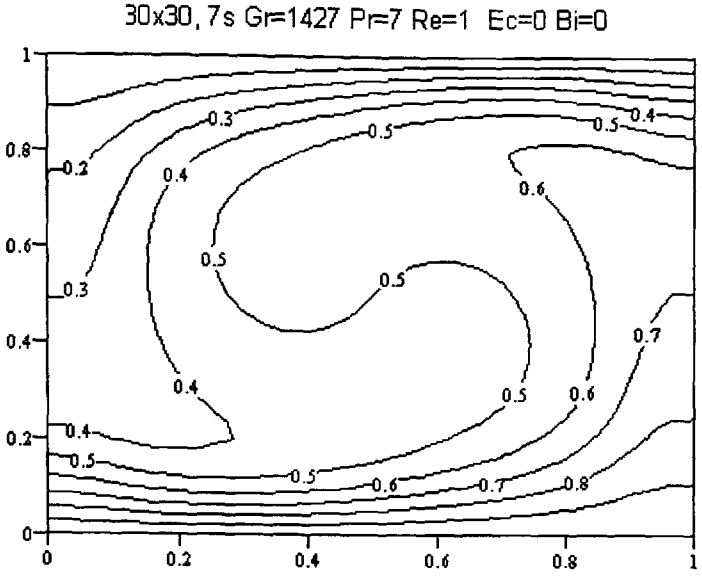

Figure (5.23); Temperature contours for viscous pseudoplastic fluid in thermal case

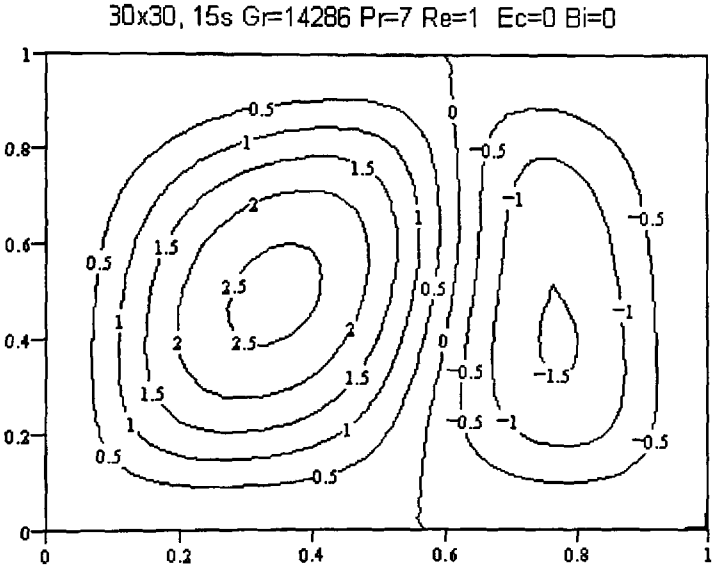

Figure (5.24); Streamline contours for viscous dilatant fluid in thermal case

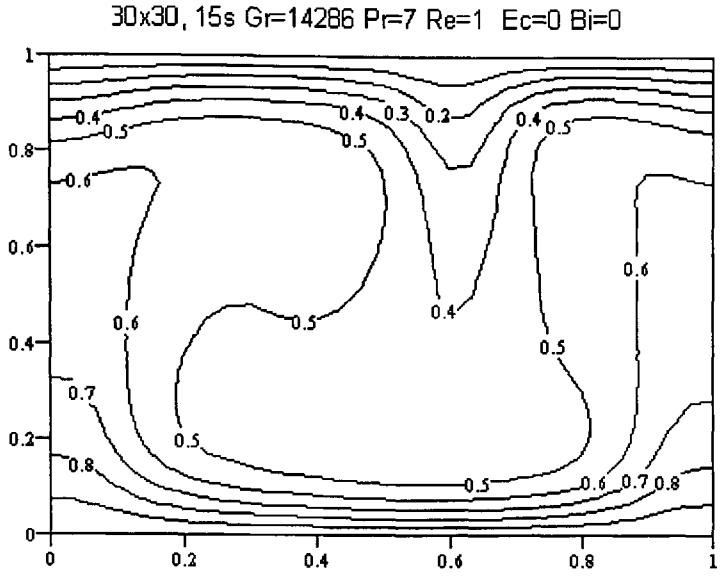

Figure (5.25); Temperature contours for viscous dilatant fluid in thermal case

For a Newtonian fluid with non-zero Ec at $Ra=10^4$, due to the viscous heating the flow pattern becomes two mirror image counter rotating rectangular cells which are equal and symmetric as shown in fig(5.26). The corresponding temperature profile is shown in fig(5.27). The warmer fluid rises in the cavity centre, colder fluid is located near the top wall and temperature contours are symmetric vertically. Moroever by considering the Biot condition we have similar behaviour for Bi=1 and Bi=10 for a Newtonian and dilatant fluids as shown in fig(5.28). In fact there is little difference between the two. We also have two mirror image counter rotating rectangular cells in the case of $Ra=10^5$ for the Newtonian and Boger fluids with Bi=10. For $Ra=10^6$ the viscous heating and Biot boundary condition do not make any difference in flow, therefore instability occurs in flow and the system becomes unstable and loses its equilibrium. In the case of viscoelastic flow, similar behaviour was seen for Boger fluid when compared with its Newtonian counterpart by considering the Biot boundary condition and viscous heating effect.

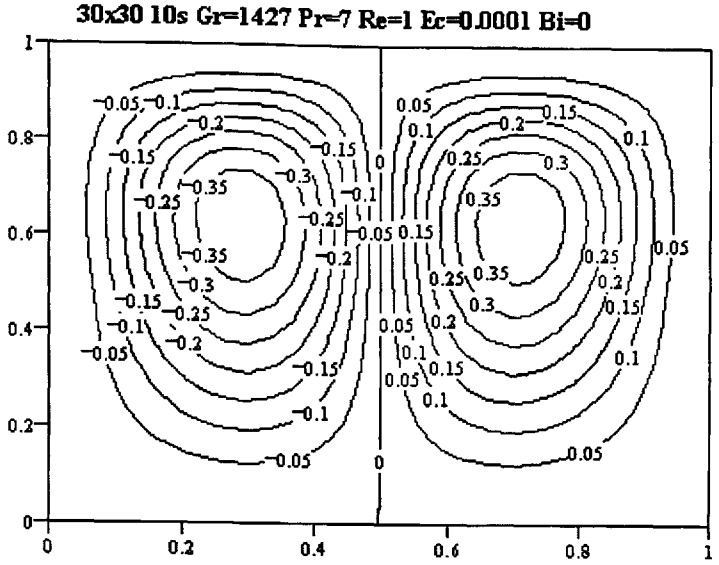

Figure (5.26); Streamline contours for Newtonian fluid in thermal case

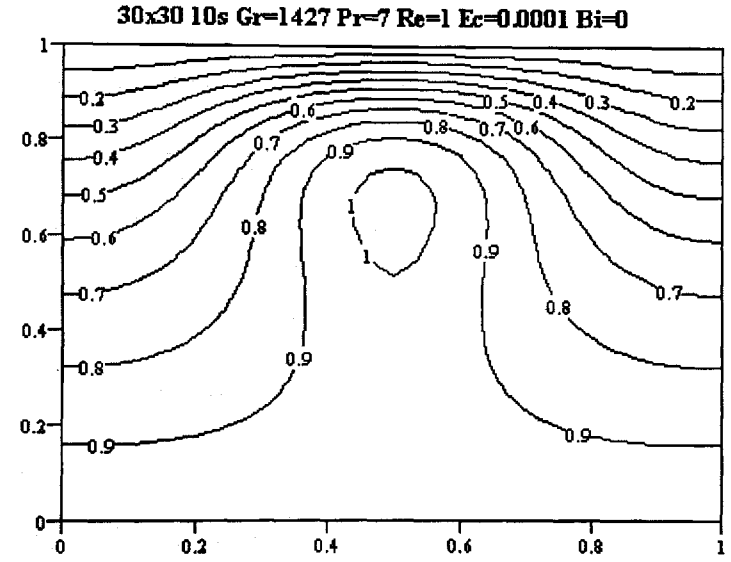

Figure (5.27) ; Temperature contours for Newtonian fluid in thermal case

In the case of a viscous dilatant fluid when we form the temperature condition on the side boundary using the Biot boundary condition, flow emerged as two unequal cells shown in fig(5.28). When Bi increases, the flow pattern becomes one vortex only and it is more compact. On considering a dilatant viscoelastic type fluid similar behaviour was observed.

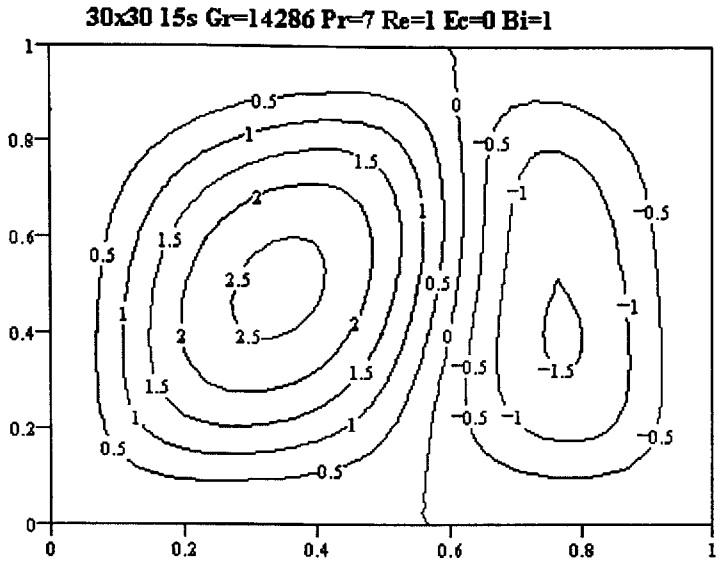

Figure (5.28) ; Streamline contours for viscous dilatant fluid in thermal case

When we compare the viscoelastic dilatant fluid with its viscous counterpart similar behaviour is observed except at $Ra=10^5$. In this case we have a two vortex solution with Bi=1. When Ec is not zero, no result was found with Bi=0, 1, and 10 for the dilatant fluid so it can be said that the dilatant fluid shows some destabilisation for $Ra=10^5$ with $Ec \neq 0$.

In the case of a viscous pseudoplastic fluid for all Ra numbers considered we have one cell vortex with Bi=0 and Ec=0. When we take Bi=1 the flow produces two mirror image counter rotating cells, reduced in size with the motion confined to the top half of cavity where the viscosity is lowest as shown in fig(5.29). The warmer fluid rises in the cavity's centre and colder fluid is located near the top wall for the corresponding temperature profile as shown in fig(5.30). This figure indicates that the convection term dominate flow between top and bottom walls. The Biot number influence has warmer fluid rising just along the bottom wall and colder fluid descends along the top

wall. This behaviour is also valid for B=10 with or without viscous heating when $Ra=10^4$.

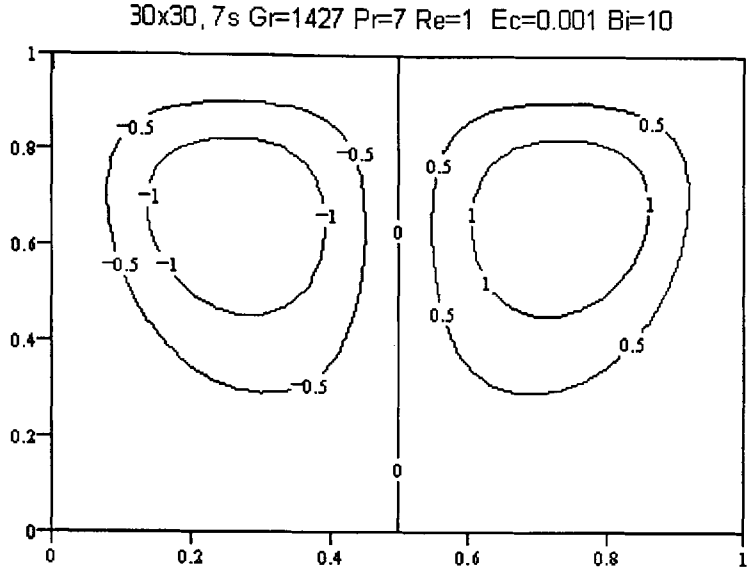

Figure (5.29) ; Streamline contours for viscous pseudoplastic fluid in thermal case

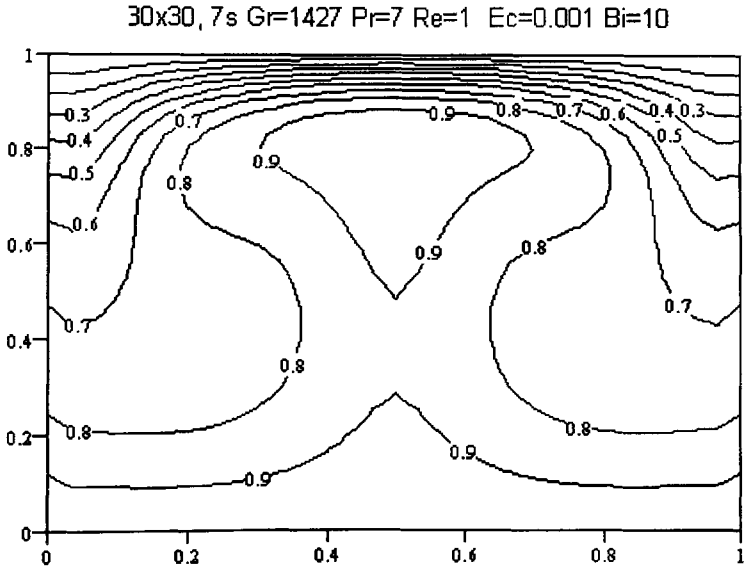

Figure (5.30) ; Temperature contours for viscous pseudoplastic fluid in thermal case

In the case of $Ra=10^5$, we have as one cell vortex without admitting viscous heating and Biot condition.

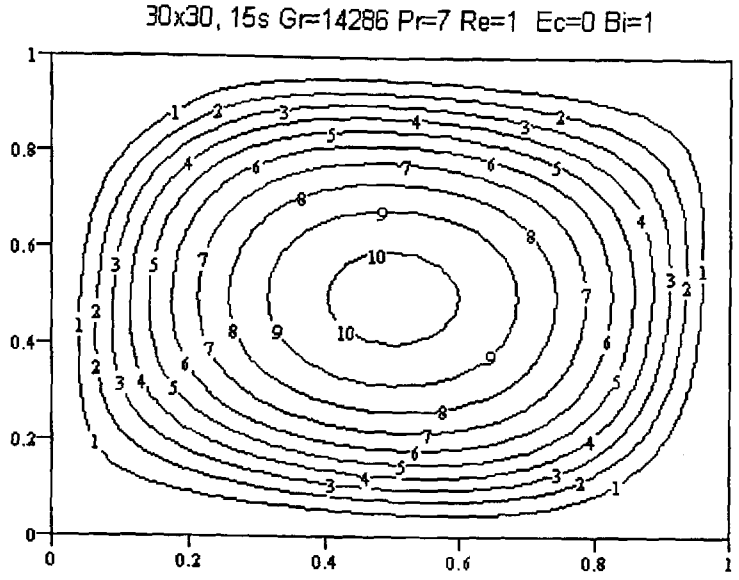

Figure (5.31) ; Streamline contours for viscoelastic pseudoplastic fluid in thermal case

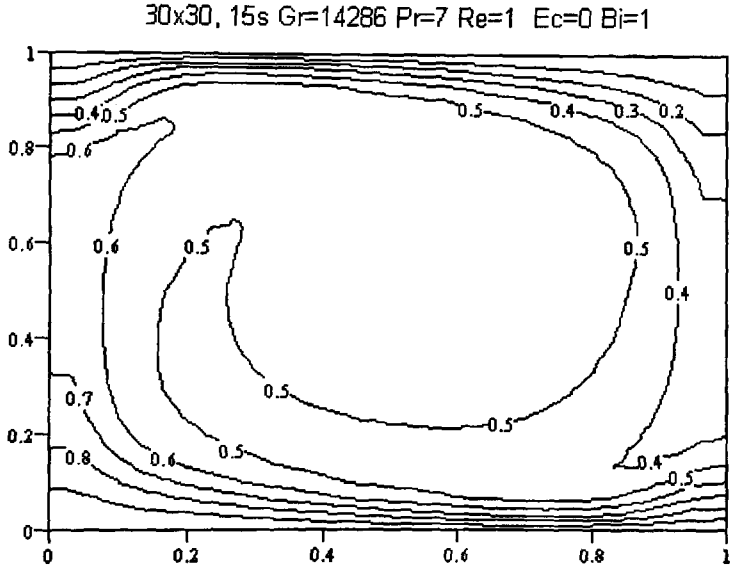

Figure (5.32) ; Temperature contours for viscoelastic pseudoplastic fluid in thermal case

Similarly the results were found for all types of viscoelastic fluid and they were seen to be in agreement with their viscous counterparts in almost all circumstances. The only different solution was seen for $Ra=10^5$ with viscous heating applied to the system and Bi=10.

We summarise all obtained results in the following table which indicates how many cells appear for a given Ra, Bi and Ec.

VISCOUS FLUID	RA=10^4	RA=10^5	VISCOELASTIC FLUID	RA=10^4	RA=10^5
NEWTONIAN	1	1	**BOGER**	1	1
PSEUDOPLASTIC	1	1	**PSEUDOPLASTIC**	1	1
DILATANT	1	2	**DILATANT**	1	2

Bi=1

VISCOUS FLUID	RA=10^4	RA=10^5	VISCOELASTIC FLUID	RA=10^4	RA=10^5
NEWTONIAN	1	1	**BOGER**	1	1
PSEUDOPLASTIC	1	2	**PSEUDOPLASTIC**	1	2
DILATANT	1	2	**DILATANT**	1	2

Bi=10

VISCOUS FLUID	RA=10^4	RA=10^5	VISCOELASTIC FLUID	RA=10^4	RA=10^5
NEWTONIAN	2	2	**BOGER**	2	2
PSEUDOPLASTIC	2	2	**PSEUDOPLASTIC**	2	2
DILATANT	1	1	**DILATANT**	1	1

Ec=0.0001 **Ec= 0.00001**

VISCOUS FLUID	RA=10^4	RA=10^5	VISCOELASTIC FLUID	RA=10^4	RA=10^5
NEWTONIAN	2	2	**BOGER**	**2**	**2**
PSEUDOPLASTIC	2	1	**PSEUDOPLASTIC**	**2**	**1**
DILATANT			**DILATANT**		

Ec=.0001, Bi=1

VISCOUS FLUID	RA=10^4	RA=10^5	VISCOELASTIC FLUID	RA=10^4	RA=10^5
NEWTONIAN	2	2	**BOGER**	**2**	**2**
PSEUDOPLASTIC	2	2	**PSEUDOPLASTIC**	**2**	**2**
DILATANT			**DILATANT**		

Ec=0.00001, Bi=10

VISCOUS FLUID	RA=10^4	RA=10^5	VISCOELASTIC FLUID	RA=10^4	RA=10^5
NEWTONIAN	2	2	**BOGER**	**2**	**2**
PSEUDOPLASTIC	2	1	**PSEUDOPLASTIC**	**2**	**1**
DILATANT			**DILATANT**		

Table (5.1) ; Number of cells obtained at a given Ra for solid wall flow

In this section by using a solid wall condition for vorticity on the boundary we sought the nature of flow and number of cells obtained in the fluid. Table (5.1) shows that both viscous and viscous fluids produced the same number of cell for all cases considered. As Ra increases from 10^4 the computer program failed to converge to a solution. Therefore we only have steady solutions for all cases at Ra=10^4 and

$Ra=10^5$. On the other hand, when Ec increases the system loses its equilibrium and instability occurs in the fluid. Moroever the system usually produced a one cell solution without Bi and Ec except for the dilatant fluid at $Ra=10^5$ in both viscous and viscoelastic cases. When $Bi \neq 0$ two mirror image counter rotating cells are obtained in the fluid. For example Bi=1 non-Newtonian fluids produced a two cells solution at $Ra=10^5$. When Bi increases both constant viscosity and pseudoplastic fluids produced a two cells solution at $Ra=10^4$ and $Ra=10^5$. When Ec is introduced the system usually produced a two cells solution with or without Bi but instability occurred in the dilatant fluid.

5.6.3 The Rayleigh-Benard Problem of Cavity Driven Flow

Here boundary vorticity is zero and flow is differentially heated between bottom and top walls and we have Biot boundary conditions on the side walls. We take our parameter values as in the previous section. In the case of the Newtonian fluid for $Ra=10^4$ we have one vortex and it is symmetric both horizontally and vertically. Similar behaviour is to be seen for Bi=1 but while the Biot number increases the flow produce to two mirror image counter rotating rectangular cells shown in fig(5.33). The corresponding temperature profile is shown in fig(5.34), where the colder fluid descends near the cavity's centre while warmer fluid rises in convective motion near the walls. When we consider Ec there is no change from the Bi=0 case. When Ra increases, for example for $Ra=10^5$ it is seen that a one cell solution is found which is always the same for Bi=0, 1, 10 as shown in fig(5.35). In this case introducing the Ec number produced unsteady results. The temperature profile is shown in fig(5.36) for $Ra=10^5$ and Bi=0. Warm fluid rises near the bottom wall and colder fluid descends along the top. These behaviour was also seen for Bi= 1 and 10 as well.

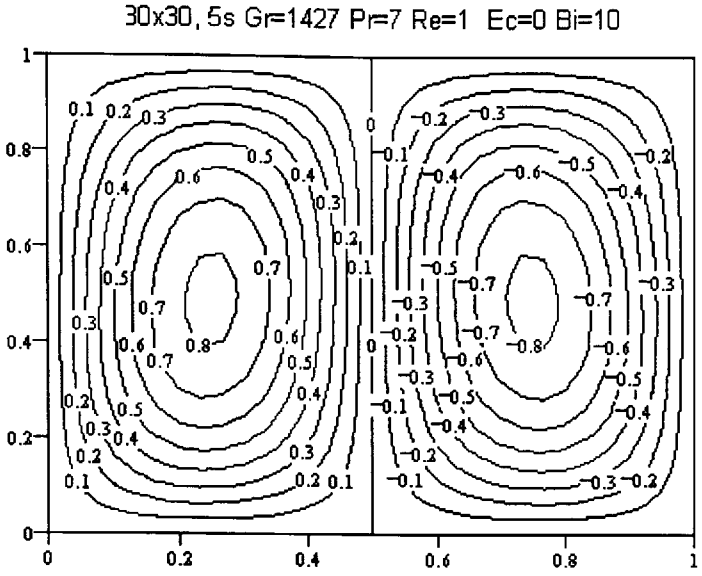

Figure (5.33) ; Streamline contours for Newtonian fluid in Rayleigh-Benard case

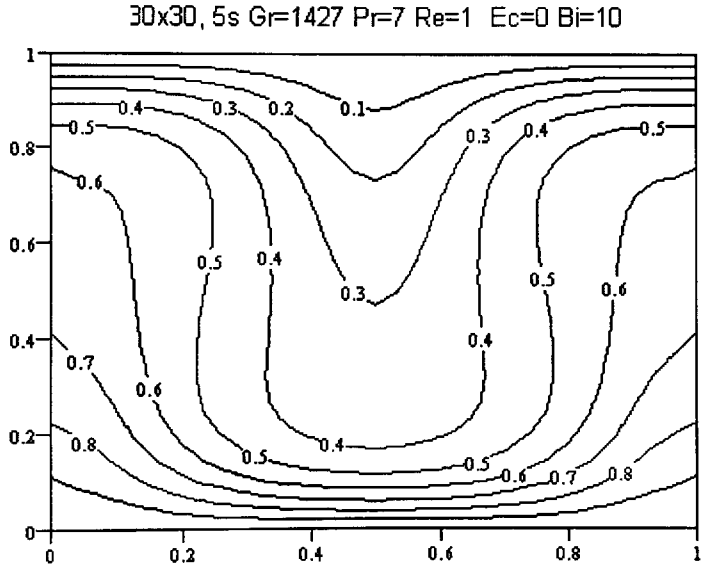

Figure (5.34) ; Temperature contours for Newtonian fluid in Rayleigh-Benard case

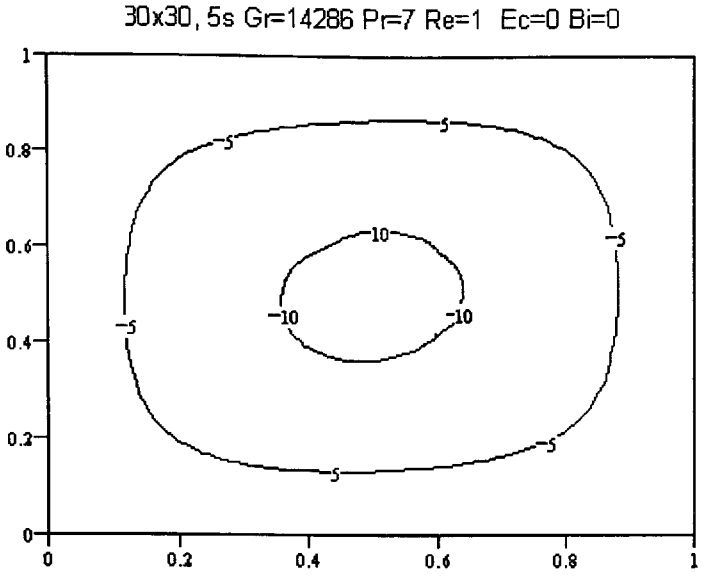

Figure (5.35) ; Streamline contours for Newtonian fluid in Rayleigh-Benard case

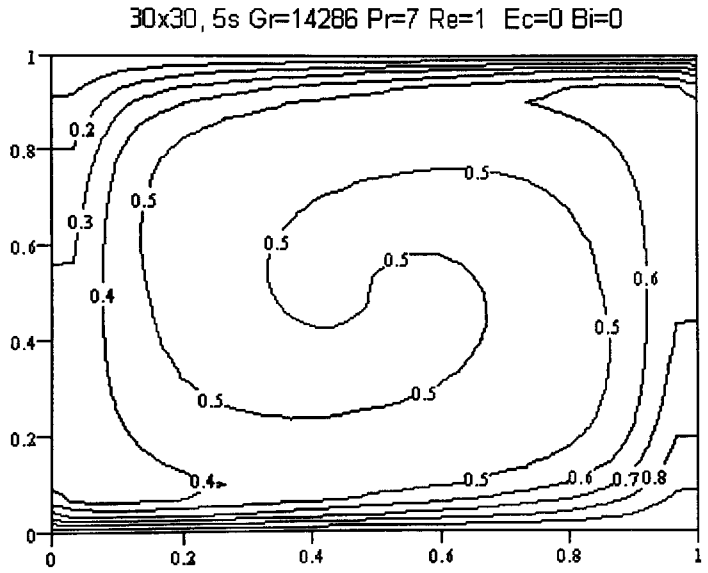

Figure (5.36) ; Temperature contours for Newtonian fluid in Rayleigh-Benard case

When $Ra=10^6$ we have a one cell vortex and it appears similar to the case of $Ra=10^5$ for Bi=0 apart from the flow pattern's direction. In this case the inertial force dominates the flow. When the Biot boundary condition is applied we still have one vortex but the direction of rotation changes, and for Bi=10 we have qualitatively similar flow pattern with Bi=0.

To consider viscous dilatant fluid flow under the same circumstances, for example at $Ra=10^4$, we have two mirror image counter rotating rectangular cells with Bi=0 and Ec=0 as shown in fig(5.37), whereas in the Newtonian case we have one vortex. As the Biot and Eckert numbers are used we have still similar behaviour. When Ec number is used with or without the Biot number, two mirror image counter rotating vortices are found and they become more oval than rectangular. The corresponding temperature profile is shown in fig(5.38) warm fluid rising near the bottom wall and centre of the cavity's while colder fluid descends along the top and side walls. For $Ra=10^5$ we have one vortex with Bi=0 and Ec=0 as shown in fig(5.39). When the Biot condition is used, we have again one vortex with the direction of rotation now reversed. Also there is an effect on the temperature distribution for Bi=1, and 10 as well. So that while Bi=0 the warm fluid rises near the bottom wall and at the centre of the cavity, and colder fluid descends near the top and side walls. In the case of Bi=1 we have again one vortex but when Bi increases for example Bi=10, two mirror image counter rotating vortices are found as shown in fig(5.40). The corresponding temperature profile is shown in fig(5.41) warm fluid rises near the bottom and inside the cavity and colder fluid descends near the top wall. These behaviour is only seen for the pseudoplastic fluid.

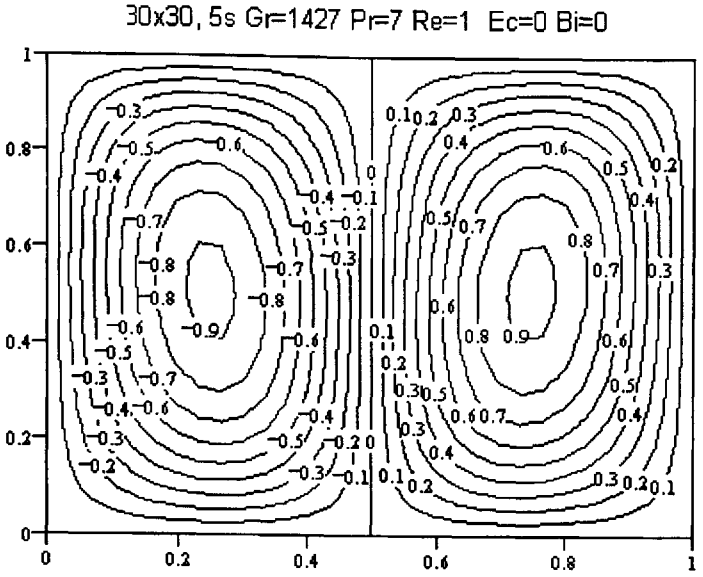

Figure (5.37) ; Streamline contours for viscous dilatant fluid in Rayleigh-Benard case

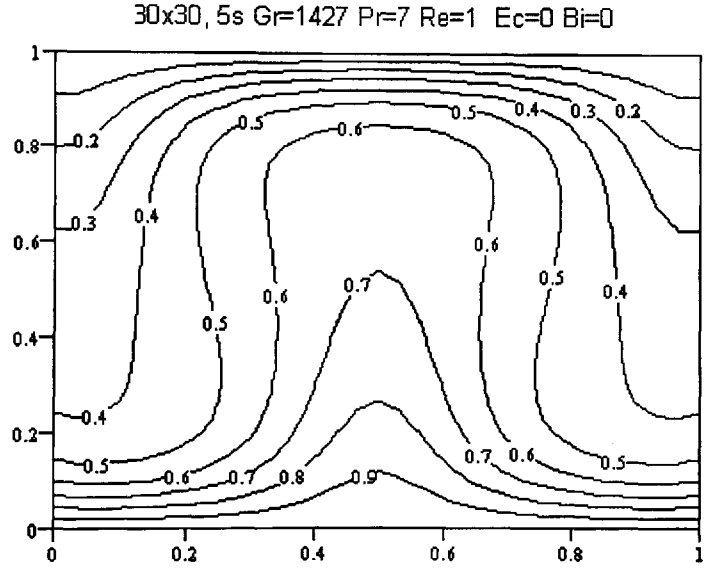

Figure (5.38) ; Temperature contours for viscous dilatant fluid in Rayleigh-Benard case

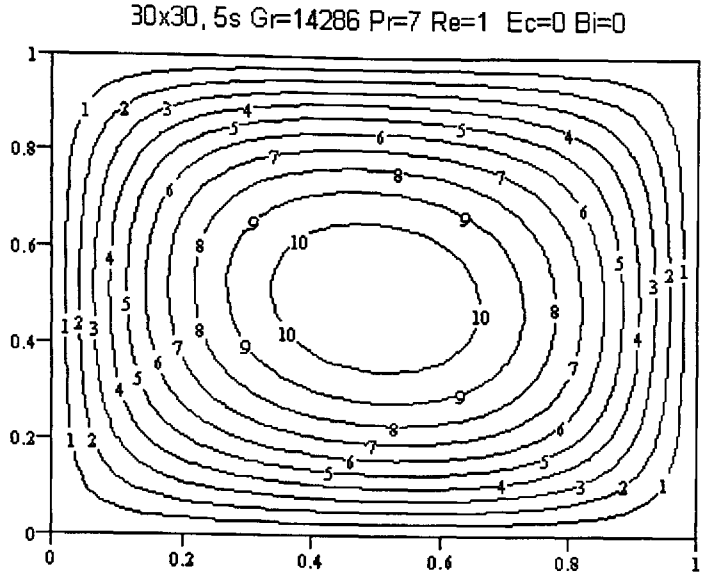

Figure (5.39) ; Streamline contours for viscous dilatant fluid in Rayleigh-Benard case

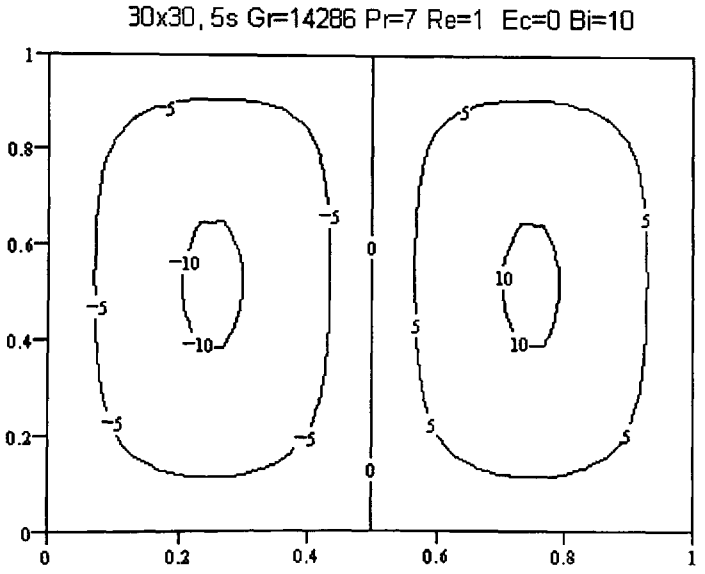

Figure (5.40) ; Streamline contours for viscous pseudoplastic fluid in Rayleigh-Benard case

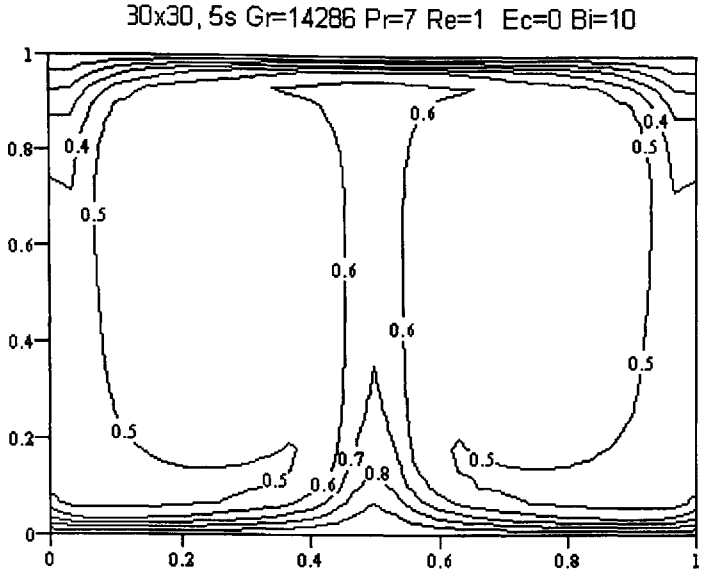

Figure (5.41) ; Temperature contours for viscous pseudoplastic fluid in Rayleigh-Benard case

For Ra=10^6 we have one cell vortex for Bi=0, 1, and 10 we see that the Bi number influence changes the flow directionand an increase in cell number.

Viscoelastic fluid flow results show that the fluid exhibit similar behaviour to their viscous counterparts respectively, without taking the Biot number boundary condition or viscous heating into account. When the Bi=1 we still have a similar behaviour for the Boger and pseudoplastic fluids with Newtonian and viscous pseudoplastic fluids respectively at all Ra considered. However, we have different behaviour in the case of the a dilatant fluid so that while the viscous dilatant fluid produces two mirror images counter rotating cells, the viscoelastic solution gives rise to a one cell vortex solution. For Bi=10 we have similar results at all values of Ra for all fluids. When Ec is used the computer program failed to converge to the solution at a given Ec number as indicated in the following table.

VISCOUS FLUID					VISCOELASTIC FLUID				
RA NUMBER	**3600**	10^4	10^5	10^6	**RA NUMBER**	**3600**	10^4	10^5	10^6
NEWTONIAN	1	1	1	1	**BOGER**	**1**	**1**	**1**	**1**
PSEUDOPLASTIC	1	1	1	1	**PSEUDOPLASTIC**	**1**	**1**	**1**	**1**
DILATANT	1	2	1	1	**DILATANT**	**1**	**2**	**1**	**1**

Bi=1

VISCOUS FLUID				VISCOELASTIC FLUID			
RA NUMBER	10^4	10^5	10^6	**RA NUMBER**	10^4	10^5	10^6
NEWTONIAN	1	1	1	**BOGER**	**1**	**1**	**1**
PSEUDOPLASTIC	2	1	1	**PSEUDOPLASTIC**	**2**	**1**	**1**
DILATANT	2	1	1	**DILATANT**	**2**	**1**	**1**

Bi=10

VISCOUS FLUID				VISCOELASTIC FLUID			
RA NUMBER	10^4	10^5	10^6	**RA NUMBER**	10^4	10^5	10^6
NEWTONIAN	2	1	1	**BOGER**	**2**	**1**	**1**
PSEUDOPLASTIC	2	2	1	**PSEUDOPLASTIC**	**2**	**2**	**1**
DILATANT	2	1	1	**DILATANT**	**2**	**1**	**1**

Table (5.2) ; Number of cells obtained at a given Ra number for shear-free flow

It was seen that the system produced steady solution at given Ra from 10^4 to 10^6 with or without Bi. Ec was found to be a cause of instability in flow, therefore no steady solution was found at a any given simulation time. However, the system usually produced a one cell solution in both viscous and viscoelastic cases without any Biot

condition except for the dilatant fluid at $Ra=10^4$. The dilatant fluid had two mirror image counter rotating cells at $Ra=10^4$. When $Bi \neq 0$, for example Bi=1, a two cells solution was obtained for non-Newtonian fluids at $Ra=10^4$. Similarly as Bi increased both constant and variable viscosity fluids exhibited an increase in cell number and a two cells solution was found in this case at $Ra=10^4$. For $Ra=10^5$ only the pseudoplastic fluid produced a two cells solution. The system was seen to produce a one cell solution with or without Bi at $Ra=10^6$.

5.6.4 Temperature Dependent Viscoelastic Fluid

In this section we investigate the Rayleigh-Benard system. This type of flow is possible in many geophysical flows that exist within the Earth's mantle. For simplicity we compare our results with other authors, taking Pr=7. In fact the Prandtl number can be considered to be infinite in a mantle system due to the very viscous liquid rock that exists there. Torrance and Turcotte**[93]** have produced some results for Ra up to 3600 for various constant 'k' values in which vorticity is zero on the boundary as of shear-free boundary conditions. We take k values of 1, 5, and 10 and increase Ra from 10^4 to 10^6. We produced results for both viscous and viscoelastic fluids and in most cases we saw that corresponding viscous and viscoelastic flow are in agreement under the same k value and Ra. For instance when Ra is taken as 10^4 and $k = 1$, only a dilatant fluid produced two mirror image counter rotating cells in both viscous and viscoelastic cases after 10s as shown in fig(5.42). For Newtonian and pseudoplastic flow we have a one cell vortex. As the k value increases with $Ra=10^4$, we could not get any results for the dilatant fluid for both viscous and

viscoelastic cases. However for k=10 the Newtonian fluid has two mirror image counter rotating cells. Moreover for k=1 and k=5, we have one vortex. We therefore present two results for $Ra=10^4$ with various k values in the following figures which are for viscous dilatant and Newtonian fluids, respectively, along with their corresponding temperature profiles. As shown in fig(5.43) for the dilatant fluid the corresponding temperature profile has the warmer fluid rising in cavity's centre while colder fluid descends near the vertical walls, and similar behaviour was seen for viscoelastic dilatant case for k=1.

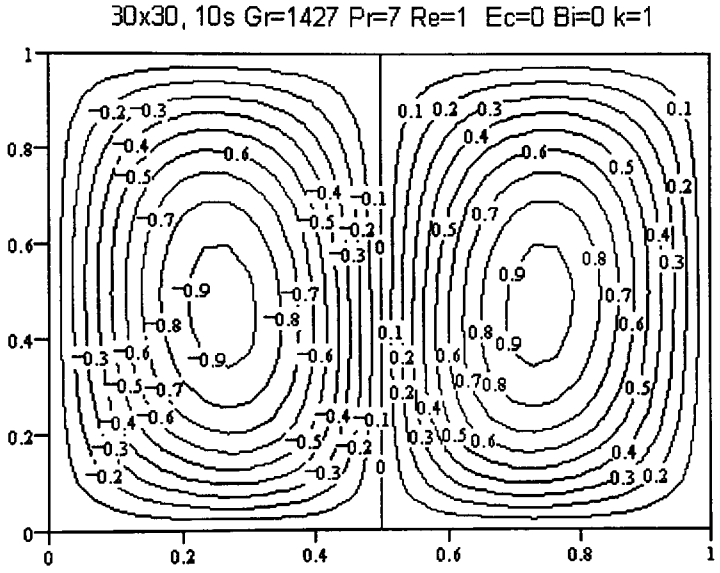

Figure (5.42) ; Streamline contours for viscous dilatant fluid

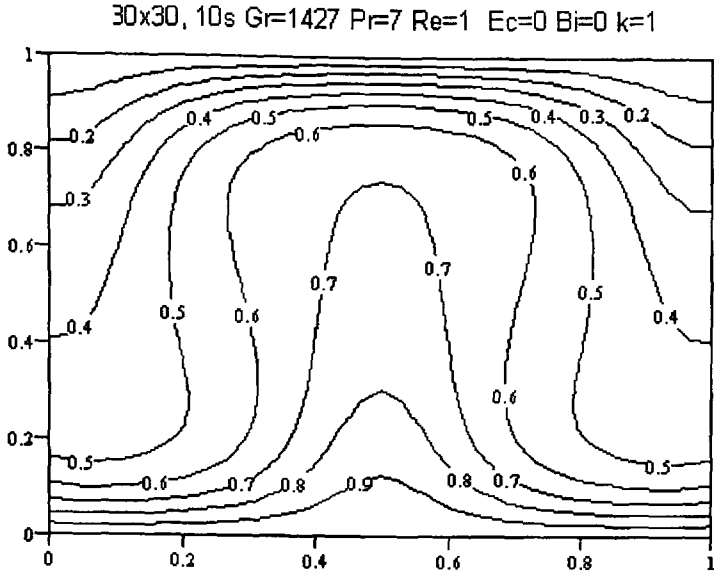

Figure (5.43) ; Temperature contours for viscous dilatant fluid

By considering the Ec and Bi we see that the Ec number causes instability and no steady solution is obtained. When we consider the Bi number as 1 or 10 some results are seen to be totally different from the their counterpart in which Bi number is zero. For example in case of the k=1 while we have one vortex solution for Bi=0 and Bi=1, we have two mirror image counter rotating rectangular cells for the Newtonian fluid flow shown in fig(5.44) for Bi=10. Similarly we obtained similar two mirror image counter rotating cells for k=10 with Bi=1 and Bi=10.

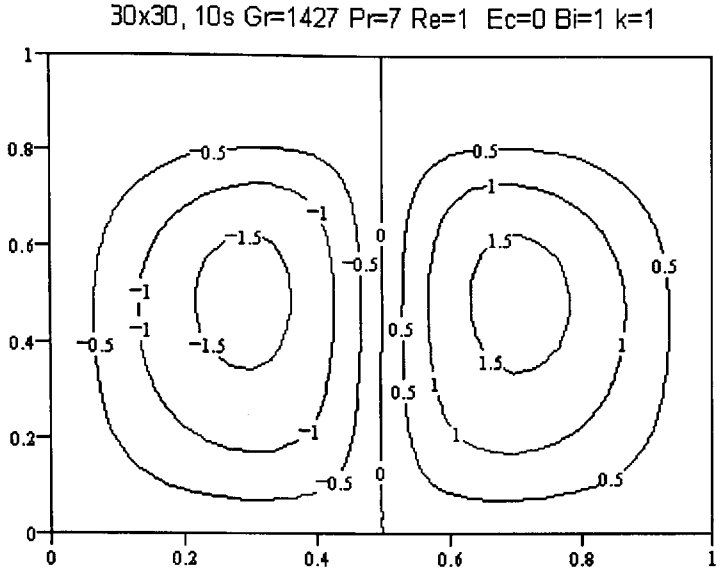

Figure (5.44) ; Streamline contours for Newtonian fluid

The corresponding temperature profile is shown in fig(5.45), in which the warmer fluid rises in the cavity's centre and colder fluid descends near the vertical walls.

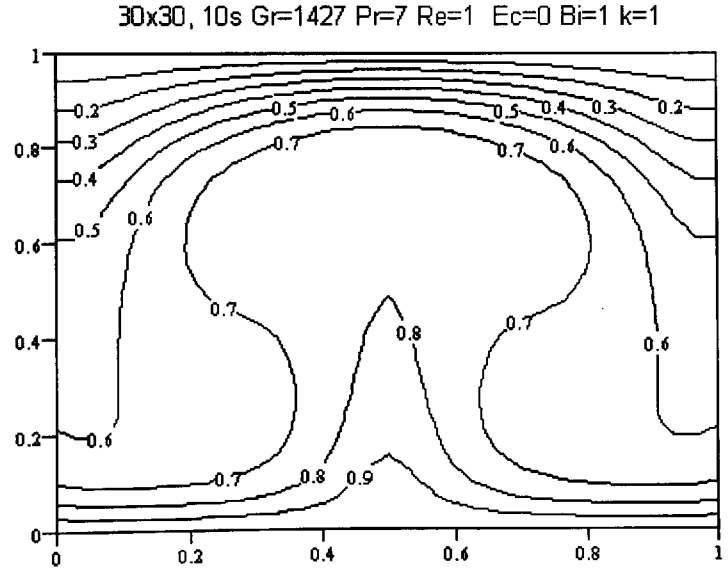

Figure (5.45) ; Temperature contours for Newtonian fluid

VISCOUS FLUID

Ra=10^4 **Ra**=10^5

	k=1	k=5	k=10	k=1	k=5	k=10
NEWTONIAN	1	1	1	1	1	1
PSEUDOPLASTIC	1	1	1	1	1	1
DILATANT	2			2		

VISCOELASTIC FLUID

Ra=10^4 **Ra**=10^5

	k=1	k=5	k=10	k=1	k=5	k=10
BOGER	1	1	1	1	1	1
PSEUDOPLASTIC	1	1	1	1	1	1
DILATANT	2			2		

VISCOUS FLUID WITH Bi NUMBER

Ra=10^4 **Ra**=10^5

	Bi=1		**Bi=10**		**Bi=1**		**Bi=10**	
	k=1	**k=10**	**k=1**	**k=10**	**k=1**	**k=10**	**k=1**	**k=10**
NEWTONIAN	1	2	2	2	1	1	1	1
PSEUDOPLASTIC	2	1	2	1	1			
DILATANT	2		2		1		1	

VISCOELASTIC FLUID WITH Bi NUMBER

	Ra=10^4				Ra=10^5			
	Bi=1		Bi=10		Bi=1		Bi=10	
	k=1	k=10	k=1	k=10	k=1	k=10	k=1	k=10
BOGER	1	2	2	2	1	1	1	1
PSEUDOPLASTIC	2	1	2	1	1			
DILATANT	2		2		1		1	

Table (5.3) ; Number of cells obtained at a given Ra number for k values

Table (5.3) shows number of cells obtained at a given Ra for various 'k' values. The stability properties still depend on Ra, Bi, and Ec also depend on 'k' values as well. The Eckert number was seen to cause instability in flow therefore no steady solution was found. Also as Ra increases, for example at Ra=10^6 for any non-zero 'k' value the computer solution failed to converge to a solution, whereas for k=0 the Rayleigh-Benard case usually produce one vortex cell solution. Moreover, for the non-Newtonian dilatant fluid in both viscous and viscoelastic cases we only have a steady solution and it was found to have two mirror image counter rotating cells at Ra=10^4 for k=1. For k=5 and k=10 the dilatant fluid did not produce any steady solution. Therefore it can be said that as k increases the computer solution failed to converge to a solution in the dilatant fluid at any Ra considered. When $Bi \neq 0$, for example for Bi=1 and k=1 a two cells solution is obtained in both variable and constant fluid cases at Ra=10^4. As Bi increases both constant and variable viscosity fluids produced a two

cells solution as well. When Ra increases the system always produced one cell solution at all k values considered.

CHAPTER VI: CYLINDRICAL DRIVEN CAVITY FLOW IN 3D

6.1 FLOW GEOMETRY AND PREVIOUS WORK

Previously we sought a computational solution and the stability properties of cavity driven flows in a bounded rectangular geometry in 2D. The literature shows there has also been much research undertaken in various other cavities such as cylindrical containers, concentric cylinders, spheres etc. For simplicity most studies are based in cylindrical cavities in 'two dimensions' because of the way 3D flows problem can be reduced to 2D through axisymmetry. We choose to study 3D cylindrical driven cavity flow where there is no dependence on flow in the rotational θ direction $\left(\frac{\partial}{\partial\theta}=0\right)$ and the number of independent variables reduce from three to two. In this study we seek a numerical solution for cylindrical driven cavity flow in three categories namely

i. Cylindrical Cavity Driven Flow,

ii. Concentric Cylindrical Cavity Driven Flow,

iii. The Flat Free Surface Problem.

Various flow problems generated by cylinders or discs for a range of Reynolds numbers and both Newtonian and non-Newtonian fluids have been studied computationally by a number of authors. The configuration generally considered is the disc driven or wall driven flow problem. Our consideration is to extend this study for viscous and viscoelastic fluid with various moving walls for both cylinder driven and thermally driven cases. The thermally driven case will be considered in Chapter 7.

The main feature of the cylindrical flow driven by walls rotating with constant angular velocity are the primary flow in the direction of rotation, and the secondary flow perpendicular to the primary flow. Pao[73] studied an incompressible viscous liquid in a bounded cylinder, with the top and side walls rotating with constant angular velocity and bottom wall stationary. Pao obtained many solutions up to Re=8600 and the flow appeared steady and laminar. Griffiths et al.[37], Griffiths and Walters[36] and Kuriyama et al.[46] solved the governing equations numerically for the Newtonian fluid and slow motion steady rotation of the stirrer, obtaining results for both fluid velocity and shear-rate. Kramer[44] studied a viscometric flow driven by a disk rotating cylinder. He developed a perturbation theory for a weak secondary flow and illustrated flow patterns for a second order fluid where the fluid elasticity effect is zero. Waters and Keeley[97] carried out a numerical analysis of the stability interface where two liquids act on each other, with a solution sought for the two Oldroyd-B liquids which were flowing in the different layers. Later Shu-Min et al.[87] investigated for the steady CEF model fluid behaviour in a cylinder. They indicated the bifurcation area located in Weissenberg-Reynolds space and showed that the bifurcation solution is near this area. Recently, Ling and Zhang[53] conducted a mixing study in a corotating cavity for a generalised Newtonian fluid and they found mixing took place in the parameter space by using bifurcation analysis and geometrical construction of periodic orbits. Also Liao and Chukwu[52] studied the Couette flow of non-Newtonian power-law fluids. In this study the flow is generated in narrow eccentric annuli.

In the case of concentric cylinder driven cavity flow, which is also called Taylor-Couette flow, Taylor[92] considered the stability of the steady flow between two concentric cylinders rotating with a constant angular velocity and discovered the now famous Taylor vortices. Further research studies have considered various Taylor-Couette flows, including the effect of time-periodic outer cylinder oscillation. The Taylor-Couette flow problem became an important study for viscoelastic instabilities and a test problem for constitutive equations of viscoelastic fluids. In the case of a Newtonian fluid, the instability is increased as the Reynolds' number is increased. This situation is well reported by Drazin and Reid[27], and Di Prima and Swinney[26]. Recently a linear stability analysis and numerical solution has been conducted for an Oldroyd-B model fluid by Larson et al[48], Shaqfeh et al[85], Northey et al[66], Avgousti et al[2], Surehkumar et al[90]. Ramkissoon[76] investigated a Taylor-Couette problem for a second-order fluid with both constant and time-dependent angular velocity, and obtained an exact solution to the governing PDEs. Recent experimental studies of Taylor-Couette driven flow are by Escudier et al[31] and Brandon[11]. They investigated Taylor-vortex behaviour for both Newtonian and shear-thinning liquids.

6.2 CYLINDER CAVITY DRIVEN FLOW EQUATIONS OF 3D FLOW

To consider an incompressible viscoelastic CEF fluid in a closed cylinder cavity, we study both steady and unsteady flows with the density of fluid taken as constant and assume that the flow is axisymmetric i.e. there is no flow dependence in the θ direction. The velocity vector $V_i = (u, r\Omega, w)$ where $\Omega = \frac{v}{r}$. The stream

function, concentration equation, and the path of a fluid particle are as in Chapter 3. The rotational speed equation can be derived from the equation of motion which is in the θ direction, and the equations of the stream function and the vorticity define the secondary flow. The governing equations of the motion can be given non-dimensionally as:

Conservation of Mass

$$\frac{\partial u}{\partial r}+\frac{u}{r}+\frac{\partial w}{\partial z}=0, \tag{6.1}$$

where u and w can be defined in terms of a stream function Ψ as

$$u=-\frac{1}{r}\frac{\partial \Psi}{\partial z},\ w=\frac{1}{r}\frac{\partial \Psi}{\partial r}$$

Conservation of Momentum

$$\rho\left(\frac{\partial u}{\partial t}+u\frac{\partial u}{\partial r}-\frac{v^2}{r}+w\frac{\partial u}{\partial z}\right)=\frac{1}{r}\frac{\partial}{\partial r}\left(r\sigma_{rr}\right)+\frac{\partial}{\partial z}\left(\sigma_{zr}\right)-\frac{1}{r}\sigma_{\theta\theta}-\frac{\partial P}{\partial r}+\rho F_r \tag{6.2}$$

$$\rho\left(\frac{\partial v}{\partial t}+u\frac{\partial v}{\partial r}+\frac{uv}{r}+w\frac{\partial v}{\partial z}\right)=\frac{1}{r^2}\frac{\partial}{\partial r}\left(r^2\sigma_{r\theta}\right)+\frac{\partial}{\partial z}\left(\sigma_{z\theta}\right)+\rho F_\theta \tag{6.3}$$

$$\rho\left(\frac{\partial w}{\partial t}+u\frac{\partial w}{\partial r}+w\frac{\partial w}{\partial z}\right)=\frac{1}{r}\frac{\partial}{\partial r}\left(r\sigma_{rz}\right)+\frac{\partial}{\partial z}\left(\sigma_{zz}\right)-\frac{\partial P}{\partial z}+\rho F_z \tag{6.4}$$

Here F_r, F_θ and F_z are the body forces per unit mass in the respective directions (r,θ,z) and for our case there are no body forces in the r and θ direction in equations (6.2) and (6.3). Only gravity acts as a body force in the direction of z in equation (6.4) and the body force is thus $F=(0,0,-g)$. As previously in Chapter 3 we can obtain

$$\rho\frac{D\omega}{Dt}=\frac{M}{2}\left(\sigma_{rr}-\sigma_{zz}\right)+\frac{1}{r}\frac{\partial}{\partial z}\left(\sigma_{rr}-\sigma_{\theta\theta}\right)$$
$$+L\left(\sigma_{rz}\right)-\frac{1}{r}\frac{\partial}{\partial r}\sigma_{rz}+\frac{1}{r^2}\sigma_{rz}+\frac{\rho}{r}\frac{\partial}{\partial z}\left(r\Omega\right) \qquad 6.5$$

where now $M(\bullet)=2\frac{\partial^2}{\partial r\partial z}(\bullet)$, $L(\bullet)=\left(\frac{\partial^2}{\partial z^2}-\frac{\partial^2}{\partial r^2}\right)(\bullet)$. The extra-stress tensor σ_{ik} is defined as in the previous chapters with the elastic part of the extra-stress modelled by the CEF equation[9]. The deformation rate for the flow is now

$$\left(\dot{\gamma}\right)^2=\left\{2\left(d_{rr}^2+d_{\theta\theta}^2+d_{zz}^2+2d_{rz}^2+2d_{r\theta}^2+2d_{\theta z}^2\right)\right\}.$$

The vorticity equation, rotational speed equation, concentration equation and the motion of fluid particles can be summarised as:

Vorticity equation

$$\omega=\frac{\partial u}{\partial z}-\frac{\partial w}{\partial r} \qquad 6.6$$

Rotational Speed Equation

$$\rho\frac{D}{Dt}\left(r^3\Omega\right)=\frac{\partial}{\partial r}\left(\sigma_{r\theta}\right)+\frac{\partial}{\partial z}\left(\sigma_{z\theta}\right) \qquad 6.7$$

Concentration Equation

$$\rho\frac{DC}{Dt}=K_c\nabla^2C \qquad 6.8$$

Motion of a Fluid Particle

$$\frac{dr}{dt}=u=-\frac{1}{r}\frac{\partial\Psi}{\partial z}$$
$$\frac{dz}{dt}=w=\frac{1}{r}\frac{\partial\Psi}{\partial r} \qquad 6.9$$

6.3 NON-DIMENSIONALISATION

The flow equation can be non-dimensionalised by using the same ideas as previously prior to Chapter 3 with equation (6.2) becoming

Vorticity-Stream function

$$\frac{\partial \omega}{\partial t} = \frac{1}{r^2 \,\mathrm{Re}} H_1\left(r^3, \eta; \frac{\omega}{r}\right) + F_\omega \qquad 6.10$$

where

$$H_1\left(r^3, \eta; \frac{\omega}{r}\right) = \left\{\frac{\partial}{\partial r}\left[r^3 \frac{\partial}{\partial r}\left(\eta \frac{\omega}{r}\right)\right] + \frac{\partial}{\partial z}\left[r^3 \frac{\partial}{\partial z}\left(\eta \frac{\omega}{r}\right)\right]\right\} \qquad 6.11$$

and

$$F_\omega = \frac{1}{\mathrm{Re}}\left\{F_{\Omega I} + F_{\omega\eta} + F_{\omega\Omega} + F_{\omega S}\right\}$$

$$F_{\omega I} = -\mathrm{Re}\left\{\frac{\partial}{\partial r}[u\omega] + \frac{\partial}{\partial z}[w\omega]\right\}, \qquad 6.12$$

$$F_{\omega\eta} = 2\left\{\frac{\partial^2 \eta}{\partial z^2}\frac{\partial w}{\partial r} - \frac{\partial^2 \eta}{\partial r^2}\frac{\partial u}{\partial z}\right\} + \left\{\frac{\partial u}{\partial r} - \frac{\partial w}{\partial z}\right\} M(\eta) \qquad 6.13$$

$$F_{\omega\Omega} = \frac{1}{r}\mathrm{Re}\frac{\partial}{\partial z}\left(r^2\Omega^2\right) \qquad 6.14$$

$$F_{\omega S} = \frac{1}{2} M\left(S_{rr} - S_{zz}\right) + L\left(S_{rz}\right) + \frac{1}{r}\frac{\partial}{\partial z}\left(S_{rr} - S_{\theta\theta}\right) - \frac{1}{r}\frac{\partial}{\partial r}\left(S_{rz}\right) + \frac{1}{r^2} S_{rz} \qquad 6.15$$

where $\mathrm{Re} = \rho\Omega R^2 / \eta(0)$ and R is the outer radius of the cylinder container considered.

Rotational speed Equation

$$\frac{\partial \Omega}{\partial t} = \frac{1}{r^3 \,\mathrm{Re}} H_2\left(r^3, \eta; \Omega\right) + \frac{1}{r^3} F_\Omega \qquad 6.16$$

where

$$H_2\left(r^3,\eta;\Omega\right)=\frac{\partial}{\partial r}\left[r^3\eta\frac{\partial\Omega}{\partial r}\right]+\frac{\partial}{\partial z}\left[r^3\eta\frac{\partial\Omega}{\partial z}\right] \qquad 6.17$$

and

$$F_\Omega=\frac{1}{\mathrm{Re}}\left\{F_{\Omega S}+F_{\Omega I}\right\} \qquad 6.18$$

$$F_{\Omega I}=-\mathrm{Re}\left\{\frac{\partial}{\partial r}\left[r^2u\Omega\right]+\frac{\partial}{\partial z}\left[r^2w\Omega\right]\right\} \qquad 6.19a$$

$$F_{\Omega S}=\frac{\partial}{\partial r}\left(r^2S_{r\theta}\right)+\frac{\partial}{\partial z}\left(r^2S_{z\theta}\right) \qquad 6.19b$$

Concentration Equation

$$\frac{\partial C}{\partial t}=\frac{1}{\mathrm{Re}Sc}\nabla^2C+\frac{1}{r}F_C \qquad 6.20$$

where

$$F_C=-\left\{\frac{\partial}{\partial r}\left[ruC\right]+\frac{\partial}{\partial C}\left[rwC\right]\right\} \qquad 6.21$$

Stream Function

$$\frac{\partial}{\partial z}\left(\frac{1}{r}\frac{\partial\Psi}{\partial z}\right)+\frac{\partial}{\partial r}\left(\frac{1}{r}\frac{\partial\Psi}{\partial r}\right)=-\omega\,. \qquad 6.22$$

6.4 BOUNDARY CONDITIONS

Equations (6.10), (6.16) and (6.20) are solved numerically using suitable boundary conditions and initial values. We still depend on the vorticity boundary conditions as in Chapter 3. The velocity components may be taken as $u=0,w=0$ on the boundaries. We take the rotational speed in the cavity as $\Omega=\frac{v}{r}$. The stream function

remains constant and is taken as zero on the boundaries. We, therefore, give the boundary condition on each type of cylinder cavity geometry by considering the vorticity-stream function boundary formulation, as follows:

i.Cylinder Driven Cavity Flow

In the case of cylinder driven flow the symmetry line $(r = 0)$ is 'kept fixed' and the remaining walls rotate with a constant angular velocity. We have chosen the aspect ratio as always unity in many circumstances.

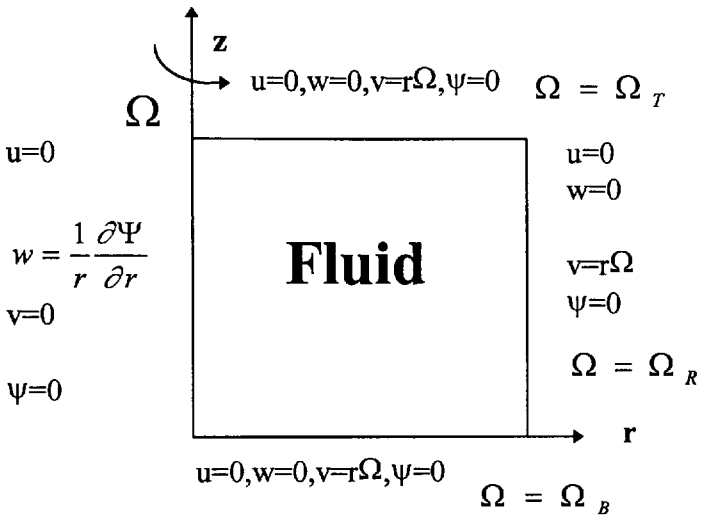

Figure 6.1; Boundary conditions for cylinder driven cavity flow

ii.Concentric Cylinder Driven Cavity Flow

We consider Taylor-Couette flow where the flow is driven by the four walls and on the walls $u = 0, w = 0$ and $v = r\Omega$.

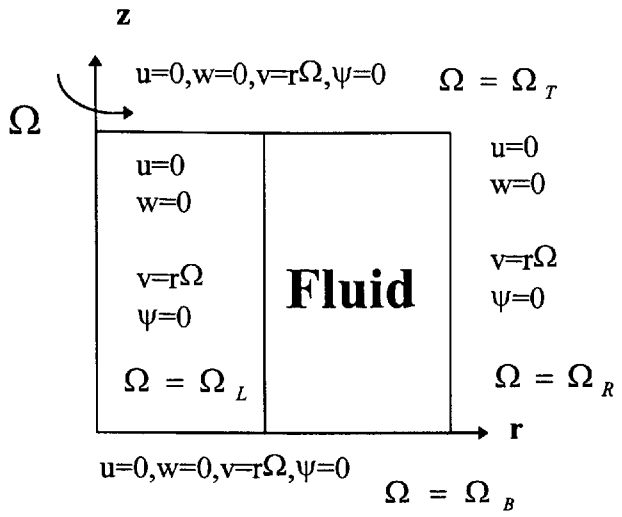

Figure 6.2; Boundary conditions for concentric cylinder driven cavity flow

iii.Free Surface Cylinder Driven Flow

In this case we consider free-surface flow where the flow is generated by the right wall and the bottom wall. The boundary conditions are similar to the cylinder driven flow except for the top wall condition. As seen from figure (6.3) the only difference between the flat free surface and cylinder driven flow is that there is no angular velocity imposed on the top wall and the remaining velocity components $u \neq 0$ and $w = 0$. Also there is no shear-stress on the top wall therefore $\frac{\partial \Omega}{\partial z} = 0$. The other wall boundary conditions remain the same.

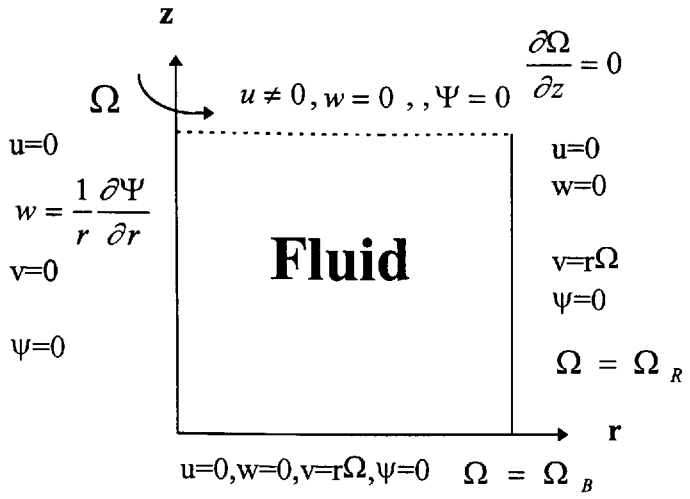

Figure 6.3; Boundary conditions for free-surface cylinder driven cavity flow

6.5 DISCRETISION OF THE FLOW EQUATION

In this section, we solve the equations (6.10), (6.16) and (6.20) numerically by finite differences for the steady and time-dependent flow cases. We have two different time-dependent approximations which are the simple explicit and Peaceman-Rachford methods. The stability and consistency criteria for the solutions have been given in previous chapters.

i)Steady State

In this case, we only seek numerical solution for the stream function and flow equation. By considering equation (3.34) the stream function is discretised and the coefficients of the equation now become

$$B_1 = \alpha^2\left(\frac{1}{r^p + 0.5h} + \frac{1}{r^p - 0.5h}\right) + \frac{2}{r^p},$$

$$B_2 = \alpha^2\left(\frac{1}{r^p + 0.5h}\right), \; B_3 = \alpha^2\left(\frac{1}{r^p - 0.5h}\right)$$

$$B_4 = B_5 = \frac{1}{r^p}, \; B_6 = k^2 r^p \zeta^p$$

where the vorticity is defined as $\omega = r\zeta$, and from now on we use this formulation for the vorticity equation.

Considering equation (3.34) where the dependent function is ζ, we now have

$$B_1 = \frac{0.25\alpha^2}{r^{2p}\eta^p}\left[\left(r^p + 0.5h\right)^3\left(\eta^E + \eta^P\right)^2 + \left(r^p - 0.5h\right)^3\left(\eta^W + \eta^P\right)^2\right]$$

$$-\frac{\alpha^2}{r^{2P}}\left[\left(r^p + 0.5h\right)^3\left(\eta^E - \eta^P\right) - \left(r^p - 0.5h\right)^3\left(\eta^P - \eta^W\right)\right]$$
$$+\frac{0.25r^P}{\eta^P}\left[\left(\eta^N + \eta^P\right)^2 + \left(\eta^S + \eta^P\right)^2\right] - 2r^P\left[\left(\eta^N - \eta^P\right) - \left(\eta^P - \eta^S\right)\right]$$
$$-r^P\left[\left(\eta^N - \eta^P\right) - \left(\eta^P - \eta^S\right)\right],$$

$$B_2 = \alpha^2\left[\frac{0.25}{r^{2P}\eta^P}\left(r^p + 0.5h\right)^3\left(\eta^E + \eta^P\right)^2 - 0.5\,\mathrm{Re}\,h(ru)^E\right]$$

$$B_3 = \alpha^2\left[\frac{0.25}{r^{2P}\eta^P}\left(r^p - 0.5h\right)^3\left(\eta^W + \eta^P\right)^2 + 0.5\,\mathrm{Re}\,h(ru)^W\right]$$

$$B_4 = \frac{0.25r^P}{\eta^P}\left(\eta^P + \eta^N\right)^2 - 0.5\,\mathrm{Re}\,k(rw)^N$$

$$B_5 = \frac{0.25r^P}{\eta^P}\left(\eta^P + \eta^S\right)^2 + 0.5\,\mathrm{Re}\,k(rw)^S$$

$$B_6 = k^2 F_\zeta^P.$$

However, at in the rotational speed equation coefficients take the form

$$B_1 = 0.5\alpha^2\left[\left(r^P + 0.5h\right)^3\left(\eta^E + \eta^P\right) + \left(r^P - 0.5h\right)^3\left(\eta^W + \eta^P\right)\right]$$

$$+0.5\left[r^{3P}\left(\eta^N + \eta^S\right) + r^{3P}\left(\eta^S + \eta^P\right)\right]$$

$$B_2 = 0.5\alpha^2\left[\left(r^P + 0.5h\right)^3\left(\eta^E + \eta^P\right) - h\,\mathrm{Re}\left(r^3u\right)^E\right]$$

$$B_3 = 0.5\alpha^2\left[\left(r^P - 0.5h\right)^3\left(\eta^W + \eta^P\right) + h\,\mathrm{Re}\left(r^3u\right)^W\right]$$

$$B_4 = 0.5\left[r^{3P}\left(\eta^N + \eta^P\right) - k\,\mathrm{Re}\left(r^3 w\right)^N\right]$$

$$B_5 = 0.5\left[r^{3P}\left(\eta^S + \eta^P\right) + k\,\mathrm{Re}\left(r^3 w\right)^S\right]$$

$$B_6 = k^2 F_\Omega^P$$

where $\alpha = k/h$ is the aspect ratio of the cylinder cavity grid.

ii)Unsteady state

We solve the flow vorticity, rotational speed and concentration equations in both simple explicit and Peaceman-Rachford methods respectively for the cylinder driven cavity flow at various aspect ratios. In both cases the stream function is calculated as above. We use the simple explicit model to solve the coupled partial differential equations as in chapter 3. When we consider the dependent variable ζ in equation (3.35) then we have at in the vorticity equation coefficients take the form

$$B_1 = 1 - rr\left[\frac{\left(r^P + 0.5h\right)^3\left(\eta^E + \eta^P\right)^2 + \left(r^P - 0.5h\right)^3\left(\eta^W + \eta^P\right)^2}{4\,\mathrm{Re}\,r^{3P}\eta^P}\right.$$

$$\left.\frac{\left(r^P + 0.5h\right)^3\left(\eta^E - \eta^P\right) - \left(r^P - 0.5h\right)^3\left(\eta^P - \eta^W\right)}{\mathrm{Re}\,r^{3P}}\right]$$

$$-s\left[\frac{\left(\eta^N + \eta^P\right)^2 + \left(\eta^S + \eta^P\right)^2}{4\,\mathrm{Re}\,\eta^P} - \frac{\left(\eta^N - \eta^P\right) - \left(\eta^P - \eta^S\right)}{\mathrm{Re}}\right]\Bigg\},$$

$$B_2 = rr\left\{\frac{\left(r^P + 0.5h\right)^3\left(\eta^E + \eta^P\right)^2}{4\,\mathrm{Re}\,r^{3P}\eta^P} - \frac{h}{2r^P}(ru)^E\right\},$$

$$B_3 = rr\left\{\frac{\left(r^P - 0.5h\right)^3\left(\eta^W + \eta^P\right)^2}{4\,\mathrm{Re}\,r^{3P}\eta^P} + \frac{h}{2r^P}(ru)^W\right\},$$

$$B_4 = s\left\{\frac{\left(\eta^N + \eta^P\right)^2}{4\,\mathrm{Re}\,\eta^P} - \frac{k}{2}(w)^N\right\},$$

$$B_5 = s\left\{\frac{\left(\eta^S + \eta^P\right)^2}{4\,\mathrm{Re}\,\eta^P} + \frac{k}{2}(w)^S\right\},$$

$$B_6 = \frac{\Delta t}{2r\,\mathrm{Re}}F_n^P.$$

The coefficients of the equation of (3.43) for rotational speed incorporate

$$B_1 = \left\{1 - rr\left[\frac{\left(r^P + 0.5h\right)^3\left(\eta^E + \eta^P\right) + \left(r^P - 0.5h\right)^3\left(\eta^W + \eta^P\right)}{2\,\mathrm{Re}\,r^{3P}}\right]\right.$$

$$\left. - s\left[\frac{\left(\eta^N + \eta^P\right) + \left(\eta^S + \eta^P\right)}{2\,\mathrm{Re}}\right]\right\},$$

$$B_2 = rr\left[\frac{\left(r^P + 0.5h\right)^3\left(\eta^E + \eta^P\right)}{2\,\mathrm{Re}\,r^{3P}} - \frac{h}{2r^{3P}}\left(r^3u\right)^E\right],$$

$$B_3 = rr\left[\frac{\left(r^P - 0.5h\right)^3\left(\eta^W + \eta^P\right)}{2\,\mathrm{Re}\,r^{3P}} + \frac{h}{2r^{3P}}\left(r^3u\right)^W\right],$$

$$B_4 = s\left[\frac{\left(\eta^N + \eta^P\right)}{2\,\mathrm{Re}} - \frac{k}{2}(w)^N\right],$$

$$B_5 = s\left[\frac{\left(\eta^S + \eta^P\right)}{2\,\mathrm{Re}} + \frac{k}{2}(w)^S\right],$$

$$B_6 = \frac{\Delta t}{2r^3\,\mathrm{Re}} F_n^P \quad .$$

For the concentration equation we have

$$B_1 = \left\{1 - rr\left[\frac{\left(r^P + 0.5h\right) + \left(r^P - 0.5h\right)}{rSc\,\mathrm{Re}}\right] - s\left[\frac{(2)}{Sc\,\mathrm{Re}}\right]\right\},$$

$$B_2 = rr\left[\frac{\left(r^P + 0.5h\right)}{rSc\,\mathrm{Re}} - \frac{h}{2r}(ru)^E\right],$$

$$B_3 = rr\left[\frac{\left(r^P - 0.5h\right)}{rSc\,\mathrm{Re}} + \frac{h}{2r}(ru)^W\right],$$

$$B_4 = s\left[\frac{1}{Sc\,\mathrm{Re}} - \frac{k}{2}w^N\right],$$

$$B_5 = s\left[\frac{1}{Sc\,\mathrm{Re}} + \frac{k}{2}w^S\right],$$

$$B_6 = 0.$$

Here $rr = \dfrac{\Delta t}{h^2}$ and $s = \dfrac{\Delta t}{k^2}$.

For the A.D.I method when we put ζ in equations (3.42) and (3.43) as a dependent variable we have the vorticity equation which in discretised form is

$$\zeta^*_{i,j} - rr\left(A_1\zeta^*_{i+1,j} + A_2\zeta^*_{i-1,j} - 2A_3\zeta^*_{i,j}\right) + rr\frac{h}{2r}(ur)\left(\zeta^*_{i+1,j} - \zeta^*_{i-1,j}\right)$$

$$= \zeta^n_{i,j} + s\left(A_4\zeta^n_{i+1,j} + A_5\zeta^n_{i-1,j} - 2A_6\zeta^n_{i,j}\right) - s\frac{k}{2}w\left(\zeta^n_{i,j+1} - \zeta^n_{i,j-1}\right) + \frac{\Delta t}{2}f^n \qquad 6.23$$

and

$$\zeta^{n+1}_{i,j} - s\left(A_4\zeta^{n+1}_{i+1,j} + A_5\zeta^{n+1}_{i-1,j} - 2A_6\zeta^{n+1}_{i,j}\right) + s\frac{k}{2}w\left(\zeta^{n+1}_{i,j+1} - \zeta^{n+1}_{i,j-1}\right)$$

$$= \zeta^*_{i,j} + rr\left(A_1\zeta^*_{i+1,j} + A_2\zeta^*_{i-1,j} - 2A_3\zeta^*_{i,j}\right) - rr\frac{h}{2r}(ur)\left(\zeta^*_{i+1,j} - \zeta^*_{i-1,j}\right) + \frac{\Delta t}{2}f^n, \qquad 6.24$$

where

$$A_1 = \left\{\frac{\left(r^P + 0.5h\right)^3\left(\eta^E + \eta^P\right)^2}{8\,\mathrm{Re}\,r^{3P}\eta^P}\right\},$$

$$A_2 = \left\{\frac{\left(r^P - 0.5h\right)^3\left(\eta^W + \eta^P\right)^2}{8\,\mathrm{Re}\,r^{3P}\eta^P}\right\},$$

$$A_3 = \left\{\left(\frac{\left(r^P + 0.5h\right)^3\left(\eta^E + \eta^P\right)^2 + \left(r^P - 0.5h\right)^3\left(\eta^W + \eta^P\right)^2}{8\,\mathrm{Re}\,r^{3P}\eta^P}\right)\right.$$

$$\left. - \left(\frac{\left(r^P + 0.5h\right)^3\left(\eta^E - \eta^P\right) - \left(r^P - 0.5h\right)^3\left(\eta^P - \eta^W\right)}{2\,\mathrm{Re}\,r^{3P}}\right)\right\},$$

$$A_4 = \left\{\frac{\left(\eta^N + \eta^P\right)^2}{8\,\mathrm{Re}\,\eta^P}\right\},$$

$$A_5 = \left(\frac{\left(\eta^N + \eta^P\right)^2 + \left(\eta^S + \eta^P\right)^2}{8\,\mathrm{Re}\,\eta^P} + \frac{\left(\eta^N - \eta^P\right) - \left(\eta^P - \eta^S\right)}{2\,\mathrm{Re}}\right),$$

$$A_6 = \left\{\frac{\left(\eta^S + \eta^P\right)^2}{8\,\mathrm{Re}\,\eta^P}\right\}.$$

For cylinder driven cavity flow the A.D.I. solution process is similar to the 2D cavity driven flow and the stability condition of the (M-1)(N-1) equations can be determined as previously. This solution process is stable when

$$-\frac{\left(r^3\eta^2\right)_{i-1,j}}{hr_{i,j}^2\eta_{i,j}} \le \frac{(ru)}{2} \le \frac{\left(r^3\eta^2\right)_{i+1,j}}{hr_{i,j}^2\eta_{i,j}}, \text{ and, } \frac{\left(\eta^2\right)_{i,j-1}}{k\eta_{i,j}} \le \frac{w}{2} \le \frac{\left(\eta^2\right)_{i,j+1}}{k\eta_{i,j}}.$$

Similarly, when we consider Ω as a dependent function in the equation (3.42) and (3.43) we have

$$\Omega_{i,j}^* - rr\left(A_1\Omega_{i+1,j}^* + A_2\Omega_{i-1,j}^* - 2A_3\Omega_{i,j}^*\right) + rr\frac{h}{2r^{3P}}\left(ur^3\right)\left(\Omega_{i+1,j}^* - \Omega_{i-1,j}^*\right)$$

$$= \Omega_{i,j}^n + s\left(A_4\Omega_{i+1,j}^n + A_5\Omega_{i-1,j}^n - 2A_6\Omega_{i,j}^n\right) - s\frac{k}{2}w\left(\Omega_{i,j+1}^n - \Omega_{i,j-1}^n\right) + \frac{\Delta t}{2}f^n \qquad 6.25$$

and

$$\Omega_{i,j}^{n+1} - s\left(A_4\Omega_{i+1,j}^{n+1} + A_5\Omega_{i-1,j}^{n+1} - 2A_6\Omega_{i,j}^{n+1}\right) + s\frac{k}{2}w\left(\Omega_{i,j+1}^{n+1} - \Omega_{i,j-1}^{n+1}\right)$$

$$= \Omega_{i,j}^* + rr\left(A_1\Omega_{i+1,j}^* + A_2\Omega_{i-1,j}^* - 2A_3\Omega_{i,j}^*\right) - rr\frac{h}{2r^{3P}}\left(ur^3\right)\left(\Omega_{i+1,j}^* - \Omega_{i-1,j}^*\right) + \frac{\Delta t}{2}f^n, \quad 6.26$$

with

$$A_1 = \frac{\left(r^P + 0.5h\right)^3\left(\eta^E + \eta^P\right)}{4\mathrm{Re}r^{3P}}$$

$$A_2 = \frac{\left(r^P - 0.5h\right)^3\left(\eta^W + \eta^P\right)}{4\mathrm{Re}r^{3P}}$$

$$A_3 = \frac{\left(r^P + 0.5h\right)^3\left(\eta^E + \eta^P\right)}{4\mathrm{Re}r^{3P}} + \frac{\left(r^P - 0.5h\right)^3\left(\eta^W + \eta^P\right)}{4\mathrm{Re}r^{3P}}$$

$$A_4 = \left(\frac{\eta^N + \eta^P}{4\mathrm{Re}}\right),\ A_5 = \left(\frac{\eta^S + \eta^P}{4\mathrm{Re}}\right), \text{ and } A_6 = \left(\frac{\eta^N + \eta^S + 2\eta^P}{4\mathrm{Re}}\right).$$

For the concentration equation we have

$$C_{i,j}^* - rr\left(A_1C_{i+1,j}^* + A_2C_{i-1,j}^* - 2A_3C_{i,j}^*\right) + rr\frac{h}{2r^P}\left(ur\ \right)\left(C_{i+1,j}^* - C_{i-1,j}^*\right)$$

$$= C_{i,j}^{n} + s\left(A_1\Omega_{i+1,j}^{n} + A_2 C_{i-1,j}^{n} - 2A_3 C_{i,j}^{n}\right) - s\frac{k}{2}w\left(C_{i,j+1}^{n} - C_{i,j-1}^{n}\right) + \frac{\Delta t}{2}f^{n} \qquad 6.27$$

and

$$C_{i,j}^{n+1} - s\left(A_4 C_{i+1,j}^{n+1} + A_5 C_{i-1,j}^{n+1} - 2A_6 C_{i,j}^{n+1}\right) + s\frac{k}{2}w\left(C_{i,j+1}^{n+1} - C_{i,j-1}^{n+1}\right)$$

$$= C_{i,j}^{*} + rr\left(A_1 C_{i+1,j}^{*} + A_2 C_{i-1,j}^{*} - 2A_3 C_{i,j}^{*}\right) - rr\frac{h}{2r^{P}}\left(ur\right)\left(C_{i+1,j}^{*} - C_{i-1,j}^{*}\right) + \frac{\Delta t}{2}f^{n}, \qquad 6.28$$

where

$$A_1 = \frac{\left(r^{P} + 0.5h\right)}{\mathrm{Re}\,Scr^{P}},\ A_2 = \frac{\left(r^{P} - 0.5h\right)}{\mathrm{Re}\,Scr^{P}},\ \text{and}\ A_3 = \frac{\left(r^{P} + 0.5h\right) + \left(r^{P} - 0.5h\right)}{\mathrm{Re}\,Scr^{P}}$$

$$A_4 = \frac{1}{\mathrm{Re}\,Sc} = A_{C5},\ \text{and}\ A_6 = \frac{2}{\mathrm{Re}\,Sc}.$$

The stability conditions for the rotational speed and concentration equations are calculated as before and we obtain respectively

$-\frac{\left(r^3\eta\right)_{i-1,j}}{h} \le \frac{\left(r^3 u\right)}{2} \le \frac{\left(r^3\eta\right)_{i+1,j}}{h}$ in equation (6.25), and $\frac{(\eta)_{i,j-1}}{k} \le \frac{w}{2} \le \frac{(\eta)_{i,j+1}}{k}$ in equation (6.26). Also we require $\frac{h(ru)\,\mathrm{Re}\,Sc}{\left(r^{P} + 0.5h\right)} \le 2$ in equation (6.27) and $(kw)\,\mathrm{Re}\,Sc \le 2$ in equation (6.28).

6.6 THE NUMERICAL CHECKS IN 3D FLOW MODELS

For axisymmetric flow in cylindrical polar co-ordinates we have three constraints on cylinder cavities which are stream function-vortivity, concentration and temperature equation constraints. These constraints are only second order in discretisation and evaluated by the trapezium integration rule over the solution area. Therefore the

numerical checks in general have been done for the vorticity-stream function over a cylinder where the inner radius is $a \le r \le b$ as follows

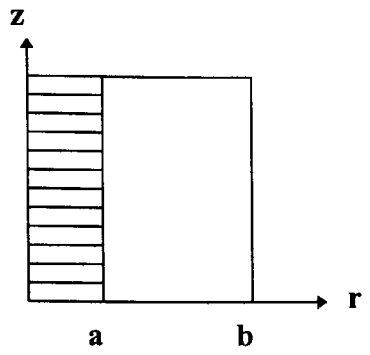

Figure 6.4; Diagram for concentric cylinder driven cavity flow

$$\iint_A \omega dA = \iint_A curlV_i dA \qquad 6.29$$

Applying Stokes' theorem to (6.29) we have

$$\iint_A \left(\frac{\partial u}{\partial z} - \frac{\partial w}{\partial r}\right) drdz = \int_a^b (U_T - U_B) dr + \int_0^h w dz, \qquad 6.30$$

where U_T and U_B represent top and bottom wall speeds respectively. The first integration on the right hand is zero in (6.30). Similarly the concentration constraint is taken as

$$\frac{\partial}{\partial t}\iint_A rCdA = \frac{\partial}{\partial t}\iint_A rCdrdz = \frac{\partial}{\partial t}\oint_{\delta A} r\frac{\partial C}{\partial n}. \qquad 6.31$$

Due to $\frac{\partial C}{\partial n} = 0$ on the boundaries, we have $\iint_A Cdrdz = c$ where c is constant value.

6.7 THE NUMERICAL SOLUTION OF THE FLUID PARTICLE EQUATIONS

The ordinary differential equations for the fluid particle in the cylindrical co-ordinate system (r,θ,z) are

$$\frac{d}{dt}\left(\underline{x}_i(t)\right) = V_i\left(\underline{x}_i(t)\right) \tag{6.32}$$

where $i = 1,2$, $x_1 = r$, and $x_2 = z$. The variable V_i is defined from the velocity components in the r and z direction respectively.

We have initial conditions $r(0) = r_0$ and $z(0) = z_0$.The velocity field is found numerically as explained previously by considering the velocity components in terms of a stream function in the r and z direction, so that $u = -\frac{1}{r}\frac{\partial \Psi}{\partial z}$ and $w = \frac{1}{r}\frac{\partial \Psi}{\partial r}$. We only sought the solution of this system for the unsteady case by using either simple explicit or Peaceman-Rachford methods. The pertinent equations are

$$\underline{x}_{i+1} = \underline{x}_i + \frac{\Delta t}{2}\left[V_i^0\left(\underline{x}_i\right) + V_i^N\left(\underline{y}_i\right)\right] \tag{6.33}$$

where $\underline{y}_i = \underline{x}_i + \Delta t V_i^0\left(\underline{x}_i\right)$. Then the Modified-Euler method, (6.33) is used as in section (3.13).

6.8 RESULTS FROM THE 3D CYLINDER DRIVEN CAVITY FLOW

We solve the time-dependent flow equations by using the simple-explicit method and Peaceman-Rachford methods. However, we present the Peaceman-Rachford solution results only as they are more accurate than the simple-explicit solutions. Furthermore we follow all types of fluid cases as in chapter 5. In fact, we deal with fluid behaviour in both Newtonian and non-Newtonian cases by using constant and variable shear-rate models. Consideration is given to three different cylinder cavity driven flows and the flow motion is generated by rotation of the walls. We first consider the convergence of the solution by comparing calculations for various grid widths denoted by h. Results have been evaluated near the top wall $(r = 0.4, z = 0.8)$ for the Newtonian and non-Newtonian fluids. fig(6.5) and (6.6) show results for the vorticity in both time-dependent and time-independent driven flow respectively and it is evident that convergence to 4 decimal places has been achieved at Re=10 as h decreases. In this case both Newtonian and Boger fluid take the same convergence values as shown in fig(6.5) and (6.6). Secondly we compared our results qualitatively and quantitatively with Pao[73] and it was seen that our results are in agreement with his results which can be seen in cylindrical driven flow case later.

The reader should note that the streamline plot results produced by this author in section 6.8 have been scaled by value of 100.

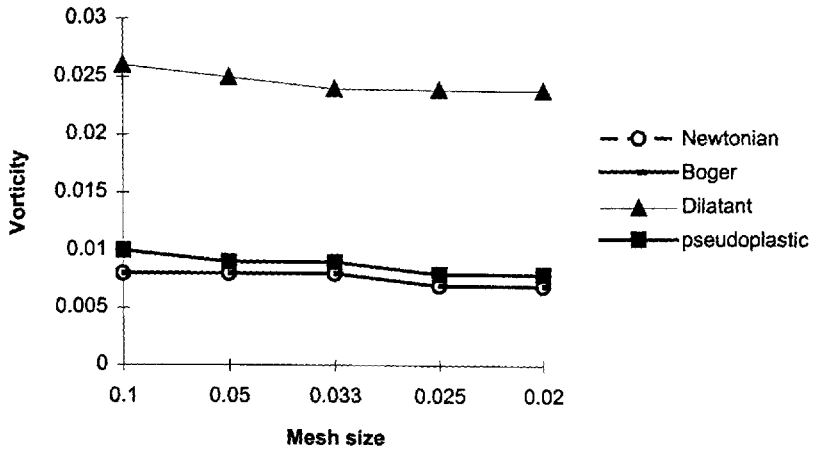

Figure 6.5 ; Convergence criterion for vorticity at Re=10 for time-dependent fluid flow

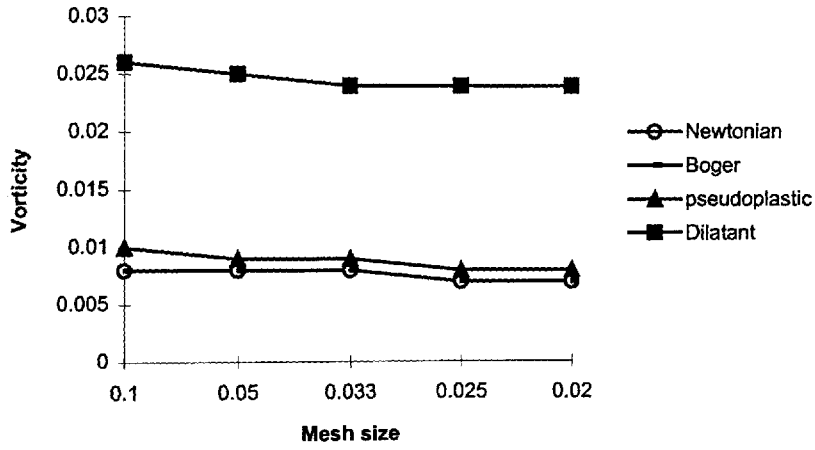

Figure 6.6 ; Convergence criterion for vorticity at Re=10 for time-independent fluid flow

We, therefore, presented our results 30x30 for the time-dependent and 40x40 for the time-independent flow. We solve our problems computationally in three categories as follows and some results which are generated in this chapter are entirely new.

i.Cylindrical Driven Cavity Flow,

ii.Concentric Cylinder Driven Cavity Flow,

iii.Free Surface Cylinder Driven Flow.

6.8.1 Cylindrical Driven Cavity Flow

Here flow is generated by wall movement such as top wall moving with a constant angular speed etc. We therefore produced results under the following headings,

i. Top and side walls rotating

ii.Two walls rotating in opposite direction

iii.Two walls rotating in same direction

iv.Top wall rotating

i. Top and side walls rotating

In this case the top and side walls rotate with positive angular velocity and the bottom wall is kept stationary. In this particular case we made to compare our solution with Pao[73], shown in fig(6.10)-(6.12). He produced some solutions for 'small' Reynolds number as well as for 'high' Reynolds number in both steady and unsteady cases . Our results for flow pattern and circulation contours are in agreement with his solution both qualitatively and quantitatively. For steady state solutions we produce Newtonian and non-Newtonian results with Re up to 300. With Re=1 we have one vortex and its centre is located approximately at (0.6. 0.4) as shown in fig(6.7) while as Reynolds number increases the vortex gets bigger and its centre moves to the right hand side bottom corner due to the inertial effect fig(6.8). The corresponding circulation ($\Gamma = r^2\Omega$) is presented at Re=100 and it can be seen that the circulation increases outward from the axis, as shown in fig(6.9). We therefore present this behaviour at

Re=1 and Re=100 for flow pattern and circulation contours as follows. In this case we found that all type of fluids produced similar behaviour at the same Reynolds number, with constant viscosity as well as variable viscosity, except for small differences due to the non-Newtonian nature of the fluids itself. For time dependent flows we found results from each type of fluid in agreement for both viscous and viscoelastic cases. They are also in agreement with their steady state counterpart solutions at Re=1 and Re=100.

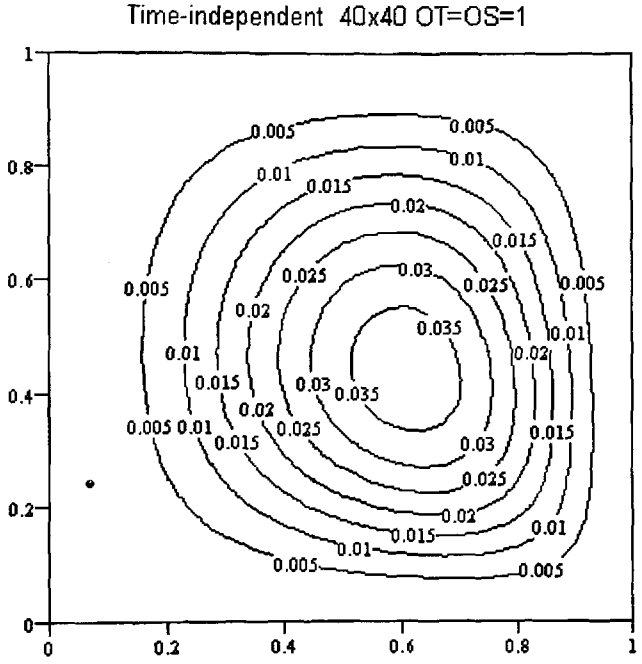

Figure (6.7) ; Streamline contours for Newtonian fluid at Re=1

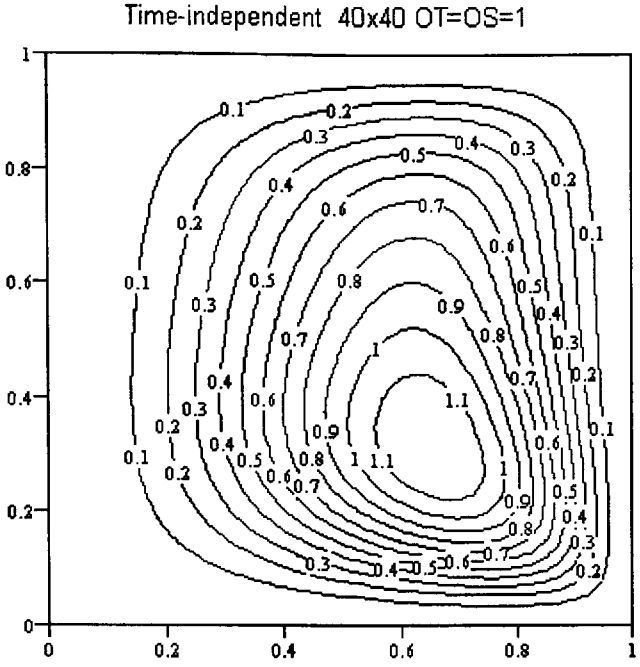

Figure (6.8) ; Streamline contours for Newtonian fluid at Re=100

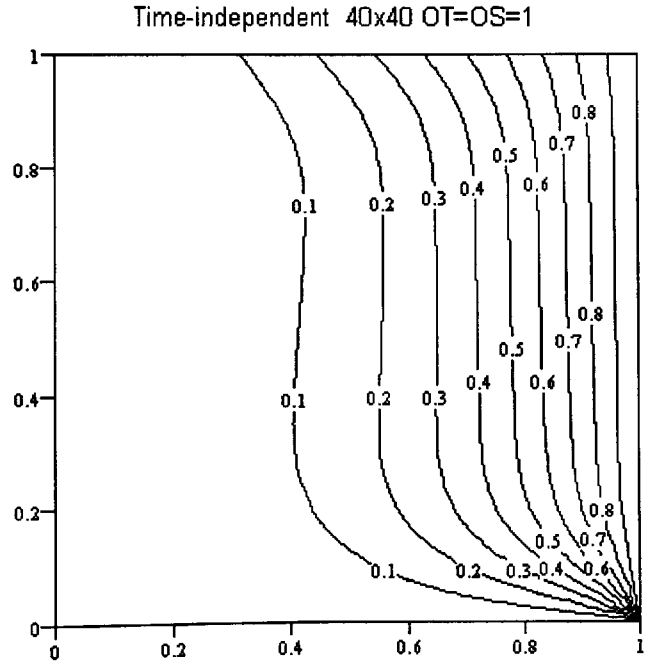

Figure (6.9) ; Circulation contours for Newtonian fluid at Re=100

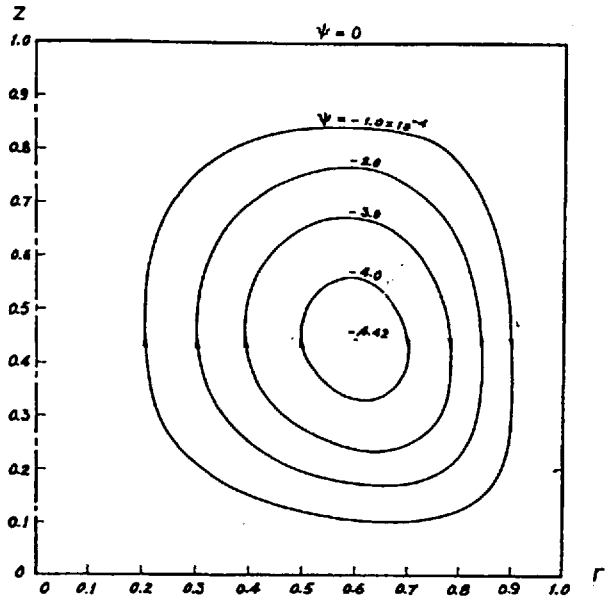

Figure (6.10) ; Streamlines contours for Newtonian fluid by Pao[73]at Re=1

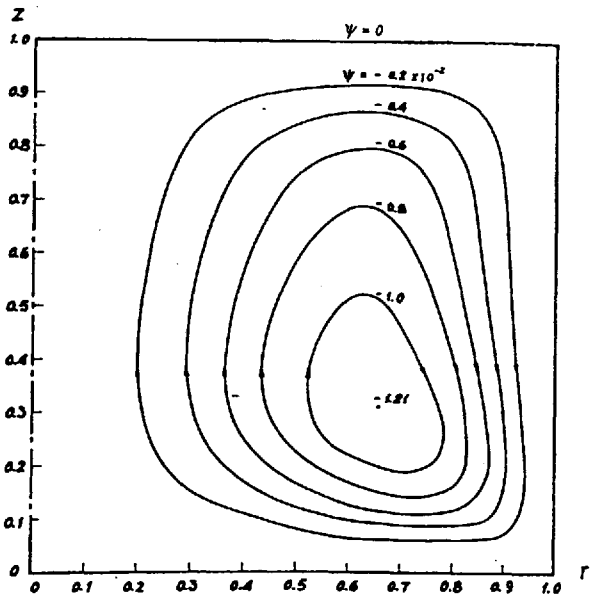

Figure (6.11) ; Streamlines contours for Newtonian fluid by Pao[73]at Re=100

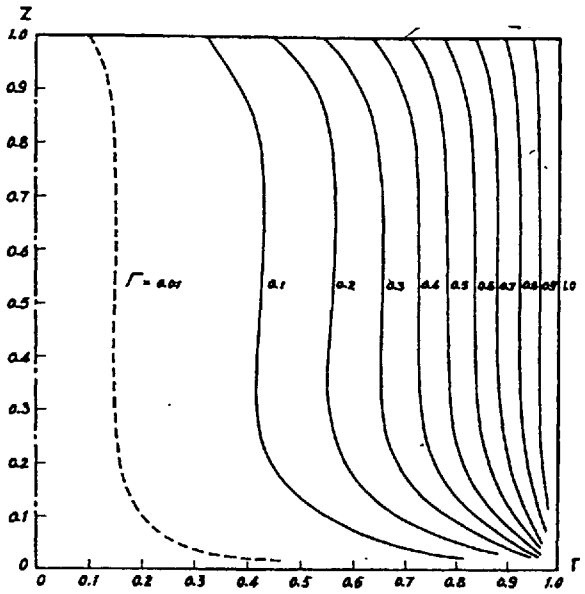

Figure (6.12) ; Circulation contours for Newtonian fluid by Pao[73]at Re=100

ii.Two walls rotating in opposite direction

In this case the flow is generated by top and bottom walls. Therefore the side walls are held fixed. Similarly we produced results with various Reynolds and Weissenberg numbers for both viscous and viscoelastic fluids. It was seen that two main vortices are produced, being symmetrical mirror images of each other. The streamlines are symmetrical about the cavity's horizontal mid-line, the vortex centres being found at approximately (0.65, 0.25) and (0.65, 0.75) shown in fig(6.13) at Re=1. In this case constant and variable viscosity fluids produced almost similar results except the viscoelastic dilatant fluid. Here the vortex centres were found to move to the corners and streamlines become larger due to inertia effect as shown in fig(6.14).

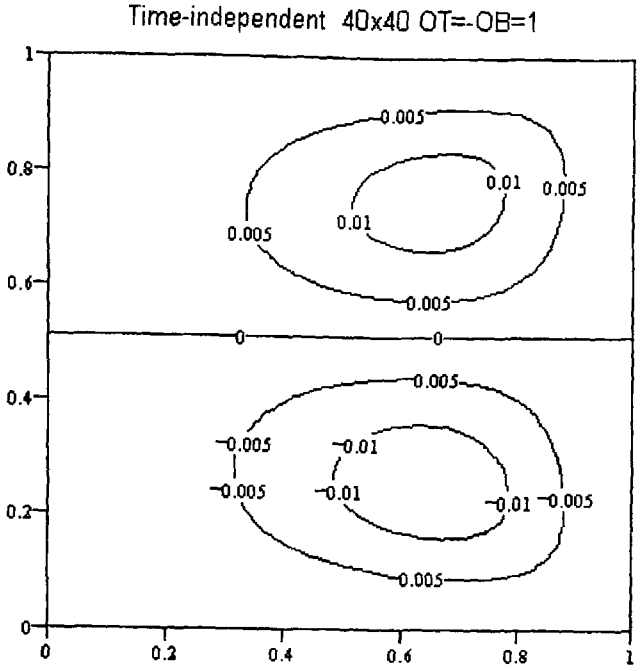

Figure (6.13) ; Streamline contours for Boger fluid at Re=1

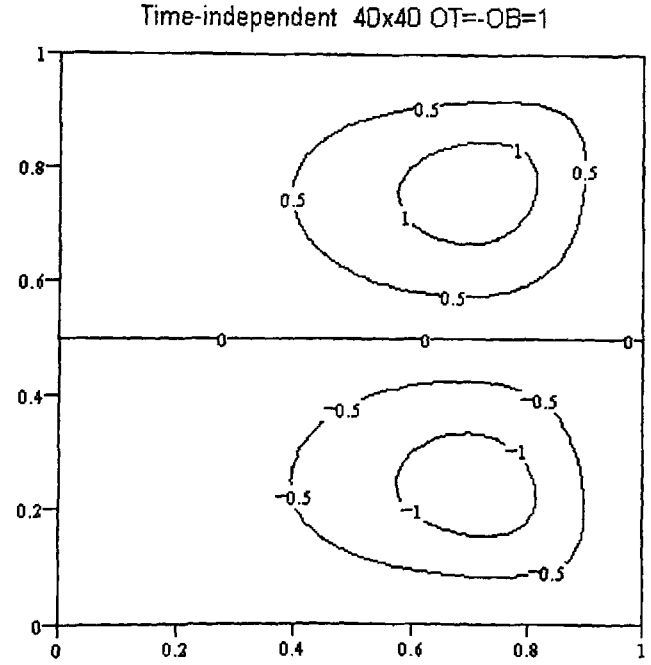

Figure (6.14) ; Streamline contours for viscoelastic dilatant fluid at Re=1

For a time dependent solution we usually obtained a steady solution very rapidly at low Reynolds number. Similarly when Re increases vortex centres move to the corners.

iii.Two walls rotating in same direction

In this case the fluid motion is generated by two walls where the top and bottom wall rotate in a clockwise direction with constant angular velocity and the side wall is kept fixed. We produced results with Reynolds number up to 300 for the steady state flow equations. At low Reynolds number, for example Re=1 two main vortices are produced, being symmetrical about the cavity's horizontal mid-line and vortex centres are located at (0.65, 0.2) and (0.65, 0.8) from bottom and top walls of the cavity respectively as shown in fig(6.15). Both viscous and viscoelastic fluids produced almost similar results quantitatively and quantitatively.

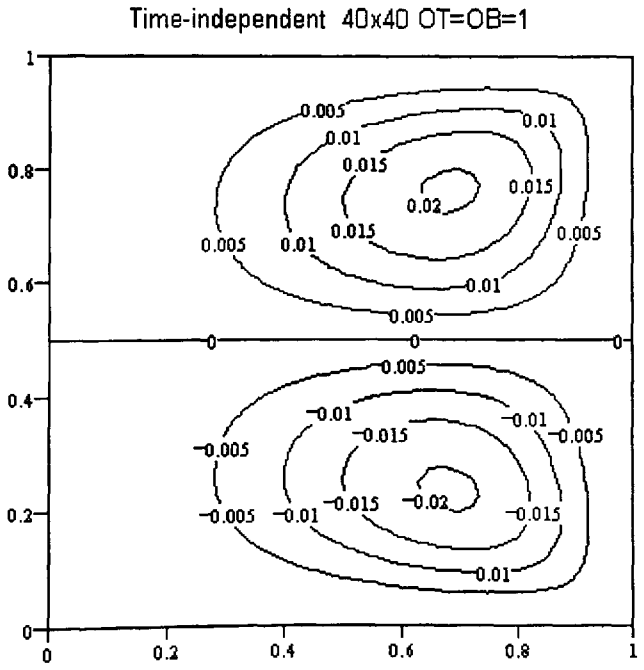

Figure (6.15) ; Streamline contours for viscoelastic pseudoplastic fluid at Re=1

As Re increases the vortex centres move to the corners and are located at (0.7, 0.2) and (0.7, 0.8) with streamlines being symmetrical about the cavity horizontal mid-line and become more compact due to inertia effect, shown in fig(6.16)

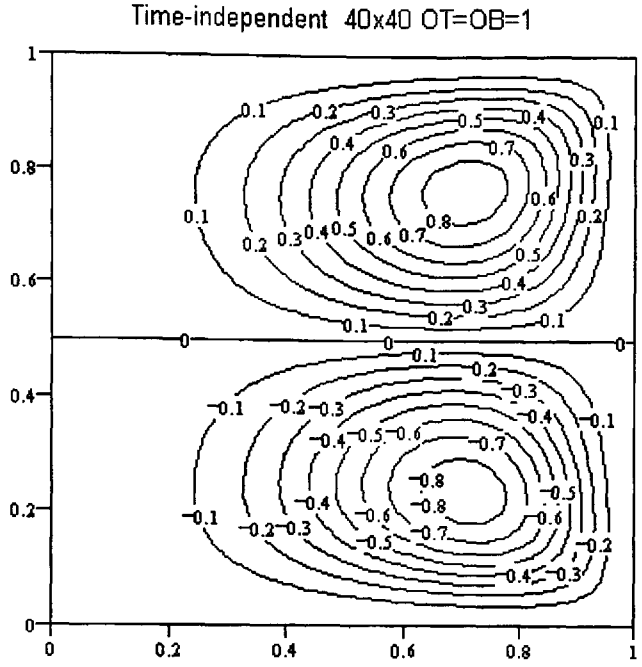

Figure (6.16) ; Streamline contours for Newtonian fluid at Re=100

However in the viscous and viscoelastic fluid cases all results are in agreement with the unsteady state solution when compared with their steady counterparts. We illustrated in fig(6.17) viscoelastic pseudoplastic fluid behaviour at Re=100 where it can be seen that two main vortices produced and the streamlines are symmetrical about the cavity's horizontal mid-line. Vortex centres are located at (0.7, 0.2) and (0.7, 0.8) as happened in the steady state case.

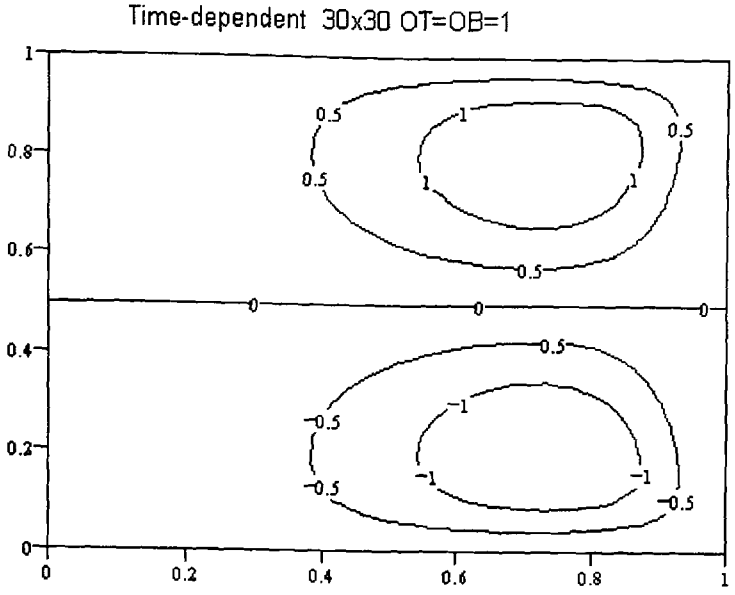

Figure (6.17) ; Streamline contours for viscoelastic pseudoplastic fluid at Re=100

iv.Top wall only rotating

In this case the flow is generated by rotation with a constant angular velocity on the top wall and the rest of the walls being kept stationary. In the steady flow case we produce results for various Reynolds number up to 300 in both viscous and viscoelastic fluid cases. We saw that in both cases the flow exhibited similar behaviour. We have one vortex which moves to the right top corner. Fig(6.18) shows that one main vortex produced and the vortex centre is located at (0.6, 0.7) at Re=1. The streamlines are more circular around the vortex centre but they become 'flatter' near the cavity's wall. Fig(6.19) shows that as Re increases the vortex is found to move to the top corner and its centre located at (0.7, 0.7) at Re=100. In this case the streamlines become larger due to inertia effect much stronger than Re=1. It can be seen that there is a more pronounced inertial effect around the top corner vertically as well as horizontally. In the case of the unsteady flow solutions we saw that both

viscous and viscoelastic fluid flow produce the same behaviour and they are very similar to the steady state solution.

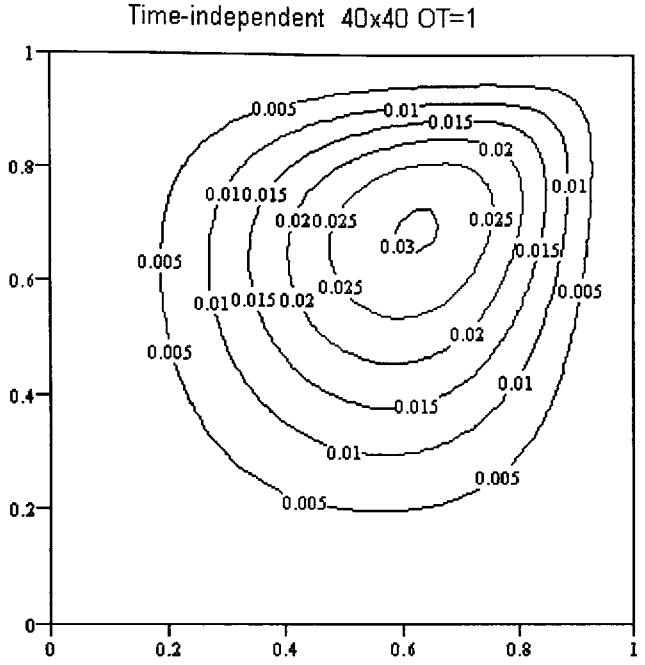

Figure (6.18) ; Streamline contours for viscoelastic pseudoplastic fluid at Re=1

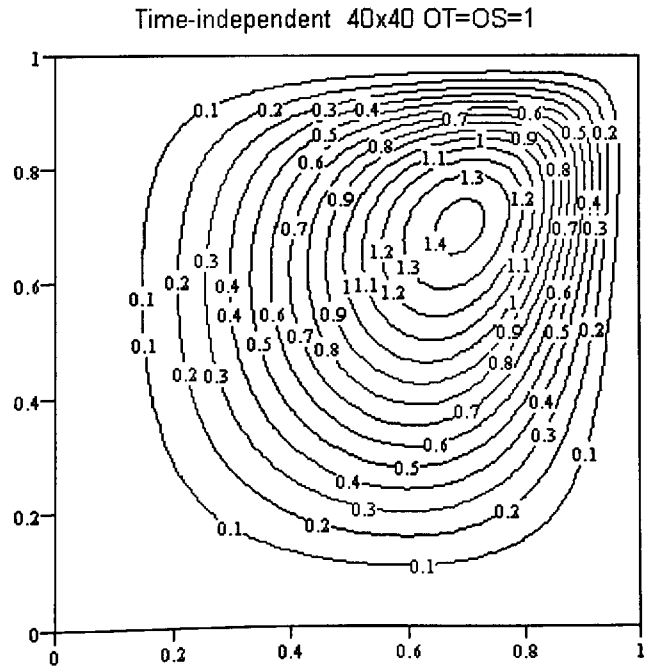

Figure (6.19) ; Streamline contours for viscoelastic dilatant fluid at Re=100

6.8.2.Concentric Cylinder Driven Cavity Flow Problem

In this section the fluid flow is generated by two concentric cylinder walls rotating with constant angular velocity. Similarly we produce flow results by considering the same conditions which have been explained before. We consider four different cases:

i.Two walls rotating in same direction with constant angular velocity,

ii.Two walls rotating in opposite direction with constant angular velocity,

iii.Four walls rotating with constant angular velocity,

iv.Top wall rotating with constant angular velocity.

We produce results in this section for both the viscous and the viscoelastic case by solving the steady state and the unsteady state flow equation.

i.Two walls rotating in same direction

In this section the fluid flow is generated by top and bottom walls rotating with constant angular velocity in a clockwise direction and the side walls being kept stationary. We solve the flow equation in both the steady and the unsteady cases. However a more accurate solution is found by using the A.D.I. method as appeared to simple explicit for the unsteady flow equation. For the steady state case we produced results with Reynolds number up to 300 with constant shear-rate and Reynolds number up to 300 with variable shear-rate. We saw that at Re=1 all types of fluid produced a pair of equal mirror image and the symmetry line is always maintained. For Newtonian and Boger fluid flow the inertial effect is stronger. We present a results for the steady state flow in fig(6.20). It can be seen that vortex centres are located approximately at (0.75, 0.0.2) and (0.75, 0.8) with streamlines being symmetrical about the cavity's vertical and horizontal mid-lines.

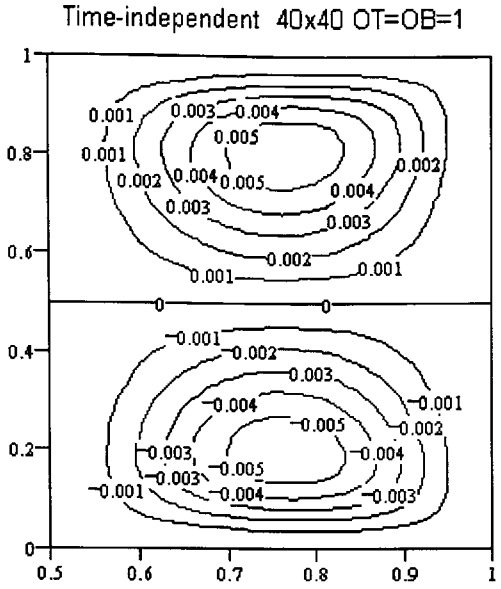

Figure (6.20) ; Streamline contours for Newtonian fluid at Re=1

As the Reynolds number increases the inertial effect increases and both vortices move to the corner. They also change their shape so that while they look more 'oval' at Re=1 they almost take a 'square' shape at Re=300 as shown in fig(6.21). Their vortex centres are located at (0.82, 0.2) and (0.82, 0.8). This behaviour was observed in both cases.

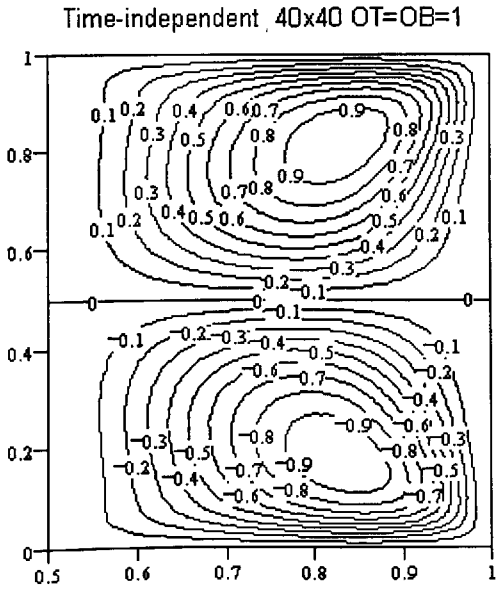

Figure (6.21) ; Streamline contours for viscoelastic pseudoplastic fluid at Re=300

For the time dependence case similar behaviour is observed in the viscous and viscoelastic cases as with their steady state counterparts. At low Reynolds number, for example at Re=1 two mirror images vortices are produced and vortex centres are located at (0.75, 0.15) and (0.75, 0.85) shown in fig(6.22). As Re increases the streamlines become more compact and for the Newtonian fluid the vortex centres are located approximately at (0.75, 0.15) and (0.75, 0.85) in the fluid domain, as shown in figure(6.23).

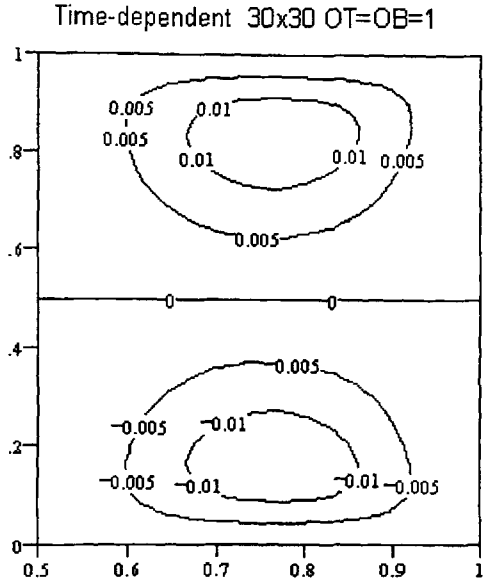

Figure (6.22) ; Streamline contours for viscoelastic pseudoplastic fluid at Re=1

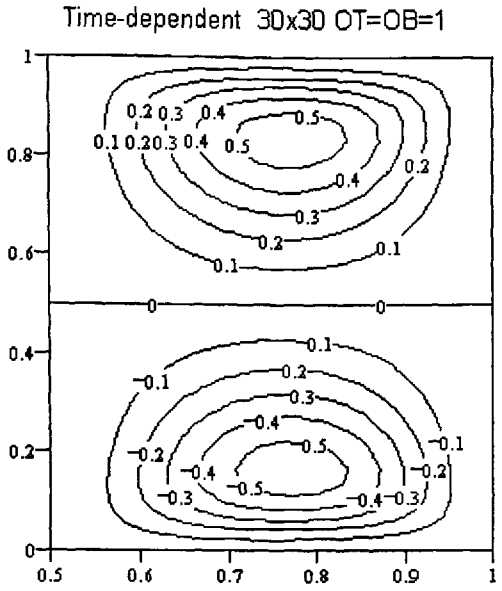

Figure (6.23) ; Streamline contours for Newtonian fluid at Re=100

ii.Two walls rotating in opposite direction

In this section the fluid flow is generated by top and bottom walls rotating with constant angular velocity with the top wall rotating in a clockwise direction and the bottom wall rotating in the opposite direction. In the case of the steady state flow equation the solutions exist at various Reynolds and Weissenberg numbers. In this case we have seen different behaviour for each fluid case. With Re=1 we have similar behaviour results for all type of fluid for Newtonian and non-Newtonian fluids in both the viscous and the viscoelastic case as shown in fig(6.24). A pair of equal and symmetric vortices are located in the top and bottom halves of the cavity and their centres are located at (0.75, 0.2) and (0.75, 0.8) from bottom and top walls of cavity respectively.

As the Reynolds number increases the vortices become more compact and change their shape and position in each half of the flow domain. Their centres also change

due to the inertial effect and are located at (0.85, 0.2) and (0.85, 0.8) as shown in fig(6.25).

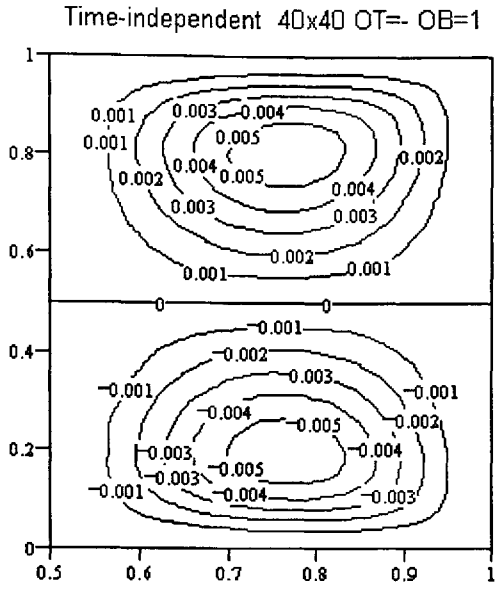

Figure (6.24) ; Streamline contours for Newtonian fluid at Re=1

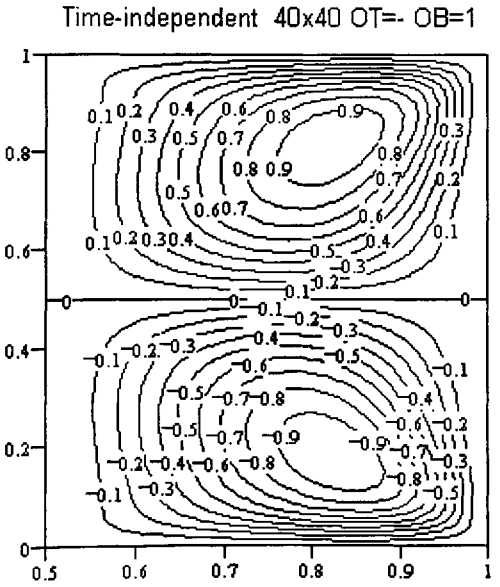

Figure (6.25) ; Streamlines contours for viscoelastic pseudoplastic fluid at Re=300

In the case of the time-dependent we have the same results for each flow in viscous and viscoelastic cases respectively. However the main difference in the time-

dependent case from the time-independent case is that of a more pronounced inertial effect that occurs with the Newtonian and Boger fluid at Re=1 and Re=100. Fig(6.26) shows that two main vortices produced are symmetrical about the cavity's horizontal mid-line. The vortex centres are located at approximately (0.8, 0.15) and (0.8, 0.85) at Re=1.

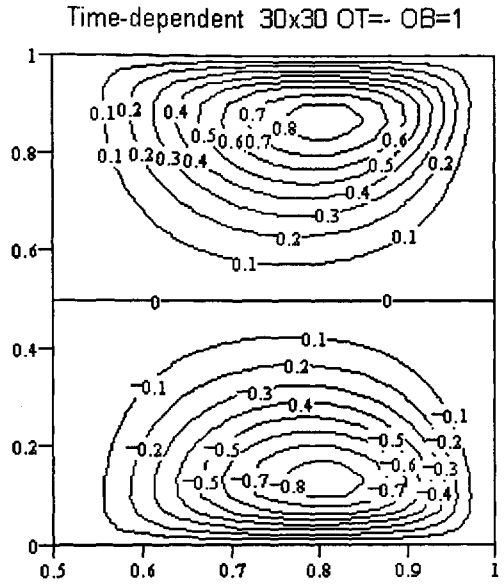

Figure (6.26) ; Streamline contours for viscoelastic pseudoplastic fluid at Re=1

iii.Four walls rotating

In this section the fluid motion is generated between concentric cylinders by four rotating walls with constant angular velocity. We produced results for both viscous and viscoelastic fluids in both the steady state and the transient cases.

For the steady state solution we always have two equal rotating vortices and the symmetry line is maintained at Re=1 for Newtonian and non-Newtonian fluid in both cases. When the Reynolds number increases we were unable to obtain results for a dilatant fluid, whereas we have results for pseudoplastic and Newtonian fluids. For example at Re=100 pseudoplastic, Newtonian and Boger fluids exhibit similar

qualitative behaviour although Newtonian flow is more compact than pseudoplastic at Re=1. In this case we present two time-dependent solution as follows. Fig(6.27) shows that two main vortices are produced and the streamlines are symmetrical about the cavity's vertical and horizontal mid-lines. The vortex centres are located at (0.75, 0.25) and (0.75, 0.75) from bottom and top walls of the cavity respectively.

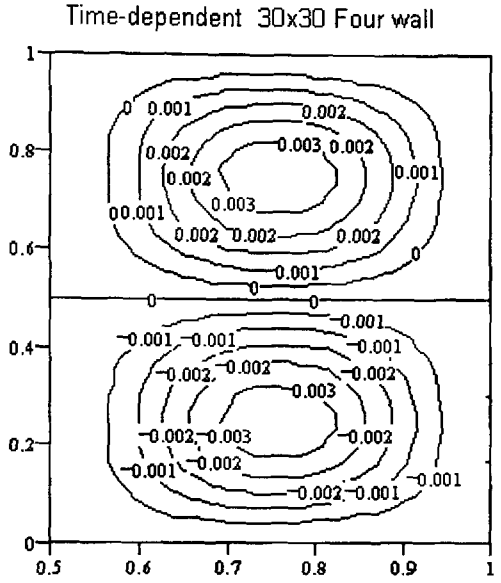

Figure (6.27) ; Streamline contours for dilatant fluid at Re=1

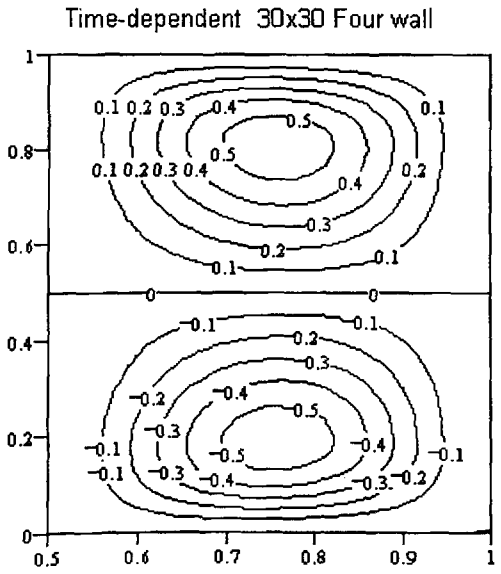

Figure (6.28) ; Streamline contours for viscoelastic pseudoplastic fluid at Re=100

However as Re increases the streamlines become more compact and larger and a pair of vortices are located at (0.75, 0.2) and (0.75, 0.8) in the fluid as shown in fig(6.28). In the case of the time-dependence, similar solutions were found for viscous and viscoelastic fluids at the Reynolds number 1 and 100.

iv.Top wall rotating with constant angular velocity

We have solved the concentric cylinder driven cavity flow numerically, and the fluid motion is generated between concentric cylinders by the top wall rotating for viscous and viscoelastic fluids. We consider the Reynolds number up to 300 in both cases and produced results for Newtonian and a variety of non-Newtonian fluids. With Re=1 we found one vortex which was located nearer the top wall rather than bottom wall of the cavity. It is located at (0.75, 0.8) in both cases, and the inertial effect is seen to be very strong as shown in fig(6.29). As the Reynolds number increases the vortex seems to move towards the top. For example at Re=100 the vortex centre is located at (0.8, 0.85) in both the steady state and the unsteady cases. With Re=300 the vortex gets bigger due to the inertial effect and fills up more of the flow domain than at Re=1. Then its centre is located near the top wall at (0.8, 0.8) shown in fig(6.30). Similar behaviour is observed in the case of the steady state solution.

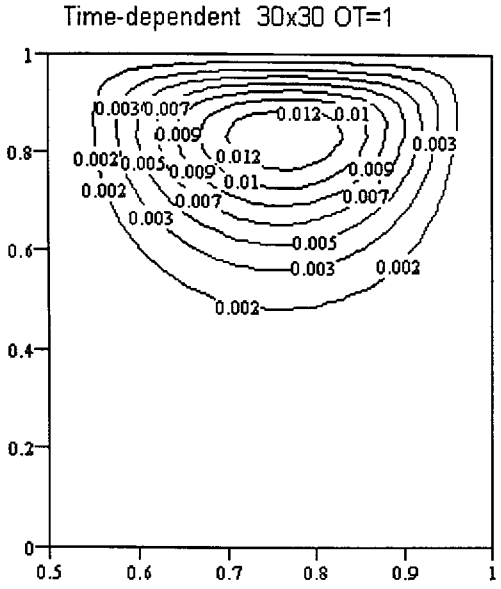

Figure (6.29) ; Streamline contours for viscous pseudoplastic fluid at Re=1

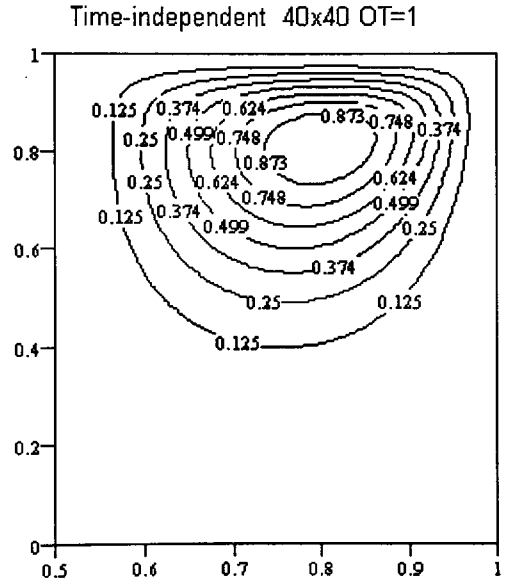

Figure (6.30) ; Streamline contours for Newtonian fluid at Re=300

6.8.3. Free Surface Cylinder Driven Flow

In this section we consider a whole cylinder bounded by three sides except for the top that is a flat free surface. Therefore flow is generated in two different cases; as the right wall rotates, or the bottom wall rotates. In either case the other sides are

stationary. We shall present the results firstly by considering the flow generated by the bottom wall rotating.

i.Bottom wall rotating

We found that in both the steady state and the unsteady state cases flow exhibited the same kind of behaviour for the same Reynolds number. In particular at Re=1 Newtonian and non-Newtonian flow results look similar, and we have one vortex whose centre is located at (0.6, 0.3) as shown in fig(6.31). The streamlines are more circular around the vortex centre and the inertial effect is much weaker for the pseudoplastic case than the other cases considered. Similarly at Re=100 we have similar behaviour in both cases but the vortex centre moves to the bottom right corner as expected. While the Reynolds number increases the vortex becomes 'rectangular' vertically as shown in fig(6.32), and its centre is located at (0.75, 0.25) at Re=100. We therefore present two figures as follows for steady flow at Re=1 and Re=100 for the Newtonian and pseudoplastic flow respectively.

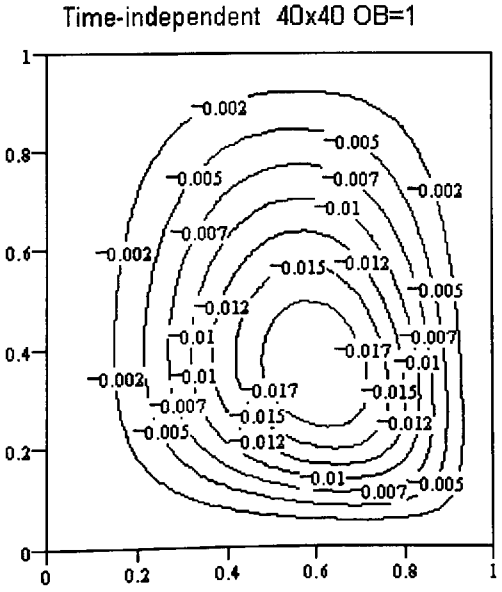

Figure (6.31) ; Streamline contours for Newtonian fluid at Re=1

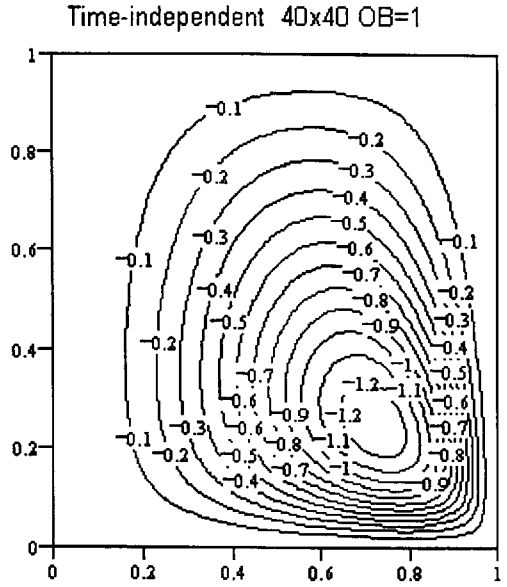

Figure (6.32) ; Streamline contours for viscous pseudoplastic fluid at Re=100

For the time-dependent case for all type of fluids results are in agreement with their steady state solution counterparts at Re=1 and Re=100. At Re=100 we found that the vortex centre moves to the right bottom corner and it is very compact around the corner. The vortex shape looks more circular around the vortex centre and its centre is located at (0.75, 0.25) as shown in fig(6.33).

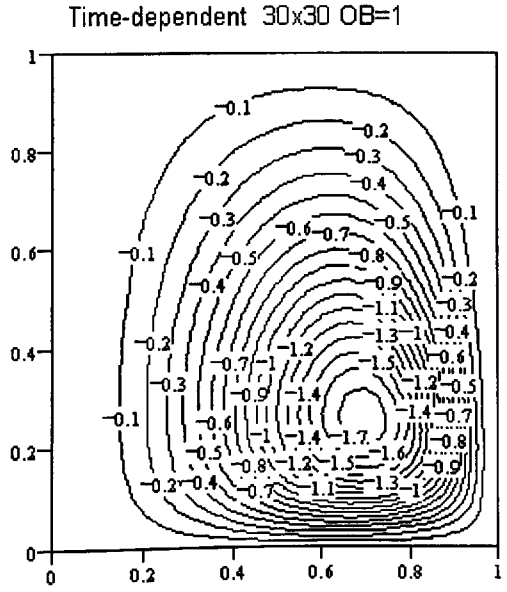

Figure (6.33) ; Streamline contours for viscous dilatant fluid at Re=100

ii.Right wall rotating

In this case the flow is generated by the right wall rotating. We have different behaviour for each case so that although one vortex appears in the flow domain with various Reynolds numbers in case of time-independence, we have two vortices for the time-dependent case.

For the steady state case one main vortex is produced and vortex centre is located at (0.6, 0.4) as shown in fig(6.34). As Re increases the vortex centre is found to move to the right bottom corner and its centre is located at (0.7, 0.2) as shown in fig(6.35).

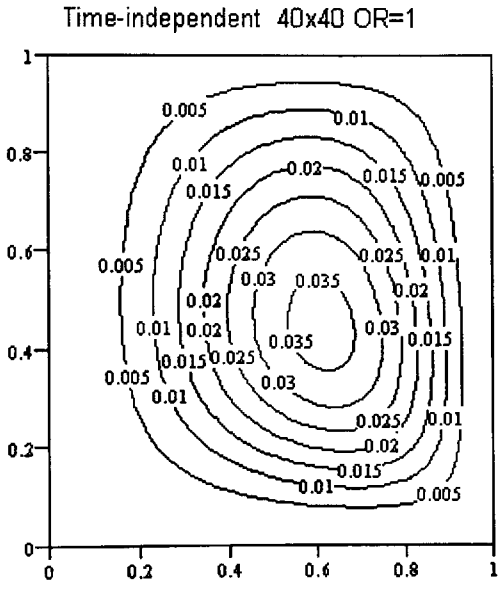

Figure (6.34) ; Streamline contours for Newtonian fluid at Re=1

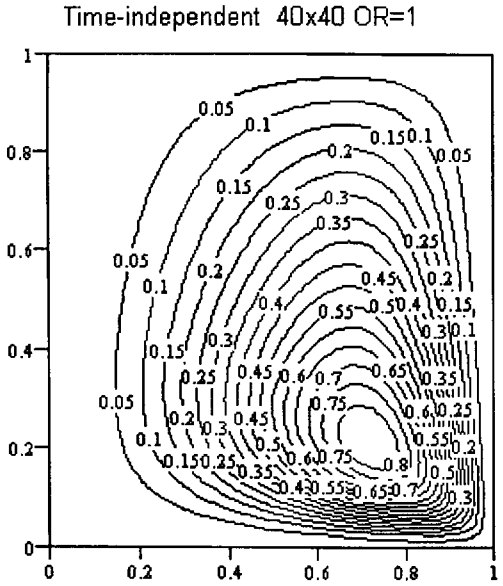

Figure (6.35) ; Streamline contours for viscous pseudoplastic fluid at Re=100

We have two vortices solution; each vortex is located in the half top and bottom of the cavity. As shown in fig(6.36) and (6.37) for time-dependent flow the symmetry between two vortices is lost. Fig(6.36) shows that two main vortices are produced and vortex centres are located at (0.7, 0.3) and (0.7, 0.8) at Re=1. They change their location and their centres move toward the corners and inertial effect becomes stronger though increasing Re as shown in fig(6.37).

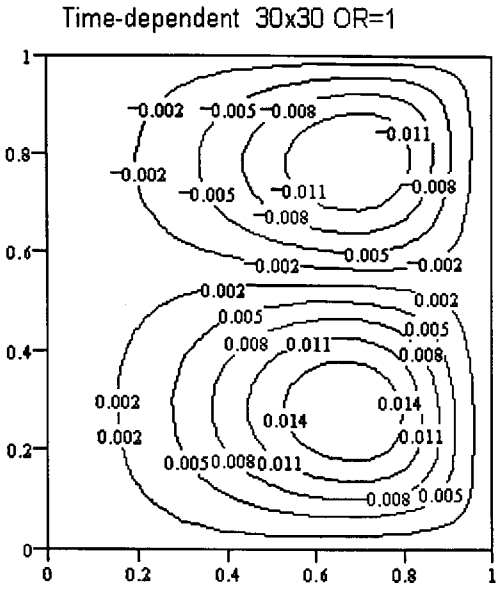

Figure (6.36) ; Streamline contours for viscoelastic pseudoplastic fluid at Re=1

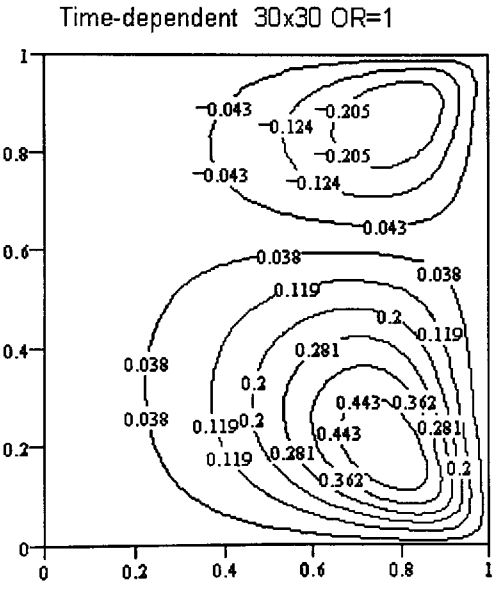

Figure (6.37) ; Streamline contours for viscous pseudoplastic fluid at Re=100

6.9. CONCENTRATION RESULTS OF THE VARIOUS CYLINDER DRIVEN CAVITY FLOWS

We consider the same problem for cylinder driven cavity flow in two different categories namely whole cylinder and concentric cylinder flow. We similarly assume that the dye initially occupies in the top half of the cavity region, and there is no chemical reaction within the flow. Our main consideration is to solve the concentration equation numerically in the cylinder configuration and then compare our results with those of the 2D cavity. We have two main parameters which are Reynolds number Re and Schmidt number Sc. The Schmidt number is usually taken as 50 and the Reynolds number is taken as 1, 10 and 100.

6.9.1.Cylinder Driven Cavity Flow

Here we consider the concentration contours as generated in two cases such as two walls rotating in the same direction, as well as in opposite directions, respectively. In this case we have no other authors with whom to compare our results with this geometry. Here initially the coloured fluid is injected into the cavity region while the fluid is rest and its quantity is measured as 4 for the geometry considered due to the average value throughout the geometry is being set as 1. We usually find the viscoelastic fluid flow results to be almost indistinguishable from viscous flow for the same Reynolds number.

With Re=1 we have a linear distribution of the colour band horizontally and this behaviour is seen in all types of fluid cases as shown in fig(6.38). When the Reynolds number increases the advection force begins to dominate the flow so that the colour band is spread out quickly about the mid of the cavity horizontally. This behaviour

can be seen in fig(6.39) at Re=10. Therefore the advection term firmly dominates the flow and the colour band spreads out between streamlines in the centre region. The coloured band is nearer the left wall as there is small circulation near the wall shown in fig(6.40).

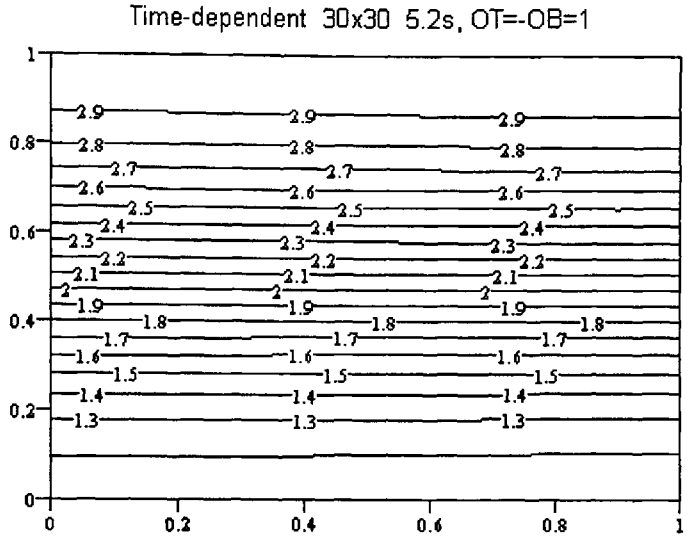

Figure (6.38) ; Concentration contours for Newtonian fluid at Re=1, Sc=50

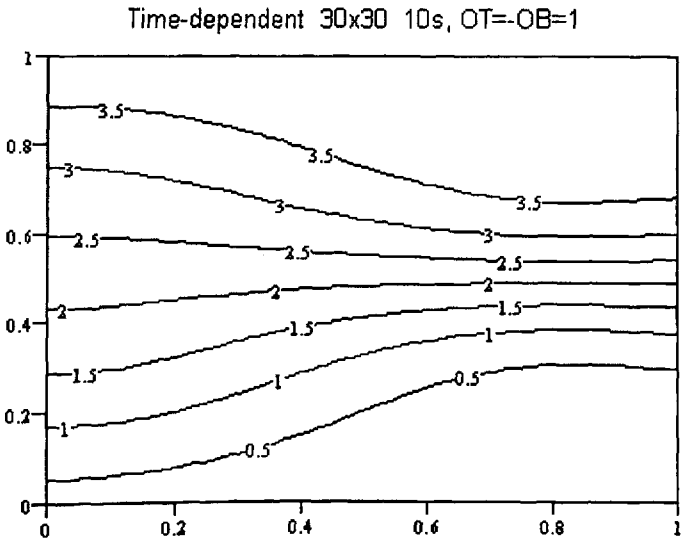

Figure (6.39) ; Concentration contours for viscoelastic dilatant fluid at Re=10, Sc=50

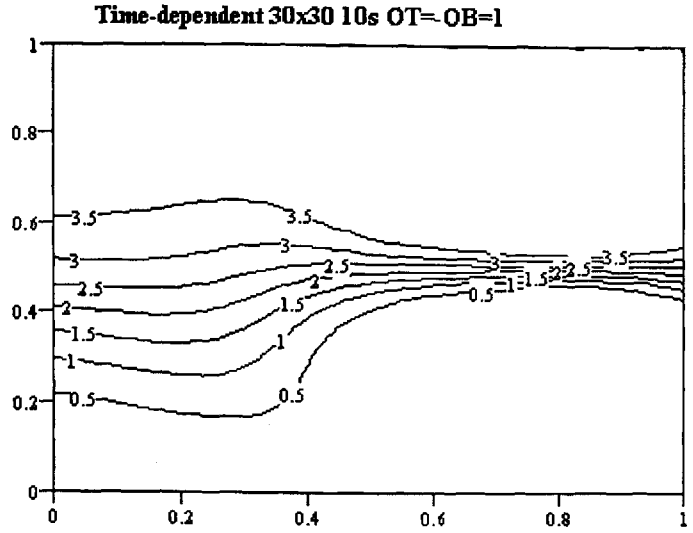

Figure (6.40) ; Concentration contours for viscoelastic pseudoplastic fluid at Re=100, Sc=50

In the case of two walls rotating in same direction with constant angular velocity we have results for all type fluid cases at Re=1, 10 and 100. For Re=1 we again have a linear distribution of the colour band horizontally due to small secondary flow but in this case it seems to be more compact than previously. Also at Re=10 the advection force becomes dominant but the separation of the colour band covers a larger area than in the previous case as shown in fig(6.41). With Re=100 the advection force dominates the flow therefore the colour band is quickly spread out between the streamlines in the centre region as shown in fig(6.42). It is also slightly more spread out near the left wall as the circulation is weaker there for the Newtonian fluid.

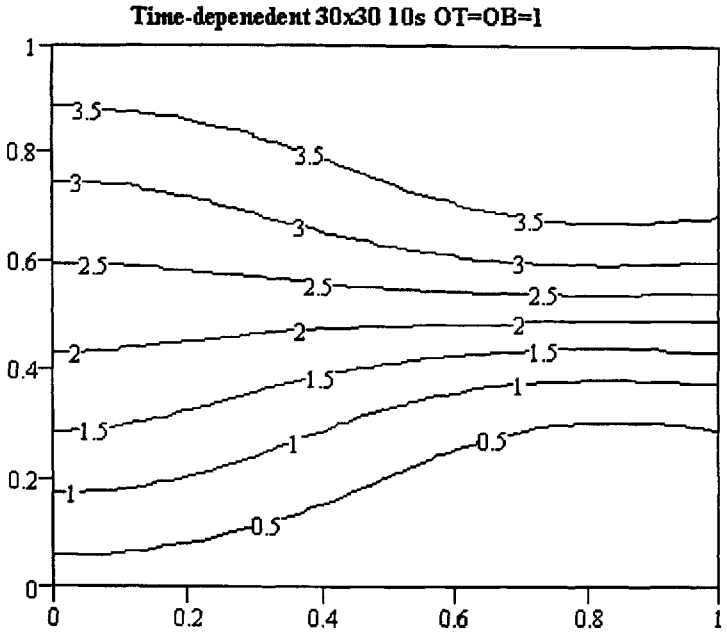

Figure (6.41) ; Concentration contours for viscous dilatant fluid at Re=10, Sc=50

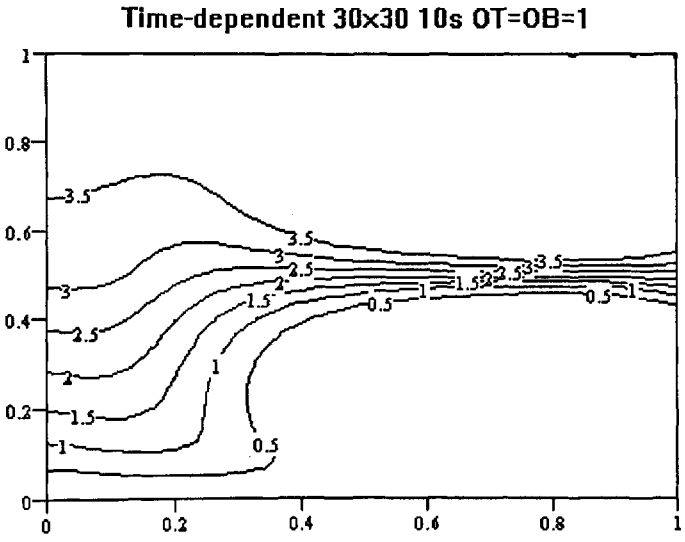

Figure (6.42) ; Concentration contours for Newtonian fluid at Re=100, Sc=50

6.9.2. Concentric Cylinder Driven Cavity Flow

In this section we similarly undertake the concentration problem by considering two walls rotating in same direction and also in opposite directions. We find that there is not much qualitative difference between the viscous and viscoelastic flow propagation

in the flow domain. The dye is similarly injected into the flow domain while the fluid is at rest but in this case its quantity is measured as 16/3 because the average value throughout the geometry set as 1. We produce results at Re=1, 10, and 100 when Sc=50. As the two walls rotate in the same direction we have a linear distribution horizontally of the colour band throughout the flow region. Similarly as the Re number increases the advection term dominates the flow and at Re=100 the colour is highly dispersed in the centre region and it usually follows the flow. Moreover the colour band is spread out slightly more due to small diffusion, where the circulation is weaker.

We illustrate some figures at Re=1, 10 and 100 in fig(6.43) - (6.46). Similarly at Re=100 we see that in the case of the non-Newtonian fluid the colour spreads out more quickly near the left wall due to non-Newtonian nature of the fluid itself.

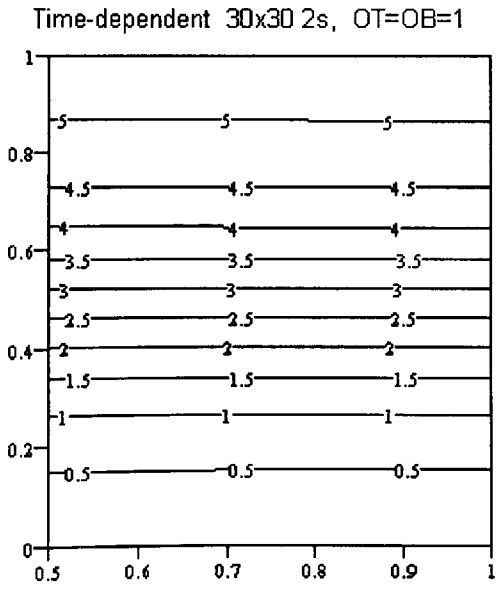

Figure (6.43) ; Concentration contours for viscous dilatant fluid at Re=1, Sc=50

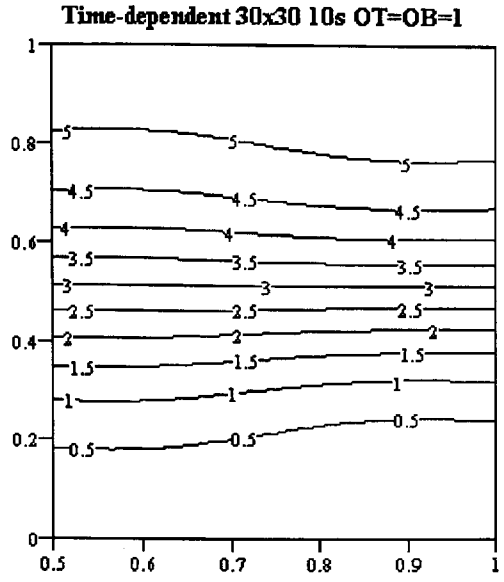

Figure (6.44) ; Concentration contours for viscous pseudoplastic fluid at Re=10, Sc=50

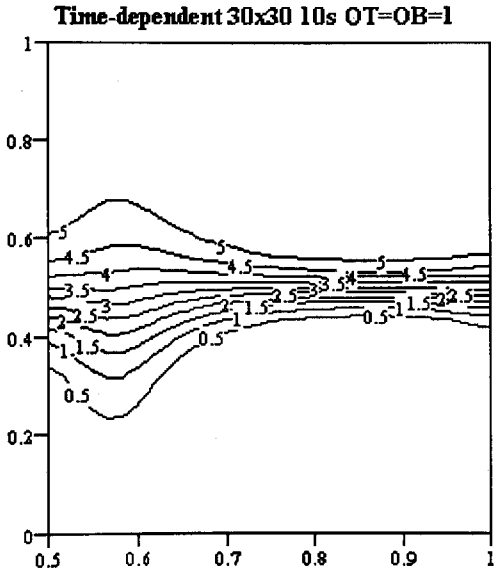

Figure (6.45) ; Concentration contours for viscous pseudoplastic fluid at Re=100, Sc=50

In the case of the two walls rotating in opposite we still have a linear distribution of the colour in the flow domain at Re=1 in both viscous and viscoelastic cases with constant and variable viscosity since there is small secondary flow. A similar distribution is observed at Re=10 and Re=100 shown in fig(6.46) and (6.47). With Re=100 the Boger fluid colour is spread out more quickly near the left wall than in the

previous case. However for the non-Newtonian fluid the concentration contours follows the flow pattern shape and the band spreads out more quickly in the centre region.

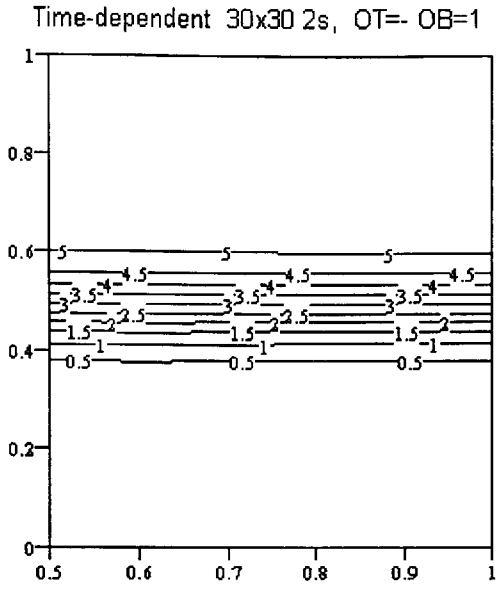

Figure (6.46) ; Concentration contours for Newtonian fluid at Re=1, Sc=50

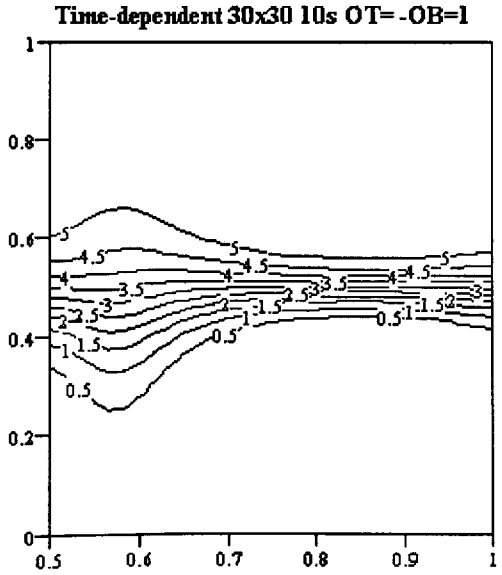

Figure (6.47) ; Concentration contours for Boger fluid at Re=100, Sc=50

6.10 PARTICLE PATHS AND DISCONTINUOUS PERIODIC 3D CAVITY FLOW

In this section we seek particle paths of the fluid generated by a discontinuous periodic motion as the top and bottom walls of the cylinder rotate with periodic motion as shown in figure (6.48). Although this motion is related to a mixing process, we only deal with particle paths of the flow fluid and omit an analysis of chaotic motion. We consider the fluid motion in two different cases when the flow motion is generated in a whole cylinder as well as in concentric cylinder geometries. This is shown in figure (6.48) for up to four periods of motion. The solution of the flow then depends on either the period of motion (**T**) or the Reynolds and Wi numbers. Initially the top wall moves with period **T.** Whenever the end of cycle is reached the top wall stops and the bottom wall starts moving in same direction as the top wall with the same time period. The cycle is repeated until a set time has elapsed. We usually give 100 seconds of simulation time to find the particle paths with the period of motion **T** usually taken as 2.

In this case we do not have any studies about the fluid particle paths to compare, so we generate some novel solutions for viscous and viscoelastic fluids. We also use various Re values to see how the system's behaviour is changed as the inertial force increases. Results are presented for fluid particle paths in (r,z) cylindrical co-ordinate system of the cylinder cavity.

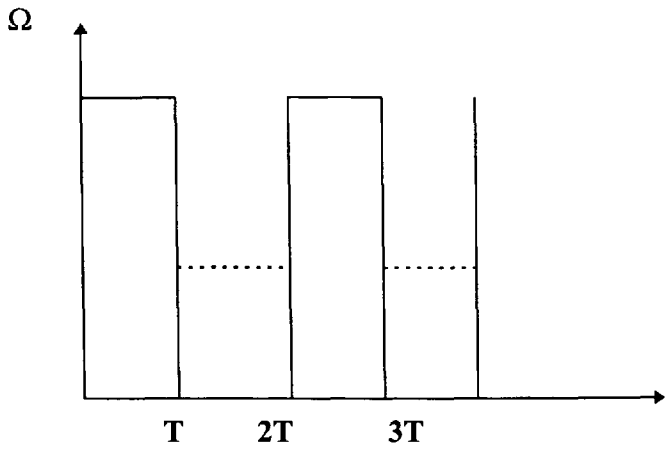

Figure (6.48) ; The diagram of the Periodic motion

We consider three particles which are initially located in the mid-cavity vertical line equally spaced, for example $(r = 0.5)$ of the cylinder driven flow domain.

6.10.1. The Particle Paths of the Cylinder Driven Cavity Flow

In this case both viscous and viscoelastic fluid results are in agreement for the Newtonian and Boger fluids at Re=10, and the results are shown in fig(6.49). This can be described as the trace paths of three particles at Re=1. The particles being placed initially in a vertical line. The outer particle is placed initially at $(r = 0.5, z = 0.3)$ and occurs at more place in the cavity. In contrast the inner particle is placed initially at $(r = 0.5, z = 0.7)$ and occurs less frequently in the cavity. However the particle is placed initially in the cavity centre and seem to be located between inner and outer particles paths. Also, all three particle paths become 'flatter' near the top wall of the cavity. This behaviour is shown in fig(6.49) at Re=10 for Newtonian fluid. The middle and lower figures show the traces obtained of the periodic motion of the particles by considering the r and z positions with time

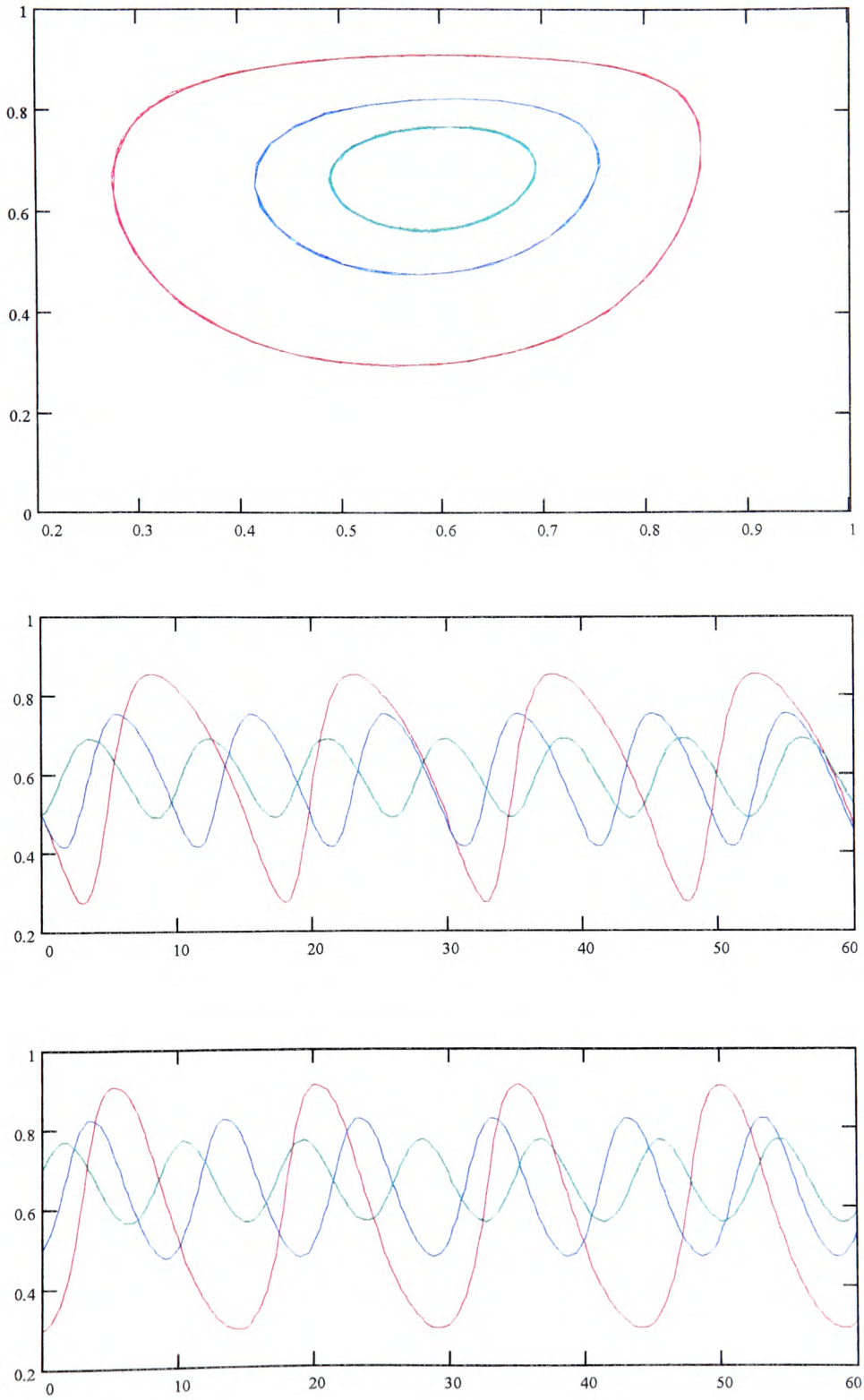

Figure (6.49) ; Re=10, Newtonian fluid after 100s, T=2s Initially placed in vertical line

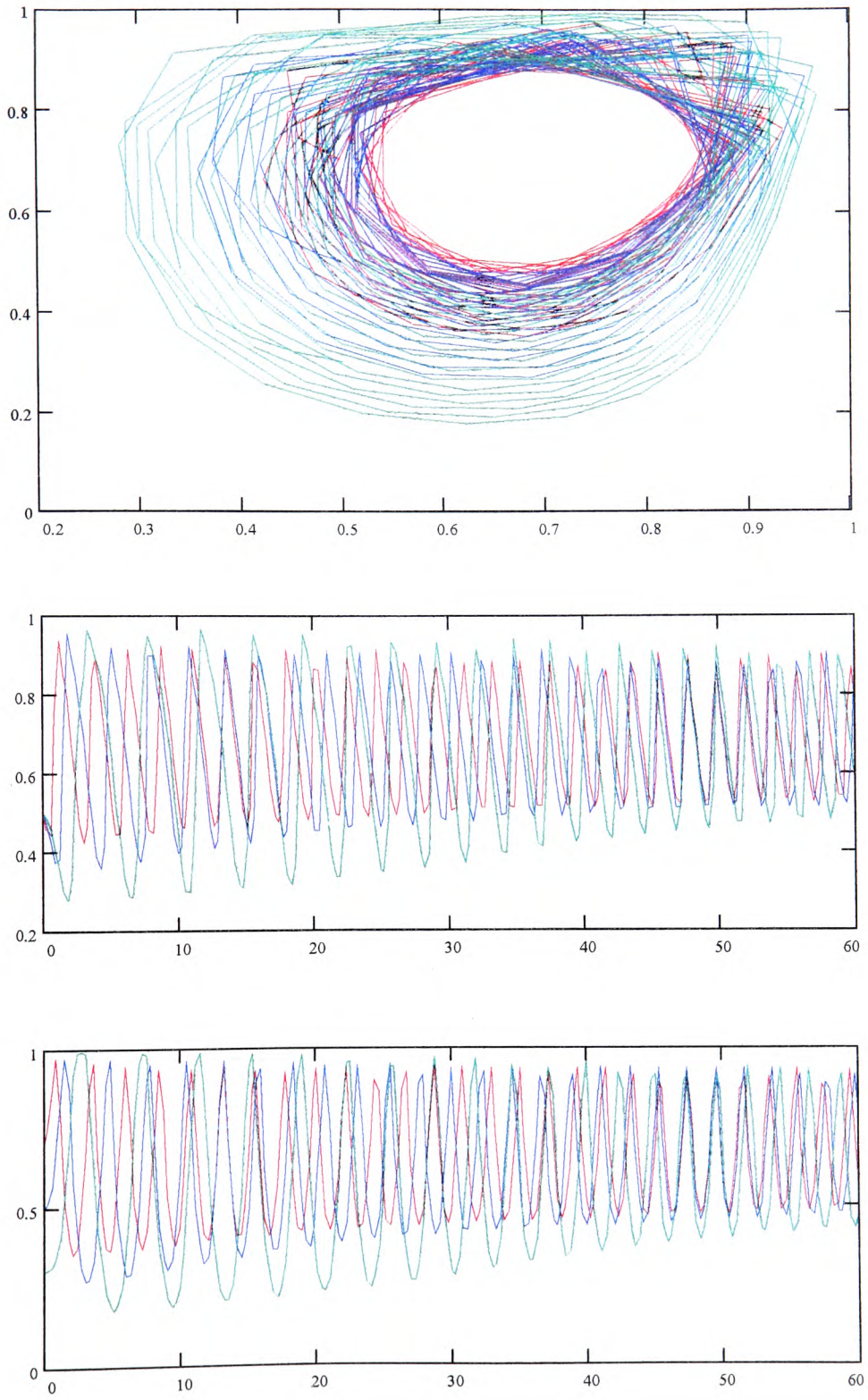

Figure (6.50) ; Re=100, pseudoplastic fluid after 100s, T=2s Initially placed in vertical line

As Re increases, for example Re=100 it is found all three particles move faster and travel more widely due to advection dominating flow. Fig(6.50) shows that all three particle paths become more 'tightly bound' together in the flow. The middle and lower figures show the traces obtained of the periodic motion of the particles by considering the r and z with time.

6.10.2. The particle Paths of the Concentric Cylinder Driven Cavity Flow

In this case, initially the particles being placed in the mid-cavity vertical line equally spaced ($r = 0.75$). However due to trace the particles paths for concentric cylinder case we select the points in the z-direction as $z = 0.5,0.6,0.7$. Fig(6.51) shows the trace paths of three particles at Re=10. The outer particle (top figure) is placed initially at $(0.75,0.5)$ and occurs at more place in the cavity. In contrast the inner particle is placed initially at $(0.75,0.7)$ and occurs less placed in the cavity. Moreover, all three particle become 'flatter' near the top wall of the cavity. This behaviour shown in fig(6.51) for the Newtonian fluid after 80s in simulation time. Fig (6.52) shows the trace of three particles at Re=20. In this case as Re increases the outer particle (top figure) is placed initially at $(0.75,0.5)$ and moves to the top wall where it remains thereafter. Moreover, the inner particles move faster and occurs at more places in the cavity. Also, it can be seen that the particle paths are 'tightly bound' due to advection term dominates to flow. The middle and lower figures show the traces obtained of the periodic motion of the particles by considering the r and z with time.

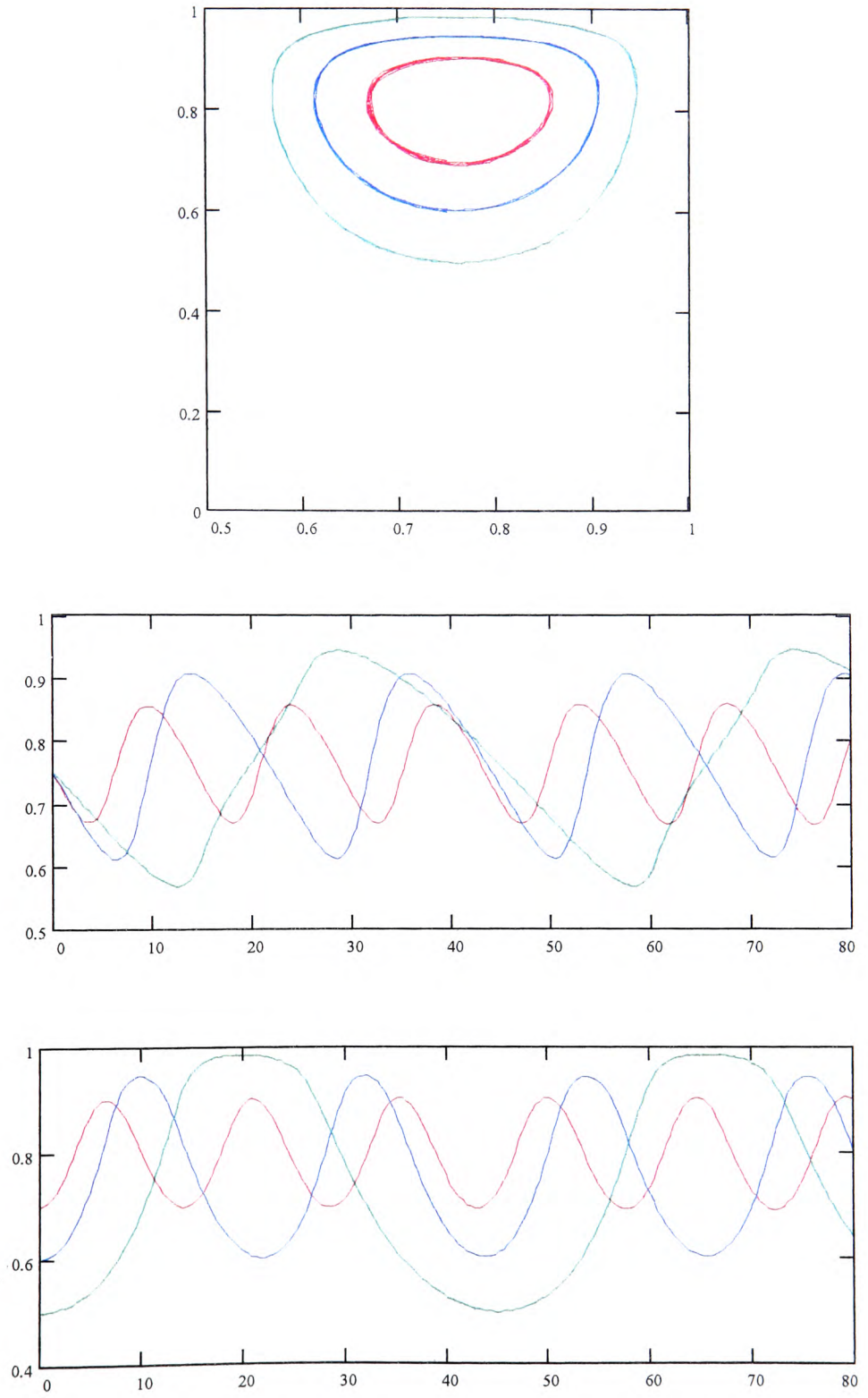

Figure (6.51) ; Re=10, Newtonian fluid after 80s, T=2s Initially placed in vertical line

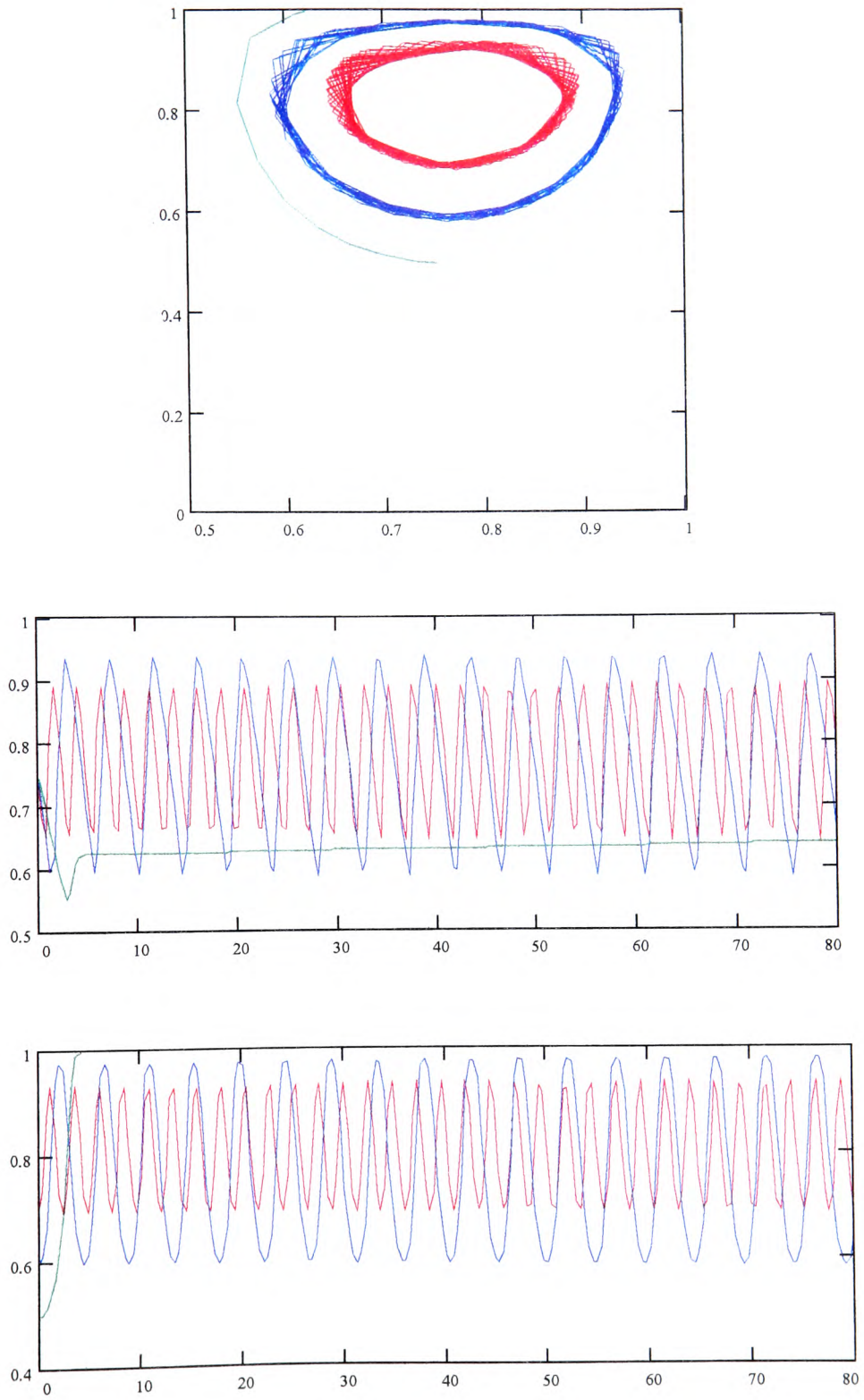

Figure (6.52) ; Re=20, pseudoplastic fluid after 80s, T=2s Initially placed in vertical line

In conclusion the trace paths of three particles was found at Re=10, 20 and 100 in both cylinder and concentric cylinder cases. We select the three equally spaced particles as placed in the middle of the cavity. At low Re, for example Re=1 all three particle paths seem to be more circular and become 'flatter' nearer the top wall. As re increases the advection term dominates to flow then all particle paths become 'tightly bound' together in the cavity. Moreover in concentric cylinder case the outer particle path was found to stop against the top wall at Re=20.

CHAPTER VII: THERMALLY DRIVEN CYLINDRICAL 3D FLOW

7.1 FLOW GEOMETRY AND PREVIOUS WORK

In this chapter we study fluid flow in a bounded cylinder cavity region with thermally forced convection models. Fluid transportation within horizontal cylinders heated from below, and vertical cylinders heated from side walls, has been previously studied analytically and experimentally. In the thermally driven cylinder flow problem, the main governing parameters are the Grashof (Gr) and Prandtl (Pr) numbers, therefore the flow behaviour is characterised mainly by the Rayleigh number. Lewis[51] studied a horizontal cylinder problem by using a perturbation analysis, and reported that the conduction term was dominant over the heat transfer. Martini and Churchill[56] sought to find an air measurement within a horizontal cylinder in which each half part of cylinder was differentially heated. They produced results by examining the Rayleigh numbers effects to flow between $2.10^5 \leq Ra \leq 8.10^6$. Recently a numerical approach using the novel spectral method has been used by Pasquetti and Bwemba[74].

Fluid transportation in a horizontal concentric cylinder has also been studied. This configuration is used widely in nuclear reactors, electronic equipment, transmission cables, thermal storage systems and concentrating solar collector receivers. Flow between horizontal concentric isothermal cylinder surfaces was first considered and measured by Beckman[6] for various compressible fluids. Kraussold[45] and Liu et al[54] studied the same flow system and examined the effect of the Prandtl number for several different fluids. In this case, it is easy to see that different flow regimes may

have arisen by the Rayleigh number influence. In thermally driven cylinder cavity flow, apart from the naturally driven case, the only difference is the buoyancy term involved in the flow equation.

In the chapter 6 we considered the flow as generated by a rotating cylinder with fluid viscosity depending on shear-rate. In this chapter the fluid flow is generated in the same geometry and the fluid viscosity depends on shear-rate as well as temperature. We impose a Torrance and Turcotte**[93]** viscosity model and the walls are kept stationary i.e., there is no angular velocity contribution on the material surface. Throughout this chapter vorticity is calculated on the boundary by using the solid wall condition.

7.2 THERMALLY DRIVEN CYLINDRICAL FLOW EQUATION

By considering incompressible viscoelastic cylindrical driven cavity flow with respect to various aspect ratios the governing equations can be defined as

$$\rho(T) = \rho_0\left(1-\beta\left(T-T_0\right)\right) \tag{7.1}$$

$$\frac{\partial \omega}{\partial t} = \frac{1}{r^2\,\mathrm{Re}} H\left(r^3, \eta; \frac{\omega}{r}\right) - Gr\left(c\theta\frac{\partial T}{\partial r} + s\theta\frac{\partial T}{\partial z}\right) + F_\omega \tag{7.2}$$

$$\frac{\partial T}{\partial t} = \frac{1}{r\,\mathrm{Pr}\,\mathrm{Re}}\nabla^2 T + \frac{1}{r}F_T + \frac{Ec}{r\,\mathrm{Re}}\Phi \tag{7.3}$$

$$\omega = \frac{\partial u}{\partial z} - \frac{\partial w}{\partial r} \tag{7.4}$$

$$\frac{1}{r}\frac{\partial}{\partial r}(ru) + \frac{\partial w}{\partial z} = 0 \tag{7.5}$$

In non-dimensional form as in chapter 5, we use the same notation for $H\left(r^3, \eta; \frac{\omega}{r}\right)$ and F_ω. In equation (7.3) the convection term F_T is now given by

$$F_T = -\left\{\frac{\partial}{\partial r}(urT) + \frac{\partial}{\partial z}(rwT)\right\}.$$

The non-dimensional parameter Grashof number is now defined as $Gr = \frac{g\rho^2\beta R^3(T - T_0)}{\eta_0^2}$, where R is the radius of the outer cylinder, and the Prandtl and Eckert numbers are defined as previously.

7.3 BOUNDARY CONDITIONS

Before solving equations (7.2) and (7.3) numerically we need the relevant boundary conditions for each of the cases to be considered. When the flow domain is heated from below we have a Biot condition on the vertical walls, and top wall is kept cool. When we consider the vertical cylinder flow domain heat comes from the outside and we have a Biot condition on the horizontal walls. As before the stream function is a constant on the boundary, and vorticity is calculated by using well known Woods-stream formulation**[21]** on each boundary.

For brevity we only illustrate the boundary conditions of the cylinder configuration in each case. The others type of cylinder domain boundary conditions can be easily calculated by using similar ideas.

Boundary conditions of the thermally driven cavity flow

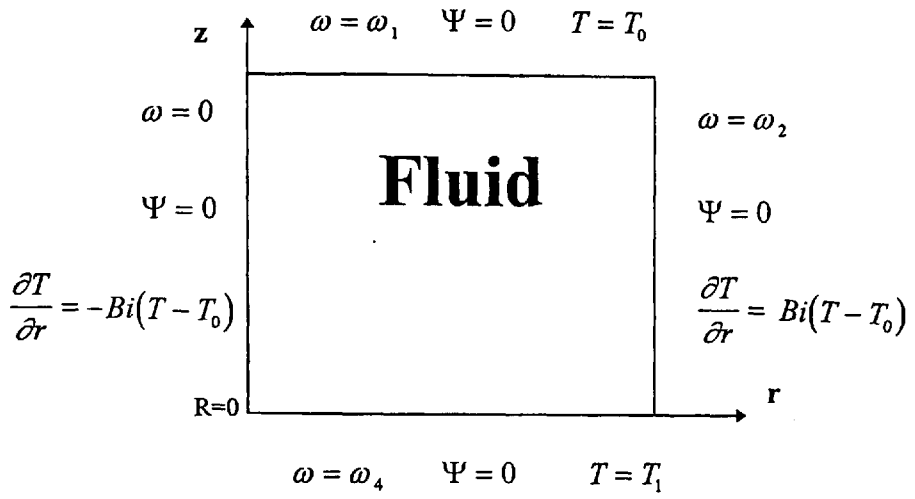

Figure 7.1 ; Boundary conditions for thermally driven cavity flow

In the thermal driven cavity flow the stream function is taken as zero on the boundaries. Vorticity is zero on the symmetry line. For the temperature equation we have two boundary conditions of either Dirichlet or Biot type so that on the horizontal walls we have the conditions $T_1 = 1$ and $T_0 = 0$. On the vertical walls we have Biot conditions and the temperature gradient is either zero or depends on the Biot number.

7.4 THE NUMERICAL SOLUTION, CONSISTENCY AND STABILITY OF THE THERMALLY DRIVEN CYLINDRICAL FLOW EQUATIONS

Equations (7.2) and (7.3) are solved numerically for both Newtonian and non-Newtonian viscous and viscoelastic fluids in the thermally driven cavity flow problem. We apply the finite difference approximation methods to the governing partial differential equations and seek solutions and stability properties by considering both steady and unsteady approaches. For the unsteady case the simple explicit and

Peaceman-Rachford methods are used to solve the coupled equations, as in previous chapters. We note that in the discretision process we use $A_i(i=1,...,6)$ as coefficient within the A. D. I. method and $B_i(i=1,...,6)$ are the coefficient of the parabolic equation within the simple explicit method.

We now consider T as a dependent variable in equations (3.42) and (3.43), as well as in (4.6) and (4.7). However, the temperature equation is discretised by using the A. D. I. method as follows

$$T^*_{i,j} - rr\left(A_1 T^*_{i+1,j} + A_2 T^*_{i-1,j} - 2A_3 T^*_{i,j}\right) + rr\frac{h}{2r^P}\left(ur\right)\left(T^*_{i+1,j} - T^*_{i-1,j}\right)$$

$$= T^n_{i,j} + s\left(A_1 T^n_{i+1,j} + A_2 T^n_{i-1,j} - 2A_3 T^n_{i,j}\right) - s\frac{k}{2}w\left(T^n_{i,j+1} - T^n_{i,j-1}\right) + \frac{\Delta t}{2}\frac{Ec}{\mathrm{Re}}f^n \qquad 7.5$$

and

$$T^{n+1}_{i,j} - s\left(A_4 T^{n+1}_{i+1,j} + A_5 T^{n+1}_{i-1,j} - 2A_6 T^{n+1}_{i,j}\right) + s\frac{k}{2}w\left(T^{n+1}_{i,j+1} - T^{n+1}_{i,j-1}\right)$$

$$= T^*_{i,j} + rr\left(A_1 T^*_{i+1,j} + A_2 T^*_{i-1,j} - 2A_3 T^*_{i,j}\right) - rr\frac{h}{2r^P}\left(ur\right)\left(T^*_{i+1,j} - T^*_{i-1,j}\right) + \frac{\Delta t}{2}\frac{Ec}{\mathrm{Re}}f^n, \qquad 7.6$$

where

$$A_1 = \frac{\left(r^P + 0.5h\right)}{\mathrm{Re}\,\mathrm{Pr}\,r^P},\ A_2 = \frac{\left(r^P - 0.5h\right)}{\mathrm{Re}\,\mathrm{Pr}\,r^P},\ \text{and}\ A_3 = \frac{\left(r^P + 0.5h\right) + \left(r^P - 0.5h\right)}{\mathrm{Re}\,\mathrm{Pr}\,r^P}$$

$$A_4 = \frac{1}{\mathrm{Re}\,\mathrm{Pr}} = A_5,\ \text{and}\ A_6 = \frac{2}{\mathrm{Re}\,\mathrm{Pr}}.$$

Here r^P indicates the discretisation point radius in the finite difference mesh.

The stability conditions for the concentration equation are calculated as previously to be $\frac{h(ru)\mathrm{Re}\,\mathrm{Pr}}{\left(r^P + 0.5h\right)} \le 2$ in equation (7.5), and $(kw)\mathrm{Re}\,\mathrm{Pr} \le 2$ in equation (7.6).

When equation (7.3) is discretised using the simple explicit method and T is considered as a dependent variable in equation (3.35), the coefficients of the parabolic equation (7.3) are

$$B_1 = \left\{1 - rr\left[\frac{\left(r^P + 0.5h\right)+\left(r^P - 0.5h\right)}{r\,\mathrm{Pr}\,\mathrm{Re}}\right] - s\left[\frac{(2)}{\mathrm{Pr}\,\mathrm{Re}}\right]\right\}, B_2 = rr\left[\frac{\left(r^P + 0.5h\right)}{r\,\mathrm{Pr}\,\mathrm{Re}} - \frac{h}{2r}(ru)^E\right]$$

$$B_3 = rr\left[\frac{\left(r^P - 0.5h\right)}{r\,\mathrm{Pr}\,\mathrm{Re}} + \frac{h}{2r}(ru)^W\right],\ B_4 = s\left[\frac{1}{\mathrm{Pr}\,\mathrm{Re}} - \frac{k}{2}w^N\right],\ B_5 = s\left[\frac{1}{\mathrm{Pr}\,\mathrm{Re}} + \frac{k}{2}w^S\right],$$

$B_6 = \frac{\Delta t}{2\,\mathrm{Re}}F_T^n$, where $rr = \frac{\Delta t}{h^2}$ and $s = \frac{\Delta t}{k^2}$ and F_T^n is defined as in previously.

7.5. RESULTS FROM THE 3D THERMALLY DRIVEN CYLINDER FLOW EQUATION

In this section we derive some results for the time-dependent flow equation where the flow is generated by buoyancy forces in a cylindrical geometry. We obtained the solutions with both numerical methods used and they were found to be in close agreement; therefore we only present results which are derived by the Peaceman-Rachford method as there are found to be generally more accurate than those of the simple-explicit method. In this case we have our main parameters as Rayleigh number (Ra) which is the product of the Prandtl number (Pr) and Grashof number (Gr). We also have the Reynolds number (Re) which is always taken as 1, also the Weissenberg number (Wi), Eckert number (Ec) and Biot number (Bi). We take the Ra number in the range 10^4 to 10^6 and Pr number from 1 to 7. Although we have results for different Pr numbers we present results for Pr=7 only because both sets of Pr results are similar. Moreover we do not present any results for the Eckert

number as the small Eckert numbers admitting solutions did not make any significant effect on flow. Similarly when Bi is taken as 1 or 10 we find that these values cause divergence for the flow equation. Also as expected there is no much thermal increase due to dissipation of energy. We therefore present results when Ec=0 and Bi=0.1. In this section we usually use a simulation time up to 20 seconds to get a steady solution. Our results are in agreement and consistent in a grid size range between 10x10 and 50x50, and we present the results for 30x30 grid. The initial distribution of the temperature equation is $T(r,z)=0$ or $T(r,z)=1-z$ at t=0 and thereafter the flow domain is heated from below. This initial distribution to the system will soon disappear and then the system alters its equilibrium state. We start by taking Bi=0 on the side walls so that no heat is allowed to leave the flow domain and subsequently we take Bi=0.1. Moreover when the temperature difference is applied between top and bottom walls this difference is defined in terms of the Rayleigh number. Therefore significant changes can be expected in this case and it is always possible to observe that the lighter fluid is located on the bottom. We are confident about our results on comparison of the previous chapter results which are in agreement with Pao**[73]**.

7.5.1 Thermally Driven Cylinder Cavity Flow

a) Shear Dependent Viscoelastic Fluid

For Bi=0 with Ra=10^4 in both viscous and viscoelastic case we see that flow produced one steady vortex flow for Newtonian, Boger and dilatant fluids, and the vortex centre is located at (0.57, 0.4) as shown in fig(7.2). Whereas we have different kind of solution for the pseudoplastic fluid where the vortex moves to right top corner

and a small negative vortex appears on the right bottom corner. The vortex centre is located at (0.62, 0.7) as shown in fig(7.3). Here the corresponding temperature profile are shown in fig (7.4) - (7.5). The warm fluid rises along the bottom and the right wall vertically, and the cold fluid descends along the top and the left wall for the Newtonian, Boger and dilatant fluids. For a pseudoplastic fluid the temperature profile is shown in fig(7.5). The warm fluid rises along the bottom wall, the cold fluid descends nearer the right wall and top plate. For $Ra=10^5$ we only have a steady solution for constant viscosity fluids. For non-Newtonian fluids, the flow always shifting and never become steady. We always have two vortices but they are far from being symmetric and equal, and always shift as shown for the pseudoplastic case shown in fig(7.6). We can therefore say that in case of thermally driven cylinder the computer solution failed to converge to a solution as Ra increases.

As the Biot number is used, we have steady solutions for $Ra=10^4$ and $Ra=10^5$ for both viscous and viscoelastic flow cases and both produce similar results.

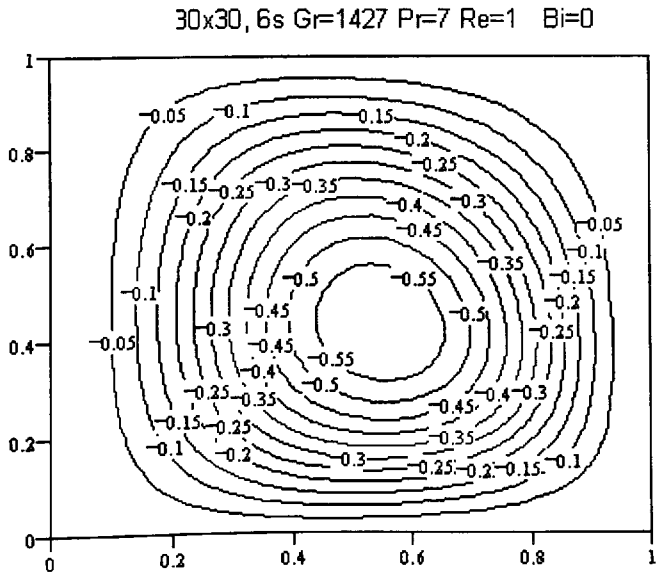

Figure (7.2) ; Streamline contours for Newtonian fluid Gr=1427, Pr=7

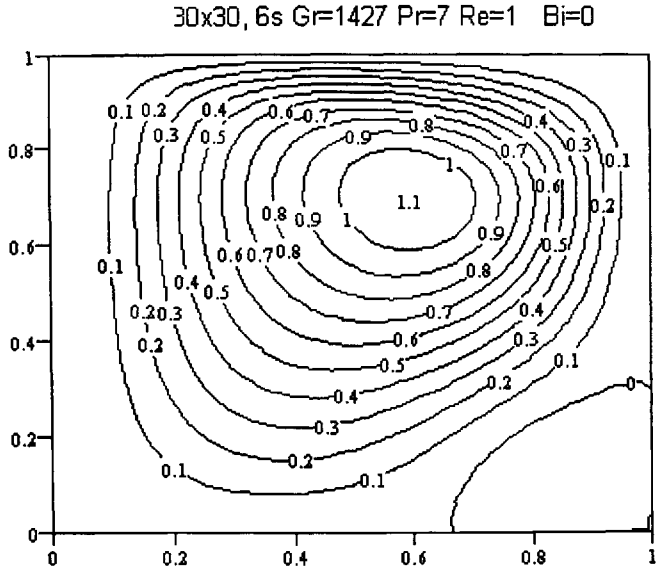

Figure (7.3) ; Streamline contours for viscoelastic pseudoplastic fluid Gr=1427, Pr=7

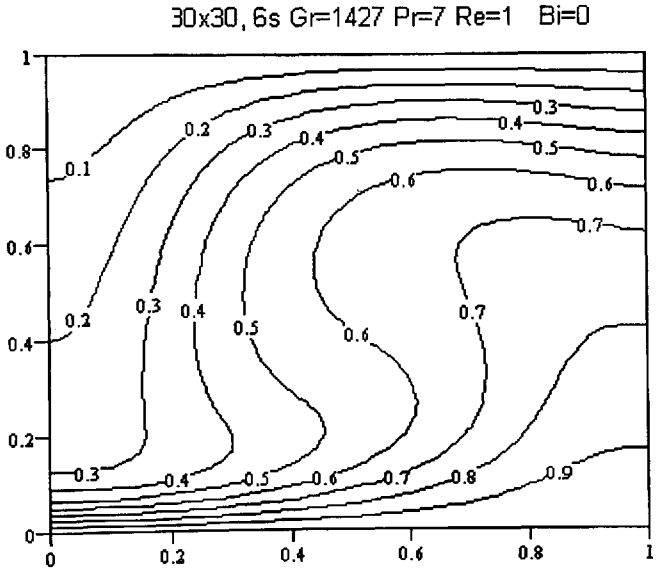

Figure (7.4) ; Temperature contours for Newtonian fluid Gr=1427, Pr=7

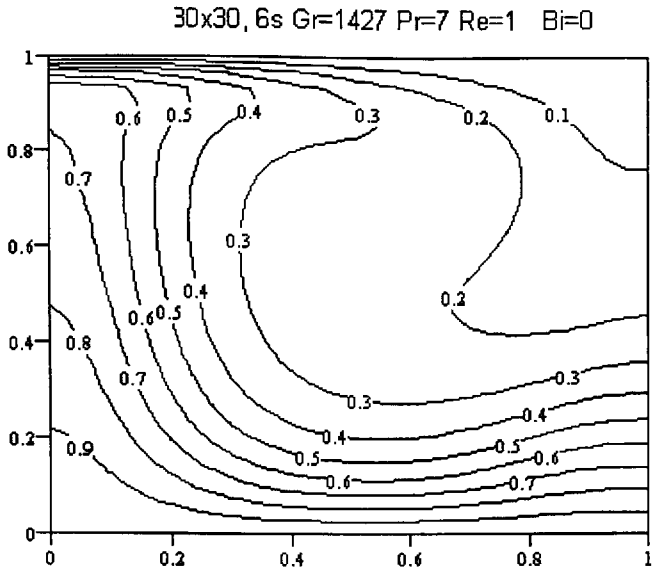

Figure (7.5) ; Temperature contours for viscoelastic pseudoplastic fluid Gr=1427, Pr=7

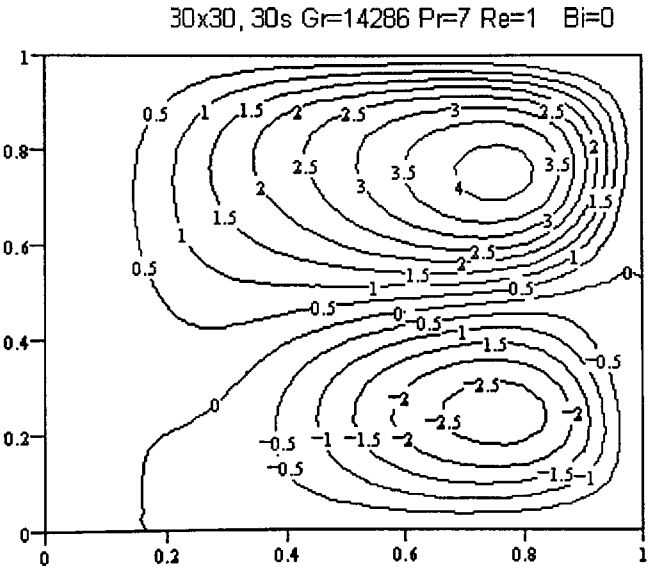

Figure (7.6) ; Streamline contours for viscous pseudoplastic fluid Gr=14286, Pr=7

b) Temperature Dependent Viscoelastic fluid

In this section we seek a numerical solution for viscous and viscoelastic flow equations with temperature dependent fluids. Following Torrance and Turcotte[93] we define the temperature dependent viscosity as in chapter 4. The main parameter is still

the Rayleigh number and we investigate the solution at various Ra values by taking 'k' as 1 and 10 in the Turcotte and Torrance formulation. We see that when k=1 the viscous fluid produces steady results for $Ra=10^4$. Fig(7.7) shows that at $Ra=10^4$ one main vortex produced and the streamlines 'circular' around the cavity's centre. The vortex centre is located at (0.6, 0.4) and the corresponding temperature profile is shown in fig(7.8). The warm fluid rises along the bottom wall and around the cavity's centre, whereas the cold fluid descends along the top wall.

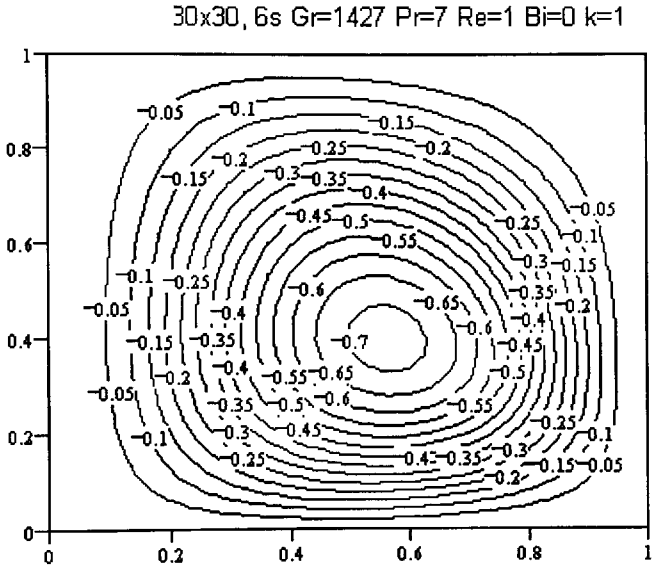

Figure (7.7) ; Streamline contours for viscous dilatant fluid, temperature dependent

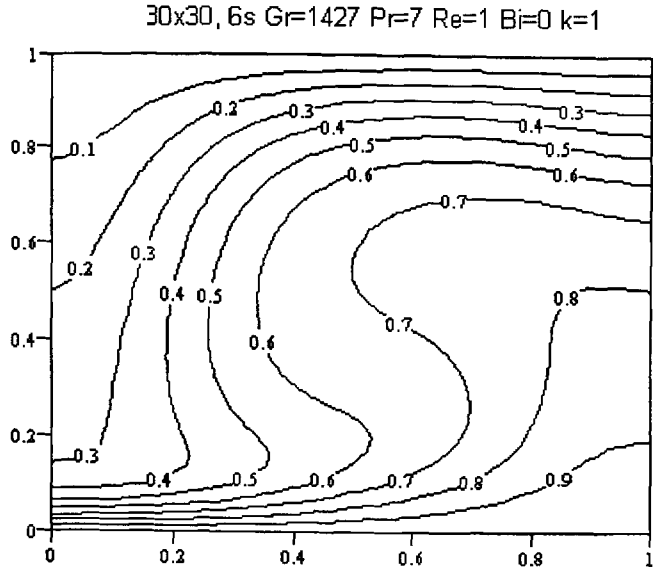

Figure (7.8) ; Streamline contours for viscous dilatant fluid, temperature dependent

As Ra increases the system becomes more unstable and loses its equilibrium and therefore instability occurs in the fluid. When Bi is taken as 0.1, the system still produced a one cell solution with all k numbers considered. Similarly as Ra increases instability occurs in the fluid.

7.5.2.Thermally Driven Concentric Cylinder Cavity Flow

a) Shear Dependent Viscoelastic Fluid

In this flow domain with $Ra=10^4$ we have a one vortex solution which is steady in both viscous and viscoelastic cases. Fig(7.9) shows a viscous dilatant fluid behaviour. The vortex centre is located almost in the middle of the cavity and the streamlines are 'circular' around the cavity's centre. The corresponding temperature profile is shown in fig(7.10) in case of a non-Newtonian dilatant fluid. It is almost 'parallel' temperature distribution due to the small secondary flow.

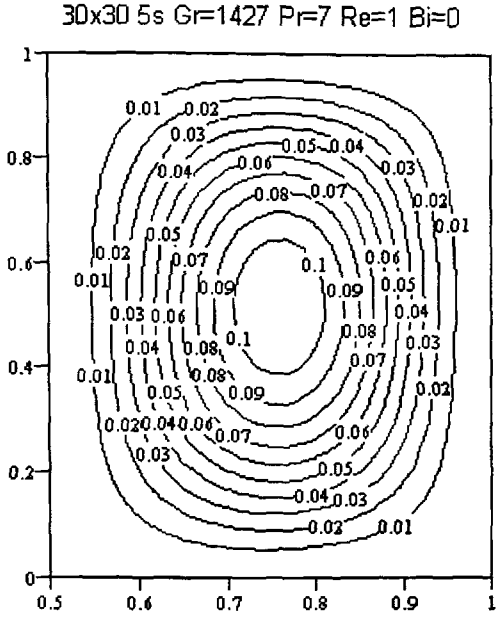

Figures (7.9) ; Streamline contours for viscous dilatant fluid

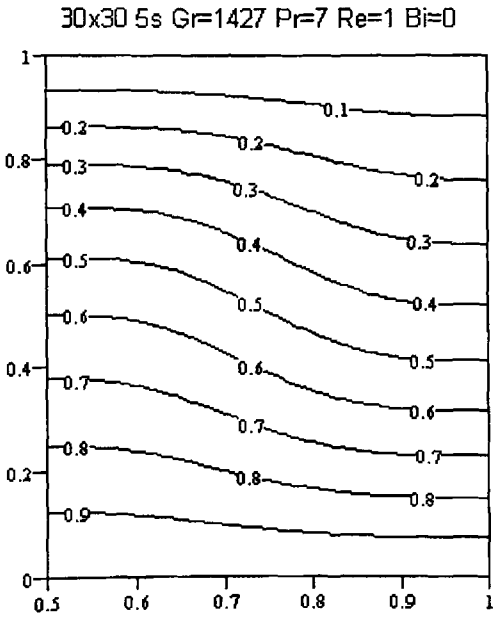

Figure (7.10) ; Temperature contours for viscous dilatant fluid

As Ra increases, for example $Ra=10^5$, a solution exists which is steady for Newtonian and non-Newtonian fluids. Fig(7.11) shows that one main vortex is produced with negative small vortex around the right bottom corner. The streamlines are 'circular' around the cavity's centre of the constant viscosity fluid. For the non-Newtonian

dilatant fluid, two main vortices are produced which are always shifting and the streamlines are not symmetric about the cavity's horizontal mid-line as shown in fig(7.12). With Ra=10^6 the computer solution failed to converge to a solution.

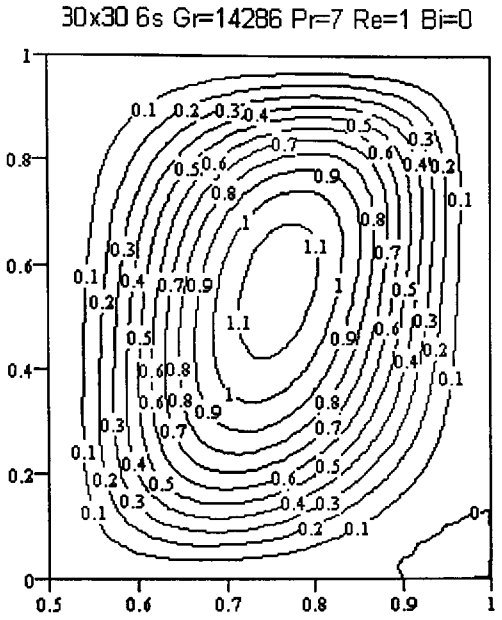

Figure (7.11) ; Streamline contours for Newtonian fluid

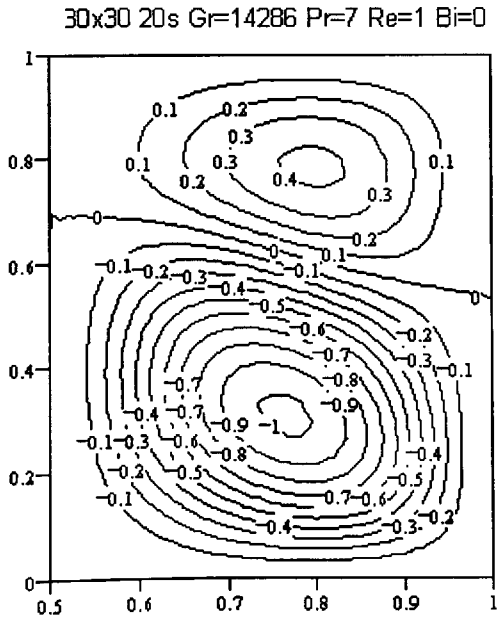

Figure (7.12) ; Streamlines contours for dilatant fluid

When the Biot number=0.1 we similarly have a one vortex solution for $Ra=10^4$, for all fluids in both viscous and viscoelastic cases. With $Ra=10^5$ we see significant differences from the previous case so that when Bi=0.1 the Newtonian fluid produces a two vortex solution. In fact for the Newtonian fluid case, as shown in fig(7.13), a positive vortex appears around the left bottom corner. In the case of a pseudoplastic fluid the solution does not become steady, always shifting in the fluid. We therefore illustrate this behaviour in fig(7.14) .With $Ra=10^6$ the flow does not admit a steady solution with or without non zero Bi number. Therefore instability occurs in the computer solution.

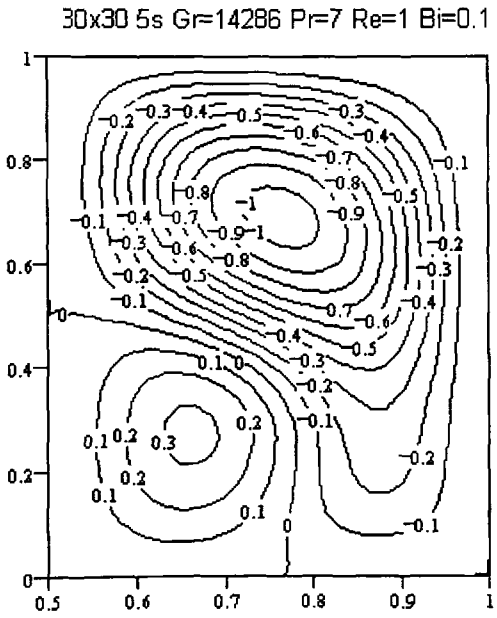

Figure (7.13) ; Streamline contours for Newtonian fluid

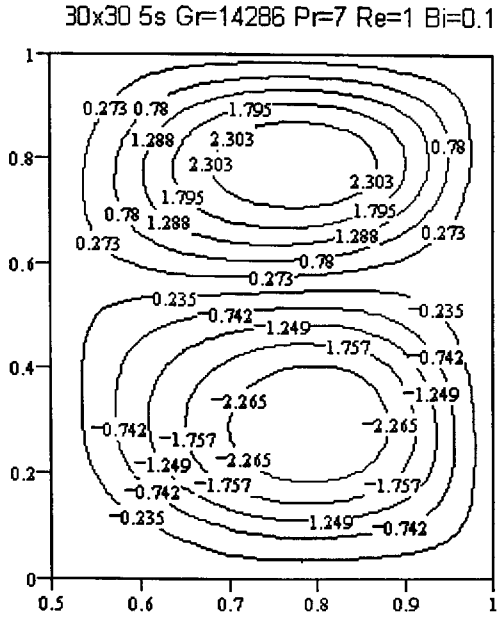

Figure (7.14) ; Streamline contours for pseuudoplastic fluid

b) Temperature Dependent Viscoelastic Fluid

In this section the flow is generated by a buoyancy force and the flow domain lies between two concentric cylinders. The fluid viscosity is dependent on temperature and we derive solutions with various Ra and 'k' numbers. The 'k' values are taken as 1 and 10 respectively and we find that both 'k' values generate similar kinds of flow with the same Rayleigh number and same fluid respectively. With $Ra=10^4$ we have exactly similar results as in the shear dependent viscosity case for each fluid. Moreover we see that when $Ra=10^5$ the fluids with constant and variable viscosity fluids allow steady solutions. For example in fig(7.15) which has one vortex that is similar both qualitatively and quantitatively with shear-dependent fluid shown in fig(7.11). But for a dilatant fluid one main vortex is produced with a small positive vortex around the right top corner shown in fig(7.16). The corresponding temperature

profile with Ra=10^5 in the case of Newtonian and dilatant fluids is shown in fig (7.17) - (7.18). The warm fluid lifts near the bottom and left wall vertically, while the colder fluid drops near the top and right wall in the case of the Newtonian fluid. For the dilatant fluid the warmer fluid rises upwards near the bottom and right walls and the cold fluid descends near the top and left walls. As the Ra increases the system is again found to be more unstable and therefore instability occurs in the computer solution.

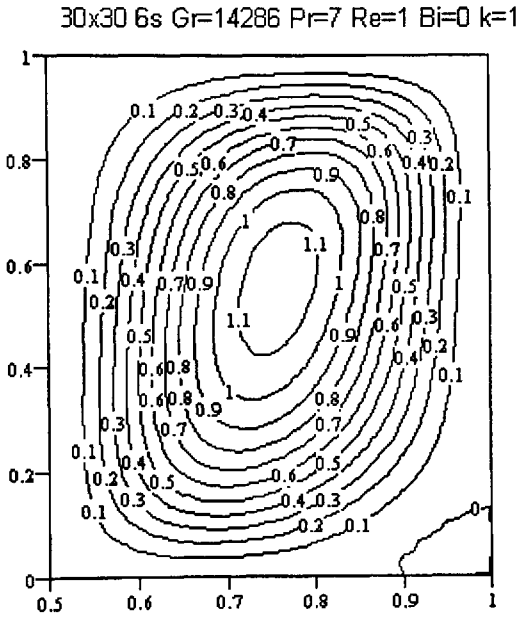

Figure (7.15) ; Streamline contours for Newtonian fluid

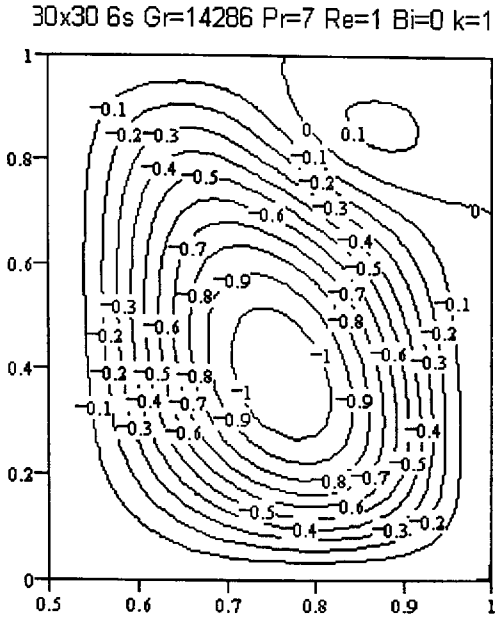

Figure (7.16) ; Streamline contours for dilatant fluid

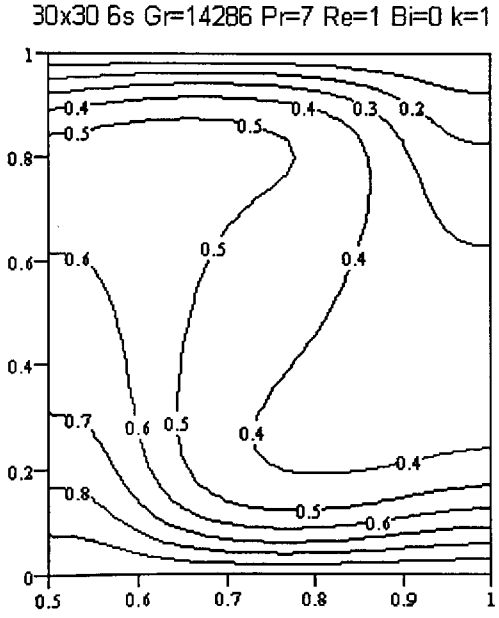

Figure (7.17) ; Temperature contours for Newtonian fluid

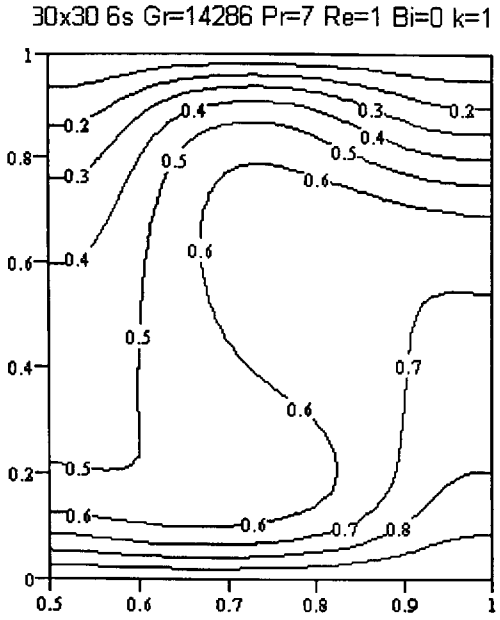

Figure (7.18) ; Temperature contours for dilatant fluid

When we incorporate a non-trivial Bi condition similar kinds of behaviour are observed in the case of shear dependence viscosity flow with Bi=0.1. Here both k=1 and k=10 produce results as before. A more oval vortex is seen in case of $Ra=10^4$ for all types of fluids and when Ra increases this vortex becomes much bigger and 'rectangular'. Similarly one small positive vortex appear around left bottom corner and it becomes stronger and occupies almost a quarter of the cavity in the case of the dilatant fluid. This behaviour is shown in fig(7.19) and is almost similar behaviour as in fig(7.13) both qualitatively and quantitatively.

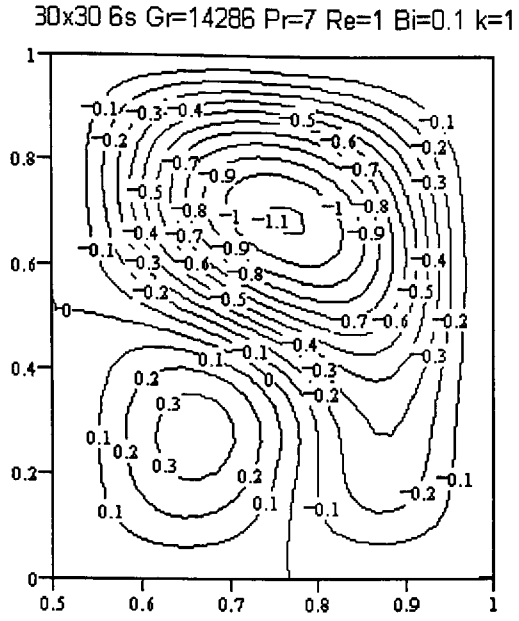

Figure (7.19) ; Streamline contours for dilatant fluid

7.5.3.Thermally Driven Cylinder Free-Surface Flow

a) Shear Dependent Viscoelastic Fluid

This section considers viscous and viscoelastic flows which are generated by a free-surface cylindrical cup with differentially heated walls. On the top, the velocity component w is taken as zero as well as the stream function.. We have results for $Ra=10^4$ which are steady solutions. In this case we have a one vortex solution and more or less similar behaviour is seen in both as viscous and viscoelastic fluid cases. The vortex centre is located at the cavity centre shown in fig(7.20). The corresponding temperature profile is shown in fig(7.21), with the warmer fluid rising near the bottom wall and right wall, whereas the cold fluid descends near the top and left walls. However when Ra increases the system becomes unstable and loses its equilibrium and therefore instability occurs in the computer solution.

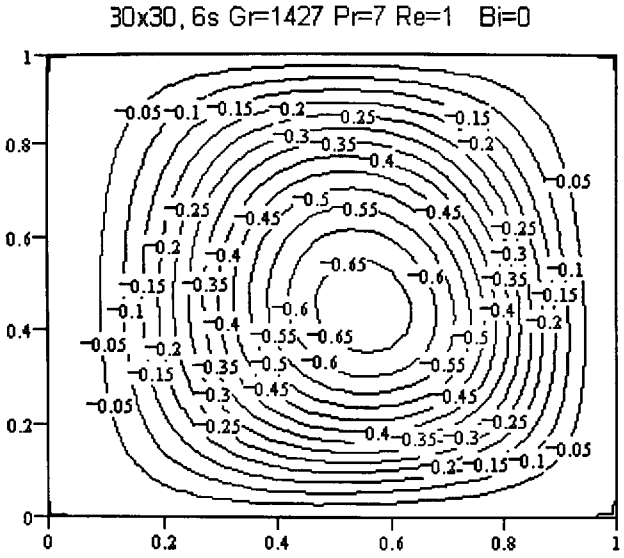

Figure (7.20) ; Streamline contours for Newtonian fluid

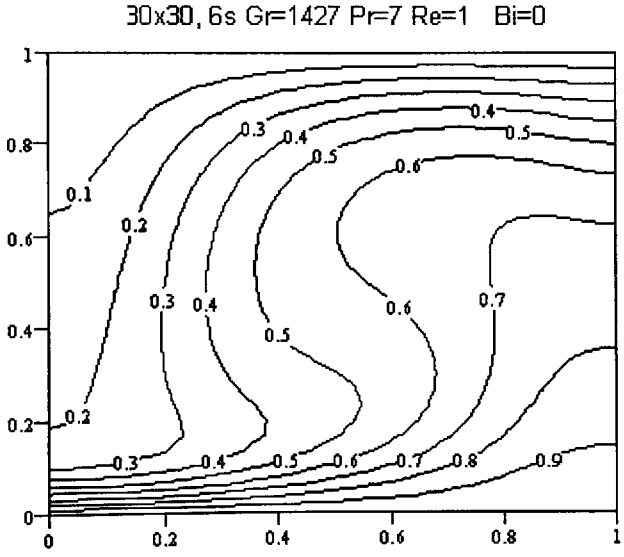

Figure (7.21) ; Temperature contours for Newtonian fluid

With non-zero Bi values, we see that instability occurs in any program results in the pseudoplastic fluid for both viscous and viscoelastic cases. Similarly we have a one vortex solution at $Ra=10^4$ for Newtonian, Boger and dilatant fluids with Bi=0.1. Moreover at $Ra=10^5$ we have a steady solution, which is a one vortex solution, with

Bi=0.1, shown in fig(7.22). Therefore the Biot number is seen to make the system more stable in this case. Both Newtonian and dilatant fluids produce similar behaviour so that one vortex occurs in the flow domain and its centre is located at the centre of the cavity and its shape is more 'circular'. The corresponding temperature profile is shown in fig(7.23). Warmer fluid rises near the bottom wall and the colder fluid falls near the top wall. However as Ra increases the system gets more unstable and loses its equilibrium and instability occurs in the computer solution.

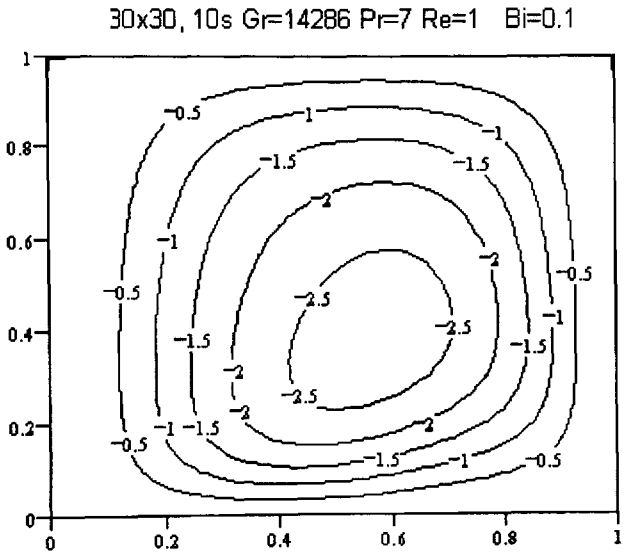

Figure (7.22) ; Streamline contours for dilatant fluid

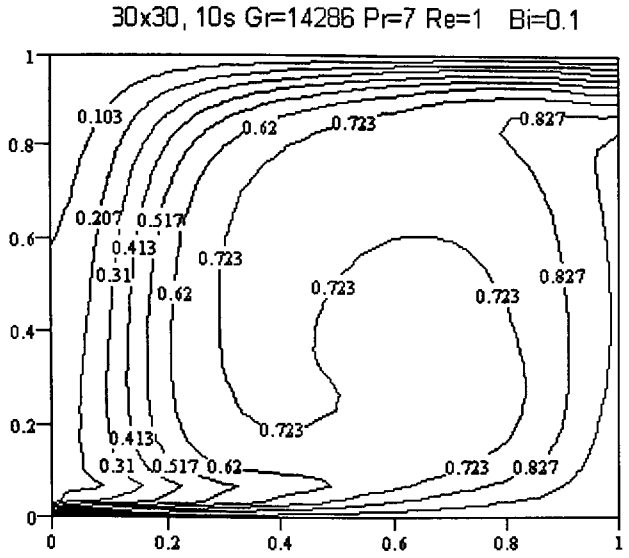

Figure (7.23) ; Temperature contours for dilatant fluid

b) Temperature Dependent Viscoelastic Fluid

In this case we see that both 'k' values produce similar results with the same Ra numbers and fluids. With $Ra=10^4$ for a Newtonian fluid, shown in fig(7.24), we have similar behaviour as in the above case, and for the dilatant fluid we see that although the flow pattern takes a similar form, its vortex centre moves toward the top wall. The corresponding temperature profile is shown in fig(7.25); it is asymmetric and the warmer fluid rises near the top and left walls, whereas the cold fluid drops near the top and right walls. Similarly the system loses its equilibrium and becomes unstable as Ra increases. As seen in previous cases for thermally driven cavity flow solution the Rayleigh number plays a vital role in this problem and as Ra increased the computer program failed to converge to a solution.

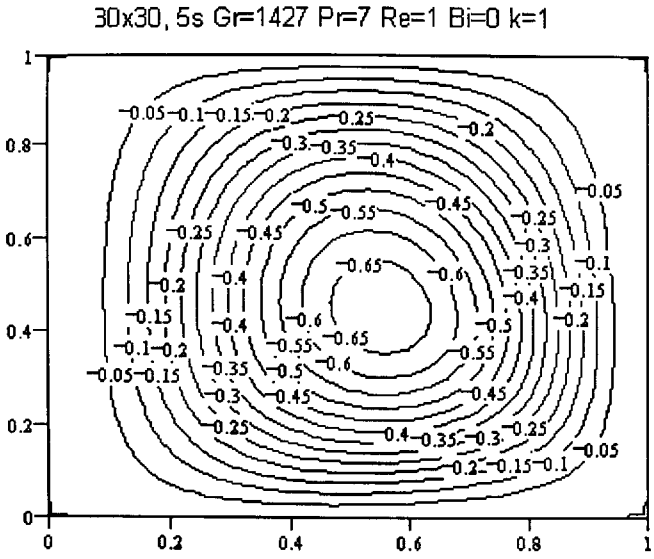

Figure (7.24) ; Streamline contours for Newtonian fluid

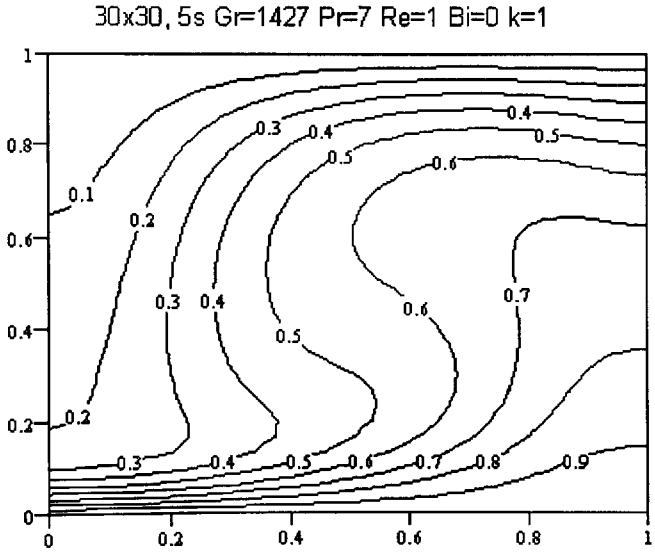

Figure (7.25) ; Temperature contours for Newtonian fluid

Finally in this chapter the Bi condition is used for free-surface cylinder driven cavity flow, where the fluid viscosity depends on temperature as well as shear-rate. Similarly the solution is generated for k=1 as well as k=10, and it is seen that similar behaviour is obtained for all k values in both viscous and viscoelastic cases. With $Ra=10^5$ two

vortices are produced and always shift. The streamlines are not symmetric about the cavity's horizontal mid-line, as shown in fig(7.26)

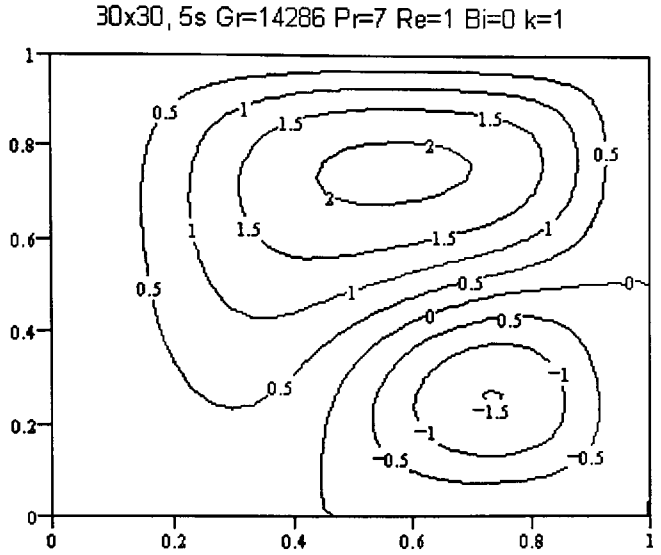

Figure (7.26) ; Streamline contours for dilatant fluid

The corresponding temperature profile is shown in fig(7.27) where the warm fluid rises along the bottom and left walls, whereas the cold fluid descends along the top and right walls.

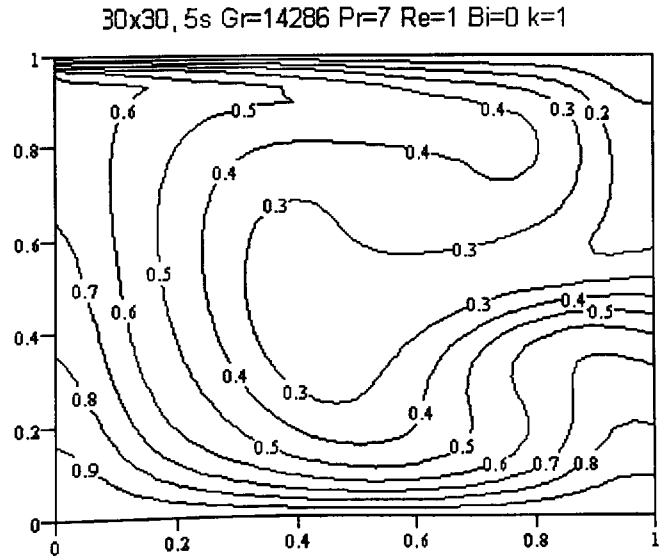

Figure (7.27) ; Temperature contours for dilatant fluid

In this chapter thermally driven cavity flow was studied with various cylinder container. The fluid viscosity was considered to depend on shear-rate as well as temperature. In this case Ra number play very important role for the final solution to seek the stability properties of the flow. Also we sought Biot condition and viscous heating effect for the stability condition as well. The Eckert number always causes instability in the program therefore steady solution is not possible to be found. When the Biot number is taken as 0.1 steady solution is found. Moreover, if the Biot number is bigger than 0.1 our program didn't give the steady solution due to not converge to a solution. When Ra number is taken as 10^4 one main vortex produced in all cylinder cases considered. As Ra increases the system becomes unstable and loses its equilibrium and then instability occurs in the program. For Ra=10^5 two main vortices are produced but they are far from symmetric. Also shifting vortex behaviour was obtained. In this case two vortices always shift and the solution never become steady.

CHAPTER VIII : SPHERICALLY DRIVEN CAVITY FLOW IN 3D

8.1 FLOW GEOMETRY AND PREVIOUS WORK

In this chapter we introduce a numerical solution of the spherically driven cavity flow for an incompressible purely viscous fluid in the steady case only. The reason why we only derive a steady state solution is due to the time available for this research project. In industry, this problem has been subject of much research in engineering, meteorology and geophysics. We assume axi-symmetric fluid motion and therefore the flow domain is effectively 2D. Since $\frac{\partial}{\partial \phi} = 0$ there is no contribution to this flow in the ϕ direction (Figure 8.1). However the flows employed for spherical driven cavity flow fall into five categories as

i.Spherical driven cavity flow,

ii. Concentric sphere driven cavity flow,

iii. Hollow sphere driven cavity flow,

vi. The hemispherical fixed wall problem,

v.Free-surface problem for a hemisphere.

We associate the governing equations of motion of the axi-symmetric steady-state viscous fluid with the spherical polar co-ordinate system (r, ϕ, θ) and velocity vector $V_i = (u, v, w)$, where $w = R\Omega$. In this chapter, we derive the flow pattern, circulation, with various spherical driven flows.

In the literature we found some relevant papers for concentric sphere, where the flow between two axial spheres is generated by one or more wall movements,

Marcus and Tuckerman[55] carried out a numerical study of flow between concentric rotating spheres and they examined self-consistency by computing spherical Couette flows with various Taylor numbers up to 2. They compared their results with experimental results and observed that the Taylor vortices' size depended on Reynolds number. Moreover, they obtained symmetric flow patterns whose symmetry line is the equatorial line. Later, a numerical study was carried out by Schwengels and Schultz[83] for the flow between rotating concentric spheres. They used the FDM to examine the flow pattern and the circulation contours. Buhler[12] carried out numerical and experimental work by using symmetric flow between two rotating spheres. He also considered the flow to be asymmetric with respect to the equator. Gulwadi and Elkouh[38] made a numerical study of an incompressible Newtonian fluid between concentric spheres using an iterative technique, but the solution is only valid for small Reynolds numbers. Recently, Ni and Nigro[64] conducted a finite element study of the axisymmetric motion of an incompressible viscous fluid. They obtained results for the flow pattern, rotational speed and vorticity with respect to Reynolds number variations and several radius ratios of the geometry.

8.2 SPHERICAL CAVITY DRIVEN FLOW EQUATIONS OF 3D FLOW

We only deal with viscous flow in a steady state in both Newtonian and non-Newtonian cases with respect to spherical polar co-ordinates.

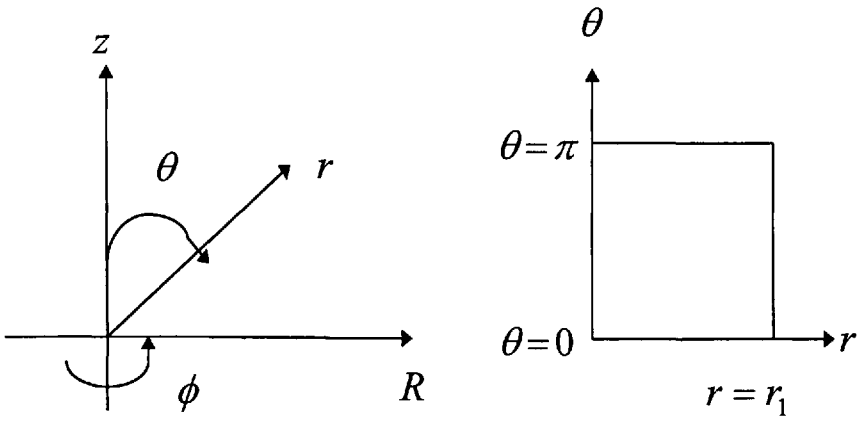

Figure (8.1) ; Spherical geometry

The governing equations of motion can be expressed as:

Conservation of Mass

$$\frac{1}{r}\frac{\partial}{\partial r}\left(r^2 u\right)+\frac{1}{rs}\frac{\partial}{\partial \theta}\left(vs\right)=0 \qquad 8.1$$

where u and v can be defined in terms of stream function as following

$$u=\frac{1}{r^2 s}\frac{\partial \Psi}{\partial \theta} \text{ and } v=-\frac{1}{rs}\frac{\partial \Psi}{\partial r}.$$

Here r is defined as a radial distance, u and v are the velocity components in the direction of radial and meridional direction respectively, and for simplicity we let $s=\sin\theta$ and $c=\cos\theta$.

Conservation of Momentum

The axisymmetric steady state conservation of momentum equations in spherical polar co-ordinates (r,θ,ϕ) are

$$\rho\left(u\frac{\partial u}{\partial r}+\frac{v}{r}\frac{\partial u}{\partial \theta}-\frac{\left(v^2+w^2\right)}{r}\right)=\frac{1}{r^2}\frac{\partial}{\partial r}\left(r^2\sigma_{rr}\right)$$

$$+\frac{1}{rs}\frac{\partial}{\partial \theta}\left(s\sigma_{r\theta}\right)-\frac{\partial P}{\partial r}-\frac{1}{r}\left(\sigma_{\theta\theta}+\sigma_{\phi\phi}\right)+F_r \qquad 8.2$$

$$\rho\left(u\frac{\partial v}{\partial r}+\frac{v}{r}\frac{\partial v}{\partial \theta}+\frac{uv}{r}-\frac{c}{rs}w^2\right)=\frac{1}{r^3}\frac{\partial}{\partial r}\left(r^3\sigma_{r\theta}\right)$$

$$+\frac{1}{rs}\frac{\partial}{\partial \theta}\left(s\sigma_{\theta\theta}\right)-\frac{1}{r}\frac{\partial P}{\partial \theta}-\frac{c}{rs}\sigma_{\phi\phi}+\frac{1}{r}F_\theta \qquad 8.3$$

$$\rho\left(u\frac{\partial w}{\partial r}+\frac{v}{r}\frac{\partial w}{\partial \theta}+\frac{uw}{r}\frac{c}{rs}vw\right)=\frac{1}{r^3}\frac{\partial}{\partial r}\left(r^3\sigma_{r\phi}\right)$$

$$+\frac{1}{rs}\frac{\partial}{\partial \theta}\left(s\sigma_{\theta\phi}\right)+\frac{c}{rs}\sigma_{\theta\phi}+F_\phi \qquad 8.4$$

where $F_i=\left(F_r,F_\theta,F_\phi\right)$ denotes body forces per unit mass. In our case the only body force is due to gravity in the negative z direction. We only consider the solvent part of fluid model and neglect the polymeric part. Therefore we have $\sigma_{ik}=2\eta\left(\dot{\gamma}\right)d_{ik}$.

However by taking the curl of the Navier-Stokes equations we obtain.

$$\rho\left\{\frac{1}{rR}\left[\frac{\partial}{\partial r}(ru\omega)+\frac{\partial}{\partial \theta}(v\omega)\right]\right\}=\frac{1}{r\ R^3}\left\{\frac{\partial}{\partial r}\left(rR^3\frac{\partial}{\partial r}\left(\eta\frac{\omega}{R}\right)\right)+\frac{\partial}{\partial \theta}\left(\frac{R^3}{r}\frac{\partial}{\partial \theta}\left(\eta\frac{\omega}{R}\right)\right)\right\}$$

$$+F_{\omega\Omega}+F_{\omega B} \qquad 8.5$$

where $R=rs$ and from now on we consider the vorticity equation as $\omega=\zeta rs=R\zeta$ in spherical polar co-ordinates. Here

$$F_{\omega\Omega}=\frac{\rho}{r^2s^2}\left(cs^2\frac{\partial}{\partial r}(r\Omega)^2-rs\frac{\partial}{\partial \theta}(r\Omega)^2\right)$$

where $\Omega = \frac{w}{R} = \frac{w}{rs}$,

$$F_{\omega B} = -\frac{1}{Rr}\left\{\frac{\partial}{\partial r}(rsF_z) + \frac{\partial}{\partial \theta}(cF_z)\right\}.$$

$$F_{\omega\eta} = \frac{2}{r^2 s^3}\left\{\left[\frac{\partial}{\partial \theta}(uc) - \frac{\partial}{\partial \theta}(vs)\right]\left[c\frac{\partial^2}{\partial r^2}(\eta) - \frac{s}{r}\frac{\partial^2}{\partial r \partial z}(\eta) - s\frac{\partial}{\partial \theta}(\eta)\frac{\partial}{\partial r}\left(\frac{1}{r}\right)\right]\right.$$

$$-\left[\frac{\partial}{\partial r}(uc) - \frac{\partial}{\partial r}(vs)\right]\left[c\frac{\partial^2}{\partial r \partial z}(\eta) - \frac{s}{r}\frac{\partial^2}{\partial z^2}(\eta) - \frac{c}{r}\frac{\partial}{\partial \theta}(\eta)\right]$$

$$+\left[\frac{\partial}{\partial \theta}(us) + \frac{\partial}{\partial \theta}(vc)\right]\left[s\frac{\partial^2}{\partial r^2}(\eta) + \frac{c}{r}\frac{\partial}{\partial r \partial z}(\eta) + c\frac{\partial}{\partial \theta}(\eta)\frac{\partial}{\partial r}\left(\frac{1}{r}\right)\right]$$

$$\left.-\left[\frac{\partial}{\partial r}(uc) + \frac{\partial}{\partial r}(vs)\right]\left[s\frac{\partial^2}{\partial r \partial z}(\eta) + c\frac{\partial}{\partial r}(\eta) + \frac{1}{r}\frac{\partial^2}{\partial \theta^2}(\eta c)\right]\right\}.$$

Rotational Speed Equation

This equation is easily derived from equation (7.4) and takes the form

$$\rho\left\{\frac{1}{r^2 R^2}\left[\frac{\partial}{\partial r}\left(u\Omega r R^3\right) + \frac{\partial}{\partial \theta}\left(v\Omega R^3\right)\right]\right\}$$

$$= \frac{1}{r^2 R^2}\left\{\frac{\partial}{\partial r}\left(\eta r R^3 \frac{\partial \Omega}{\partial r}\right) + \frac{\partial}{\partial \theta}\left(\frac{\eta R^3}{r}\frac{\partial \Omega}{\partial \theta}\right)\right\} \qquad 8.6$$

Vorticity Equation

We define

$$\omega = \frac{1}{r}\left\{\frac{\partial}{\partial r}(rv) - \frac{\partial}{\partial \theta}(u)\right\},$$

or

$$-\zeta = \frac{1}{r^2}\left\{\frac{1}{s}\frac{\partial^2}{\partial r^2}(\Psi) + \frac{1}{r^2}\frac{\partial}{\partial\theta}\left(\frac{1}{s}\frac{\partial}{\partial\theta}(\Psi)\right)\right\}$$

with velocity components $u = \frac{1}{r^2 s}\frac{\partial\Psi}{\partial\theta}$, $v = -\frac{1}{rs}\frac{\partial\Psi}{\partial r}$ and $\omega = R\zeta$. In spherical flows the shear-rate is given as

$$\left(\dot{\gamma}\right)^2 = 2\left\{d^2_{rr} + d^2_{\theta\theta} + d^2_{\phi\phi} + 2d^2_{r\theta} + 2d^2_{\theta\phi} + 2d^2_{r\phi}\right\} \qquad 8.7$$

where d_{ik} represents the first rate of strain tensor with components

$$d_{rr} = \frac{\partial u}{\partial r}, \quad d_{\theta\theta} = \frac{1}{r}\frac{\partial v}{\partial\theta} + \frac{u}{r}, \quad d_{\phi\phi} = \frac{u}{r} + \frac{v}{r}\cot\theta$$

$$d_{r\theta} = d_{\theta r} = \frac{1}{2}\left\{r\frac{\partial}{\partial r}\left(\frac{v}{r}\right) + \frac{1}{r}\frac{\partial u}{\partial\theta}\right\}, \quad d_{r\phi} = d_{\phi r} = \frac{1}{2}\left\{r\frac{\partial}{\partial r}\left(\frac{w}{r}\right)\right\}$$

$$d_{\theta\phi} = d_{\phi\theta} = \frac{1}{2}\left\{\frac{s}{r}\frac{\partial}{\partial\theta}\left(\frac{w}{s}\right)\right\}$$

These equations are complicated and have been checked with Gosman[46].

8.3 NON-DIMENSIONALISATION

As previously in Chapter 3 and 5, the flow equations can be re-written by using non-dimensional transformations. Here we take R_1 (the radius of the outer sphere) as a reference length and the non-dimensional form the vorticity flow equation (7.5) and the rotational speed equation (7.6) takes the form :

Vorticity Equation

$$\mathrm{Re}\left\{\frac{1}{r^2 s}\left[\frac{\partial}{\partial r}\left(ur^2\zeta s\right) + \frac{\partial}{\partial\theta}\left(vr\zeta\right)\right]\right\} = \frac{1}{r^4 s^3}H\left(r^4 s^3, r^2 s^3, \eta.\zeta\right) + F_\zeta \qquad 8.8$$

where

$$H\left(r^4s^3, r^2s^3, \eta.\zeta\right) = \frac{\partial}{\partial r}\left[rR^3\frac{\partial}{\partial r}(\eta\zeta)\right] + \frac{\partial}{\partial\theta}\left[\frac{R^3}{r}\frac{\partial}{\partial\theta}(\eta\zeta)\right]$$

and

$$F_\zeta = rR\left(F_{\zeta\Omega} + F_{\zeta B} + F_{\zeta\eta} + F_{\zeta S}\right).$$

Here the elastic part $F_{\zeta S}$ is taken as zero and $\mathrm{Re} = \dfrac{\rho\Omega R_1^2}{\eta(0)}$.

Rotational Speed Equation

$$\mathrm{Re}\left\{\frac{1}{r^4s^2}\left[\frac{\partial}{\partial r}\left(ur^4\Omega s^3\right) + \frac{\partial}{\partial\theta}\left(vr^3\Omega s^3\right)\right]\right\} = \frac{1}{r^4s^2}H\left(\eta rR^3, \eta\frac{R^3}{r}; \Omega\right) \qquad 8.9$$

where

$$H\left(\eta rR^3, \eta\frac{R^3}{r}; \Omega\right) = \frac{\partial}{\partial r}\left(\eta rR^3\frac{\partial\Omega}{\partial r}\right) + \frac{\partial}{\partial\theta}\left(\eta\frac{R^3}{r}\frac{\partial\Omega}{\partial\theta}\right)$$

and the stream function takes a form as

$$-\omega = \frac{1}{r}H\left(p, q, \Psi\right), \qquad 8.10$$

where

$$H(p,q,\Psi) = \frac{\partial}{\partial r}\left(\frac{p}{s}\frac{\partial\Psi}{\partial r}\right) + \frac{\partial}{\partial\theta}\left(\frac{q}{r^2s}\frac{\partial\Psi}{\partial\theta}\right).$$

Here $p = 1$ and $q = 1$.

8.4 BOUNDARY CONDITIONS

The flow equation, rotational speed equation and vorticity-stream equation are solved numerically by using appropriate boundary conditions on solid walls. We have no-slip boundary conditions on solid walls and the stream function is taken as zero. The

vorticity is calculated on each boundary by using the Woods-stream formulation. Finally, the rotational speed is taken as constant, usually taking a zero or unit value as appropriate.

8.4.1 Spherical Driven Cavity Flow

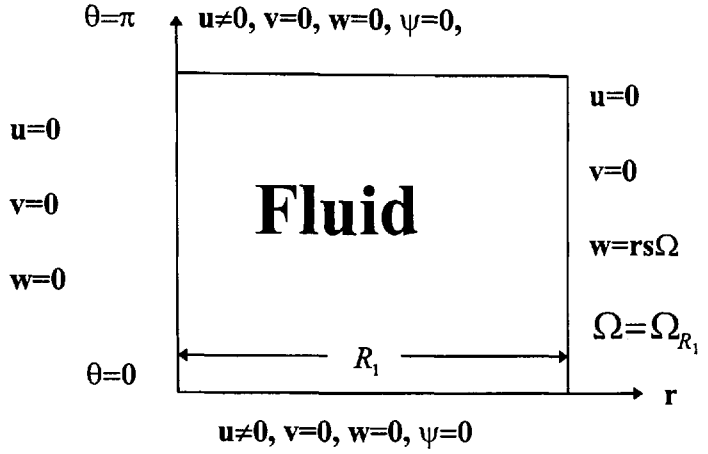

Figure (8.2) ; Boundary conditions for spherical driven cavity flow

On $\theta=0,\pi$ all velocity components become zero except for $u \neq 0$ and $w = R_1\Omega$ on the $R = R_1$. We also have $\frac{\partial \Omega}{\partial r} = 0$ on the vertical walls as well as $\frac{\partial \Omega}{\partial \theta} = 0$ on the horizontal walls due to symmetry.

8.4.2 Concentric Cylinder Driven Cavity Flow

Axisymmetric spherical Couette driven flow between concentric rotating spheres is a famous subject. The boundary conditions for this case are almost similar to the above apart from the left wall. These are as in the figure (8.3) below.

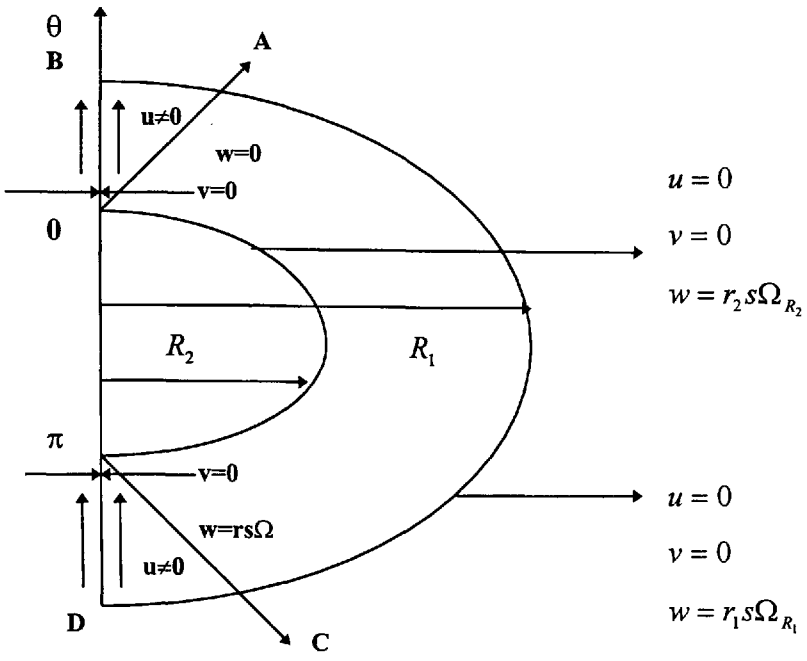

Figure(8.3) ; Flow geometry for concentric sphere driven cavity flow

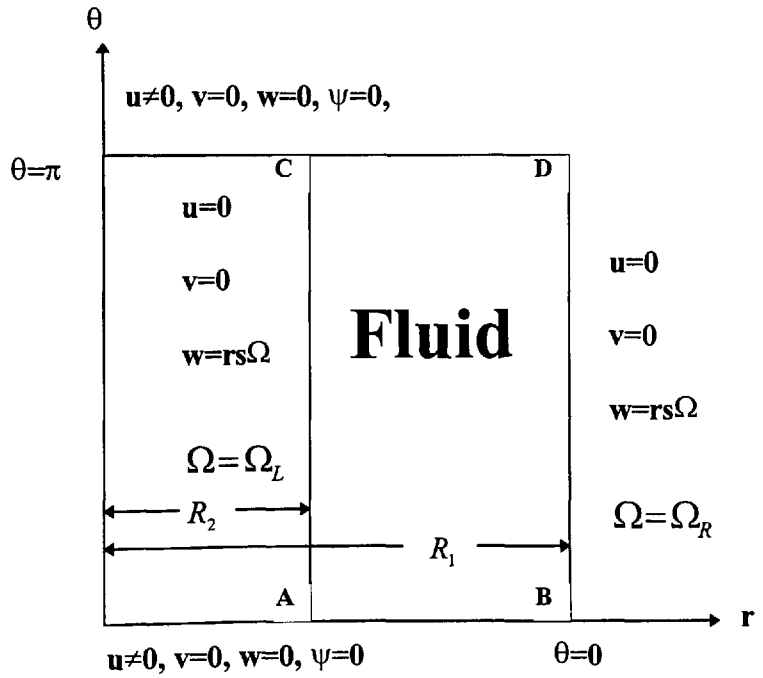

Figure(8.4) ; Boundary conditions for concentric sphere driven cavity flow

8.4.3 Hollow Sphere Driven Flow

Assuming the radius of the inner sphere tends to zero, the configuration becomes one whole sphere. As seen in the figure (8.5), we only express the particular boundary conditions at $r = 0$. The other conditions are as in section 8.4.1.

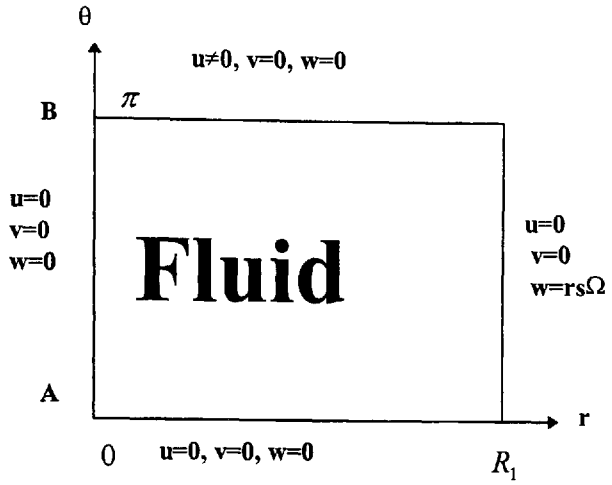

Figure(8.5) ; Boundary conditions for hollow sphere driven cavity flow

At $r = 0$, we have $\Psi = 0$ and $u = v = 0$, and $\omega = 0$. Therefore there are no velocity components on the symmetry line on $r = 0$. The boundary condition for the rotational speed equation is $\frac{\partial \Omega}{\partial r} = 0$.

8.4.4 Fixed Wall Driven Flow

The fluid flow is derived from a bottom hemisphere rotating with constant angular velocity, and the top wall is the flat disk. We can, therefore, present the two figures in this case as follows.

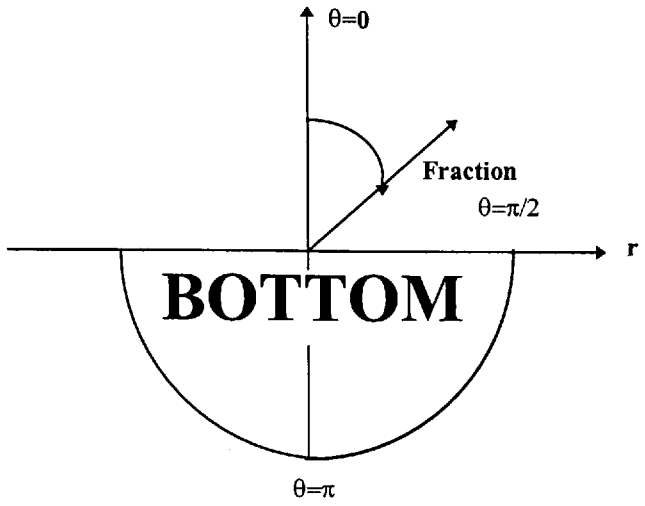

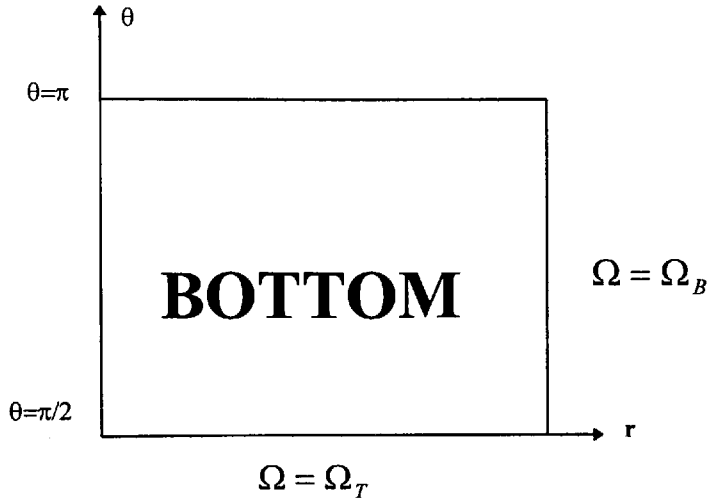

Figure (8.6) ; Flow geometry and boundary conditions for fixed wall driven cavity flow

The velocity components, stream function are defined on the boundaries as before. In this case at the junction of plate and hemisphere there is a boundary singularitie due to different speeds at $\theta = \frac{\pi}{2}$, therefore the shear rate is singular and the viscosity becomes $\eta = \eta(\infty)$.

8.5.5 Free-Surface Driven Flow

The final sphere configuration which is considered is that of hemisphere with a free surface at $\theta = \frac{\pi}{2}$. Here we have the assumed free-surface conditions, on the surface , zero vorticity , zero shear-rate therefore $\frac{\partial \Omega}{\partial \theta} = 0$. The flow geometry is similar to figure (8.6).

8.5 THE NUMERICAL SOLUTION, CONSISTENCY AND STABILITY OF THE SPHERICAL DRIVEN CAVITY DRIVEN FLOW EQUATIONS IN SPHERE

In order to apply the finite difference method, the flow domain is discretised as in figure (8.7) and the differential equations are replaced by a difference operations which are then solved by computer. According to the figure (8.7) which seen below, the computational points are presented as

$E = (i+1, j)$, $W = (i-1, j)$, $N = (i, j+1)$, and $S = (i, j-1)$. The radius of the sphere takes a different value on the each grid point. Also between two grid points we have intersection points of the mesh sides and we refer them as $e = (i+0.5, j)$, $w = (i-0.5, j)$, $n = (i, j+0.5)$, and $s = (i, j-0.5)$. On these points the radius function becomes $r^e = r^P + 0.5h$, $r^w = r^P - 0.5h$, $r^n = r^s = r^P$.

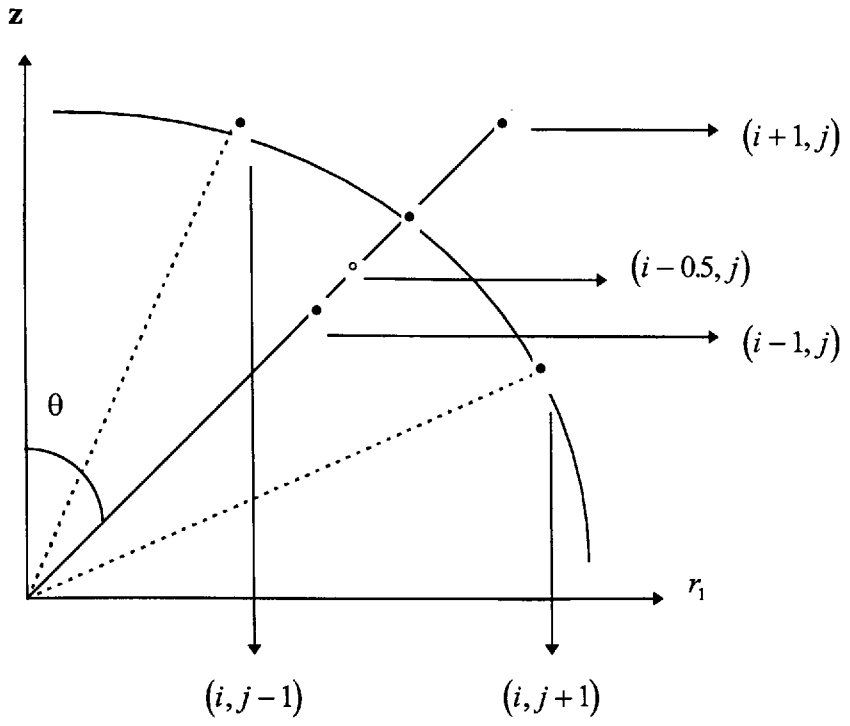

Figure(8.7) ; Diagram of the mesh structure on spherical cavity geometry

The non-linear partial differential equations are solved by the FDM with truncation error $O(\Delta r^2, \Delta\theta^2)$. The co-ordinates of the grid and notation used are shown in the above figure

$$r = r_1 + i\Delta r \qquad i = 0,1,\ldots,M \qquad 8.11$$

$$\theta = j\Delta\theta \qquad j = 0,1,\ldots,N. \qquad 8.12$$

Here R_1 is defined as a radius of inner sphere and Δr is defined the mesh spacing in the direction of increasing r, whereas $\Delta\theta$ denotes the mesh increments in the direction of θ. We define the finite difference approximations to derivatives as previously. Therefore we are now ready to discretise the governing equation of motion by using the finite difference method as follows.

Now considering the stream function as a dependent function in equation (3.42) we have

$$B_1 = 2\frac{\alpha^2}{s^P} + \frac{1}{r^{2P}s^n} + \frac{1}{r^{2P}s^s}$$

$$B_2 = \frac{\alpha^2}{s^P}, \quad B_3 = \frac{\alpha^2}{s^P}, \quad B_4 = \frac{1}{r^{2P}s^n}, \quad B_5 = \frac{1}{r^{2P}s^s}$$

$$B_6 = k^2 r^P \omega^P = k^2 r^{2P} s^P \xi^P$$

where the stability condition is given by $B_1 \geq B_2 + B_3 + B_4 + B_5$ and, $B_2 \geq 0$, $B_3 \geq 0$, $B_4 \geq 0$, $B_5 \geq 0$ as in Chapter 3.

For the rotational speed equation we have the following coefficients

$$B_{\Omega 1} = \alpha^2 \left\{ \left(\eta^E + \eta^P\right) r^{4e} s^{3P} + \left(\eta^W + \eta^P\right) r^{4w} s^{3P} \right\}$$

$$+ \left\{ \left(\eta^N + \eta^P\right) r^{2P} s^{3n} + \left(\eta^S + \eta^P\right) r^{2P} s^{3s} \right\}$$

$$B_{\Omega 2} = \alpha^2 \left\{ \left(\eta^E + \eta^P\right) r^{4e} s^{3P} - \mathrm{Re}\, h u^E r^{4E} s^{3P} \right\}$$

$$B_{\Omega 3} = \alpha^2 \left\{ \left(\eta^W + \eta^P\right) r^{4w} s^{3P} + \mathrm{Re}\, h u^W r^{4W} s^{3P} \right\}$$

$$B_{\Omega 4} = \left\{ \left(\eta^N + \eta^P\right) r^{2P} s^{3P} - \mathrm{Re}\, k v^N r^{3P} s^{3N} \right\}$$

$$B_{\Omega 5} = \left\{ \left(\eta^S + \eta^P\right) r^{2P} s^{3P} - \mathrm{Re}\, k v^S r^{3P} s^{3S} \right\}$$

$$B_{\Omega 6} = 0.$$

For ξ we have

$$B_{\xi 1} = \frac{1}{\eta^P r^{2P} s^{2P}} \left\{ \alpha^2 \left[\left(\eta^E + \eta^P\right)^2 r^{4e} s^{3P} + \left(\eta^W + \eta^P\right)^2 r^{4w} s^{3P} \right] \right.$$

$$- \alpha^2 \left[\eta^P \left(\eta^E - \eta^P\right) r^{4e} s^{3P} - \eta^P \left(\eta^P - \eta^W\right) r^{4w} s^{3P} \right]$$

$$+ \left[\left(\eta^P + \eta^N\right)^2 r^{2P} s^{3n} + \left(\eta^P + \eta^S\right)^2 r^{2P} s^{3s} \right]$$

$$\left. - \left[\eta^P \left(\eta^N - \eta^P\right) r^{2P} s^{3n} - \eta^P \left(\eta^P - \eta^S\right) r^{2P} s^{3s} \right] \right\},$$

$$B_{\xi 2} = \alpha^2 \left\{ \frac{1}{\eta^P r^{2P} s^{2P}} \left[\left(\eta^E + \eta^P \right)^2 r^{4e} s^{3P} \right] - \mathrm{Re}\, h u^E r^{2E} s \right\},$$

$$B_{\xi 3} = \alpha^2 \left\{ \frac{1}{\eta^P r^{2P} s^{2P}} \left[\left(\eta^W + \eta^P \right)^2 r^{4w} s^{3P} \right] + \mathrm{Re}\, h u^W r^{2W} s \right\},$$

$$B_{\xi 4} = \left\{ \frac{1}{\eta^P r^{2P} s^{2P}} \left[\left(\eta^N + \eta^P \right)^2 r^{3n} s^{2P} \right] - \mathrm{Re}\, k v^N r^P s^N \right\},$$

$$B_{\xi 5} = \left\{ \frac{1}{\eta^P r^{2P} s^{2P}} \left[\left(\eta^S + \eta^P \right)^2 r^{3s} s^{2P} \right] + \mathrm{Re}\, k v^S r^P s^S \right\}$$

$$B_{\xi 6} = 2k^2 r^2 s F_{ik}\,.$$

We solve the resulting equations by the Gauss-Seidel method. We discussed consistency and stability of the methods used in chapter 3 and we explained the numerical check for vorticity equation briefly. Since we work in (r,θ) system the vorticity constraint is determined as

$$\iint_A \omega dA = \iint_A Curl V_i dA = \qquad 8.13$$

$$\iint_A rs\xi dr d\theta = \iint_{(r,\theta)} f(r,\theta)\xi dr d\theta = \iint_A \left\{ \left[\frac{\partial}{\partial r}(rv) - \frac{\partial u}{\partial \theta} \right] dr d\theta \right\} =$$

$$\int_{\theta=0}^{\theta=\beta} \left[rv \right]_{r=R_1}^{r=R_2} d\theta - \int_{r=R_1}^{r=R_2} \left[u \right]_{\theta=0}^{\theta=\pi} dr = - \int_{r=R_1}^{r=R_2} \left[u(\theta=0) - u(\theta=\pi) \right] dr\,.$$

Here $u(\theta=0)$ and $u(\theta=\pi)$ represent the bottom and top wall velocity components in the r direction respectively.

8.6 RESULTS FROM THE 3D SPHERICAL DRIVEN CAVITY FLOW

We generated results for various grids ranging from 10x10 to 50x50. All grid sizes give similar results and we give illustrations for a 40x40 grid. Most results derived from this problem are new except for the concentric sphere driven case.

8.6.1 Spherical driven cavity flow

We have results for Newtonian, pseudoplastic and dilatant fluid up to Reynolds number 100 generated by a rotating right wall. We have the same results qualitatively for all fluids considered so that two main vortices are produced and the streamlines are symmetric about the cavity's horizontal and vertical mid-lines, shown in fig(8.7) at Re=1. As Re increases the inertial force affects to the flow and therefore enlarged vortices behaviour is observed for all fluids considered, shown in fig(8.8).

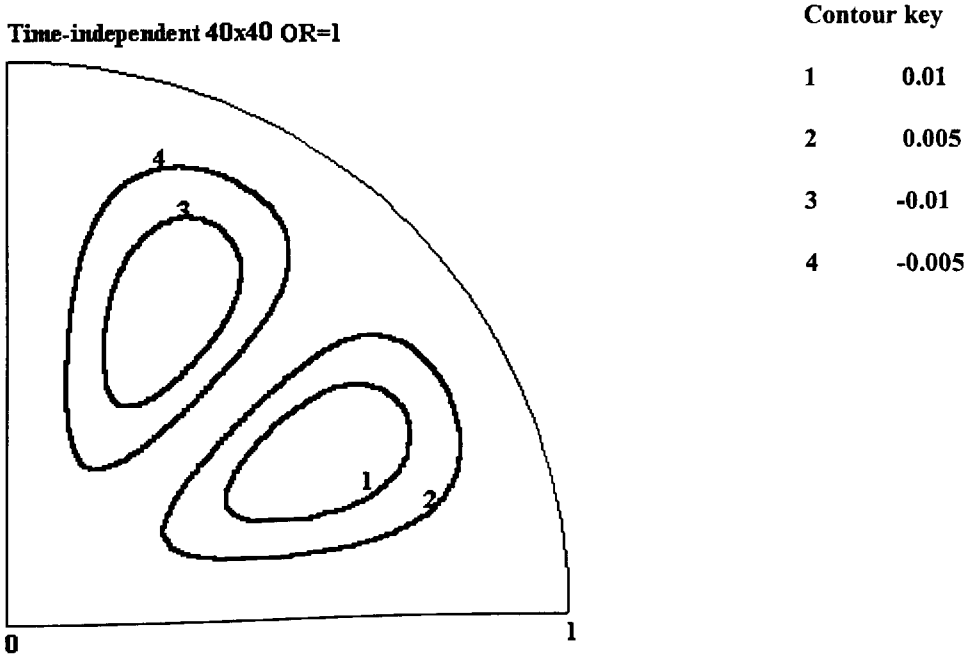

Figure (8.7) ; Streamline contours for dilatant fluid at Re=1

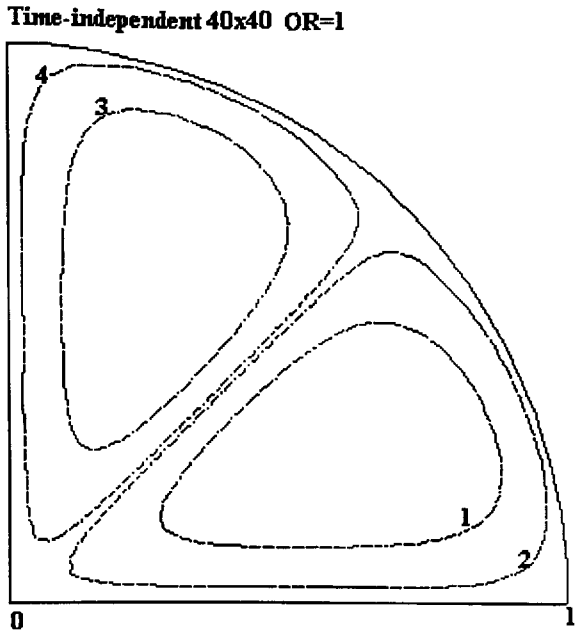

Contour key

1	0.01
2	0.03
3	-0.01
4	-0.03

Figure (8.8) ; Streamline contours for Newtonian fluid at Re=100

8.6.2 Concentric sphere driven cavity flow

In this section we have results for the concentric driven sphere case. In the case of the left wall rotating, two main vortices are produced and the streamlines are symmetric about the cavity's mid-lines. They appear to be more circular in the fluid, shown in fig(8.9) - (8.10) at Re=1 and Re=100 respectively. This behaviour is valid in both Newtonian and inelastic non-Newtonian fluid cases.

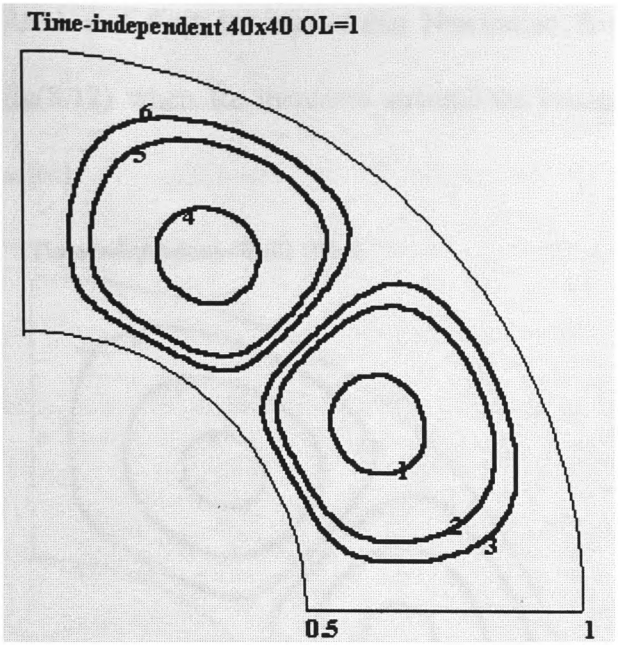

Contour key	
1	0.01
2	0.03
3	0.005
4	-0.01
5	-0.03
6	-0.005

Figure (8.9) ; Streamline contours for pseudoplastic fluid at Re=1

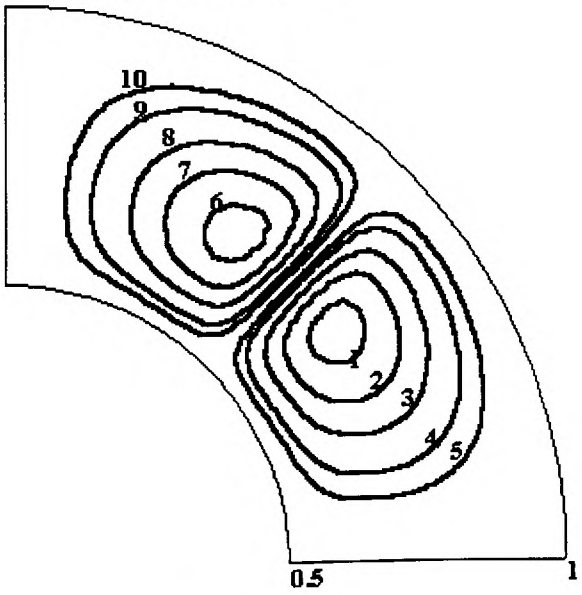

Contour key	
1	4
2	3
3	2
4	1
5	0.5
6	-4
7	-3
8	-2
9	-1
10	-0.5

Figure (8.10) ; Streamline contours for pseudoplastic fluid at Re=100

In case of the right wall rotating, two main vortices are obtained in the fluid and the streamlines are symmetric about the cavity's vertical and horizontal mid-lines for all fluids considered. Fig(8.11) shows that inelastic pseudoplastic fluid behaviour at

Re=1 and fig(8.12) shows that Newtonian fluid behaviour at Re=100. As seen in fig(8.12) when Re increases streamlines becomes more compact due to the inertia effect.

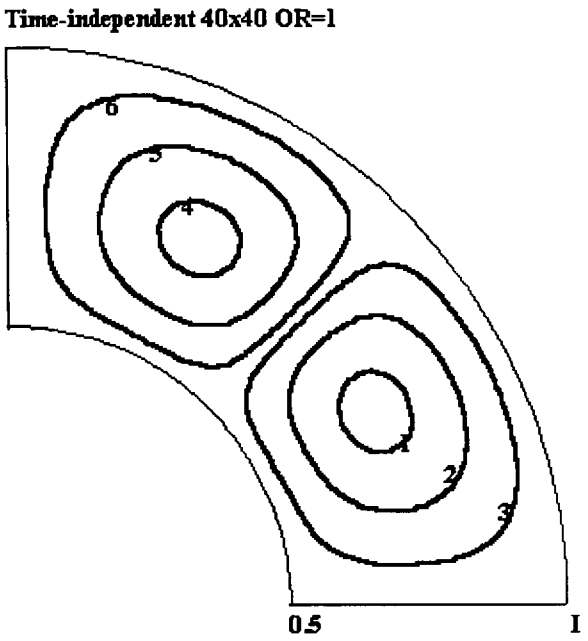

Contour Key	
1	0.1
2	0.01
3	0.05
4	-0.1
5	-0.5
6	-0.05

Figure (8.11) ; Streamline contours for pseudoplastic fluid at Re=1

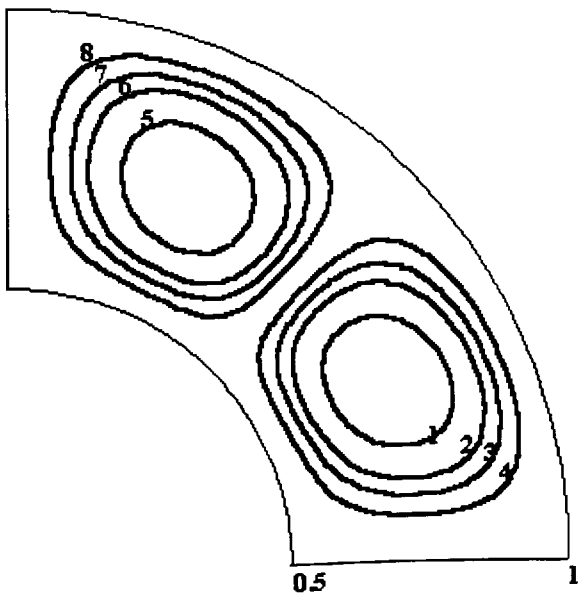

Contour key	
1	2.5
2	1.5
3	1
4	0.5
5	-2.5
6	-1.5
7	-1
8	-0.5

Figure (8.12) ; Streamline contours for Newtonian fluid at Re=100

The final problem considered in the case of the concentric sphere driven flow is that generated by two side walls which rotate in opposite direction. Similarly two main vortices are observed and the streamlines are symmetric, shown in fig(8.13). This behaviour is valid for both Newtonian and non-Newtonian fluids. As Re increases we still have similar behaviour in the fluid.

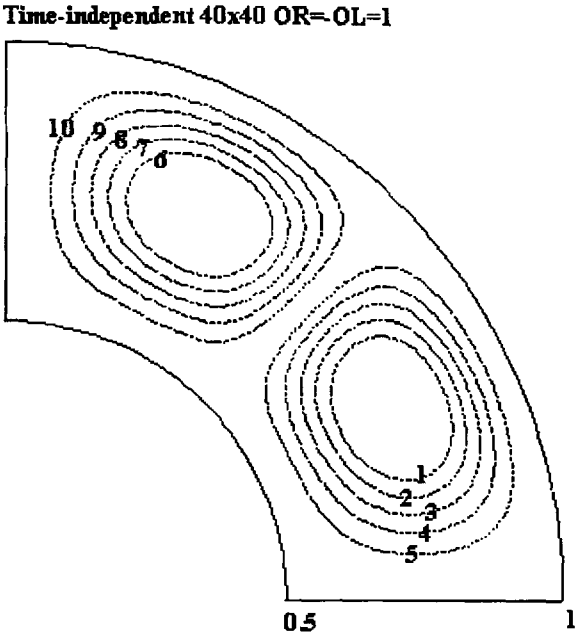

Contour key	
1	0.1
2	0.08
3	0.006
4	-0.004
5	-0.002
6	-0.1
7	-0.08
8	-0.006
9	- 0.004
10	-0.002

Figure (8.13) ; Streamlines contours for dilatant fluid at Re=1

7.6.3 Hollow sphere driven cavity flow

In this section fluid flow is generated by a hollow sphere as defined previously with constant rotating angular velocity and we have results in both Newtonian and non-Newtonian fluids with various Reynolds numbers. We have two equal and symmetric vortices in flow domain. As the Reynolds number increases the streamlines become more compact and stronger. As shown in fig(8.14) we illustrate the Newtonian fluid at Re=1.

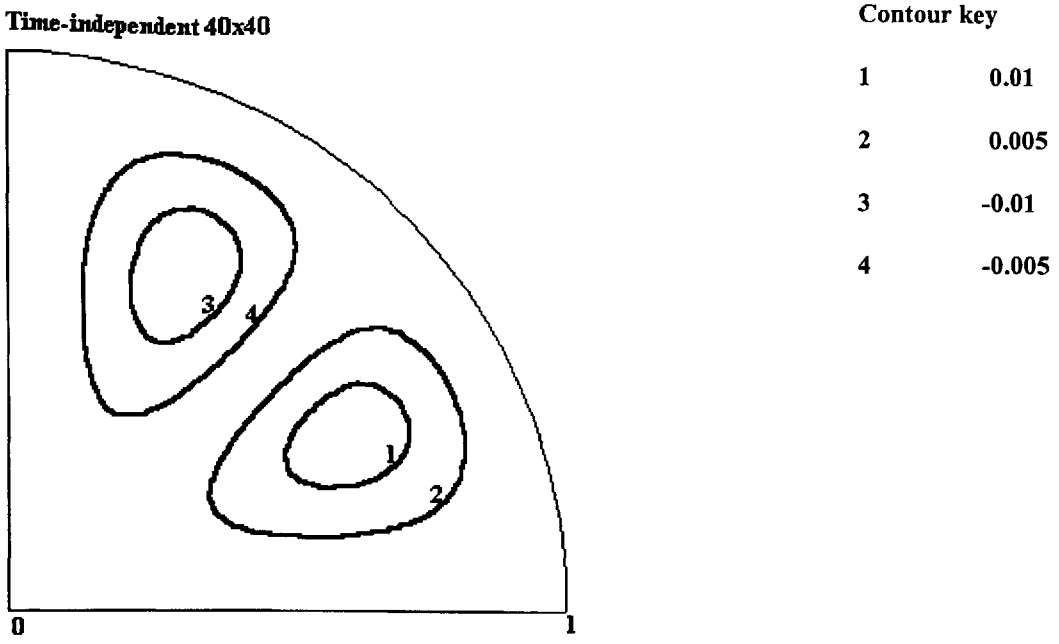

Figure (8.14) ; Streamline contours for Newtonian fluid at Re=1

7.6.4 The hemispherical fixed wall problem

In this case the flow is derived by rotation of the top and bottom walls. We have results in both Newtonian and non-Newtonian fluids by considering one wall rotating with a constant angular velocity. Fig (8.15) presents results for bottom wall rotation. With Re=1 we have one vortex in the flow. This result is valid for both Newtonian and non-Newtonian fluids.

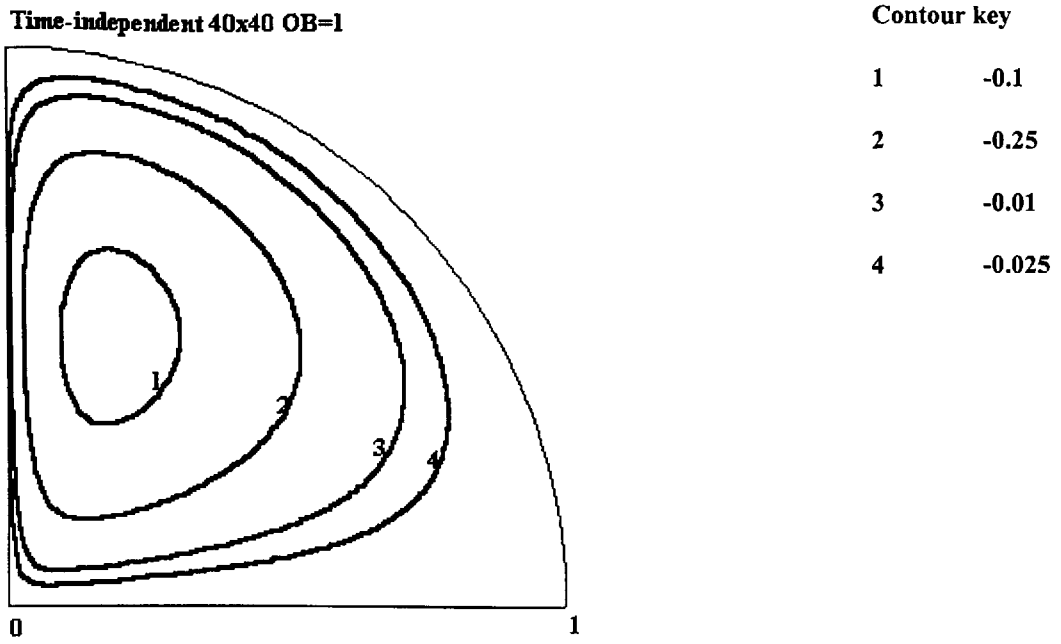

Figure (8.15) ; Streamline contours for Newtonian fluid at Re=1

As the Reynolds number increases, the vortex exist over larger area in the flow domain and streamlines become more compact in flow, and the shape of the flow change. We observed a second vortex in case of a dilatant fluid shown in fig(8.16). For the Newtonian and pseudoplastic fluids, results are similar to the dilatant fluid without a second vortex materialising.

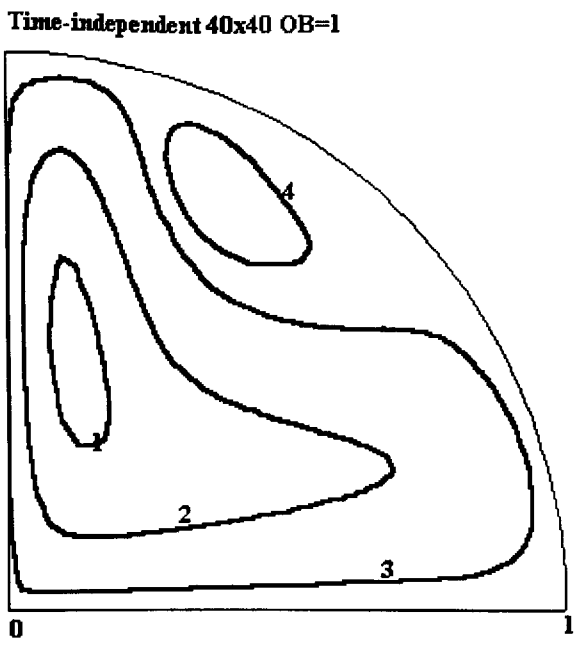

Figure (8.16) ; Streamline contours for dilatant fluid at Re=100

Flow is generated by top wall rotation and one main vortex is observed for all fluids considered. The vortex centre is located at approximately (0.1, 0.5), shown in fig(8.17). As Re increases the vortex exist over larger area and its centre moves to the top plate. Its centre is located at (0.1, 0.65) in the fluid, shown in fig(8.18).

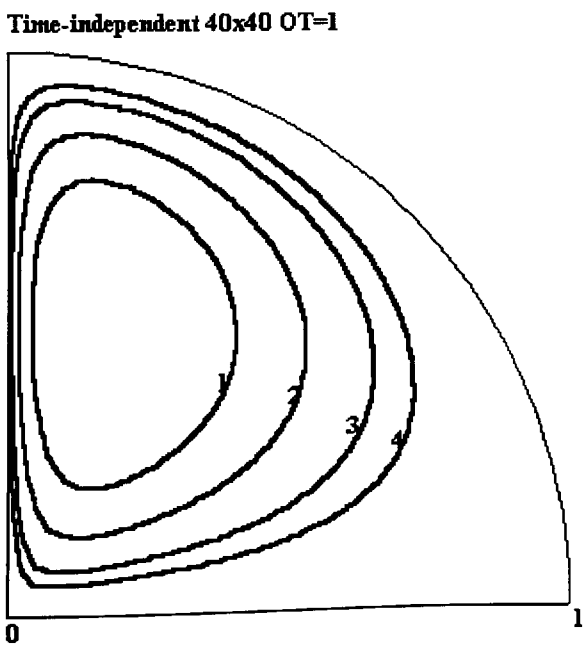

Figure (8.17) ; Streamline contours for Newtonian fluid at Re=1

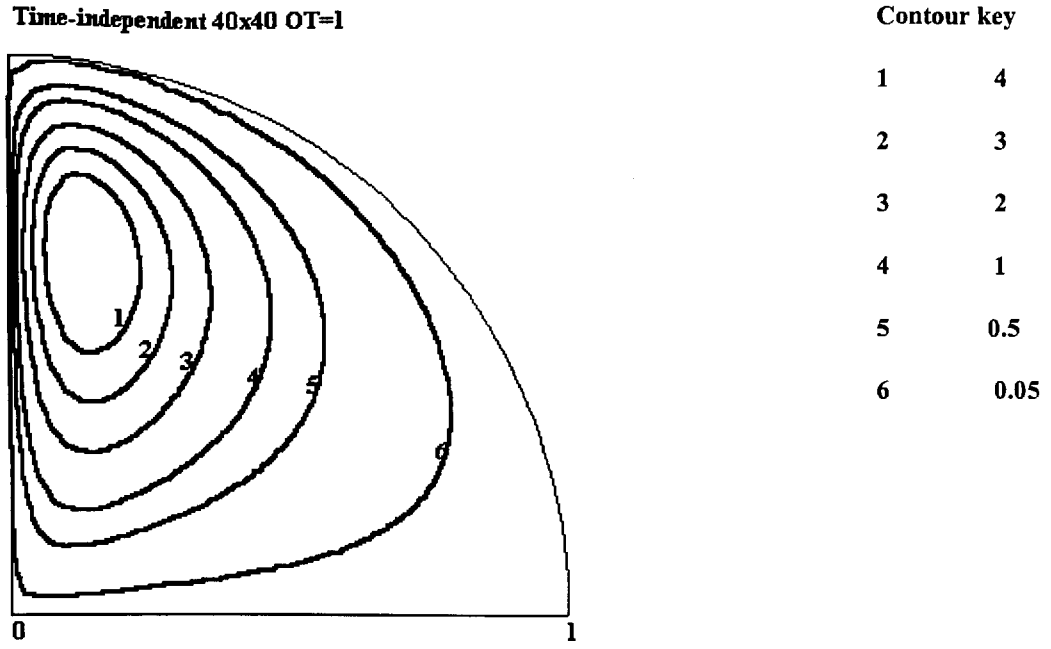

Figure (8.18) ; Streamline contours for dilatant fluid at Re=100

7.6.5 Free-surface problem for hemisphere

Here flow is only generated by rotation of the bottom wall. We have results up to Re=200. Fig(8.19) shows that one main vortex is produced and the vortex centre is located at (0.3, 0.7). As Re increases the vortex moves to the top wall and its centre is located at (0.2, 0.8) approximately at Re=100.

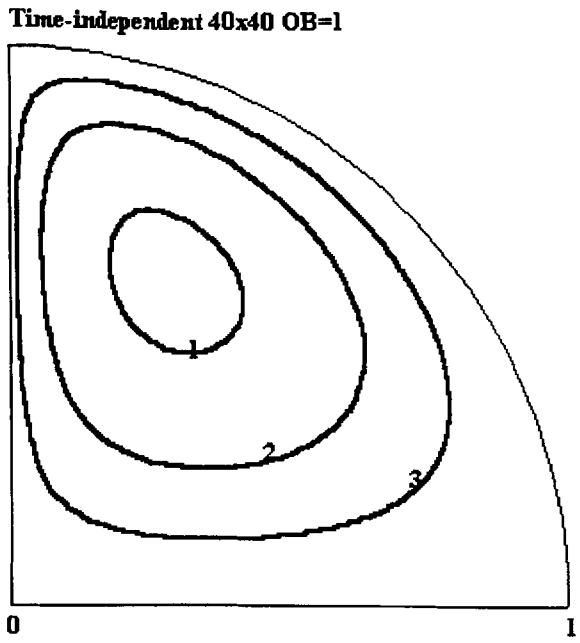

Contour key

1	-0.25
2	-0.1
3	-0.025

Figure (8.19) ; Streamline contours for Newtonian fluid at Re=1

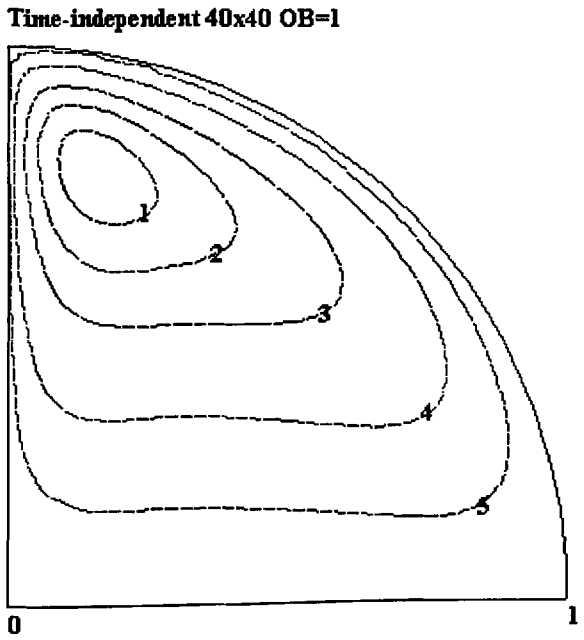

Contour key

1	-3.5
2	-2.5
3	-1.5
4	-0.5
5	0.1

Figure (8.20) ; Streamline contours for dilatant fluid at Re=100

In conclusion the steady state incompressible viscous flow usually generated a pair of vortices and the streamlines are symmetric about the cavity's vertical and horizontal

mid-lines for all fluids considere for spherical, concentric sphere and hollow sphere container. As the Re increases the vortices exist over large area in flow. For fixed wall and free-surface sphere container one main vortex produced and as Re increases a second vortex is observed at Re=100 in the case of dilatant fluid for hollow sphere container.

CHAPTER IX: SUMMARY, CONCLUSIONS AND FUTURE WORK

9.1: INTRODUCTION

This research project mainly consists of the computer simulation and analysis of the stability properties of viscous and viscoelastic fluids in both 2D and 3D geometries.

The stability of wall driven and thermally driven cavity flow was investigated for a wide range of non-Newtonian fluids. The effects of inertia, elasticity, temperature gradients, viscous heating and Biot boundary conditions were of particular interest. The flow was generated by the following cases.

i) Wall driven motions in a 2D rectangular cavity as well as by the wall rotating with a constant angular velocity in cylindrical and spherical cavities.

ii) Thermally induced from buoyancy forces of the cavity in a 2D rectangular or 3D cylindrical geometries.

The numerical approach adopted was the Finite Difference Method since all the geometries to be considered are topologically equivalent to rectangles. The aims of the investigation were as follows:

1) To solve both the steady and transient flows of viscous and viscoelastic fluids numerically in the 2D slot, the 3D cylinder and sphere geometries.

2) To seek the flow stability properties in the wall driven and thermally driven 2D slot for viscous and viscoelastic fluids in terms of control parameters. However,

mixing properties were also investigated by tracking the motion of a selected number of fluid particles and by simulating the dispersive mixing of a 'coloured' fluid injected into the cavity while at rest.

3) To determine the rotating wall and thermal driven flow behaviour, and seek the stability properties of the viscous and viscoelastic fluids in the 3D cylinder geometry. Mixing was examined as in the previous case for the 2D geometry.

4) In the 3D sphere geometry, the numerically generated wall rotating behaviour is examined and the stability properties were sought for the steady state viscous flow only.

For the stability properties of wall driven and thermally driven cavity flow the effects of the control parameters were of interest. The instabilities are characterised by control parameters: the Reynolds, Weissenberg, Rayleigh, Biot and Eckert numbers.

In the 2D numerical simulation of viscous and viscoelastic fluids with constant or variable viscosity, we first considered the convergence properties of the numerical solutions by comparing calculations for various grid widths denoted by h. On comparing values of vorticity and stream function we had evidence that convergence to 4 decimal places has been achieved at Re=1 and Re=100 as h decreased. We also checked the effect of the convergence tolerance, ε, on the accuracy of the solution for both vorticity and stream function. It was found that when ε ranged from 10^{-1} to 10^{-5} for both vorticity and stream function, the solution was seen to be more quickly convergent with respect to the mesh size.

A second comparison was made to check the convergence of the vorticity test criterion. This was seen to be more strict than pointwise convergence with respect to the mesh size with slower convergence.

A third comparison was a graphical comparison of centre line u-velocity for a Reynolds number of 100 and 1000 for both Newtonian and non-Newtonian fluids. In the literature only Newtonian fluid data was found with which to compare our results. Our results agree very well with Tosoka et al.**[94]** both qualitatively and quantitatively. In addition, non-Newtonian pseudoplastic results were obtained at Re=100 and Re=1000 and displayed an interesting and significant change from the Newtonian case. Here there is less viscosity near the top wall and flow is faster there. However Boger and dilatant fluids flow show similar behaviour to the Newtonian fluid.

Finally to establish the accuracy of the results obtained in this research we compared our results qualitatively and quantitatively with those obtained by Cliffe et al**[17]**, Ottino**[67-68]**, Chien et al**[15]**, Davies**[23]** and Harvard**[40]** and found favourable agreement. The study was then extended to viscoelastic fluids to seek the qualitatively different dynamical behaviour arising from the tendency of elasticity to opposite inertia. In this case we obtained different flow patterns attributed to elasticity at various aspect ratios of the geometry. For example, two main vortices were produced being symmetrical mirror images of each other in the case of two walls moving in the same direction with unit aspect ratio for inelastic flow. When elasticity was incorporated the symmetry between two vortices was broken at Re=1. As Re

increases the symmetry line becomes straighter. This elasticity effect was also seen when for an aspect ratio of 2.

The corner singularity in the 2D flow was also investigated. It was determined that flow near the corner singularity for the shear dependent Newtonian and non-Newtonian purely viscous flows can be regarded as Stokesian flow. When the same analysis was undertaken for the viscoelastic fluids it was found that they can behave as Stokesian flow near the corner for the constant viscosity case. However the problem remains unresolved for variable viscosity fluids.

In the thermal driven case we firstly considered the convergence of the solutions by comparing calculations for various mesh sizes, as before, in both the A. D. I. and simple explicit cases. In this case we chose the Bench-Mark problem where the control parameters are taken as Re=1, Pr=1 and $Ra=10^5$. By comparing values of vorticity and temperature it was evident that convergence to 4 decimal places was achieved as grid width decreased, and the A. D. I. method was found be more desirable than simple explicit method. Therefore the A. D. I. method was chosen to illustrate the results.

The second comparison was to establish the accuracy to the results obtained with those obtained by Torrance and Turcotte**[93]**, Mckenzie**[57, 58]**, and De Vahl Davis**[24]**. This comparison showed that our results agreed well with the latter author's results. This study was then extended to investigate the stability properties and cell behaviour for viscoelastic fluids. A number of control parameters such as Ra, Bi and Ec numbers were used. In this case a number of significant results were established as follows:

1) For both viscous and viscoelastic fluids the Biot and Ec numbers were found to have a significant role in the flow causing one cell to flow into two cells and vice-versa. As the Ra number increased the computer program failed to converge to a solution.

2) All two vorticity boundary conditions have been found to have a significant role in determining the outcome of the final solution. When a solid wall boundary condition was considered, the cell configuration produced was more curved in appearance and a 'oval' shape due to shear-stresses effects on each of the cavity's walls and free-shear flow produced more 'rectangular' and symmetric cells due to the absence of wall stresses. Also the zero vorticity boundary condition was found to converge to a solution for all Ra considered.

3) The non-zero vorticity boundary values (solid wall) produced similar results for both viscous and viscoelastic fluids and the same number of cells were found for both cases. It was seen that the computer program failed to converge to a solution at $Ra=10^6$. When the Biot number and Eckert numbers are used together or separately, two mirror image counter rotating cells were usually found. It is possible to state that Biot condition and viscous heating produced different solutions and increased the number of vortex cells.

4) The zero vorticity boundary values produced similar results for both viscous and viscoelastic fluids up to $Ra \leq 10^6$. Again two mirror image counter rotating cells for both viscous and viscoelastic fluids were obtained. This case is also known as the Rayleigh-Benard configuration where the Biot number was seen to have a major role in determining the final solution. When the Biot number increased, two

mirror image counter rotating cells were common especially at $Ra=10^4$. Moreover the Eckert number caused instability in most cases with or without the Biot number. Similarly we can say that the Biot number produced a number of different vortex solutions with various Ra values in this case as well.

5) Interesting results were found when the fluid viscosity varied with temperature in the Rayleigh-Benard case. When the constant 'k' (in the exponential term which governs the rate at which the viscosity changes with temperature) values increased, two cell production occurred for the Newtonian and dilatant fluid at k=1. The Biot condition was similarly seen to have a significant role in determining the final solution. In fact at $Ra=10^4$ it was usual to have two mirror image counter rotating cells, and then as Ra increases the cell numbers decrease and the computer program did not give any solution for non-Newtonian fluids.

In the 3D cylindrical case we first considered the convergence of the solution by comparing calculations for various grid widths for the Newtonian and non-Newtonian fluids. For the vorticity in both time-dependent and time-independent wall driven flow it was evident that convergence to four decimal places had been achieved at Re=10 as grid size decreased. Secondly we compared our results qualitatively and quantitatively with Pao[73] and it was seen that our results were in agreement. The study was then extended to viscoelastic fluids to examine the rotating wall effect on fluid flow and to seek the stability properties in three different categories such as cylinder, concentric cylinder and free-surface cylinder driven flow. Similar consideration was given to the mixing problem as in 2D.

In this case a number of results were established in the following areas:

1) Cylinder driven cavity flow: In the case of the two walls rotating in opposite directions, two main vortices were produced being symmetrical mirror images of each other. As Re increased the vortex centres moved to the cavity's outer corner at Re=100. The case of two walls rotating in the same direction produced similar behaviour as the above. When only the top wall rotates one oval vortex was produced at low Re. As the Re increases the vortex shifts and changes its shape and location in the cavity.

2) Concentric cylinder driven cavity flow: Two main vortices were produced being symmetrical mirror images of each other, when the two walls were rotating in either the same or in opposite direction. The only cause for the vortices change of shape and size was due to inertial effects. Also as the flow became stronger the vortex centres were found to move to the cavity's corner as before. When four wall motion was undertaken two main vortices were produced and the symmetry was maintained between them. In the case of the top wall rotating, one main vortex was produced and as the Re increased the vortex was found to move towards the top right corner.

3) Free-surface cylinder driven flow: In this case the steady state and unsteady state cases produced different solutions. Two main vortices were produced that were asymmetrical for the unsteady case. By contrast, one main vortex was produced for the steady state case.

For the concentration and particle paths new results for shear-dependent viscoelastic fluid flow were found. We sought mixing properties in two cases, either by simulating the dispersive mixing of a 'coloured' fluid injected into the cavity while

at rest, or by tracking the motion of a selected number of fluid particles which were initially distributed vertically within the cavity, by using discontinuous periodic wall motion. For low Reynolds number the 'coloured' band spread out horizontally in the cavity's centre region because of the relatively weak flow induced and diffusion was dominant. As the Reynolds number increases there is better fluid transportation and associated dispersive mixing. On considering mixing properties by tracking particles paths, it was found that for low Reynolds number the particles followed the streamline and paths became 'flatter' nearer the top plate. Moreover as Re increases the particle paths become more 'tightly bound' in the flow for both the cylinder and concentric cylinder cases.

For the thermally driven cylinder cavity flow where flow was generated by solid wall boundary conditions, it was found that the computer program's convergence to a final solution was more sensitive with respect to the control parameters. In this case only small Ec values gave solutions and had little effect on flow. The Biot number was taken as 0 or 0.1. It was found that as Ra increased the computer program failed to converge to a solution . It was also found that different fluids produced different solutions. When the viscosity varies with temperature, instability occurs in the flow domain through the elastic effect as Ra increases. When k increased the stability was again lost and we did not have any solution.

In the case of the concentric cylinder driven cavity flow, it was found that the fluid properties played a significant role in determining the final solution. In the case of variable viscosity fluids almost a 'parallel' temperature distribution was found as with the initial condition for the non-Newtonian dilatant fluid at $Ra=10^4$. Also two

rotating cells emerged from one at $Ra=10^5$. When Bi was taken as 0.1 constant viscosity fluids did not permit any solutions.

In the spherical case, two main vortices were produced being symmetrical mirror images of each other with various Re for whole sphere, concentric sphere, and hollow hemi-sphere wall driven cavity flows. Interesting results were found in the case of the fixed wall sphere flow cases, since the secondary flow created a second vortex at Re=100.

9.2: RECOMMENDATIONS FOR FUTURE WORK

On the basis of research carried out we therefore have some ideas for future work developed on that presented already.

1) The research on cavity driven flows may be developed to obtain more detailed numerical solutions for vortex dynamics and evaluation to examine the stability properties for both viscous and viscoelastic fluids by using the discontinuous periodic motion in 2D. This may be achieved in both wall and thermal driven cases.

2) The work carried out for the two dimensional cavity driven flow may be extended with a different gravity angle (sloped cavity) to obtain numerical results in both wall and thermal driven cases.

3) A further development of the thermally driven cylindrical cavity flow would be to study the vortex development and stability conditions by using discontinuous periodic motion for both viscous and viscoelastic fluids. In addition to this study a 'different gravity angle' may be chosen.

4) For the spherical wall and thermal driven cases, a further development can be to consider the time-dependent flow solutions in both viscous and viscoelastic cases. Also the mixing efficiency, particle paths and stability properties can be included in this case.

5) Similarly by using the discontinuous periodic motion the vortex development can be studied in the spherical case for both wall and thermal driven cases. Also a 'different gravity angle' may be studied.

REFERENCES

1. **AREF H.,** J. Fluid Mech. **143**, 1-21, 1984.
2. **AVGOUSTI M. et al.,** Int. J. Num. Meth. Fluids **17**, 49-74, 1993.
3. **BATCHELOR G . K .,** J. Fluid Mech. **1(2)**, 177-190, 1956.
4. **BATCHELOR G . K .,**Introduction to Fluid Dynamics, Cambridge University Press, 1967.
5. **BATCHELOR G. K.** Quarterly Appl. Maths. **12,** 209-233, 1954.
6. **BECKMANN W.,** Forsch. Geb. Ingenieurwes **2(5)**, 165, 1931.
7. **BIRD R. B., ARMSTRONG R. C. and HASSAGER O.,**Dynamics of Polymeric Liquids, Vol. 1, Fluid Dynamics,John Wiley and Sons New York 1977.
8. **BIRD R. B., STEWART W. E. and LIGHTFOOT E. D.,** Transport Phenomena, John Wiley and Sons, New York 1960.
9. **BODALIA V.,** Ph.D Thesis, Depts. of Chem. Eng., Maths and Computing, The Polytechnic of Wales, 1986.
10. **BOZEMANN J. D. and DALTON C.,** J. of Computational Physics, **12**, 348-363, 1973.
11. **BRANDON M. B., et al.,** Rheol. Acta **34**, 147-159, 1995.
12. **BUHLER K.,** Acta Mechanica **81**, 3-38, 1990.
13. **BURDEN R. L. and FAIRES J. D.,** Numerical Analysis, Fourth Edition, Boston, Mass., Pws-Kent Pub. co. 1989.
14. **BURGGRAF O. B.,** J. Fluid Mech.., **24**, 113-151, 1966.
15. **CHIEN W. L. et al.,** J. Fluid Mech. **170**, 355-377, 1986.
16. **CHOW, CHUEN-YEN,** An Introduction to Computational Fluid Mechanics,John Wiley and Sons, New York 1979.
17. **CLIFFE K. A. et al.,** Theoretical Physics Division, U. K. AERE, Harwell Rep. R. 9202, 1978.
18. **COMPUTER METHODS IN FLUIDS, (K. MORGAN et al.),** Pentech Press, London: Plymouth, 1980.
19. **CORMACK D. E., LEAL L. G. and IMBERGER J.,** J. Fluid Mech. **65**, 209-229, 1974.
20. **CORMACK D. E., LEAL L. G. and SEINFELD J. H.,** J. Fluid Mech. **65**, 231-246, 1974.
21. **CROCHET M . J., DAVIES A . R .and WALTERS K .,**Numerical Simulation of Non-Newtonian Flow, Rheology Series 1, Elsevier 1984.
22. **DAVIES A . R. and X .K . LI,** J. Non-Newtonian Fluid Mech., **54**, 331-350, 1994.
23. **DAVIES N. H.,** Ph.D. Thesis, Dept. of Maths and Computing, The University of Glamorgan 1993.
24. **De VAHL DAVIS G.,** Int. J. for Num. Meth. in Fluids, **3**, 249-264, 1983.
25. **DEMIR H.,** M.Sc. Thesis, Dept. of Applied Maths, University Of Wales, Aberystwyth, 1993.
26. **DI PRIMA R. C., and SWINNEY H. L.,** Springer-Verlag, New York, 1985.
27. **DRAZIN P. G., and REID W. H.,** Hydrodynamic Stability, Cambridge University Press, New York, 1981.
28. **ECKERT E. R. G. and CARLSON W. D.,** Int. J. Heat Mass Transfer, **2**, 106-120, 1961.
29. **ELDER J. W.,** J. Fluid Mech. **23**, 77-98, 1965.
30. **EMERY A. et al.,** J. Heat Transfer, **93**, 164-171, 1971.

REFERENCES

31. **ESCUDIER M. P., et al.,** Proc. R. Soc. London A, **449**, 155-176, 1995.
32. **FROBERG C. E.,** Numerical Mathematics, Benjamin/Cummings, 1985.
33. **GEBHART B., JALURIA Y., MAHAJAN R. L. and SAMMAKIA B.,** Buoyancy Induced Flows and Transport, Hemisphere, Washington, 1988.
34. **GILL A. E.,** J. Fluid Mech. **26**, 515-536, 1966.
35. **GOSMAN W. M., et al.,** Heat and Mass Transfer In Recirculating Flows, Academic Press, New York, 1969.
36. **GRIFFITHS D. F. and WALTERS K.,** J. Fluid Mech. **42**, 379, 1970.
37. **GRIFFITHS D. F. et al.,** J. Fluid Mech. **36**, 161, 1969.
38. **GULWADI S. D.,and ELKOUH A. F.,** Applied Scientific Research **49**, 147-159, 1992.
39. **GUPTA M. M. and MANOHAR R.P.,** J. of Comp. Physics, **31**, 265-268, 1979.
40. **HAVARD S. P.,** Ph.D. Thesis, Dept. of Maths and Computing, The Polytechnic of Wales 1989.
41. **IMBERGER J.,** J. Fluid Mech. **65**, 247-260, 1974.
42. **KAWAGUTI M.,** J. Physics Soc. Japan, **16**, 2307, 1961.
43. **KHAKHAR et al.,** J. Fluid Mech. **172**, 419-451, 1986.
44. **KRAMER J. M. and JOHNSON M. W.,** Trans. Rheol. **16**, 197-212, 1972.
45. **KRAUSSOLD H.,** Forsch. Geb. Ingenieurwes **5**, 186, 1934.
46. **KURIYAMA et al.,** AIChE **28**, 385, 1982.
47. **LAPIDUS L. and PINDER G. F.,**Numerical Solution of Partial Differential Equations in Science and Engineering,John Wiley and Sons Inc. New York 1982.
48. **LARSON et al.,** J. Fluid Mech. **218**, 573-600, 1990.
49. **LAX P. D.,** Numerical Solution of Partial Differential Equations: Finite Difference Methods, Oxford Applied Mathematics and Computing Series, p.72, 1985.
50. **LEONG C. W. et al.,** J. Fluid Mech. **209**, 463-499, 1989.
51. **LEWIS J. A.,** Ph.D. Thesis, Brown Univ., Providence, R. I., 1950.
52. **LIAO Y. and GODWIN A. C.,** Ind. Eng. Chem. Res. **34**, 936-942, 1995.
53. **LING F. H. and ZHANG X.,** J. of Fluids Engineering, **117**, 75-80, 1995.
54. **LIU C. Y., et al.,** Int. Dev. Heat Transfer **4**, 976, 1961.
55. **MARCUS P. S., and TUCKERMANN L. S.,** J. Fluid Mech. **185**, 1-30, 1987.
56. **MARTINI W. D., and CHURCHILL S. W.,** AIChE J. **6**, 251, 1960.
57. **McKENSIE D. P.** Scientific American , **249**, No. 3, 50-68, 1983.
58. **McKENSIE D. P., ROBERTS J. M. and WEIS N. O.,** J. Fluid Mech. **62**, 465-538, 1974.
59. **MITCHELL A. R. and GRIFFITHS D.F.,** The Finite Difference Method in Partial Differential Equations, Wiley, 1980.
60. **MOFFAT H. K.,** J. Fluid Mech. **18**, 1-18, 1964.
61. **MOON F. C.,** Chaotic and Fractional Dynamics (An Introduction For Applied Scientist And Engineers), Wiley-Interscience Publications, John Wiley and Sons Inc. New York 1992.
62. **MORTON K. Y. and MAYERS D. F.,** Numerical Solution of Partial Differential Equations, Cambridge University Press, 1994.
63. **NALLASAMY M. and KRISHNA PRASAD K.,** J. of Comp. Physics, **15**, 429-448, 1974.
64. **NI W., and NIGRO N. J.,** Int. J. for Num. Meth. in Fluids **19**, 207-236, 1994.

65. **NIEDERKORN T. C. and OTTINO J. M.,** J. Fluid Mech. **256**, 243-268, 1993.
66. **NORTHEY P. J. et al.,** J. Non-Newtonian Fluid Mech. **42**, 117-139, 1992.
67. **OTTINO et al.,** J. Fluid Mech. **269** 199-246, 1994.
68. **OTTINO J. M. and CHELLA R.,** Polymer Engineering and Science, **23**, 364-379, 1983.
69. **OTTINO J. M.,** The Kinematics of Mixing : Stretching, Chaos and Transport, Cambridge University Press, 1989.
70. **OZOE H. et al.,** J. Heat Mass Transfer **17**, 1209-1217, 1974.
71. **OZOE H. et al.,** J. Heat Mass Transfer **17**, 401-406, 1974.
72. **PAN F. and ACRIVOS A.,** J. of Fluid Mech., **28**, 643-655, 1967.
73. **PAO P. H.,** Transactions of The ASME, 470-480, 1970.
74. **PASQUETTI R., et al.**, Advanced Computational Methods in Heat Transfer II, Milan, Italy, 1992.
75. **POOTS G.,** Quart. J. Mech. and Applied Math. **11**, 258-273, 1958.
76. **RAMKISSOON H.,** Rheol. Acta, **24**, 623-626, 1985.
77. **RAYLEIGH,** Phil. Mag. S. 6. 32, No. 192, 1916.
78. **ROACHE P. J.,**Computational Fluid Dynamics, Alberquerque, Hermosa Publishers, 1976.
79. **ROPKE K. J., SCHUMMER P.,** Rheol. Acta **21**, 540-542, 1982.
80. **ROUX B. et al.,** Numer. Heat Transfer, **1**, 331-349, 1978.
81. **SASMAL G. P.,** J. of Non-Newtonian Fluid Mech. **56**, 15-47, 1995.
82. **SCHNIPKE R. J. and RICE J. G.,** Int. J. Num. Meth. in Eng. **24**, 117-128, 1987.
83. **SCHWENGELS S., and SCHULTZ D.,** Int. J. for Num. Meth. in Fluids **9**, 1099-1111, 1989.
84. **SCRATON R. E.,** Further Numerical Methods In Basic, Edward Arnold, 1987.
85. **SHAQFEH E. S. G. et al.,** J. Fluid Mech. **235**, 285-317, 1992.
86. **SHENOY A. V.,** Natural Convection Heat Transfer to Viscoelastic Fluids, Encyclopedia of Fluid Mech. Ed. Cheremisinoff, N. P., Gulf, Houston, 1988.
87. **SHU-MIN F. CHIAO and HUSEH-CHIA CHANG,** J. of Non-Newtonian Fluid Mech. **36**, 361-394, 1990.
88. **SIGINER A. and VALENZUELA R.,** Int. J. Engrg. Sci., forthcoming, 1994.
89. **SMITH G. D.,**Numerical Solution of Partial Differential Equations:Finite Difference Methods, Second Edition, Clarendon Press, Oxford, 1978.
90. **SURESHKUMAR R. et al.,** Proc. R Soc. London A, 1994.
91. **TANNER R. I.,** Engineering Rheology, Clarendon Press, Oxford, 1985.
92. **TAYLOR G. I.,** Philos. Trans. R. Soc. London Ser. A **223**, 289, 1923.
93. **TORRANCE K. G. and TURCOTTE D. L.,** J. Fluid Mech. **47(1)**, 113-125, 1971.
94. **TOSOKA N. et al.,** Int. J. Solid Structure **31**, 1847-1859, 1994
95. **TUCKERC. L.,**Fundamentals of Computer Modelling for Polymer Processing,Hanser Publishers, Munich, Vienna, New York, 1990.
96. **WALTERS K.,**Rheometry : Industrial Applications John Wiley and Sons, 1980.
97. **WATERS N. D. and KEELEY A. M.,** J. of Non-Newtonian Fluid Mech. **24**, 161-181, 1987.
98. **WILKES J. O. and CHURCHILL S. W.,** AIChE J. **12**, 161-166, 1966.
99. **YOUNG D.,** Academic Press, New York, 1971.